DEVELOPMENT OF A NUMERICAL TECHNIQUE FOR MODELLING OF MULTI-STAGE HYDRAULIC FRACTURING IN SHALE RESERVOIRS

Behnam Sobhaniaragh

Tese de Doutorado apresentada ao Programa de Pós-graduação em Engenharia Civil, COPPE, da Universidade Federal do Rio de Janeiro, como parte dos requisitos necessários à obtenção do título de Doutor em Engenharia Civil.

Orientadores: Webe João Mansur
Franciane Conceição Peters

Rio de Janeiro
Agosto de 2017

DEVELOPMENT OF A NUMERICAL TECHNIQUE FOR MODELLING OF MULTI-STAGE HYDRAULIC FRACTURING IN SHALE RESERVOIRS

Behnam Sobhaniaragh

TESE SUBMETIDA AO CORPO DOCENTE DO INSTITUTO ALBERTO LUIZ COIMBRA DE PÓS-GRADUAÇÃO E PESQUISA DE ENGENHARIA (COPPE) DA UNIVERSIDADE FEDERAL DO RIO DE JANEIRO COMO PARTE DOS REQUISITOS NECESSÁRIOS PARA A OBTENÇÃO DO GRAU DE DOUTOR EM CIÊNCIAS EM ENGENHARIA CIVIL.

Examinada por:

Prof. Webe João Mansur, Ph.D.

Prof. Franciane Conceição Peters, D.Sc.

Prof. José Claudio de Faria Telles, Ph.D.

Prof. Edivaldo Figueiredo Fontes Junior , D.Sc.

Prof. Delfim Soares Júnior, D.Sc.

RIO DE JANEIRO, RJ – BRASIL
AGOSTO DE 2017

Sobhaniaragh, Behnam

Development of a numerical technique for modelling of multi-stage hydraulic fracturing in shale reservoirs/Behnam Sobhaniaragh. – Rio de Janeiro: UFRJ/COPPE, 2017.

XXIV, 155 p.: il.; 29, 7cm.

Orientadores: Webe João Mansur

Franciane Conceição Peters

Tese (doutorado) – UFRJ/COPPE/Programa de Engenharia Civil, 2017.

Referências Bibliográficas: p. 133 – 155.

1. Hydraulic fracturing. 2. Cohesive phantom node method. 3. Non-planar crack propagation. 4. Cohesive crack model. 5. Stress shadowing effect. 6. Multi-lateral horizontal wellbores. 7. Numerical simulation. 8. Fracture process zone. 9. Shale reservoir. 10. Computational mechanics. I. Mansur, Webe João *et al.* II. Universidade Federal do Rio de Janeiro, COPPE, Programa de Engenharia Civil. III. Título.

Dedicated to my parents,
Ali and Azam

Acknowledgement

First and foremost, I would like to really thank my first supervisor Prof. Webe João Mansur for his guidance and strong support, for putting his trust in me by giving ample resources during my research period at Laboratório de Métodos de Modelagem e Geofísica Computacional (LAMEMO). He has always encouraged me to go one step further. My sincere thanks and appreciation to my second supervisor Prof. Franciane Conceição Peters for the opportunity to work for her and for her outstanding help, support, and valuable discussions during my stay in Brazil and the United Kingdom (UK).

I am also greatly indebted to Prof. Jon Trevelyan who guided me during my stay at Durham university, UK. He provided a productive environment, exposed me to many interesting subjects and challenged me with constructive criticism.

I would express my deepest gratitude to Prof. Vinh Phu Nguyen from Monash University, Australia, for valuable discussions and insightful suggestions on chapter 4 of this work.

Special thanks are reserved for examination committee members, particularly for Prof. Telles, Prof. Soares Jr and Prof. Fontes Jr for their useful comments and considerations.

My gratitude goes to Prof. Magd Abdel Wahab, my PhD supervisor in Ghent University, Belgium, who has been a valuable mentor and broadened my horizons in research.

I would also thank to Ivone Araújo, manager of our laboratory, for her help and lightening administrative burden.

Good work is impossible without a good atmosphere. I will never forget the nice moments with Pedro, Mohsen, Sebastioão, Jandyr, Eduardo, Edivaldo, Cid, Raphael, André, Katia, Ivan, Luciana, Anna Regina, Lívia, Paulo, Kymie, Flavio, Edmundo, and Natália at LAMEMO. I would also like to appreciate Gabriel, Hamed, Amir, Michael, Ben, and Mahmood for all of technical discussions and help during my stay at Durham.

I gratefully acknowledge CNPq for a doctorate fellowship. I would also like to acknowledge CAPES for a research grant for my stay at Durham University.

Most of all, I would like to give my deepest gratitude to my family, my dear parents Ali and Azam, my brother Babak, my sister Samira, without my family's unending encouragement, support, and love this work would have not been done. I am deeply grateful to Reza and Pegah for their great support. I also would like to appreciate my lovely nieces, Parmis and Sania for gifting so much laughter.

Resumo da Tese apresentada à COPPE/UFRJ como parte dos requisitos necessários para a obtenção do grau de Doutor em Ciências (D.Sc.)

DESENVOLVIMENTO DE UMA TÉCNICA NUMÉRICA PARA MODELAGEM DO FRATURAMENTO HIDRÁULICO DE MÚLTIPLOS ESTÁGIOS EM RESERVATÓRIOS DE XISTO

Behnam Sobhaniaragh

Agosto/2017

Orientadores: Webe João Mansur
Franciane Conceição Peters

Programa: Engenharia Civil

A eficiência da produção em reservatórios não convencionais, com baixa permeabilidade, demanda técnicas de perfuração de poços horizontais e fraturamento hidráulico (FH) de múltiplos estágios. As mudanças no campo de tensões, conhecidas como "stress shadowing", afetam significativamente o arranjo das fraturas e suas geometrias. Nesta tese, para apresentar uma técnica numérica capaz de capturar a propagação de trincas com caminhos imprevisíveis e enfrentar a viabilidade de emergência de múltiplas fraturas coesivas em meio poroso com zona de processo de fratura na ponta da trinca, é estabelecido o método dos segmentos coesivos combinado com o método do nó fantasma, cuja sigla em inglês é CPNM. O arcabouço numérico é implementado em um pacote para o método dos elementos finitos (ABAQUS®) por meio de rotinas definidas pelo usuário. Considerando um xisto de múltiplas camadas quase friável, dois cenários com FH sequencial e simultâneo com poço único são investigados. A validação da técnica numérica foi feita comparando a solução para uma fratura com a solução de Khristianovic-Geertsma-de Klerk (KGD) e fraturas duplas na presença de "stress shadowing". Depois disso, a análise foi estendida para dois poços laterais. Nesta parte, a maior contribuição é a investigação detalhada do efeito da alteração no campo de tensões como função do espaçamento das fraturas nos diversos projetos de FH em poços laterais adjacentes. Atenção particular é dada a projeto MZF com o objetivo de mitigar efeitos colaterais do "stress shadowing", melhorando a complexidade das fraturas, levando à modificação do projeto MZF, sendo este denominado M2ZF. Os resultados obtidos iluminam as vantagens do MZF, e em particular do M2ZF, na ativação de planos de fragilidade pré-existentes e fraturas naturais pelo efeito das mudanças no campo de tensões.

Abstract of Thesis presented to COPPE/UFRJ as a partial fulfillment of the requirements for the degree of Doctor of Science (D.Sc.)

DEVELOPMENT OF A NUMERICAL TECHNIQUE FOR MODELLING OF MULTI-STAGE HYDRAULIC FRACTURING IN SHALE RESERVOIRS

Behnam Sobhaniaragh

August/2017

Advisors: Webe João Mansur
Franciane Conceição Peters

Department: Civil Engineering

Production efficiency from low permeable unconventional reservoirs demands promoting techniques including horizontal well drilling and multi-stage Hydraulic Fracturing (HF) stimulation. What significantly affects the fractures arrangement, and associated geometries is the stress field changes, referred to as "stress shadowing". In this dissertation, in order to present a numerical technique, which is capable of capturing the non-planar hydraulically driven crack propagation with unpredictable path, on one hand, and tackling the feasible emergence of multiple cohesive cracks in a porous medium with fracture process zone at the crack tip, on the other hand, the Cohesive segments method in combination with Phantom Node Method, termed CPNM, is established. This numerical framework is implemented into a finite element analysis package (ABAQUS®) along with user-defined subroutines. Considering a quasi-brittle multi-layer shale, two key scenarios including sequentially and simultaneously multi-stage HF from an individual wellbore are investigated. Validation of the numerical technique has been performed by comparing the solution for an individual fracture with a Khristianovic-Geertsma-de Klerk (KGD) solution and double fractures in the presence of stress shadowing. Afterwards, the analysis is extended to two lateral horizontal wellbores. The main contribution of this part is the detailed investigation of the stress shadowing effects as a function of the fracture spacing at various HF design in adjacent lateral wellbores. A particular attention is devoted to MZF design with the aim of mitigating side-effects of stress shadowing and enhancing the far-field fracture complexity, leading to introducing a modification to MZF design, termed M2ZF. The results obtained are shedding light on the advantages of the MZF and in particular M2ZF in the activation of pre-existing planes of weakness and natural fractures through stress shadowing effects.

Contents

List of Figures

List of Tables

List of Symbols

Δ	Displacement jump vector, p. 75
G	Energy release rate, p. 23
G_{IC}	Critical energy release rate for mode I, p. 33
G_{eq}^{c}	Equivalent critical energy release rate, p. 77
$H(\mathbf{x})$	Heaviside step function, p. 44
J	J-integral, p. 27
P_0	Potential energy of an uncracked plate, p. 23
Q	Biot's modulus, p. 68
T	Formation tensile strength, p. 51
T_n, T_s, T_t	Normal, shear, and tear components of cohesive traction, p. 75
W_s	Work done to enhace the crack, p. 22
Δh	Typical element dimension, p. 72
Δt	Time increment, p. 72
Φ	Airy stress function to evaluate the singularity at the crack tip, p. 24
Ξ	Total energy of the system, p. 22
α	Wellbore azimuth, p. 49
$\bar{G}$	Shear modulus, p. 68
$\bar{q}$	Local fracturing fluid flow rate per unit width, p. 69
$\bar{\alpha}$	Biot's coefficient, p. 51
β	Wellbore inclination, p. 49

δ_n, δ_s, δ_t	Normal, shear, and tear components of displacement jump, p. 75
δ_{eq}	Effective displacement, p. 77
D	Scalar damage parameter, p. 76
E	Young module of the material, p. 22
K	Bulk modulus, p. 68
S	Set of all nodes in the FE mesh, p. 43
h	Crack height, p. 87
q	Weighting function defined over the domain of integration, p. 29
w	Strain energy density, p. 27
γ	Specific weight of pore fluid, p. 69
γ_s	Surface energy per unit area, p. 22
$\hat{Q}$	Total injection rate, p. 87
$\langle\rangle$	Macaulay bracket, p. 76
ε	Strain field, p. 39
P	Potential energy originated by the internal and external forces, p. 22
dA	Increased length of the crack, p. 23
v	Poisson's ratio, p. 25
μ	Viscosity of the fluid, p. 87
μ	Dynamic viscosity of the fluid, p. 68
σ_x, σ_y, σ_z	Stress fields in Cartesian coordinates, p. 24
$\mathbf{D}$	Material constitutive matrix, p. 39
$\mathbf{J}$	Jacobian matrix, p. 39
$\varphi(\mathbf{x})$	Signed distance measured from the crack, p. 79
k	Permeability of the porous medium, p. 68
p	Formation poe pressure, p. 51

p_j^A	Standard pressure degree of freedom for the node *j* which belongs to the element *A*, p. 80
u_x, u_y, u_z	Displacement fields in Cartesian coordinates, p. 24
x_0	Equilibrium space between two atoms, p. 22
G_c	Critical energy release rate, p. 23
G_n, G_s, G_t	Normal, shear, and tear components of fracture energy release rate, p. 77
$I^{(1,2)}$	Interaction integral for states (1) and (2), p. 28
K_T, K_S	Bulk moduli of the porous rock and the solid grains, p. 68
K_f	Bulk modulus of the pore fluid, p. 68
$K_i^{(j)}$	stress intensity factor in mode i for an auxiliary state (j), p. 28
K_I, K_{II}, K_{III}	Stress intensity factors in modes I, II, and III, p. 25
K_i	Critical stress intensity factor, p. 26
S_C	Set of nodes of elements around the crack tip, p. 43
S_H	Set of nodes of elements cut by the crack but not in S_C, p. 43
$S_{H,\max}$	Maximum in-situ horizontal stress, p. 82
$S_{h,\min}$	Minimum in-situ horizontal stress, p. 82
${T_n}^0$, ${T_s}^0$, ${T_t}^0$	Maximum normal, shear, and tear components of cohesive traction, p. 75
Γ_d	Discontinuity domain, p. 42
$\boldsymbol{\sigma'}$	Effective stress acting between solid grains, p. 67
δ'_n	Crack normal opening, p. 80
δ'_t	Tangential sliding, p. 80
$\hat{P}$	Constant fluid pressure within the crack, p. 86
$\mathbf{I}$	Second-order unit tensor, p. 67
$\mathbf{K}_e$	Stiffness matrix of an element *e*, p. 39
$\mathbf{u}^A$	Displacement field of the sub-domain A, p. 79

$\mathbf{u}^B$	Displacement field of the sub-domain B, p. 79
ϕ_0	Initial porosity, p. 68
$\psi(\mathbf{x})$	Enrichment function, p. 43
σ_c	Critical normal stress, p. 23
${\sigma_{ij}}^0$	Initial principal in-situ stress, p. 68
σ_{ij}	Stress tensor, p. 27
ε_{ii}	Volumetric strain, p. 68
ζ	Admissible test function for the fluid pressure field, p. 72
n_j	Unit outward normal vector to the contour integral, p. 27
p^0	Initial fluid pore pressure, p. 68
p_F	Pressure of the fracturing fluid along the crack surface parameterized with the curvilinear coordinate, p. 69
p_w	Internal borehole pressure, p. 50
p_{wf}	Breakdown pressure, p. 51
r_w	Borehole wall, p. 51
t_n, t_s	Normal and shear components of the 2-D traction vector, p. 48
v_i	Darcy velocity of the pore fluid, p. 68
v_{bot}	Normal flow velocities at which the fracturing fluid infiltrates through the bottom faces of the fracture into the porous medium, p. 69
v_{top}	Normal flow velocities at which the fracturing fluid infiltrates through the top faces of the fracture into the porous medium, p. 69
x_c	Crack half-length, p. 86
$\Psi^{(j)}$	Set of enrichment functions which approximate the near tip behaviour, p. 44
δ_c	Critical separation, p. 32
$\mathbf{B}_j$	Derivatives of the shape functions, p. 39

$\mathbf{N}_j$	Matrix of FE shape functions, p. 38
$\mathbf{T}$	Cohesive traction vector, p. 75
$\mathbf{n}_{\Gamma_d}, \mathbf{t}_{\Gamma_d}$	Unit vector of normal and tangential directions, respectively, p. 48
$\mathbf{q}_I^{(j)}$	Enrichment coefficients which are extra unknowns at the node, p. 44
$\mathbf{t}_d$	Cohesive traction transferred along Γ_d, p. 48
∇^s	Symmetric part of the gradient operator, p. 72
$\overline{\mathbf{N}}_j(\mathbf{x})$	Shape functions of enhanced section, p. 43
$w^{(1,2)}$	Interaction strain energy for states (1) and (2), p. 28
$\overline{\mathbf{a}}_{ij}$	Enriched degrees of freedom, p. 41
$\overline{\mathbf{u}}_i$	Standard nodal degrees of freedom, p. 41

List of Abbreviations

CO_2	Carbon dioxide, p. 2
2-D	Two-Dimensional, p. 5
3-D	Three-Dimensional, p. 5
BACS	Ball-ACtivated Systems, p. 11
BEM	Boundary Element Method, p. 52
BK	Benzeggagh-Kenane, p. 77
BPM	Bonded-Particle Model, p. 57
Bcf/d	Billion cubic feet per day, p. 6
CBM	CoalBed Methane, p. 7
CCM	Cohesive Crack Model, p. 30
CCS	Carbon dioxide Capture and Storage, p. 2
CDM	Continuum Damage Models, p. 35
CMOD	Crack Mouth Opening Displacement, p. 86
CMP	Crack Mouth Pressure, p. 86
CPNM	Cohesive Phantom Node Method, p. 15
CSG	Coal Seam Gas, p. 7
CTACS	Coiled Tubing-ACtivated Systems, p. 11
DDM	Displacement Discontinuity Method, p. 53
DEM	Discrete Element Method, p. 56
DFN	Discrete Fracture Network, p. 53

DOF	Degrees of Freedom, p. 41
ECCM	Extrinsic Cohesive Crack Model, p. 75
FEM	Finite Element Method, p. 27
FGM	Functionally Graded Materials, p. 46
FIP	Fracture Initiation Pressure, p. 5
FPP	Fracture Propagation Pressure, p. 5
FPZ	Fracture Process Zone, p. 15
FS	Fracture Spacing, p. 15
HF	Hydraulic Fracturing, p. 2
KGD	Khristianovic-Geertsma-de Klerkm, p. 10
LBM	Lattice Boltzmann Method, p. 58
LEFM	Linear Elastic Fracture Mechanics, p. 16
M2ZF	Modified MZF, p. 16
MZF	Modified Zipper-Frac, p. 16
NF	Natural Fracture, p. 53
PFP	Preferred Fracture Plane, p. 63
PKN	Perkins-Kern-Nordgren, p. 10
PNP	Plug-and-Perforate, p. 11
SIF	Stress Intensity Factors, p. 25
SRV	Stimulated Reservoir Volume, p. 13
Seq-HF-1	Double-stage sequentially HF with fracture spacing of 15 m, p. 86
Seq-HF-2	Triple-stage sequentially HF with fracture spacing of 7.5 m, p. 86
Seq-HF	Sequentially HF, p. 13
Sim-HF-1	Double-stage simultaneously HF with the fracture spacing of 15, p. 86

Sim-HF-2	Triple-stage simultaneously HF with the fracture spacing of 7.5 m, p. 86
Sim-HF	Simultaneously HF, p. 13
Tcf/d	Trillion cubic feet per day, p. 6
XFEM	eXtended Finite Element Method, p. 16

Chapter 1

Introduction

1.1 Hydraulic fracturing

Fracturing has been a crucial topic of attention in engineering science, and emerged in several multi-physics problems, ranging from thermo-mechanical fracturing to hydraulically fluid-driven fracturing at isothermal and non-isothermal conditions, fracturing owing to radiation or hydrogen embrittlement, fracturing caused by chemical effects and others. Among all of the applications of fracturing, hydraulically fluid-driven fracturing noted as "Hydraulic Fracturing (HF)", which is widely used in the petroleum industry to enhance the recovery of hydrocarbons from underground reservoirs, has attracted a lot of attention. As shown in Figure 1.1, HF is a mechanism by which a fracture is initiated and propagated in a rock material by injecting large quantities of a pressurized fluid from a borehole into the perforation. Various examples of the HF applications encompass:

- The stimulation of rock formations with poor or damaged permeability to enhance conductivity between the reservoir and the wellbore.
- Cuttings re-injection where a slurry of drill cuttings is injected into a formation to mitigate the cost and risk of surface disposal.
- Both enhanced gas recovery and Carbon dioxide (CO_2) Capture and Storage (CCS) by CO_2 injection into organic-rich gas shales (KHOSROKHAVAR *et al.*, 2014; KIM *et al.*, 2017).
- Measurement of in-situ stress with making use of balancing the fracturing fluid pressure in a hydraulically opened fracture with the geostatic stresses.
- Extraction of geothermal energy from geothermal reservoirs with high temperatures or temperature gradients (BERUMEN *et al.*, 2000).

In addition, hydraulic fractures which are naturally triggered by pressurized fluid in the host rock can be found in outcrops as joints (LACAZETTE and ENGELDER, 1992) and veins (SRIVASTAVA and ENGELDER, 1991), as well as magma-driven dikes (RUBIN, 1995). In the oil and gas industry, HF commenced during the 1930s when Dow Chemical Company discovered that by injecting a large enough fluid pressure, it was probable to fracture the rock formation to provide a more effective acid stimulation (GREBE and STOESSER, 1935). The first non-acid HF for well stimulation was proposed in Kansas in 1947 on a gas well in Hugoton field to weigh the new treatment against the available acidization technique (VEATCH JR and MOSCHOVIDIS, 1986). Nowadays, HF makes possible the production of oil and natural gas from rock formations and low permeability reservoirs, specially unconventional resources, deep below the earth's surface (1.5–6.1 Km) which is commonly considerably below groundwater reservoirs or aquifers on the reports by GREGORY *et al.* (2011); HOWARTH *et al.* (2011); VENGOSH *et al.* (2014). At

such depth, there may not be reservoir pressure or adequate permeability to permit oil and natural gas to proceed from the reservoir to the wellbore at economic flow rates. Therefore, HF technique plays a crucial role in enhancing the rock permeability.

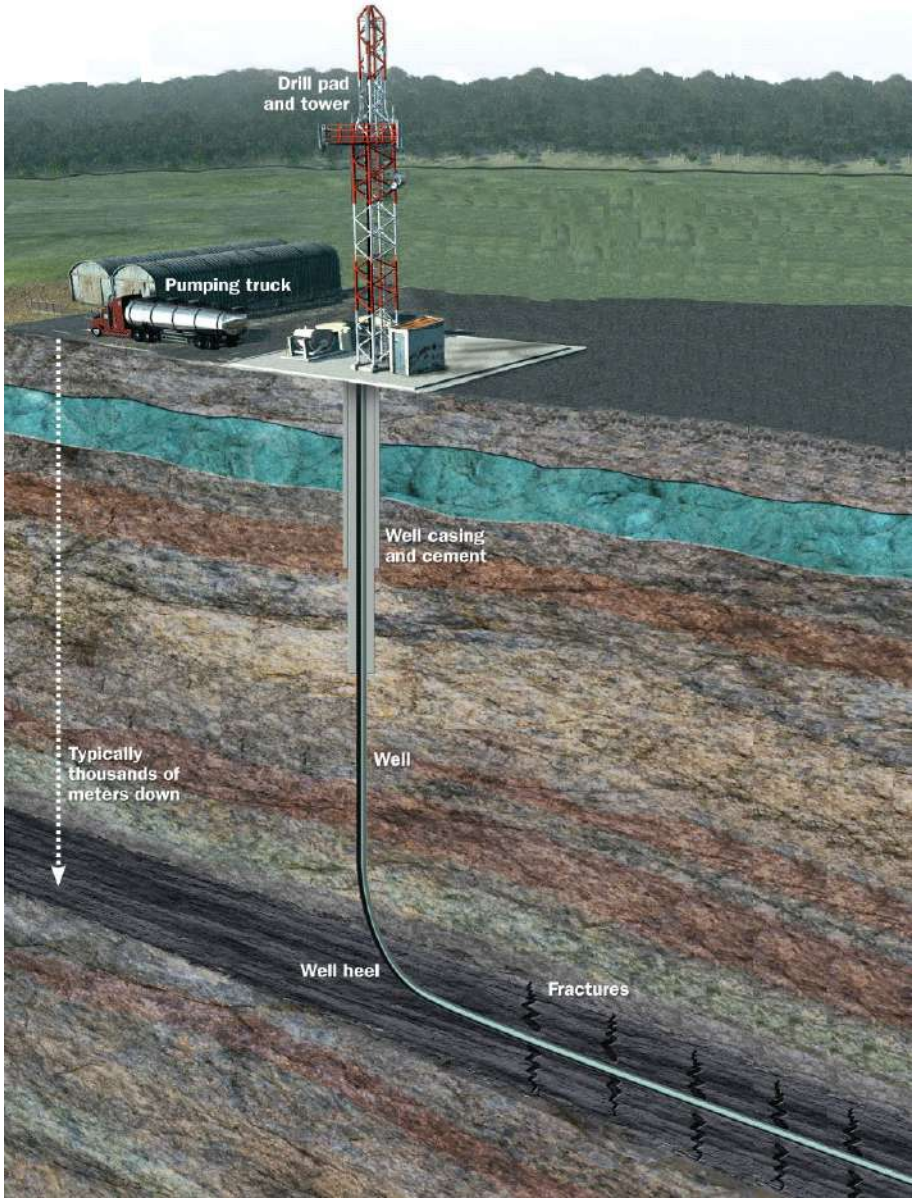

Figure 1.1: Schematic representation of hydraulic fracturing process.

HF treatment consists of two main phases (WEIJERS, 1995):

- Firstly, after perforating the casing and making finger-like perforations or weak points in the formation, a viscous fluid called a "pad" or "fracturing fluid" is pumped into the well. When the downhole pressure goes beyond "breakdown pressure" a fracture launches from the perforated interval and propagates in the surrounding rock. Whereas the fracture length and volume rise, much more fracture area is disclosed and wetted with pad fluid as a result of percolation of the fluid into the formation. Continuous pumping of fracturing fluid extends the fractures and keeps the

fractures open to provide a proper pathway to convey large quantities of propping agent inside the induced fractures. Both Newtonian fluids, such as water, and non-Newtonian fluids, such as polymer solutions, microemulsions, and macroemulsions, are often injected into the reservoir as HF fluids. The application of a non-Newtonian fracturing fluid makes greater fractures and, as a result, better well production. Nevertheless, the initial investment in HF cost is considerable higher (HARELAND *et al.*, 1993).

- In the second phase, a slurry of fluid mixed with proppant is injected into the generated fractures. The slurry transports the proppants and places them in opened (fractured) volume. The proppants prop the fracture walls and maintain a highly conductive propped way for the flow of oil and gas to the wellbore. The slurry is pumped several stages at which the concentration of the proppant is different. It is worth noting that the ultimate stage of slurry injection mainly has the greatest proppant concentration (VEATCH JR and MOSCHOVIDIS, 1986).

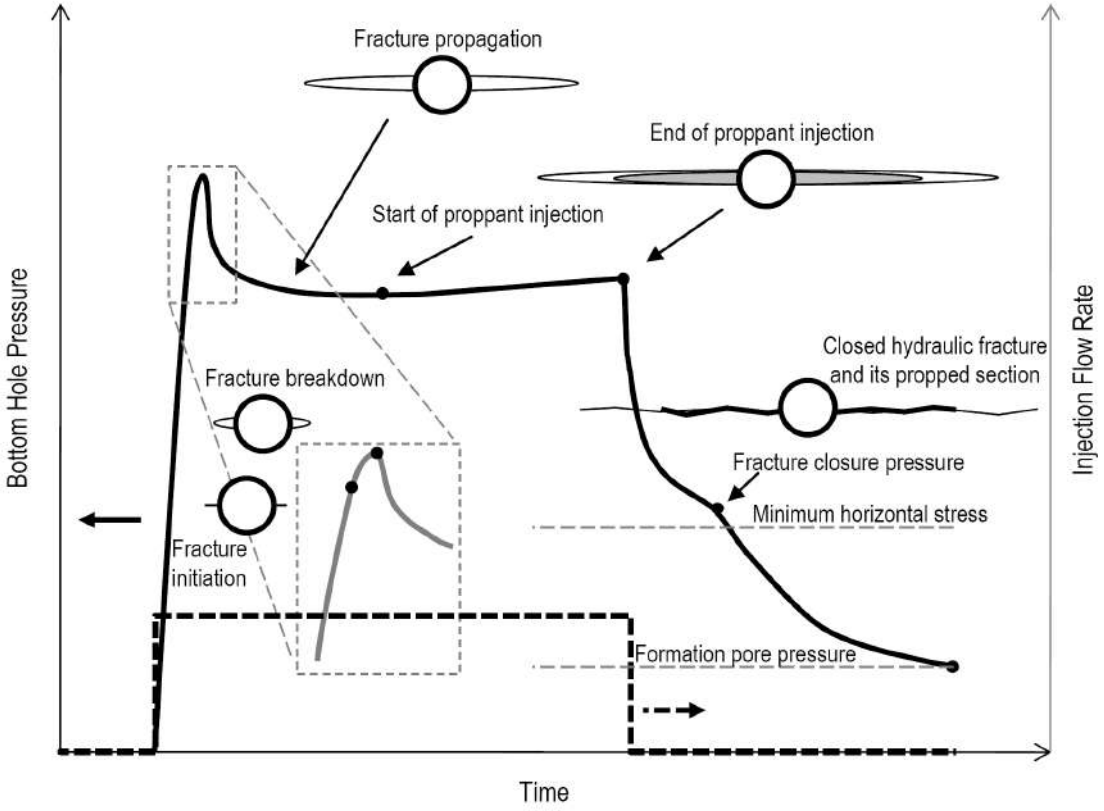

Figure 1.2: Typical pressure-time curve in a HF test (Modified after (MOOS, 2006)).

A hydraulically driven-fracture propagates in the direction normal to the smallest of the principal stresses as it tends to grow along the path of least resistance. For majority reservoir depths of interest, the smallest principal stress lies in the horizontal plane, which

limits fractures to the vertical plane. Hence, resulting fracture would be oriented and grow in the vertical direction. However, in more complicated situations a truly Three-Dimensional (3-D) simulation may be required to adequately predict the aspects of the HF event. In some cases, available 3-D models in the literature (RUNGAMORNRAT *et al.*, 2005) are computationally expensive and, as a result, Two-Dimensional (2-D) analysis on the horizontal plane shall be investigated to avoid further complexities. The 2-D model can provide a framework for supplementary developments to 3-D analysis.

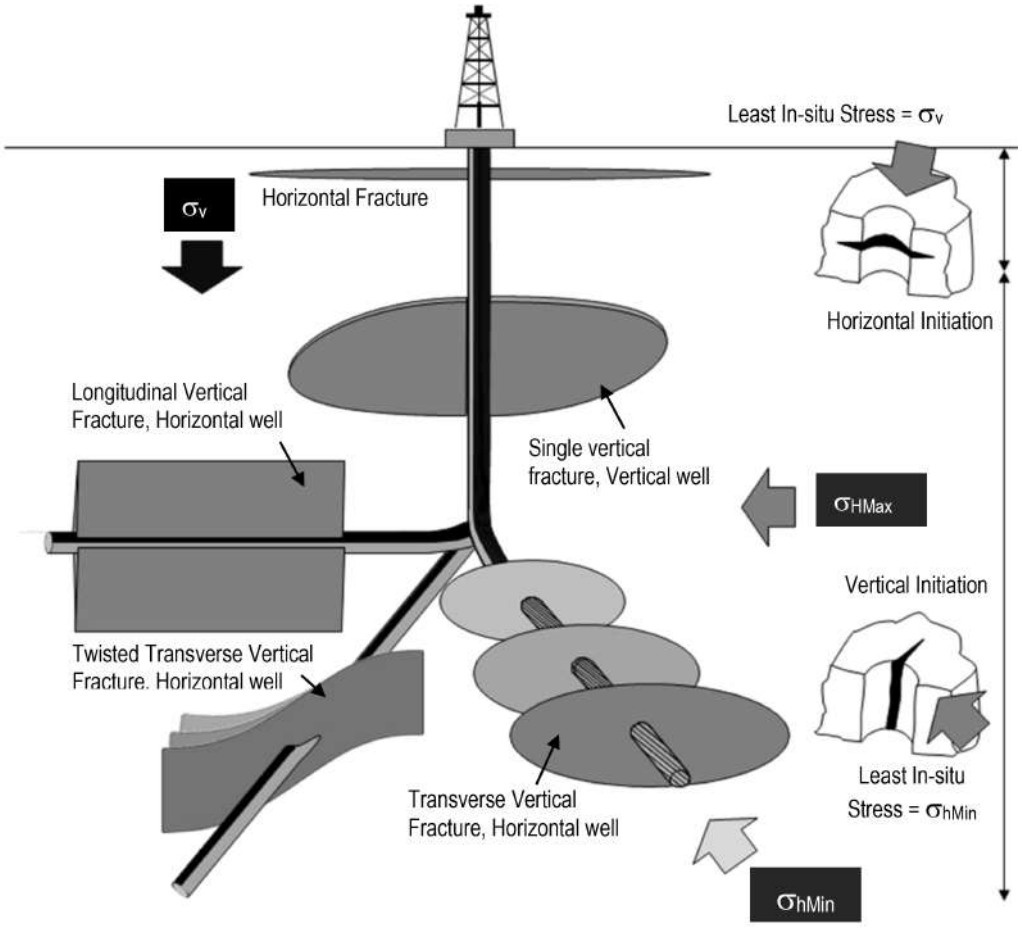

Figure 1.3: Fracture configurations from a horizontal well (Modified after (VALK and ECONOMIDES, 1995)).

A typical pressure-time curve corresponding to a HF treatment is demonstrated in Figure 1.2. As can be seen in Figure 1.2, when the traction forces attain the tensile strength of the rock formation, the fracture starts to initiate. After fractures are initiated, the fracturing fluid starts gradually entering the fracture, fracture breakdown happens, and the wellbore pressure attains the Fracture Initiation Pressure (FIP) by increasing wellbore pressure. Then the fracture propagates and the fracture pressure falls to Fracture Propagation Pressure (FPP). The nearly constant segment of the pressure-time curve belongs to the FPP. As shown in this figure, FPP is higher than the minimum horizontal stress but is lower than FIP. The growth of the fracture terminates once the maximum fracture length under

the current conditions is acquired. are the imperative data desired for a HF study. Estimation of Fracture initiation and propagation pressures, which are imperative data desired for a HF study, is not straightforward, since they are affected by a number of parameters involving formation mechanical parameters and the state of in-situ stresses.

In most HF cases, the minimum stress is the minimum horizontal stress, causing vertical fractures which are perpendicular to the direction of fracture growth. Consequently, horizontal well trajectory demonstrates two confining cases, as seen in Figure 1.3, one positioned along the minimum stress, which would end in transverse fractures; and the other drilled in the direction of the maximum in-situ horizontal stress, which would allow to achieve longitudinal fractures. Typically, the operation depth, wellbore trajectory, and the state of stresses play an important role in creating the transverse, longitudinal or different types of fracture planes (VALK and ECONOMIDES, 1995).

1.2 Unconventional reservoirs

Unconventional development of energy resource plays has evolved into a global pursuit for many oil and gas exploration companies, and launched a new way of thinking about hydrocarbon production (STEVENS, 2012). The revolution of unconventional reservoirs are altering the energy market in the worldwide, contributing to the downward pressure on gas prices across the globe and the imminent independence of the United States on natural gas imports. From 2008 to 2012, crude oil and natural gas liquids production in the evidence rocketed from 6.78 million barrels per day to 8.91 million barrels per day, an increase of over 31 percent. mainly on account of horizontal wells and HF in shale and tight formations that were previously inaccessible (WINEGARDEN, 2016). The weight on horizontal wells over vertical stems from a consequence of the former's potential to contribute more exposure to a formation.

Currently, a myriad of commercial shale resource plays are situated in North America, with the vast majority in U.S., as shown in Figure 1.4. The Marcellus Shale extended in the areal of 246,000 Km^2 in northeastern U.S. ranks as the largest play. As a remarkable evidence of the success in producing gas from shales, in 2008, the Barnett Shale became the greatest gas-producing play or formation in the evidence, contributing 7 percent of all the natural gas produced in the contiguous 48 states for that year (BOYER *et al.*, 2011), followed by success in other gas shale plays. In March 2011, after only three years of development, the prolific Haynesville-Bossier Shale in Louisiana and east Texas produced 159.1 million m^3/d [5.62 Bcf/d] of natural gas, exceeding the Barnett Shales 152.9 million m^3/d [5.40 Bcf/d]. In 2010, 137.9 billion [4.87 Tcf] of dry gas was produced from the diverse shale resource plays in U.S., as shown in Figure 1.5.

Exploration interest from unconventional reservoirs is increasing on a global scale as petroleum companies have initiated to implement HF technique commercially in other

parts of the world, such as Europe, South America and Australia. In case of Brazil as the largest country in South America, at least nine deposits of oil shale ranging from Devonian to Tertiary age have been reported in different parts of country (PADULA, 1969). Of these, two deposits have attracted the most attention: (a) the lacustrine oil shale of Tertiary age in the Paraíba Valley in the State of São Paulo northeast of the city of São Paulo; and (b) the oil shale of the Permian Iratí Formation, a widespread unit in the southern part of Brazil, as depicted in Figure 1.6.

Unconventional resources include shale oil and gas, tight oil and gas (typically sedimentary rocks), CoalBed Methane (CBM), which also is referred to as Coal Seam Gas (CSG). Unconventional reservoirs can be differentiated from conventional ones based on the amount of permeability. Reservoirs with permeability higher than 0.1 mD are regarded conventional, and those with permeability below that cutoff are named unconventional, albeit there is no scientific basis for such a classification. According to a more recent definition, unconventional reservoirs are those that can be extracted neither at economic flow

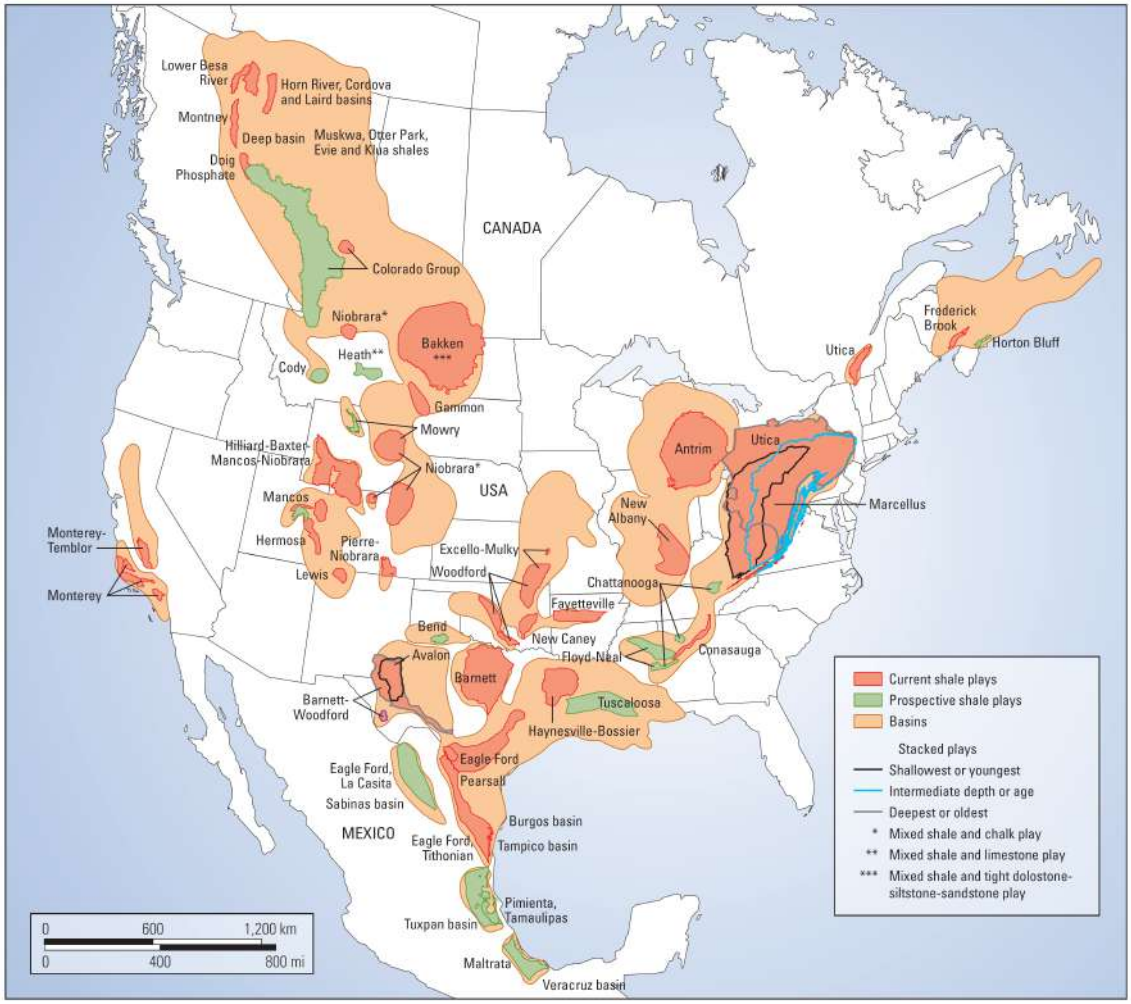

Figure 1.4: North America shale plays (UNITED STATES, ENERGY INFORMATION ADMINISTRATION, 2011).

rates nor in economic volumes unless the well is stimulated by HF or acquired by a horizontal wellbore, or other procedures to reveal further part of the reservoir to the wellbore.

1.3 Modeling of hydraulic fracturing

Contributed considerably to long-term oil and gas production, the geometry of hydraulically driven-fluid fractures including length, aperture, height, and propagation pattern, is virtually inspected by means of post-fracturing data acquisition methods such as tiltmeter fracture mapping (WRIGHT *et al.*, 1998) and micro-seismic monitoring (CIPOLLA *et al.*, 2008). However, both techniques suffer from a limitation of availability of potential monitoring wells. Also, the later method cannot determine the width of hydraulic fractures because the only detectable events using this diagnostic technique are shear slippage events (BENNETT *et al.*, 2005). In addition, the practical conditions such as rock properties, in-situ stresses, characteristics of fracturing fluids and proppants, under which HF treatments is performed, alternate widely. It is currently probable to measure the fracture geometry accurately only during or after the HF process. Therefore, the reliable modeling of the HF process is of special importance. On the other hand, in recent years the potential application of HF technology has led to great worries regarding detrimental environmental impact, especially in Europe (GANDOSSI, 2013). Deployment of high-volume HF shall potentially involves some risks to the environment such as methane infiltration in aquifers, aquifer contamination, extended surface footprint, and so on. Consequently, HF projects, in which the environmental concerns about ground water contamination is warning, the induced fractures demand to be cautiously located in order not to propagate into the upper and lower geological layers. Such a rigorous HF design requires reliable

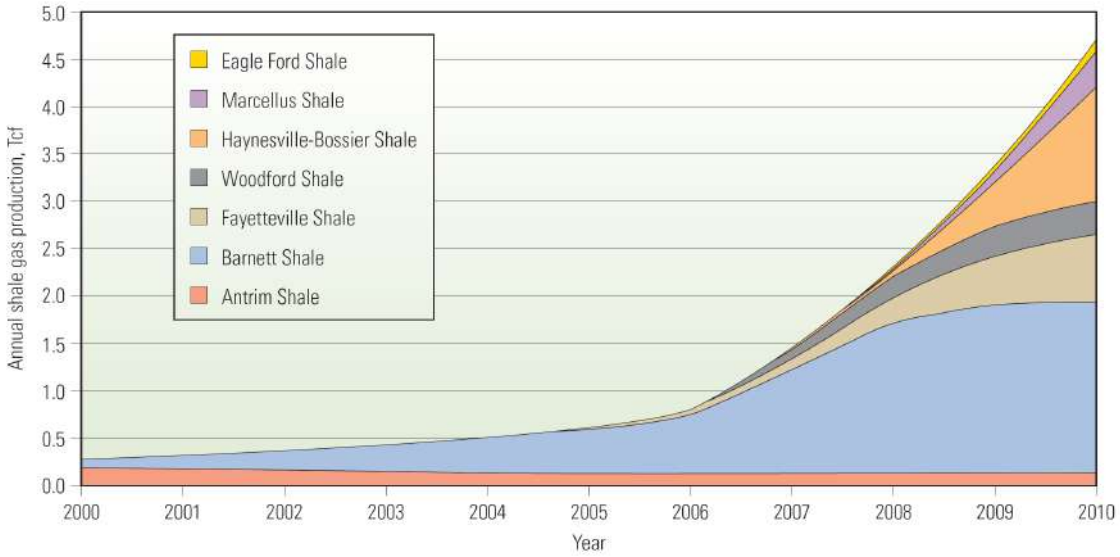

Figure 1.5: A prompt incline in gas production from shales in the United States since 2000 (BOYER *et al.*, 2011).

Figure 1.6: Deposits of oil shale in Brazil (PADULA, 1969).

and robust numerical techniques.

Generally, HF is a troublesome process to model in a poro-elastic material, as it involves the coupling of diverse and extensive range of physical mechanisms including:

- Deformation of the solid skeleton induced by the fluid pressure on the fracture surfaces,
- Flow of the pore fluid through the poro-elastic medium surrounding the fracture,
- Fluid flow within the fracture,
- Fluid exchange between the fracture and poro-elastic medium,
- The propagation of hydraulically-driven fracture.

The partial differential equations governing the propagation of hydraulic fracture in the porous medium include the equilibrium equation for the porous medium, the continuity equation for fluid flow through the surrounding porous medium and within the fracture, and

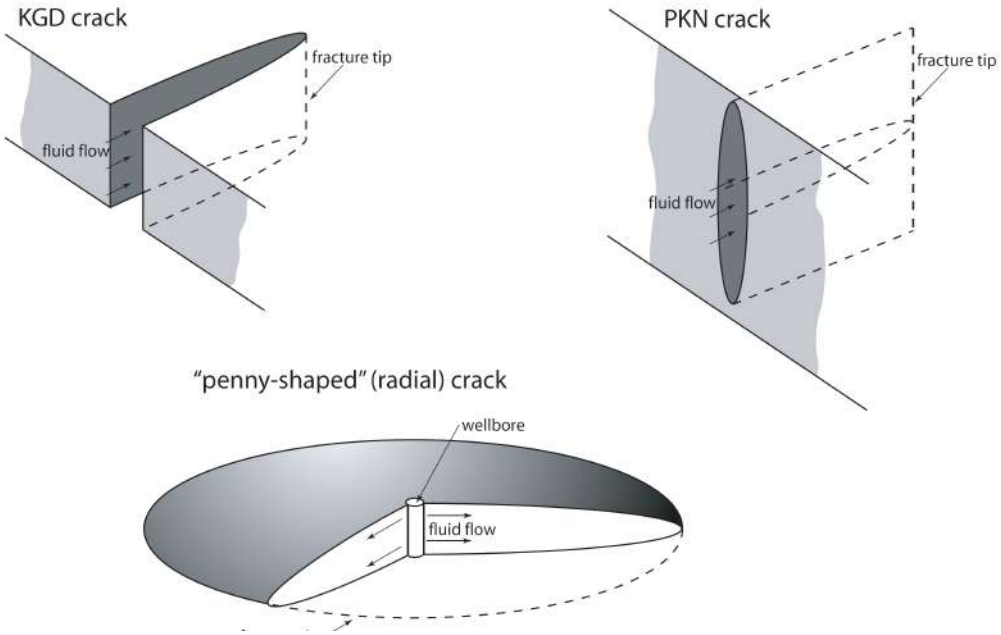

Figure 1.7: Schematic view of analytical HF models (ADACHI *et al.*, 2007; ADACHI, 2001).

momentum equation for the pore fluid and fracturing fluid. Since 1947 when the HF technique was proposed to the petroleum industry, its application has developed briskly. In the early 1950's, in response to the essential requirement of the industry to a design tool for this crucial technique, a number of 2-D closed-form models (see Figure 1.7) were established to simulate HF treatments. The first simplified theoretical hydraulic fracture models were established in the 1950s, starting with the pioneering work of PERKINS *et al.* (1961) who developed the classic Sneddon plane strain crack solution. Fluid loss was contained in this model by NORDGREN *et al.* (1972) and is now regarded as the Perkins-Kern-Nordgren (PKN) model. Later, the so-called Khristianovic-Geertsma-de Klerk (KGD) model for the plane strain HF was presented by GEERTSMA *et al.* (1969) and KHRISTIANOVIC and ZHELTOV (1955). The radial or penny-shaped model with constant fluid pressure was solved SNEDDON (1946). These models elaborated analytical expressions for deriving the fracture length, the maximum fracture opening, and the fracturing fluid pressure for a constant injection rate. Aforementioned simple analytical solutions, which simulate propagation of single planar fracture, have been considered by the industry with some success, but, as the technology has proceeded from simple low volume/rate to considerably high volume/rate treatments and far more intricate and sophisticated HF projects, the industry has necessitated more rigorous techniques so as to minimize the operational cost.

1.4 Initial fracturing wellbore completion

Thanks to astonishing advances in science and technology in recent years, combination of horizontal well drilling and multistage HF technology has unlocked vast unconventional reservoirs, launching a renaissance in oil and natural gas production. For HF job on a horizontal wellbore, completions are separated by the techniques of isolating fracturing sections and diverting fracturing fluid to perforations. Presently, three types of completions have proved to be the most effective and adequate in the North American unconventional plays. These completions are Plug-and-Perforate (PNP), Ball-ACtivated Systems (BACS) (such as the Baker Hughes FracPoint system), and Coiled Tubing-ACtivated Systems (CTACS) (such as the Baker Hughes OptiPort and OptiFrac systems) (AHMED and MEEHAN, 2016).

As can be seen in Figure 1.8, the PNP method incorporates cement to distinguish the annulus between the openhole and the steel pipe, also perforations switch the fracturing fluid into the wellbore at the desired location, and composite fracturing plugs supply iso-

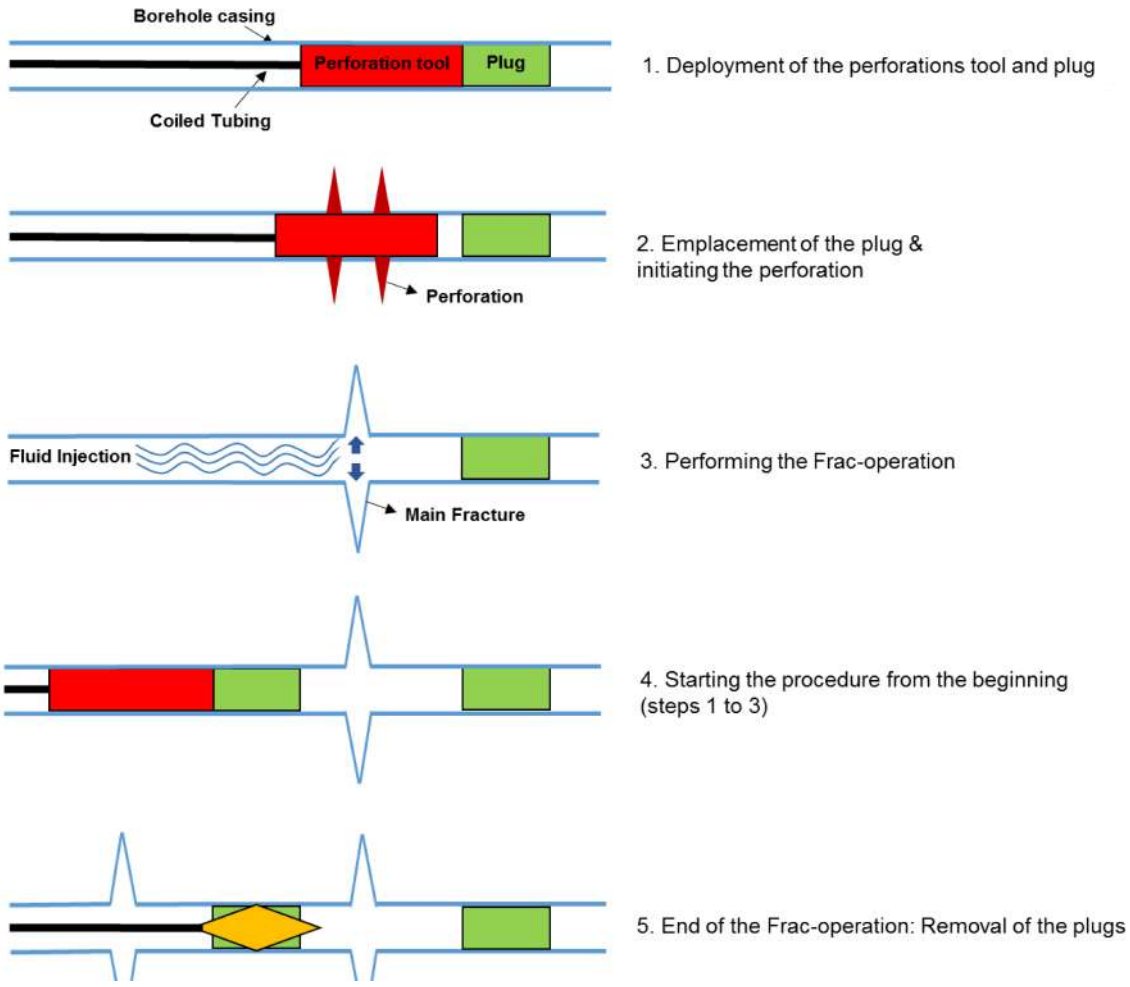

Figure 1.8: Wellbore diagram of plug-and-perforation job. (AHMED and MEEHAN, 2016).

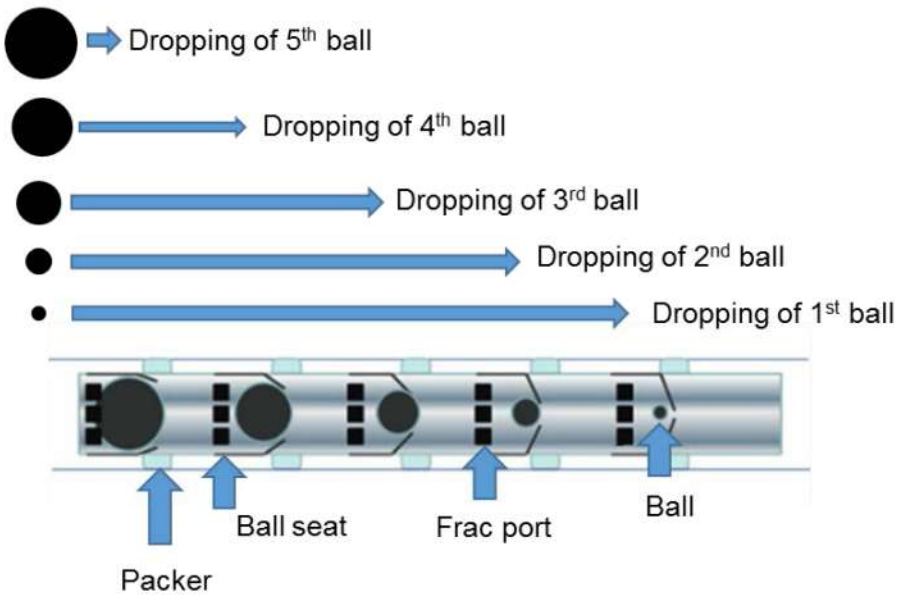

Figure 1.9: Schematic view of ball-activated systems job. (DANESHY *et al.*, 2011).

lation from the stages below. At the end of an in-tended fracturing operation, plugs are removed by a milling head. BACS (see Figure 1.9) consists of three mechanical parts integrated on a liner hanger or on a long-string as follows; Frac ports at where a fracking material is pumped; Sliding sleeves which consists of frac ports on it and shifts via pressure increase through the sealing of a dropped ball and opens frac ports; and lastly gradually sized balls fallen from surface into sliding sleeves. Sliding sleeves shift and open frac ports along an intended stage for fracturing. Frac ports can be then activated and fracturing can be performed at specific operational depth using chosen fracturing material. Balls plays an important roll in offering both activation and sealing functions, thus, HF can be conducted by gradually sized balls at different stages. CTACS shown in Figure 1.10 is a combination of packers and perforation tools integrated on a coiled tubing. Packer has the function of

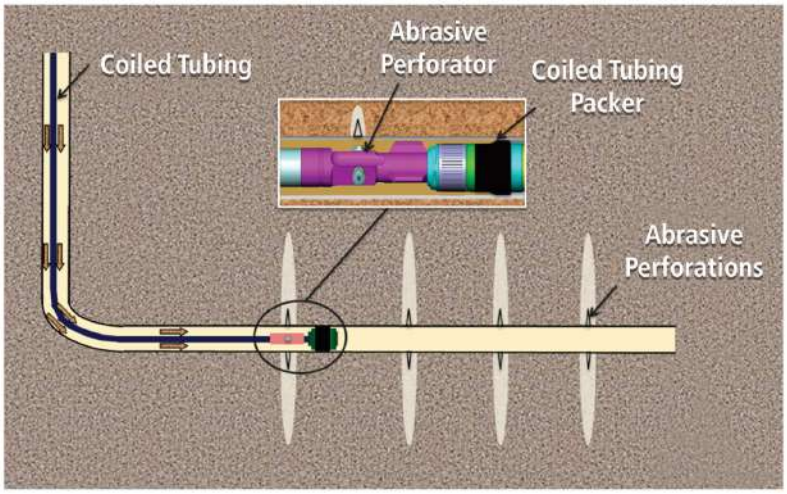

Figure 1.10: Coiled tubing-activated systems (AHMED and MEEHAN, 2016).

zonal isolation between perforated intervals, and a special tool is used to perforate through the intended stage before the stimulation will be made by selected fracturing material. In all aforementioned completions, commencing from the "toe" of the horizontal well and working back to the "heel" of the well, a horizontal well is topically fractured multiple times during series of stages, leading to create multiple fractures so as to enhance the reservoir contact area. In each stage, the well is perforated in multiple perforation clusters with the aim of creating a separate fracture within each cluster. The procedure of portioning a horizontal well into several stages and propagating multiple fractures simultaneously or sequentially is called "multistage fracturing".

1.5 Stress shadowing effect

In the oil and gas industry, the completion of HF from horizontal wells is commonly performed using one of the two well-known schemes namely, Simultaneously HF (Sim-HF) and Sequentially HF (Seq-HF). The Sim-HF deals with perforating multiple intervals at the same time with near spacing so as to not only create stress interference resulting in substantial fracture network, but also reduce the standby time during the fracturing job. Further, in Seq-HF, perforations are treated in series and, as a result, the fractures are enhanced one after another from toe to heel of the horizontal wellbore. At first glance, placing as many multi-stage and clusters per stage as possible in the horizontal well and minimizing the spacing between fractures may maximize the total Stimulated Reservoir Volume (SRV) and achieve an optimum depletion of the reservoir. However, it is not apparent that production and recovery are proportionally connected to increased number of fractures (CIPOLLA *et al.*, 2009; WARPINSKI *et al.*, 2009). Observations from enormous amount of field data demonstrate that between 20 to 30 percent of perforation clusters are unproductive. Indeed, recent post-fracturing data acquisition methods such as micro-seismic monitoring and strain sensing (SIERRA *et al.*, 2008; SPAIN *et al.*, 2015) have elaborated that all of the multiple fractures do not grow at the same time and some of them become terminated during the treatment.

Undoubtedly, the stress perturbation owing to placement of multiple fractures can affect the fracture geometry such as length, aperture, height, and propagation and orientation pattern. When multiple fractures on a single or multi-wellbores are located close enough together, stress interference effects among them, which is known as "stress shadowing" or "altered-stress fracturing" (WARPINSKI *et al.*, 1989), occur which are not taken account in single HF treatment. The stress shadowing induced by the hydraulic fractures tends to repel or attract other late-coming hydraulic fractures, depending on proposed HF scenarios. Even prior to emerging commercial HF in 1950, the interference between neighbouring fractures had been studied. For the first time, SNEDDON (1946) discussed the stress distribution in the neighbourhood of a crack in an elastic solid. In the petroleum

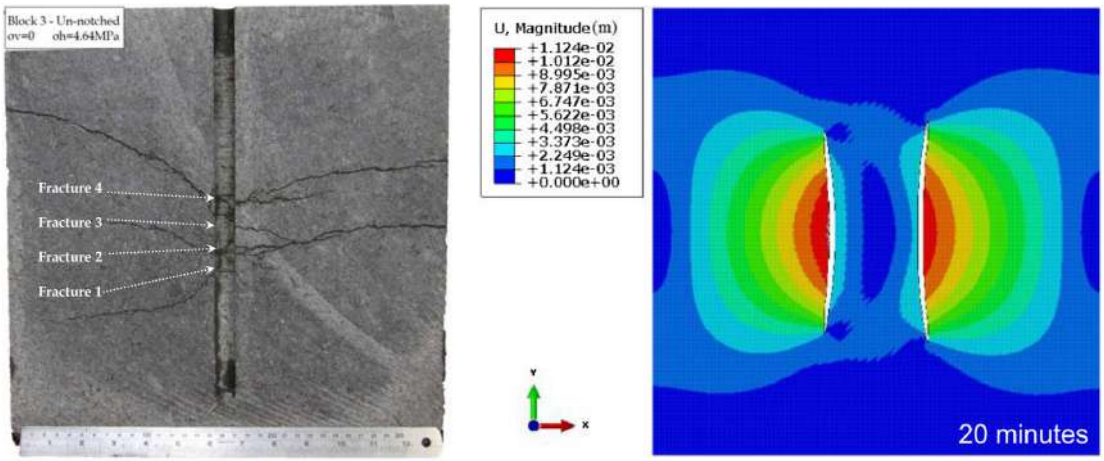

(a) (b)

Figure 1.11: **(a)**: Cross section of experiment block (BUNGER *et al.*, 2011). **(b)**: Propagating fracture geometry with fracture spacing of 19 m by using a numerical technique (WANG, 2016a).

engineering, before all else WARPINSKI *et al.* (1989) suggested taking advantage of stress reorientation in the region of effect to generate a favorable fracture orientation. Figures 1.11a (BUNGER *et al.*, 2011) and 1.11b (WANG, 2016a), which are resulted from laboratory experiment and numerical study, respectively, show that fracture spacing has a profound influence on the hydraulic fracture interactions.

It is widely approved that stress shadowing effects are potentially crucial to the design of multi-stage HF, thus, multi-stage HF treatment should not be designed identical to a single HF simulation (BUNGER *et al.*, 2012). A thorough grasp of stress shadowing brings remarkable advantages with regard to risk alleviation on the cost and profitability of multiple fracturing treatment. To accomplish a successful fracturing job with higher drainage area, a completion engineer should weigh both pros and cons of stress shadowing in multi-stage hydraulic fracturing. On one hand, stress shadowing increases the fracture complexity as a result of reducing the horizontal-stress contrast in the vicinity of closely spaced induced fractures. These zones of low stress anisotropy are far more contributory to the opening of natural fractures and can result in better connectivity with a natural-fracture network. On the other hand, the stress shadowing effect increases dramatically in completion design with closely spaced perforations and, as a result, the growth of some fractures suppresses the propagating of the others.

Based on the results obtained by Distributed Temperature Sensing (DTS) and Distributed Acoustic Sensing (DAS), SOOKPRASONG *et al.* (2014) concluded that the dominant perforation clusters are often recognized during simultaneously hydraulic fracturing. Effects of stress shadowing on the various completion procedure on multi-lateral wellbores in the upper Barnett shale have performed by VERMYLEN *et al.* (2011) using microseismic events. The results revealed that considerable discrepancies between different

completion resulted due to stress shadowing effects. A numerical evaluation of the impacts of stress shadowing on the multi-stage hydraulic fractures as a function of Fracture Spacing (FS) and in-situ stress ratio have been done by NAGEL *et al.* (2011) without considering fluid leak-off. They obtained that with sequential fracturing, the second fracture, which grows under stress shadowing of initial fracture, exhibits very little associated natural fracture shearing. ROUSSEL *et al.* (2011) employed a 3-D numerical method of stress interference for simultaneously and sequentially fracturing. They analyzed a series of the numerical modelling and supposed that stress interference or reorientation rises by the number of fractures propagated and is dependent on the sequence of fracturing. Based on enhanced 2-D displacement discontinuity model, WU *et al.* (2012) investigated the stress shadowing effects in a complex hydraulic fracture network, representing that fractures can either enhance or repel each other depending on their initial spacing due to the impacts of stress shadowing. A 2-D coupled displacement discontinuity model for simulating fracture propagation in simultaneous and sequential hydraulic fracture operations for single and multiple wells has been presented by SESETTY *et al.* (2015). It was found that in simultaneous propagation of hydraulic fractures, the outer fractures dominate the growth of inner fractures. In addition, the center fractures usually stop after they reach a certain length due to the stress shadowing between them.

1.6 Objectives

The main objective of the present dissertation is to develop generic numerical modelling within the framework of the fully coupled pore pressure/stress analysis so as to investigate the HF propagation in low-permeable quasi-brittle medium. In order to present a robust numerical technique, which is capable of capturing the non-planar hydraulically fluid-driven crack propagation with unpredictable path, on one hand, and tackling the feasible emergence of multiple cohesive cracks in a porous medium with Fracture Process Zone (FPZ) at the crack tip, on the other hand, the cohesive segments method in combination with phantom node method, called Cohesive Phantom Node Method (CPNM) herein, is established. The present simulation fully couple fracturing fluid flow inside the crack with poro-elasticity in porous formation and continuum-based leak-off on the crack surfaces, and capture the FPZ at the fracture tip in quasi-brittle shale.

This dissertation has been motivated by the fact that according to the author's literature survey, most available works overlooked the stress shadowing effects and non-planar fracture growth in completion design of individual and multi-lateral wellbores owing to the restrictions on the numerical techniques. The non-linear discrete fracture mechanics, based on cohesive crack model, which is formulated by specific traction-separation laws, independent of the constitutive behaviour of bulk material, is proposed to confront the softening effects at the fracture tip in a quasi-brittle shale. This study is performed to con-

tribute to the existing body of knowledge, particularly regarding the dealing with stress shadowing effects stemming from closely spaced fracturing scenarios. The individual objectives of the current dissertation are summarised as follows:

- Developing a 3-D finite element model, which takes into account the propagation of the multiple fractures from an individual horizontal well based on CPNM. Two different key scenarios including sequentially and simultaneously multti-stage HF in a quasi-brittle multi-layer shale are investigated.

- The analysis is extended to multi-lateral horizontal wells, which is aimed not only to comprehensively investigate the available completion designs on horizontal multi-lateral wellbores, but also to enhance the current "Modified Zipper-Frac" (MZF) (SOLIMAN *et al.*, 2013) by considering non-planar pattern of the crack propagation proceeding towards introducing a modified design, termed Modified MZF (M2ZF). This task is performed by considering stress shadowing effects in fracturing of the multi-lateral wellbores with desirably closely spaced fractures. One of the main contribution of this part is more thorough mechanistic understanding of MZF advantage in increasing the fracture complexity. To this end, studying stress anisotropy and in-plane shear stresses, which is imperative phenomenon in the micro-seismic monitoring (BENNETT *et al.*, 2005; SOLIMAN *et al.*, 2010), in the area between induced fractures plays a crucial role in better understanding of their effects on the opening the natural fractures and activating un-propped fractures, and eventually augmenting the fracture complexity.

1.7 Outline of dissertation

The introduction chapter, will be followed by succeeding chapters:

Chapter 2 is devoted to fundamental background and a literature review on relevant studies, discussing the-state-of-the-art in the fields according to scope of the present dissertation. It consists of introducing various discontinuities and fracturing processing in rocks, followed by primary review of the Linear Elastic Fracture Mechanics (LEFM). Then, the FPZ characterizing progressive softening behaviour at the crack tips is explained. Afterwards, existing approaches for simulation of the fracture are described. After that, the discussion turns into the eXtended Finite Element Method (XFEM) and a concise explanation of the XFEM crack modeling is elaborated. This chapter is followed by a literature review on the numerical simulations of HF with particular concentration on the stress shadowing effects.

Chapter 3 presents 3-D simulation of multi-stage HF propagation in unconventional reservoirs. First of all, an introduction to the problem is presented along with the main contribution of the chapter. Thereafter, the methodology including the governing equations,

fracture initiation and propagation, and cohesive phantom node method are expressed in detail. Subsequently, the 3-D computational model for HF initiation and propagation simulation, which encompasses a horizontal wellbore, perforation holes, pay zone, and barriers, are introduced. Later, the validation of numerical simulation with an analytical model is given. Lastly, the new numerical results for two key scenarios including sequentially and simultaneously multiple HF are studied comprehensively. Lastly, the conclusion of the chapter is made.

Chapter 4 is dedicated to study various completion designs on horizontal multi-lateral wellbores with consideration of stress shadowing effects. Sim-HF, Seq-HF, MZF, and M2ZF scenarios with closely spaced perforations are investigated in depth. As a matter of fact, the method proposed in chapter 3 is extended to multi-lateral wellbores to capture non-planar cracks propagation. This chapter start with a introduction to the main motivation of the chapter and the crucial contribution. Afterwards, a brief explanation on the 2-D mathematical modelling is elaborated with taking this point into consideration that the mathematical framework of this chapter is established based on the 2-D form of chapter 3. In the following, the computational model of HF from the two horizontal lateral wellbores is constructed. Next, interesting results for aforementioned scenarios are discussed and the effects of stress shadowing and stress interference on the fractures propagation on lateral wellbores are studied. The main contributions of this chapter is investigating in depth the effects of the stress shadowing as a function of the FS on the horizontal stress contrast, direction of maximum local stress, leak-off flow rate, in-plane shear stress, and pore pressure of the formation.

Chapter 5 elaborates main conclusions of the dissertation and makes suggestions for further extension of the present research.

Chapter 2

Background and Literature Survey

2.1 Overview

The main aim of this chapter is to provide an underlying background and a literature review, explaining the-state-of-the-art in the fields according to scope of the current dissertation. This chapter starts with an introduction to the various types of discontinuities and fracturing processing in rocks. After that, a primary review of the LEFM is provided. Next, the FPZ characterizing progressive softening behaviour at the crack tips is related. Subsequently, the Cohesive Crack Model (CCM) for capturing the non-linear FPZ developing in the area in front of the crack tip where the energy dissipation takes place is discussed. Next, previously developed approaches for simulation of the fracture, including smeared and discrete approaches, are discussed. Afterwards, an overview of the XFEM is presented, in which an emphasis is given on the application of the technique in crack modelling. Then, a description of the evaluation of the condition in which a fracture initiates from the borehole will be elaborated. Finally, a literature review on the numerical simulations of HF with special concentration on the stress shadowing is presented.

2.2 Discontinuities in rocks

In the literature, the terminology used for explanation of discontinuities and especially fractures are commonly used in not obviously designated meanings. This may be owing to diverse nomenclatures in various disciplines. In the present dissertation, the terms used are described in this section.

A crack is characterized as any separation in rock body, which has one or two dimensions far smaller than the third. The width to length ratio, named "crack aspect ratio", is usually between 10^{-3} to 10^{-5} (KAZERANI, 2011; SIMMONS and RICHTER, 1976). Cracks are categorized as three scale classes including micro, meso and macro. Micro-cracks are planar discontinuities whose longest dimension is in the order of one to few grain diameters. They mostly nucleate at inhomogeneities such as a cavity or a phase boundary; places where the stresses are high and the inter-atomic bonds are comparatively weak. According to their existence within the rock, they can be sorted into "grain boundary cracks" (situated at the interface between grains), "intra-granular cracks" (cracks limited to one grain), and "inter-granular cracks" (cracks cutting more than one grain) (ENGELDER, 1987). The nucleation of micro-cracks undergoes an irreversible procedure, which lessens the strength and the stiffness of the material. It is followed by the energy dissipation by virtue of plastic deformation of the adjacent bulk material and the heat production through the friction. After removing the applied load, the micro-cracks remain and the body exhibits permanent deformations. When the applied load is raised, the existing micro-cracks grow and coalesce constituting meso-cracks, which can be visible for the naked eye. A meso-crack is discontinuity extending over a vast number of grains than a micro-crack,

ultimately connecting a number of micro-cracks. The extension is one to few millimeters. The macro-crack includes several millimeters to decimeters. Typically, in rock and also in petroleum engineering, meso- and macro-cracks are referred to as “fracture”.

Figure 2.1 represents a fracture system containing the main separation and the FPZ (ATKINSON, 1987). This process zone encompasses micro- and meso-cracks. Preceding the growth of the main fracture, substantial micro-/meso-cracking emerges. Meso- or macro-cracks propagating off the fracture are termed “branching cracks”. The width of

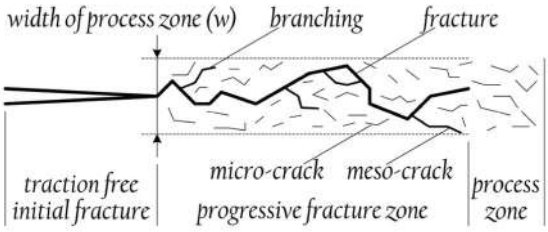

Figure 2.1: Schematic representation of a fracture system

the FPZ is dependent on grain size and loading nature (ZANG *et al.*, 2000; ZHOU *et al.*, 2005). The size of the FPZ is commonly about five to ten times the average grain size. Notwithstanding, larger values up to 40 grain diameters have been related (BARRY *et al.*, 1992). BROBERG (1999) defined the FPZ as the area in the condition of decohesion, where micro-cracks coalesce to form the main separation.

2.3 Fracturing process

The process of fracturing in geo-materials like rock materials has been frequently studied. This was performed under different loading states and for different materials, and using diverse observation scales and methodologies, e.g. interpretation of mechanical data, detection and interpretation of acoustic emission events, and microscopy at different scales. Textbooks and reviews such as POLLARD and AYDIN (1988), ATKINSON (2015) shall be appropriate reference for interested readers. When a plate with an isolated fracture is subjected to a rising tensional stress perpendicular to the fracture, it will mainly fail under rapid Mode I fracture propagation.

As identified in the meso and macroscopic observation of rocks, under compressive loading, both tensile and shear stress concentrations progress at pre-existing inclined inhomogeneities. As the compression exerted to the sample rises more, tensile cracks initiates ahead of the pre-existing fractures. These crack are termed “wing cracks”, which develop to an increasing extent in the direction of the remote major principal stress and eventually terminate (KEMENY and COOK, 1986; PETIT and BARQUINS, 1988). At the early stages of crack growth, the propagation of the stable wing crack is governed by the stress field of the original fracture. As it progresses, it begins interacting with adjacent

micro-cracks, where this interaction may cause to coalescence and finally ultimate failure. Depending on geometry and pattern of the interacting fractures and also stress condition, different coalescence behavior was seen. Generally, the wing cracks starts to propagate at the crack tips at uniaxial and low confinement biaxial condition (Figure 2.2). BOBET and EINSTEIN (1998) stated that the location of crack initiation transfers to the middle of the crack, since confining pressure inclines. The wing cracks vanishes entirely at higher confining stresses. Afterwards, secondary fractures are feasible to link the pre-existing fractures. They grow unstably and follow the direction of shear (SAGONG and BOBET, 2002). Figure 2.2 depicts the most preferred configuration of the progressive shear fractures, which is a setup with two initial fractures (BOBET and EINSTEIN, 1998).

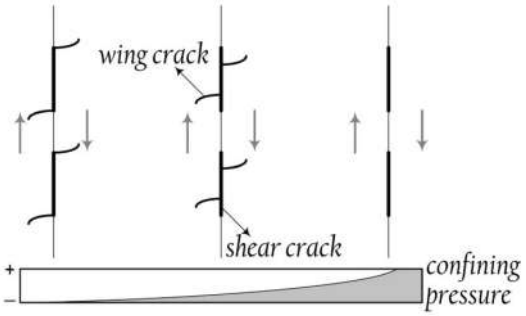

Figure 2.2: Setup for fracture coalescence and effect of confining pressure (BOBET and EINSTEIN, 1998).

2.4 Basic concept of linear elastic fracture mechanics

The LEFM primarily focused on the elastic material behavior where Hook's law was complied. In order to demonstrate the attitude of cracked area in linear elastic materials, several experiments and theories were elaborated by OROWAN (1949), IRWIN (1997a), and BARENBLATT (1962). IRWIN (1997b) and SHIH and HUTCHINSON (1976) developed the LEFM concept into non-linear behavior of materials such as plastic solids. A overall explanation of the LEFM problem is illustrated in Figure 2.3a (ANDERSON and ANDERSON, 2005), where a tension load is exerted to an infinite plate comprising a crack with the length of $2a$ at the center of the plate. The fractured sear leads to a singularity in the stress field ahead of the crack region for the elastic material. Figure 2.3b shows the mentioned singularity, where normal stress approaches an infinite value. Nonetheless, in the case of plastic materials, the crack tip experiences a plastic zone, resulting in the stress to approach a finite value identical to yield stress of the material. Several microscopic and macroscopic studies have been carried out by researchers to study the fracture behavior of the material. From the microscopic point of view, the crack is able to be propagated if potential energy of atoms goes beyond the bound energy between two

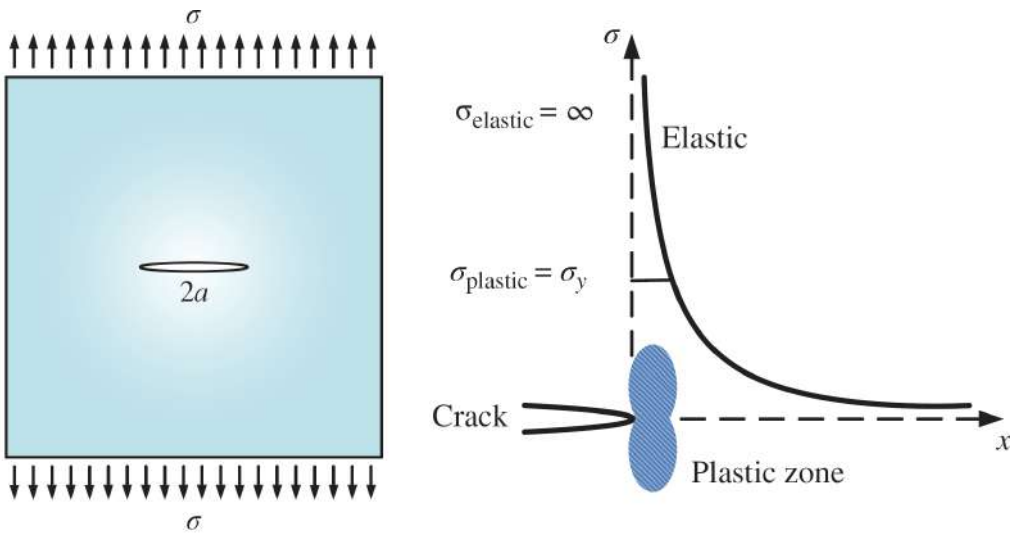

(a) (b)

Figure 2.3: **(a)**: A crack in an infinite plate under a uniform tensile stress σ. **(b)**: Plot of normal stress distribution at the crack tip. (ANDERSON and ANDERSON, 2005)

neighbouring atoms. Consider x_0 representing the equilibrium space between two atoms under the tension force, the stress value that requires to conquer the atomic bound can be acquired by (ANDERSON and ANDERSON, 2005)

$$\sigma_c = \sqrt{\frac{E\gamma_s}{x_0}} \tag{2.1}$$

where E is the Young module of the material and γ_s is the surface energy per unit area. From the macroscopic level standpoint, the crack propagation is modeled in the framework of continuum mechanics.

2.4.1 Energy balance in crack growth

The idea of energy balance in fracture mechanics was first introduced by GRIFFITH (1921). His fracture mechanics model was based on the first law of thermodynamics that relates the minimum potential energy of a cracked body can be accomplished, when the crack propagates and the system remains in equilibrium condition. Suppose the total energy of the system can be divided into two sections as (KHOEI, 2014)

$$\Xi = P + W_s \tag{2.2}$$

where Ξ is the total energy of the system, P is the potential energy originated by the internal and external forces, and W_s is the work done to promote the crack. By taking the derivation from the equation with regard to the increased value of crack surface dA, it

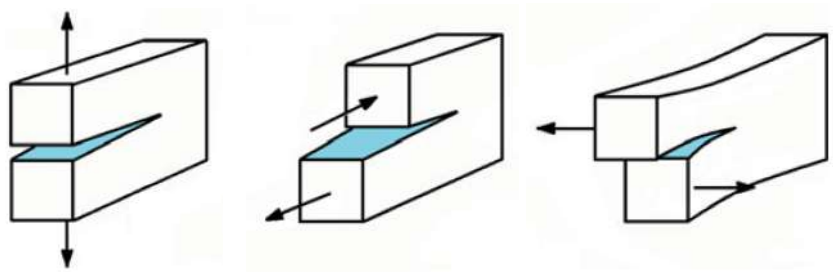

(a) (b) (c)

Figure 2.4: Basic modes of crack growth: **(a)**: Opening mode I. **(b)**: Sliding mode II. **(c)**: Tearing mode III.

results in

$$-\frac{dP}{dA} = \frac{W_s}{dA} \tag{2.3}$$

which stating that the amount of energy required to incline the length of the crack to dA equals the variation of the reduced potential energy with regard to dA. Griffith's work was restricted to the fracture of brittle materials, and his model presumed that the work of fracture was associated with only the crack surface energy. IRWIN (1948) extended Griffith's theory to ductile materials, and proposed the concept of strain energy release rate, which is the rate of change in potential energy of the linear elastic material because of crack growth, as

$$G = -\frac{\partial P}{\partial A} = 2\gamma_s \tag{2.4}$$

Assume a wide plate with the crack length of 2a and unit thickness, as depicted in Figure 2.3b, the potential energy of the plate was determined by INGLIS (1997) as $P = P_0 - \pi\sigma^2 a^2/E$, where P_0 is the potential energy of an uncracked plate. Thus, the energy release rate can be attained as

$$G = \frac{\pi\sigma^2 a^2}{E} \tag{2.5}$$

where the energy release rate is a function of the stress exerted on both edges of the crack. As can be physically noticed, the crack growth occurs by rising the tensile stress σ. By using Westgaard's elasticity solution (WESTERGAARD, 1997), IRWIN (1957) related that the stress field expansion ahead of the crack tip was associated with a constant multiplied by the coefficient of the square root of the distance from crack tip. The strain energy release rate can be identical to a critical value, G_c, which defines a condition when a crack initiates under critical normal stress, σ_c. The critical energy release rate is a measure of the crack toughness of the material, and is associated with the crack length and the material properties of the domain.

2.4.2 Displacement and stress fields ahead of crack tip

By assessment of the displacement and stress fields ahead of the crack tip, the importance of stress singularity at the crack tip was stated by WESTERGAARD (1997). To explain the behavior of crack at this area, the loading imposed on the fractured body is classified into three modes, termed the opening mode (mode I), sliding or shearing mode (mode II), and tearing mode (mode III), as demonstrated in Figures 2.4a to 2.4c. WILLIAMS (1961) employed the Airy stress function to evaluate the singularity at the crack tip by using a polar coordinate system (r, θ) as

$$\Phi = r^{\lambda+1}\left(c_1 \sin(\lambda+1)\widehat{\theta} + c_2 \cos(\lambda+1)\widehat{\theta} + c_3 \sin(\lambda-1)\widehat{\theta} + c_4 \sin(\lambda-1)\widehat{\theta}\right) \quad (2.6)$$

where c_i is the coefficient and $\widehat{\theta}$ is shown in Figure 2.5. Replacing the Airy stress function (Eq. 2.6) with the equilibrium equation of the system, which is, $\nabla^2\nabla^2\Phi = 0$ in the absence of body forces, considering the traction-free boundary conditions at the crack faces, and ignoring the higher order terms, the displacement fields ahead of the crack tip is derived for mode I loading as

$$u_x = \frac{K_I(1+v)}{E}\sqrt{\frac{r}{2\pi}}\cos\frac{\theta}{2}\left(k - 1 + 2\sin^2\frac{\theta}{2}\right) \quad (2.7)$$

$$u_y = \frac{K_I(1+v)}{E}\sqrt{\frac{r}{2\pi}}\sin\frac{\theta}{2}\left(k + 1 - 2\cos^2\frac{\theta}{2}\right) \quad (2.8)$$

$$u_z = 0 \quad (2.9)$$

and the stress fields is as follows

$$\sigma_x = \frac{K_I}{\sqrt{2\pi r}}\cos\frac{\theta}{2}\left(1 - \sin\frac{\theta}{2}\sin\frac{3\theta}{2}\right), \quad \tau_{xy} = \frac{K_I}{\sqrt{2\pi r}}\sin\frac{\theta}{2}\cos\frac{\theta}{2}\cos\frac{3\theta}{2} \quad (2.10)$$

$$\sigma_y = \frac{K_I}{\sqrt{2\pi r}}\cos\frac{\theta}{2}\left(1 + \sin\frac{\theta}{2}\sin\frac{3\theta}{2}\right), \quad \tau_{yz} = 0 \quad (2.11)$$

$$\sigma_z = \begin{cases} v(\sigma_x + \sigma_y) & \text{plane strain} \\ 0 & \text{plane stress} \end{cases}, \quad \tau_{zx} = 0 \quad (2.12)$$

The displacement fields ahead of the crack tip for the mode II loading are derived as follows

$$u_x = \frac{K_{II}(1+v)}{E}\sqrt{\frac{r}{2\pi}}\sin\frac{\theta}{2}\left(k + 1 + 2\cos^2\frac{\theta}{2}\right) \quad (2.13)$$

$$u_y = -\frac{K_{II}(1+v)}{E}\sqrt{\frac{r}{2\pi}}\cos\frac{\theta}{2}\left(k - 1 - 2\sin^2\frac{\theta}{2}\right) \quad (2.14)$$

$$u_z = 0 \quad (2.15)$$

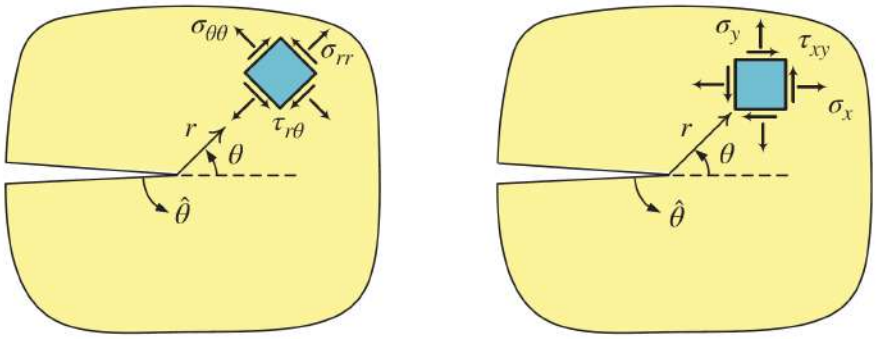

Figure 2.5: Polar coordinate system related to the crack tip.

and also the stress fields as

$$\sigma_x = -\frac{K_{II}}{\sqrt{2\pi r}} \sin\frac{\theta}{2}\left(2 + \cos\frac{\theta}{2}\cos\frac{3\theta}{2}\right), \quad \tau_{xy} = \frac{K_{II}}{\sqrt{2\pi r}} \cos\frac{\theta}{2}\left(1 - \sin\frac{\theta}{2}\sin\frac{3\theta}{2}\right) \tag{2.16}$$

$$\sigma_y = \frac{K_{II}}{\sqrt{2\pi r}} \sin\frac{\theta}{2}\cos\frac{\theta}{2}\cos\frac{3\theta}{2}, \quad \tau_{yz} = 0 \tag{2.17}$$

$$\sigma_z = v(\sigma_x + \sigma_y), \quad \tau_{zx} = 0 \tag{2.18}$$

Eventually, the displacement fields at the tip of the crack for mode III loading are as

$$u_x = 0 \tag{2.19}$$

$$u_y = 0 \tag{2.20}$$

$$u_z = \frac{K_{III}(1+v)}{E}\sqrt{\frac{r}{2\pi}}\sin\frac{\theta}{2} \tag{2.21}$$

and the stress fields are

$$\sigma_x = 0, \quad \tau_{xy} = 0 \tag{2.22}$$

$$\sigma_y = 0, \quad \tau_{yz} = \frac{K_{III}}{\sqrt{2\pi r}}\cos\frac{\theta}{2} \tag{2.23}$$

$$\sigma_z = 0, \quad \tau_{zx} = -\frac{K_{III}}{\sqrt{2\pi r}}\sin\frac{\theta}{2} \tag{2.24}$$

where v is the Poisson's ratio and k is denoted as $k = (3-v)/(1+v)$ for plane stress problems and $k = 3-4v$ for the condition of plane strain. In these formulations, K_I, K_{II}, and K_{III} are the Stress Intensity Factors (SIF) in modes I, II, and III, respectively, related

as

$$K_I = \lim_{\substack{x \to \infty \\ \theta=0}} \sigma_y \sqrt{2\pi r} \tag{2.25}$$

$$K_{II} = \lim_{\substack{x \to \infty \\ \theta=0}} \sigma_{xy} \sqrt{2\pi r} \tag{2.26}$$

$$K_{III} = \lim_{\substack{x \to \infty \\ \theta=0}} \sigma_{yz} \sqrt{2\pi r} \tag{2.27}$$

The theory of fracture mechanics expresses that unstable fracture propagation happens when one of the SIFs, K_i, or a combination of them (in the case of mixed mode propagation), approaches a critical value, K_i^c. This critical value is named "fracture toughness" and stands for the potential ability of a material to withstand a given stress field ahead of the crack tip and to resist progressive tensile crack extension. It should be noted K_i^c given as stress times square root of crack length is different from "material toughness" (critical energy release rate) with the unit of energy per unit area. When several fracture mechanisms takes place simultaneously, the overall form of the failure criterion can be stated as

$$f\left(K_I, K_I^c, K_{II}, K_{II}^c, K_{III}, K_{III}^c\right) = 0 \tag{2.28}$$

The crack propagation criterion f can be determined theoretically, from mixed mode criteria including: maximum circumferential stress, minimum strain energy density, and maximum energy release rate, or empirically from experiments (MOHAMMADI, 2008). From expressions 2.10– 2.12 and 2.16– 2.18, it can be noted that for the 2-D mixed-mode problems the stresses σ_x, σ_y, and τ_{xy} are singular in the vicinity of crack tip area, when $r \to 0$. Eventually, for mixed-mode loading the total stress and displacement fields are obtained as

$$\sigma_{ij}^{tot} = \sigma_{ij}^{K_I} + \sigma_{ij}^{K_{II}} + \sigma_{ij}^{K_{III}} \tag{2.29}$$

$$u_i^{tot} = u_i^{K_I} + u_i^{K_{II}} + u_i^{K_{III}} \tag{2.30}$$

2.4.3 Stress intensity factor

In the LEFM, the concept of the SIF ahead of the crack tip area can be employed to determine the stress, strain, and displacement fields. Thus, it is imperative to precisely evaluate the SIFs for the finite element analysis of LEFM. In literature, several techniques have been proposed for deriving SIFs, encompassing: the displacement correlation method, the modified crack closure integral, the virtual crack extension method, and the J-integral method. Principally, the computational algorithms to extract the SIFs can be classified into two classes; the direct approach and the energy approach. The direct method corresponds

to the SIF with the Finite Element Method (FEM) results directly whereas the energy approach is according to the computation of energy release rate. In overall, the energy methods are more precise than the direct ones; however, the direct techniques are more popular and are frequently used to verify the outcomes of energy methods, inasmuch as their relations are simple. Based on the theorem of energy conservation, ESHELBY (1974) proposed various path independent contour integrals. The J-integral technique was originally introduced by RICE (1968) to compute the energy release rate in crack problems with making use of a local crack tip coordinate system (x_1, x_2) as

$$J = \int_{\Gamma} \left(w\delta_{1j} - \sigma_{ij} \frac{\partial u_i}{\partial x_1} \right) n_j d\Gamma \tag{2.31}$$

in which w is the strain energy density defined as $w = \frac{1}{2}\sigma_{ij}\varepsilon_{ij}$ that σ_{ij} representing the stress tensor, u_i is the displacement field, n_j is the unit outward normal vector to the contour integral Γ, δ is the Kronecker delta, and $T_i = \sigma_{ij} n_j$ is the traction on the contour integral Γ, as shown in Figure 2.6. In the following, it will be shown that the J-integral

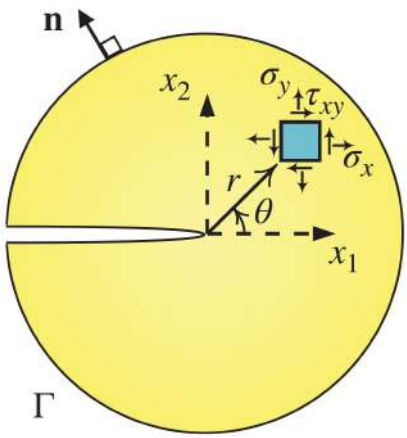

Figure 2.6: Circular path for the contour integral around the crack tip.

defined in expression 2.31 is the variation of potential energy for an infinitesimal virtual crack extension and, as a result, for linear elastic material, the energy release rate is identical to the value of J-integral (RICE, 1968). Assume two states of a cracked body, which are: the present state (1) named by $\left(u_i^{(1)}, \varepsilon_{ij}^{(1)}, \sigma_{ij}^{(1)}\right)$ and an auxiliary state (2) denoted by $\left(u_i^{(2)}, \varepsilon_{ij}^{(2)}, \sigma_{ij}^{(2)}\right)$. The J-integral for the sum of states (1) and (2) can be elaborated based on Eq. 2.31 as

$$J^{(1+2)} = \int_{\Gamma} \left(\frac{1}{2} \left(\sigma_{ij}^{(1)} + \sigma_{ij}^{(2)} \right) \left(\varepsilon_{ij}^{(1)} + \varepsilon_{ij}^{(2)} \right) \delta_{1j} - \left(\sigma_{ij}^{(1)} + \sigma_{ij}^{(2)} \right) \frac{\partial}{\partial x_1} \left(u_i^{(1)} + u_i^{(2)} \right) \right) n_j d\Gamma \tag{2.32}$$

Expanding this relation leads to

$$J^{(1+2)} = J^{(1)} + J^{(2)} + I^{(1,2)} \tag{2.33}$$

where $I^{(1,2)}$ is termed the interaction integral for states (1) and (2) written as

$$I^{(1,2)} = \int_{\Gamma} \left(w^{(1,2)} \delta_{1j} - \sigma_{ij}^{(1)} \frac{\partial u_i^{(2)}}{\partial x_1} - \sigma_{ij}^{(2)} \frac{\partial u_i^{(1)}}{\partial x_1} \right) n_j d\Gamma \tag{2.34}$$

in which $w^{(1,2)}$ is the interaction strain energy denoted by

$$w^{(1,2)} = \sigma_{ij}^{(1)} \varepsilon_{ij}^{(2)} = \sigma_{ij}^{(2)} \varepsilon_{ij}^{(1)} \tag{2.35}$$

The energy release rate for 2-D mixed-mode crack problems can be denoted according to K_I and K_{II} as

$$J \equiv G = \frac{1}{E'} \left(K_I^2 + K_{II}^2 \right) \tag{2.36}$$

where for plane stress problems $E' = E$ and for plane strain problems $E' = E/(1 - v^2)$. The J-integral concept in Eq. 2.36 can be stated for the combined states (1) and (2) as

$$J^{(1+2)} = J^{(1)} + J^{(2)} + \frac{2}{E'} \left(K_I^{(1)} K_I^{(2)} + K_{II}^{(1)} K_{II}^{(2)} \right) \tag{2.37}$$

Comparing expression 2.33 with 2.37, the interaction integration $I^{(1,2)}$ can be extracted as

$$I^{(1,2)} = \frac{2}{E'} \left(K_I^{(1)} K_I^{(2)} + K_{II}^{(1)} K_{II}^{(2)} \right) \tag{2.38}$$

If the auxiliary state (2) is presumed as the pure mode I asymptotic fields, which is, $K_I^{(2)} = 1$ and $K_{II}^{(2)} = 0$, the $K_I^{(1)}$ can be obtained according to the contour integral $I_{mode\,I}^{(1)}$ as

$$K_I^{(1)} = \frac{E'}{2} I_{mode\,I}^{(1)} \tag{2.39}$$

In a similar manner, if the auxiliary state (2) is presumed as the pure mode II asymptotic fields, which is, $K_I^{(2)} = 0$ and $K_{II}^{(2)} = 1$, the $K_I^{(1)}$ can be obtained according to the contour integral $I_{mode\,II}^{(1)}$ as

$$K_{II}^{(1)} = \frac{E'}{2} I_{mode\,II}^{(1)} \tag{2.40}$$

The contour J-integral (Eq. 2.31) can be straightly determined along a contour of FE mesh. This contour can be normally assessed by passing through the element Gauss integration points, where the stresses are calculated more precisely. But, the major problem of this

method is that the practical implementation of the method hardly shows path independence and the result becomes mesh dependent. LI *et al.* (1985) carried out the computation of J-integral by converting the contour integral to an equivalent area integral. This method, which is independence from the surface of integration, is straightforward to implement in an FE code and the numerical execution demonstrates a great accuracy. The area form of J-integral is expressed by

$$J = \int_A \left(\sigma_{ij} \frac{\partial u_i}{\partial x_1} - w\delta_{1j} \right) \frac{\partial q}{\partial x_j} dA \tag{2.41}$$

in which q is a weighting function defined over the domain of integration. The choice of the domain of integration must be done by some considerations (Figure 2.7). Firstly, it is appropriate near to the crack tip for complex crack pattern. Secondly, it must be easy to be employed in a fully automatic simulation procedure, and ultimately it requires to be consistent with the geometry and boundary restrictions in complex boundaries and multiple crack problems. The function q has the value of unity at the crack tip and disappears on an outer specified contour. According to the area of the J-integral definition stated in

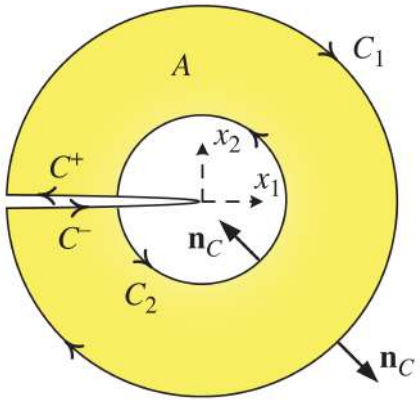

Figure 2.7: J-integral domain for mixed-mode stress intensity factors.

Eq. 2.41, the new interaction integration can be written as

$$I^{(1,2)} = \int_A \left(-w^{(1,2)}\delta_{1j} + \sigma_{ij}^{(1)} \frac{\partial u_i^{(2)}}{\partial x_1} + \sigma_{ij}^{(2)} \frac{\partial u_i^{(1)}}{\partial x_1} \right) \frac{\partial q}{\partial x_j} dA \tag{2.42}$$

The K_I and K_{II} can be achieved based on Eqs. 2.39 and 2.40 by presuming the auxiliary state (2) as a pure mode I and/or a pure mode II asymptotic fields, by determining the displacement and stress fields ahead of the crack tip, and by replacing these parameters into expression 2.42.

2.5 Fracture process zone

In the section 2.4, stress and displacement fields at the vicinity of a crack were introduced in terms of the SIFs. Assuming linear elastic behavior, singular stresses in the vicinity of the crack tip occur. In fact, this is a manifestation of Hooke's law applied beyond its limits of validity.

In front of a crack tip, the FPZ, or the non-linear softening zone, characterizes the progressive softening behavior (the white area in Figure 2.8). The outer region of this zone (the black area in Figure 2.8) is named the non-linear hardening zone which represents the hardening plasticity or perfect plasticity. Generally, the fracture process behaviour is classified based on the size of the non-linear zone (BAZANT and PLANAS, 1997), as follows:

- For the first behavior type (Figure 2.8a), both the FPZ and the non-linear hardening zone are relatively small such that the LEFM is applicable. Brittle materials such as glass, brittle ceramics and brittle metal, illustrate this type of fracture process behavior.

- For the next type of behavior (Figure 2.8b), due to the large non-linear hardening zone and the small FPZ owing to the plastic yielding, the elasto-plastic fracture mechanics can be exploited to analyze the nonlinear hardening zone. Ductile materials (e.g. ductile metals) fall into the second behavior type (PARK, 2009).

- The third type (Figure 2.8c) is related to this dissertation, which illustrates the progressive damage with material softening along the fracture process zone. These types of materials exhibit moderately strain hardening prior to reaching to the ultimate tensile capacity, similar to response of ductile materials such as high strength steels. Contrast to the latter, they are distinguished by an incline in deformation with declining tension carrying capacity, which is called strain-softening. The materials that manifest mild strain hardening prior to the ultimate tensile strength and subsequent strain-softening might be called quasi-brittle, such as geo-materials, concrete, and coarse-grained ceramics. The observed deviation of the attitude of quasi-brittle materials from the LEFM prediction is the developing of nonlinear fracture processes in front of the crack tip called the FPZ where the material progressively softens and the energy dissipation occurs due to the occurrence of micro-cracks.

2.6 Cohesive Crack Model

Non-linear fracture process behavior such as void growth and micro-crack formation can be estimated by the Cohesive (or discrete) Crack Model (CCM). The CCM is one of

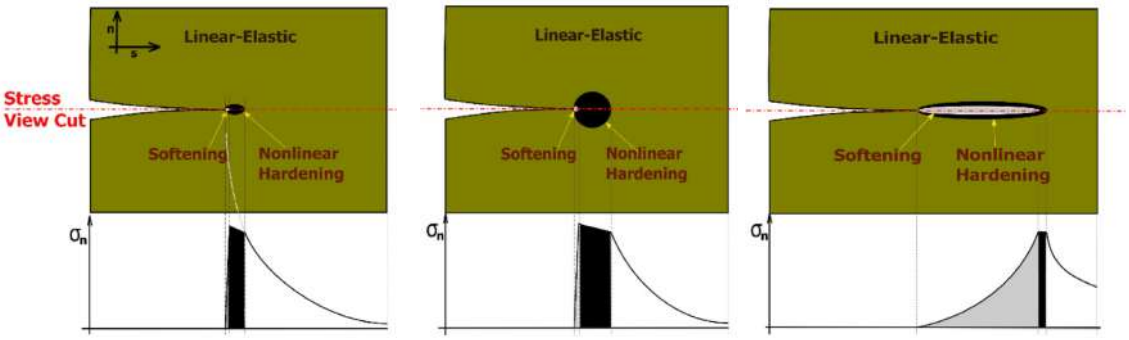

(a) (b) (c)

Figure 2.8: Types of fracture process behavior: **(a)**: Brittle material. **(b)**: Ductile material. **(c)**: Quasi-brittle material. (BAZANT and PLANAS, 1997)

the crucial methods to deal with discrete crack propagation in various types of materials particularly quasi-brittle materials.

The main concept of the CCM is based on the consideration that infinite stresses ahead of the crack tip are not realistic. Models to overcome this drawback have been proposed by DUGDALE (1960) and by BARENBLATT (1962), called strip-yield models. Both authors divided the crack in two parts: One part of the crack surfaces, region I in Figure 2.9, is stress free, the other part, region II, is loaded by cohesive stresses. Dugdale introduced the finite stress to be the yield stress, which holds only for plane stress, but the crack opening stresses can be far greater than the equivalent stress in a multi-axial stress condition.

BARENBLATT (1962), who studied the fracture of brittle materials, made various assumptions about the cohesive stresses: The extension of the cohesive zone d is constant for a given material (independent from global load) and small compared to other dimensions. The stresses in the cohesive zone follow a prescribed distribution $\sigma(x)$, where x is the ligament coordinate, which is particular for a given material but independent of the global loading conditions.

The Dugdale-Barenblatt cohesive crack was improved by HILLERBORG *et al.* (1976) to analyze the fracture mechanics of concrete. In fact, the development of an suitable numerical simulation of CCM into the FEM was originally introduced by HILLERBORG

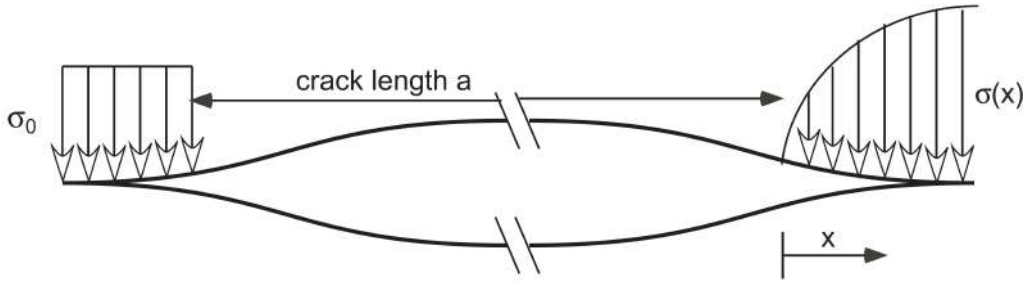

Figure 2.9: Dugdale (left) and Barenblatt (right) crack models.

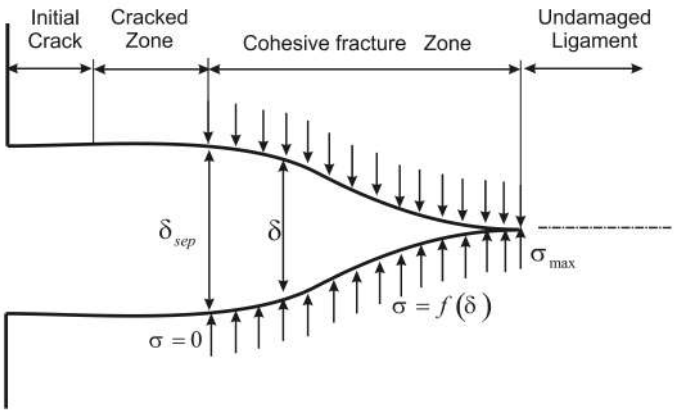

Figure 2.10: Fracture process zone model.

(1978, 1983) in order to study the localized failure of concrete bending beam with the crack opening displacement related equilibrium forces. In this model, the crack was presumed to grow when the stress ahead of the crack tip fulfill the tensile strength. The stresses imposed on the crack surfaces decline with the gain in crack opening and do not fall to zero immediately. This fact makes the crack close smoothly and no singularity exists ahead of the crack tip at the onset of crack propagation, which makes the SIF in mode I, K_I, disappears. Some resemblances stands among the Barenblatt, Dugdale, and Hillerborg models; the crack tip faces close smoothly (the SIF disappears at the crack tip in mode I propagation) and the FPZ has trivial thickness. On the other hand, the closing stresses in the FPZ are constant only in Dugdale model, whereas the size of FPZ is constant and small comparing with the length of main crack in Barenblatt model.

In the CCM, fracture nucleates as discontinuity surface, which is able to transmit tensile load before opening above a given displacement. Formation and extension of this surface demands that the maximum principal stress approaches a specified value, termed the cohesive strength of the material. When this happens, the surface initiates or grows perpendicularly to the direction of the maximum principal stress. The two faces of the surface impose on each other equal and opposite tensile stresses (cohesive stresses), whose value is a unique function $f(\delta)$ of the separation δ between the faces. Whenever the separation reaches another specified value, i.e. the critical separation, δ_c, the cohesive stress disappears and the failure occurs. Fracture includes the initiation and propagation of a crack caused by the opening and the extension of the cohesive zone (the area where the cohesive stresses perform) at of the crack tip, as illustrated in Figure 2.10.

Unlike LEFM where the microscopic mechanisms of fracture are fundamentally discarded (all material aspects are lumped into one parameter, i.e. fracture toughness), the bridging law or the traction-separation relation in the CCM depends on the material and the corresponded fracture mechanism, as shown in Figure 2.8. The bridging law, $\sigma(\delta)$, shall be determined from detailed micro-mechanics models or may be determined experimentally (COX and MARSHALL, 1991; SØRENSEN and JACOBSEN, 2003). On the

other hand, other forms of bridging laws are frequently employed in theoretical and numerical analyses. As an illustration, a triangular or trapezoidal shaped traction-separation curve is often exploited in practice (DÁVILA *et al.*, 2001; PARMIGIANI and THOULESS, 2007). In any case, the maximum stress, $\sigma_{\max}$, and the critical displacement, δ_c, are the two most important parameters that characterize the traction-separation expression. Given a traction-separation law, the the cohesive energy (for mode I) can be obtained as

$$G_{IC} = \int_0^{\delta_c} \sigma(\delta) d\delta \tag{2.43}$$

A bilinear or triangular traction-separation relation is depicted in Figure 2.11. It should be noted that the mechanical behaviour of the bulk material is independent of the softening function and can be extracted by any constitutive equation.

2.7 Simulation of fracture

Irrespective of the micro-structure of the material, the loading condition and the environmental state, the entire fracture process can be outlined as the nucleation, growth and coalescence of small cracks, or more overall, discontinuities in the material. However, In classical models, the material is modelled as a continuum. This implies that (i) it entirely fills the space that it occupies, ignoring pores and empty spaces and (ii) its properties are designated by continuous functions (MALVERN, 1969). It might be clear that this assumption not only does not permit the integration of detailed information on the micro-structure with the primary flaws, but also discard the nucleation and coalescence of the micro-separations in the FPZ. In lieu of modelling the whole micro-structure and each single micro-separation, the most typical technique is to lump the consequences of

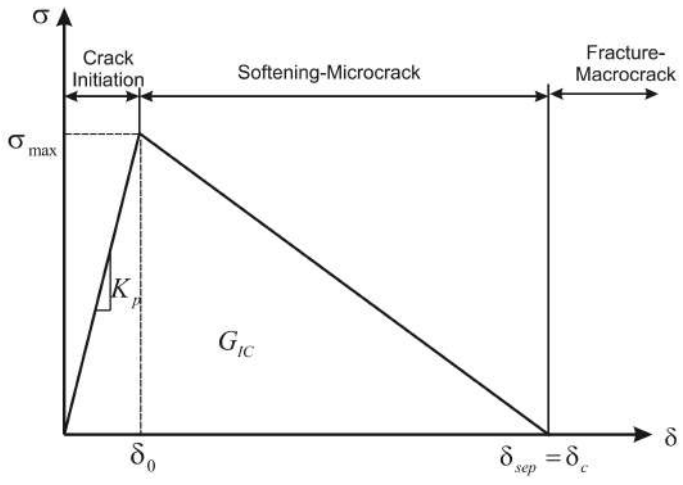

Figure 2.11: Bilinear traction-separation law.

all micro-separations in the FPZ in one single model that dominate the growth of a single prevailing crack. Such a model should desirably account for the following two essential properties of the FPZ. Firstly, the stiffness and the strength of the material must decrease in a realistic way, and secondly, this decrease of stiffness and strength must be supplemented with the correct decline of internal energy in the material.

In primitive models, the growth of an individual crack in elastic solids was modelled by means of the theorem of minimum energy. GRIFFITH (1921) proposed that a crack, which can be modelled as a discontinuity in a smooth displacement field, is merely permitted to grow over a certain length whenever the surface energy in the structure is identical to the energy required for the micro-separations in the FPZ to nucleate and propagate. IRWIN (1957) extended the Griffith's theory was extended for ductile materials introduced the concept of SIFs with respect to the energy release rate to qualify the stress states ahead of the crack tip. The extension of Griffith's work for application to elastic-plastic solids (RICE, 1968) and the application of the method in association with the FEM, has resulted in an effective tool for the modelling of crack propagation, frequently named as LEFM. In spite of the successful implementation in a variety of engineering problems, the method has several drawbacks. Firstly, as the phenomena in the FPZ are lumped in a single spot at the crack tip, the method can only be utilized in those cases where the FPZ is comparatively small. Secondly, the approach does not permit for the nucleation of a crack in undamaged-material far from a flaw. And lastly, the procedure that determines the direction of the crack propagation has not been rightly contained into the FE model. Alternatively, the results of the FE computations serve as an input for the estimation of the new crack path, and vice versa (INGRAFFEA and SAOUMA, 1985; KNOPS, 1994). This implies that when the crack is extended, the elements in the proximity of the crack tip demands remeshing, a process which restricts the applicability of LEFM. On the other hand, the progress of the FEM in engineering has promoted the development of new approaches for the simulation of fracture, typically termed as non-linear theories. Over the years, two trends can be recognized, the smeared or continuous method and the discrete or discontinuous method.

2.7.1 Smeared approach

The smeared approach to fracture initiates from the scheme that the micro-mechanical phenomena in the proximity of an integration point in the FEM are transferred into deterioration of the stiffness and the strength of the material in such point. Primarily, the material properties in all integration points are presumed to be linear elastic. When an equivalent stress in an integration point meets a prescribed criterion, e.g. the principal stress surpasses a yield limit, the linear elastic stress-strain expression changes. Complete failure of the structure is achieved when the stiffness decreases to zero. Even though the general behaviour of the model is in compliance with reality, from a structural standpoint,

a real crack is never actually introduced in the model: neither as a discontinuity in the displacement field, nor as a separation in the FE mesh. In primary studies, the stiffness parameters in the tangential direction to the crack were set to zero (COPE *et al.*, 1980). It was soon appreciated that a gentle drop of the stiffness parameters was required for a more realistic mechanical behaviour. This is fulfilled in Continuum Damage Models (CDM) where the stiffness of the material point is reduced using a damage parameter or damage tensor (LEMAITRE and CHABOCHE, 1994). Basically, when the material is fully intact, this damage parameter is identical to zero. When the stress condition in a material point suppresses a threshold figure, the damage parameter inclines based on a material damage law which states the release of internal energy within the damage procedure. The maximum value of the damage parameter is equal to 1.0, which is associated with the condition that the material has thoroughly lost its load carrying capability. The approach has become a standard method for the simulation of fracture and has been implemented in a number of applications successfully (MAZARS and PIJAUDIER-CABOT, 1989). Rather than the making of a real crack in the material (a discontinuity in the displacement field), the deformations in the FPZ will concentrate and raise the large deformation gradients in a narrow band in the FPZ, which ultimately leads to numerical problems. Furthermore, the width of this band must be at least identical to the width of a specific element in the FE mesh. Obviously, this imposes serious restrictions on the applicability of the technique to materials with comparatively small FPZ. In order to prevent such problems, models have been evolved where the large deformation gradient is included in the kinematic relation of the element as an extra strain field. These models are typically designated as embedded discontinuity methods (BELYTSCHKO *et al.*, 1988; ORTIZ *et al.*, 1987; SIMO *et al.*, 1993).

2.7.2 Discrete approach

The most prominent method among discrete fracture models is the CCM, pioneered by DUGDALE (1960) and BARENBLATT (1962). NEEDLEMAN (1987) generalised the technique by inserting cohesive constitutive relations at particular planes in the materials, whether a crack exists or not. Besides the fact that this method capture crack nucleation, there is an extra technical benefit. By defining the cohesive relation along a surface, determining the length of the cohesive zone is not mandatory. The failure characteristics of the material are dominated by an independent constitutive expression which explains the separation of the cohesive surface. This cohesive constitutive relation in combination with the constitutive relation for the bulk material and the adequate balance laws and boundary conditions, completely designate the problem.

The well-known cohesive constitutive expression is one where the cohesive surface traction is a function of the displacement jump over this surface. Conventionally, the

cohesive surfaces have been implemented in the FE mesh beforehand by using interface elements that are situated between the standard continuum elements (ALFANO and CRISFIELD, 2001; ALLIX and LADEVÈZE, 1992; SCHELLEKENS and DE BORST, 1993). Note that this technique has been implemented in ABAQUS® software successfully (HADDAD and SEPEHRNOORI, 2015a; JOUSSET and RACHIK, 2014; SCHEIDER, 2001; SCHWALBE *et al.*, 2012). The interface elements includes two surfaces that are linked to the neighbouring continuum elements. A perfect bond before cracking can be simulated by assigning a high dummy stiffness to the interface elements. When the crack path is recognised beforehand from experiments, the interface elements can be located in the FE mesh along the prescribed crack path. Nonetheless, in some real cases, the crack path is not known in advance and the placement of cohesive elements can be problematic. In (XU and NEEDLEMAN, 1993) interface elements are situated between all continuum elements in the mesh. This technique permitted the modelling of complex fracture such as crack branching (XU and NEEDLEMAN, 1994) and crack initiation away from the crack tip, as shown in Figure 2.12.

Nonetheless, the technique of inserting interface elements between all continuum elements is not thoroughly mesh independent. In fact, as the interface elements are aligned with element boundaries, cracks orientation is limited to a restricted number of angles. Additionally, if, as in (XU and NEEDLEMAN, 1993) the initial compliances are set to be non-zero, the existence of the interfaces leads to the general compliance of the body and an ill-posed problem results. The value of this error can decrease by rising the dummy stiffness which relates the elastic behaviour of the cohesive zone before fracture. Unfortunately, this can results in numerical problems.

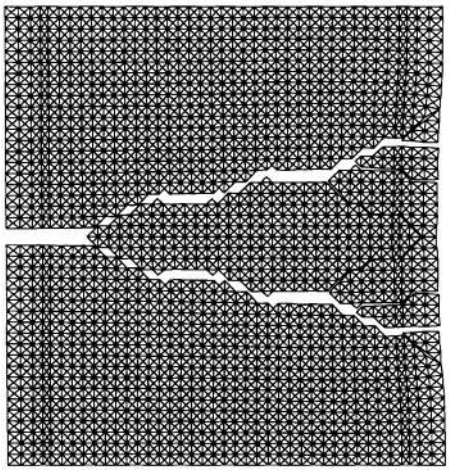

Figure 2.12: Modelling of crack branching in using inter-element cohesive surface models. (XU and NEEDLEMAN, 1994)

2.7.3 Enriched Methods

Obviously, the application of either the smeared or discrete fracture models is limited owing to mesh dependency. This can be related to practical problems, such as the inserting the interface elements in the FE mesh, and also numerical difficulties caused by large deformation gradients. In order to prevent these drawbacks, recent advancements in the field of numerical fracture mechanics have concentrated on new approaches to prevent mesh dependencies.

2.7.3.1 eXtended Finite Element Method (XFEM)

In an elegant work, which can be named as the pioneering attempt towards the XFEM, a local enrichment of the domain for crack propagation problem was proposed by BELYTSCHKO and BLACK (1999) using the partition of unity (BABUŠKA and MELENK, 1997). The enriched basis function was established by simple multiplication of the enrichment function with the standard FE basis functions. The analytical solution for the displacement and stress field near the crack tip were known from the theory of the LEFM. Thus, they used near tip enrichment functions to enrich the field in the vicinity of the crack throughout the crack length. By using this method, no re-meshing was demanded as the crack propagates, however, for severely curved cracks a re-meshing was needed in the proximity the crack root. Nonetheless, a remarkable contribution was that, the technique was able to simulate the crack arbitrarily aligned with FE mesh with minimal amount of re-meshing. Next modification to the approach was proposed by MOËS and BELYTSCHKO (1999). The modified version what is now called as XFEM removed the need for minimal mesh refinement. They represented that any type of generic function that best describes the field can be incorporated into the approximation space.

The XFEM gains from many advantages over the classical FEM, particularly for problems with moving boundaries. In the classical FEM, the crack propagates in the direction which is limited to the inter-element boundaries, involving with the trouble of mesh dependency. To remedy the problem of the sensitivity to the mesh generated, mesh adaptivity is needed (AZADI and KHOEI, 2011), which leads the simulation of the crack propagation to be computational expensive. The promising method that avoids such difficulties is the XFEM, which introduces arbitrary discontinuities into the finite element approximation without mesh dependencies. In XFEM, a crack is modelled as a discontinuity in the displacement field by employing the partition of unity property of FE shape functions.

The partition of unity approach to cohesive fracture has a variety of advantages over the conventional methods. The cohesive surface can be situated as a discontinuity anywhere in the model, in spite of the structure of the underlying FE mesh. Moreover, it is probable to extend a cohesive surface during the simulation by adjoining extra degrees of freedom. This prevents the use of high dummy stiffnesses to model a perfect bond be-

fore cracking. As degrees of freedom are just added when a cohesive surface is extended, the total number of degrees of freedom can also be smaller. Ultimately, since the technique is according to a present cohesive surface formulation, present cohesive constitutive models can still be employed. Application of the XFEM to the CCM was first done by the works of WELLS and SLUYS (2001) and MOËS and BELYTSCHKO (2002). After that, the cohesive segments method proposed by REMMERS *et al.* (2003, 2008) within the framework of XFEM permitted the simulation of the nucleation, growth, coalescence, and branching of multiple cohesive cracks in quasi-brittle materials. Indeed, the imperative attribute of the cohesive segments method was the feasible emergence of multiple cohesive cracks in a domain. In the proposed method, the magnitude of the displacement jumps, which was the representative of displacement discontinuities, was managed by the cohesive constitutive relation. In this method, the cohesive segments were only inserted through the integration point when they were needed and decohesion initiates. Inasmuch as the crack growth path did not rely on the mesh, the new cohesive segments can nucleate at arbitrary positions with arbitrary orientations, and the existing ones could grow in arbitrary paths when a critical condition is satisfied.

In the subsequent parts, a brief introduction to the application of XFEM in crack modelling will be given.

2.7.3.1.1 Concise review of FEM Consider a domain in the state of equilibrium descretized by a four-node quadrilateral FE mesh, as shown in Figure 2.13 (BATHE, 2006). Based on the FE methodology, the coordinates $\mathbf{x}^{\mathrm{T}} = (x, y)$ are interpolated from the nodal values $\bar{\mathbf{x}}^{\mathrm{T}} = (\overline{x}, \overline{y})$

$$\mathbf{x} = \sum_{j=1}^{4} \mathbf{N}_j \bar{\mathbf{x}}_j \tag{2.44}$$

In an isoparametric FE representation, displacement fields $\mathbf{u}^{\mathrm{T}} = (u_x, u_y)$ are interpolated from the nodal displacements nodal values $\bar{\mathbf{u}}^{\mathrm{T}} = (\overline{u}_x, \overline{u}_y)$

$$\mathbf{u} = \sum_{j=1}^{4} \mathbf{N}_j \bar{\mathbf{u}}_j \tag{2.45}$$

in which $\mathbf{N}_j$ is the matrix of FE shape functions,

$$\mathbf{N}_j = \begin{bmatrix} N_j & 0 \\ 0 & N_j \end{bmatrix} \tag{2.46}$$

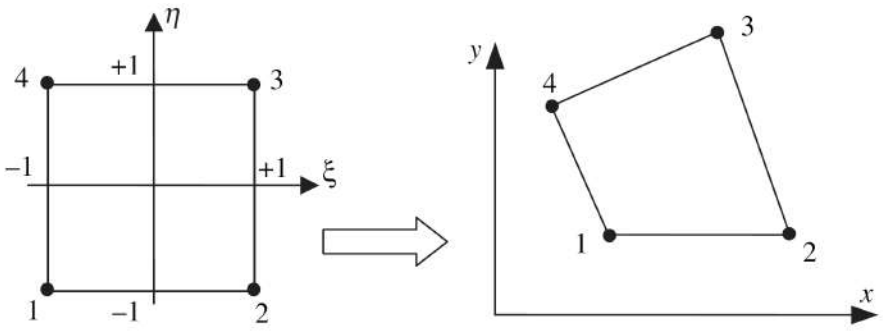

Figure 2.13: Mapping from the parent to the physical Cartesian coordinate system. (BATHE, 2006)

The strain field is derived directly from Eq. 2.46

$$\varepsilon = \sum_{j=1}^{4} \mathbf{B}_j \bar{\mathbf{u}}_j \tag{2.47}$$

in which the matrix $\mathbf{B}_j$ is defined in terms of derivatives of the shape functions $\mathbf{N}_j$ as

$$\mathbf{B}_j = \begin{bmatrix} \frac{\partial N_j}{\partial x} & 0 \\ 0 & \frac{\partial N_j}{\partial y} \\ \frac{\partial N_j}{\partial y} & \frac{\partial N_j}{\partial x} \end{bmatrix} \tag{2.48}$$

and the chain rule is invoked to compute the coefficients of $\mathbf{B}_j$

$$\begin{Bmatrix} \frac{\partial N}{\partial x} \\ \frac{\partial N}{\partial y} \end{Bmatrix} = \mathbf{J}^{-1} \begin{Bmatrix} \frac{\partial N}{\partial \xi} \\ \frac{\partial N}{\partial \eta} \end{Bmatrix} \tag{2.49}$$

where $\mathbf{J}$ is the Jacobian matrix

$$\mathbf{J} = \begin{bmatrix} \frac{\partial x}{\partial \xi} & \frac{\partial y}{\partial \xi} \\ \frac{\partial x}{\partial \eta} & \frac{\partial y}{\partial \eta} \end{bmatrix}, \qquad \mathbf{J}^{-1} = \frac{1}{\det \mathbf{J}} \begin{bmatrix} \frac{\partial y}{\partial \eta} & \frac{\partial y}{\partial \xi} \\ -\frac{\partial x}{\partial \eta} & \frac{\partial x}{\partial \xi} \end{bmatrix} \tag{2.50}$$

Ultimately, the stiffness matrix $\mathbf{K}_e$ of an element Ω_e can be derived from

$$\mathbf{K}_e = \int_{\Omega_e} \mathbf{B}^T \mathbf{D} \mathbf{B} d\Omega \tag{2.51}$$

where $\mathbf{D}$ is the material stress-strain or constitutive matrix ($\sigma = \mathbf{D}\mathbf{B}\bar{\mathbf{u}}_i$). Eq. 2.51 can be rewritten in local curvilinear coordinates ξ, η

$$\mathbf{K} = \int_{-1}^{1} \int_{-1}^{1} \mathbf{B}(\xi,\eta)^T \mathbf{D} \mathbf{B} \left(\xi,\eta\right) \left(\det \mathbf{J}\right) d\xi d\eta \tag{2.52}$$

2.7.3.1.2 Partition of unity The concept of partition of unity has been employed in a variety of computational disciplines (BABUŠKA and MELENK, 1997). A partition of unity is expressed as a set of *m* functions $f_k(\mathbf{x})$ within a domain Ω_{pu} such that

$$\sum_{k=1}^{m} f_k(\mathbf{x}) = 1 \tag{2.53}$$

It can easily be represented that by choice of any arbitrary function $\psi(\mathbf{x})$, the following property is automatically met

$$\sum_{k=1}^{m} f_k(\mathbf{x})\psi(\mathbf{x}) = \psi(\mathbf{x}) \tag{2.54}$$

This is equivalent to the definition of the reproducing condition or completeness. Completeness is represented in terms of the order of the polynomial $\psi(\mathbf{x}) = p(\mathbf{x})$, which must be expressed exactly by approximating functions $f_k(\mathbf{x})$. Afterwards, zero completeness is reached if Eq. 2.54 holds for a constant $p(\mathbf{x})$. The set of isoparametric FE shape functions, N_j, also satisfy the state of partition of unity,

$$\sum_{j=1}^{n} N_j(\mathbf{x}) = 1 \tag{2.55}$$

where *n* is the number of nodes for each FE. The idea of partition of unity accommodates a mathematical framework for the development of an enriched solution, as will be discussed in the subsequent section.

2.7.3.1.3 Enrichment The enrichment can be considered as an act of enhancing the approximation of discretization based on the properties of the problem. In this way, the approximation space used to solve the problem is improved by integrating the behavior of the undertaken phenomenon. Computationally, the enriched solution can be determined by rising the order of completeness that leads to higher accuracy of the approximation by incorporating the information extracted from the analytical solution. The selection of enrichments depends on the a priori solution of the problem; as an example, in the LEFM, this is corresponding to an incline in accuracy of the approximation where analytical crack tip solutions are added to the enrichment terms. The enrichment can be obtained by including the information, which is known in advance from singular behavior of the solution, directly into the FE space. The key feature of incorporation of local enrichment into an approximation space is based on the multiplication of enrichment functions by nodal shape functions. The enrichment can be done locally by only enriching those nodes whose intersect a region of interest. Thus, the FE approximation of enriched domain can be expressed

by

$$\mathbf{u}(\mathbf{x}) = \sum_{i=1}^{N} \mathbf{N}_i(\mathbf{x}) \left(\bar{\mathbf{u}}_i + \sum_{j=1}^{M} \mathbf{p}_j(\mathbf{x}) \bar{\mathbf{a}}_{ij} \right) \tag{2.56}$$

or

$$\mathbf{u}(\mathbf{x}) = \underbrace{\sum_{i=1}^{N} \mathbf{N}_i(\mathbf{x}) \bar{\mathbf{u}}_i}_{\text{standard interpolation}} + \underbrace{\sum_{i=1}^{N} \mathbf{N}_i(\mathbf{x}) \left(\sum_{j=1}^{M} \mathbf{p}_j(\mathbf{x}) \bar{\mathbf{a}}_{ij} \right)}_{\text{enhanced interpolation}} \tag{2.57}$$

in which $\overline{\mathbf{u}}_i$ is the standard nodal Degrees of Freedom (DOF) related to the basis $\mathbf{N}_i(\mathbf{x})$, and $\overline{\mathbf{a}}_{ij}$ are the enriched degrees of freedom related to the basis $\mathbf{p}_i(\mathbf{x})$, with *M* designating the number of enrichment functions for node *i*. The terms "standard" and "enriched" refer to the fact that the "standard" interpolation field is regarded as the background field upon which the "enriched" interpolation field is imposed. As the FE shape functions constitute a partition of unity, the interpolation of the displacement field $\mathbf{u}(\mathbf{x})$ in Eq. 2.57 can be expressed as the compound of the standard FE interpolation field and an enriched interpolation field, in which the enriched terms are employed to enhance the standard interpolation.

2.7.3.1.4 Basis of XFEM approximation The XFEM as an enriched partition of unity technique has been substantially used in numerical simulation of discontinuous problems.

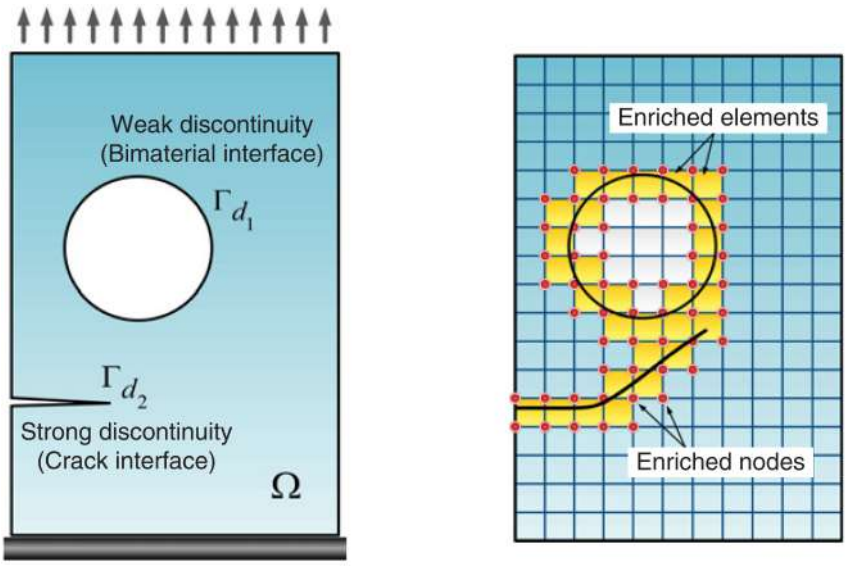

(a) (b)

Figure 2.14: Application of XFEM in modeling of weak and strong discontinuities. (**a**): Internal interfaces, including: the bimaterial interface and crack interface; (**b**) A mesh in which the circled nodes have extra DOF and enhanced functions. (KHOEI, 2014)

The approach, which is a powerful and a precise method, is employed to model weak and strong discontinuities with minimum enrichment deprived of considering their geometries. In this technique, the discontinuities are not contemplated in the mesh generation process and particular functions that are based on the nature of discontinuity are incorporated into the FE approximation. In the XFEM, the external boundaries are just considered in mesh generation process and internal boundaries, such as cracks, contact surfaces, voids, and so on, do not affect mesh configurations. This technique has adequate applications in engineering problems with moving boundaries, such as crack propagation, punching, phase changing, and shear banding. To establish the concept of discontinuous enrichment, suppose that Γ_d is a discontinuity in domain Ω, as depicted in Figure 2.14a. We aim to create an FE approximation to the field $\mathbf{u} \in \Omega$ which can be discontinuous along the discontinuity Γ_d. The conventional method is to generate the mesh to adjust to the line of discontinuity as demonstrated in Figure 2.14b, in which the element sides are aligned with Γ_d. But, this strategy definitely causes a discontinuity in the approximation, it can be complex if the discontinuity Γ_d evolves in time, or if various configurations for Γ_d are to be supposed. In the XFEM, the discontinuity across Γ_d is modeled with enriched functions, in which the mesh of Figure 2.14b is capable of modeling the discontinuity in $\mathbf{u} \in \Omega$ when the circled nodes are enhanced with functions, which are discontinuous along Γ_d.

Consider the enhanced approximation field stated in Eq. 2.56, the first sum of the second term of the right hand side of Eq. 2.56 can be skipped, if a single interface Γ_d is modeled. Therefore, the enhanced approximation for a single interface Γ_d can be obtained

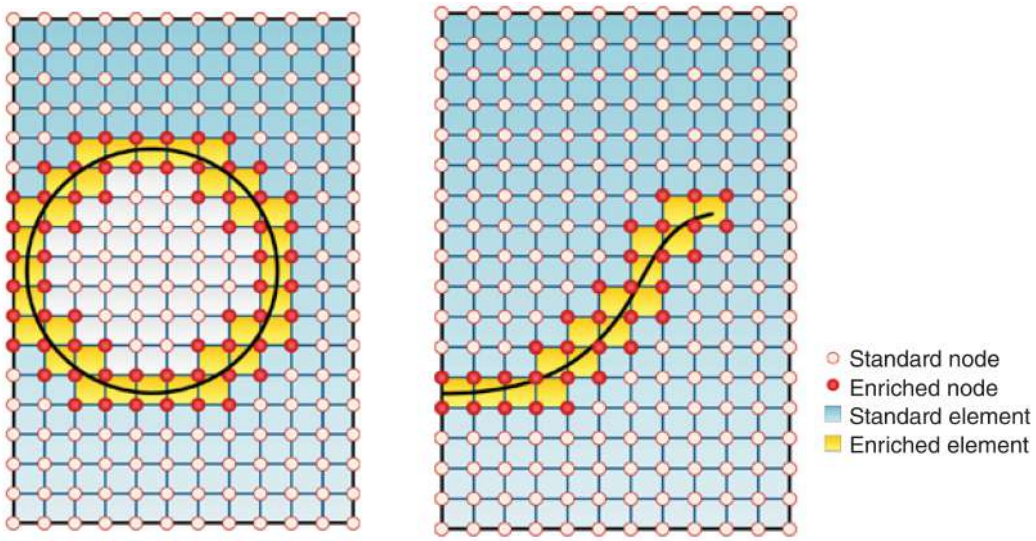

Figure 2.15: The use of XFEM for modeling of discontinuity. (**a**) The weak discontinuity as a bi-material interface; (**b**) The strong discontinuity as a crack interface.

as

$$\mathbf{u}(\mathbf{x}) = \sum_{i=1}^{N} \mathbf{N}_i(\mathbf{x})\bar{\mathbf{u}}_i + \sum_{j=1}^{M} \bar{\mathbf{N}}_j(\mathbf{x})\psi(\mathbf{x})\bar{\mathbf{a}}_j \tag{2.58}$$

where the shape functions of enhanced section $\overline{\mathbf{N}}_j(\mathbf{x})$ are selected similar to the FE shape functions $\mathbf{N}_j(\mathbf{x})$. In this equation, $\overline{u}_i$ is the standard nodal displacement, $\bar{\mathbf{a}}_i$ is the nodal DOF corresponding to the enrichment function, $\psi(\mathbf{x})$ is the enrichment function, and $\mathbf{N}(\mathbf{x})$ is the standard shape function. In Eq. 2.58, *N* is the set of all nodal points of domain, and *M* is the set of nodes of elements located on the discontinuity Γ_d. In the XFEM, the different kinds of problems demands proposing suitable enhanced functions. Various techniques shall be employed for the enrichment function; these functions are related to the kind of discontinuity and its effects on the form of solution. These methods include the signed distance function, branch function, level set function, Heaviside function, and so on. The selection of enrichment functions in displacement approximation depends on the situation of problem. If the discontinuity is due to different kinds of material properties (Figure 2.15a), the level set function can be used as an enrichment function, but, if the discontinuity is because of different displacement fields on either edges of the discontinuity (Figure 2.15b), the Heaviside function is adequate (BELYTSCHKO *et al.*, 2009).

Now we turn our attention to the description of the application of XFEM to cracks. Consider an FE model of a cracked body, as depicted in Figure 2.16. Let the set of all nodes in the FE mesh be denoted by *S*, the set of nodes of elements around the crack tip be stated by S_C and the set of nodes of elements cut by the crack, i.e. the discontinuity, but not in S_C be presented by S_H. The set of elements with nodes in S_C can be chosen by the user. Normally one element, as illustrated at crack tip B in Figure 2.16, suffices, but

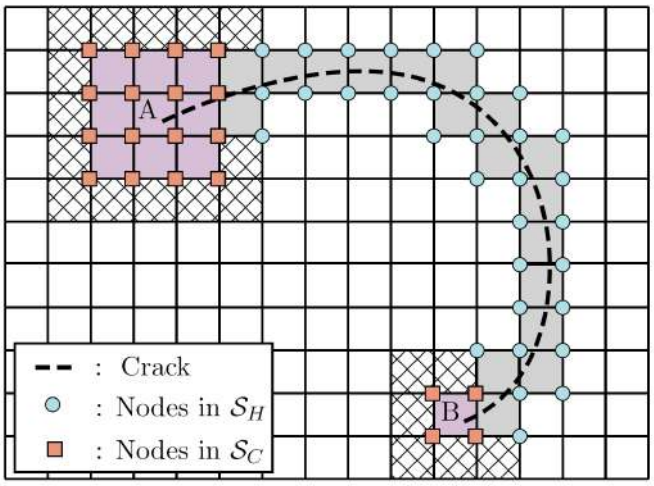

Figure 2.16: An arbitrary crack line in a structured mesh with enriched (light gray) and tip enriched (purple) elements. (BELYTSCHKO *et al.*, 2009)

some enhancements in accuracy may be achieved by using several elements, as depicted at crack tip A in Figure 2.16. Nodes in S_C and S_H are referred to as tip enriched and step enriched nodes, respectively, and all together as enriched nodes. Let the crack surface be given by an implicit function description, i.e. a level set, $\varphi(\mathbf{x})$ (expressing the crack in this way enables the technique to deal with discontinuities such as cracks without any supplementary information other than at nodal points, as discussed later) and let $\varphi(\mathbf{x})$ have opposite signs on the two edges of the crack. The XFEM displacement field for a crack is given by (BELYTSCHKO *et al.*, 2009)

$$\begin{aligned}\mathbf{u}(\mathbf{x}) = \sum_{\forall I} N_I(\mathbf{x})\mathbf{u}_I + \sum_{J\in S_H} N_J(\mathbf{x})\left[H(\varphi(\mathbf{x})) - H(\varphi(\mathbf{x}_J))\right]\mathbf{q}_J^0 \\ + \sum_j \sum_{K\in S_C} N_K(\mathbf{x})\left[\Psi^{(j)}(\mathbf{x}) - \Psi^{(j)}(\mathbf{x}_K)\right]\mathbf{q}_K^{(j)}\end{aligned} \tag{2.59}$$

in which $H(\mathbf{x})$ is the Heaviside step function provided by

$$H(\mathbf{x}) = \begin{cases} 1, & x > 0 \\ 0, & \text{otherwise} \end{cases} \tag{2.60}$$

and where $\Psi^{(j)}$ is a set of enrichment functions which approximate the near tip behaviour, $\mathbf{q}_I^{(j)}$ are the enrichment coefficients which are extra unknowns at the nodes and $\mathbf{x}_J$ is the position of node *J*. It should be noted that Eq. 2.59 is a local partition of unity on the contrary to the global form in Eq. 2.58, i.e. the enrichment is added only where it is effective. This considerably enhances the computational efficiency because generally further fewer unknowns are introduced by the enrichment than in a global partition of unity.

2.7.3.1.5 Brittle cracks Modeling the crack in brittle materials can be carried out in the framework of LEFM, in which the stresses and strain fields ahead of the crack tip are singular. The implementation of XFEM for simulation of the crack in brittle materials was commenced from the original works of XFEM by BELYTSCHKO and BLACK (1999) and MOËS and BELYTSCHKO (1999). In the work of BELYTSCHKO and BLACK (1999), the asymptotic enrichment functions were used for the entire crack path and the kinks were dealt with in the crack path by special mappings. Nonetheless, MOËS and BELYTSCHKO (1999) introduced the asymptotic enrichment functions ahead of the crack tip area and the Heaviside function across the crack path, which has been constituted as a standard procedure in the XFEM methodology. DAUX *et al.* (2000) developed the XFEM method for the modelisation of cracks with multiple branches and intersections, where a step enrichment function was proposed for crack junctions that did not rely on level-sets. The XFEM was used to 3-D crack problems by SUKUMAR *et al.* (2000). The XFEM was established by DOLBOW *et al.* (2001) for modeling crack propagation with

frictional contact on the crack faces. AREIAS and BELYTSCHKO (2005) studied the 3-D crack initiation and propagation for the quasi-static analysis of brittle and quasi-brittle solids. XIAO and KARIHALOO (2006) suggested an alternative technique to ameliorate the FE approximation with higher order terms of the asymptotic expansion of the crack tip field as enhanced functions, and extracted the SIFs directly without extra post-processing. For cracks in brittle materials, the crack tip enrichment functions, $\Psi^{(i)}$, are based on the asymptotic solution of WILLIAMS (1961), which is given by

$$\left\{\Psi^{(i)}\right\}_{i=1}^{4} = \sqrt{r}\left\{\cos\left(\theta/2\right), \sin\left(\theta/2\right), \sin\left(\theta/2\right)\sin\left(\theta\right), \cos\left(\theta/2\right)\sin\left(\theta\right)\right\} \tag{2.61}$$

Obviously, just the first asymptotic function demonstrates the discontinuity near the tip on both sides of the crack whereas the other three functions can be employed to improve the accuracy of the approximation. The application of asymptotic crack-tip functions is not limited to crack simulation in an isotropic elastic material. The same technique can be employed to capture a crack along a bimaterial interface, impinged on the bimaterial interface, or in an elastic-plastic power-law hardening material. But, in each of these three cases different features of asymptotic crack-tip functions are demanded depending on the crack location and the extent of the inelastic material deformation (ELGUEDJ *et al.*, 2006; SUKUMAR *et al.*, 2004).

2.7.3.1.6 Cohesive cracks In the following, we concentrate on the modelling of a cohesive crack, which forms the fundamental cohesive crack simulation in the present dissertation. The early implementation of an enriched FEM for modeling of cohesive crack propagation was done by WELLS and SLUYS (2001) based on the partition of unity. They used the Heaviside function along the whole crack as well as the crack tip. Nevertheless, it should be indicated that if only the Heaviside function is applied at all nodes, the XFEM approximation is not able to handle crack tips that are positioned inside elements. To overcome this obstacle, WELLS and SLUYS (2001) supposed that the crack can be practically extended to the next element edge. The XFEM was employed by MOËS and BELYTSCHKO (2002) in the cohesive crack modelling using the cohesive branch functions, where the growth of the cohesive zone was dominated by demanding the SIFs ahead of the tip of the cohesive zone to vanish. A methodology for the modelling of quasi-static cohesive crack growth in quasi-brittle materials was proposed by MARIANI and PEREGO (2003). In their technique, a cubic displacement discontinuity was employed based on the product of the Heaviside function and polynomial ramp functions, which was able to reproduce the common cusp-like shape of the process zone ahead of the crack tip. The cohesive segments method proposed by REMMERS (2006); REMMERS *et al.* (2003, 2008) within the framework of XFEM permits the simulation of the nucleation, growth, coalescence, and branching of multiple cohesive cracks in quasi-brittle materials.

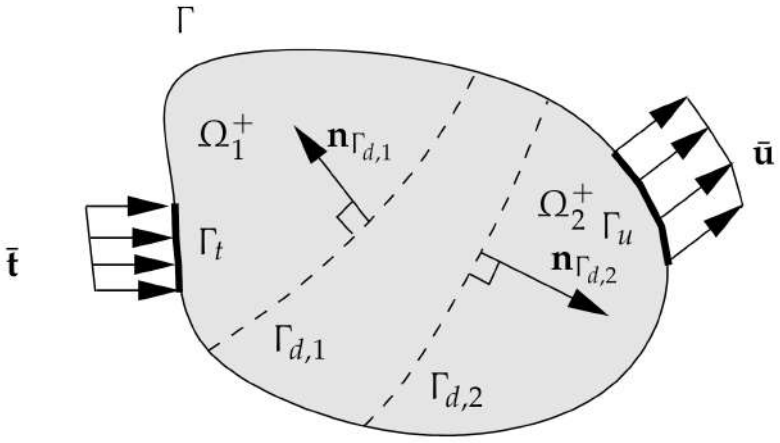

Figure 2.17: Domain Ω with two discontinuities, $\Gamma_{d,1}$ and $\Gamma_{d,2}$ (dashed lines).

Indeed, the imperative attribute of the cohesive segments method is the feasible emergence of multiple cohesive cracks in a domain. In the proposed method, the magnitude of the displacement jumps, which is the representative of displacement discontinuities, is managed by the cohesive constitutive relation. In this method, the cohesive segments are only inserted through the integration point when they are needed and decohesion initiates. Inasmuch as the crack growth path does not rely on the mesh, the new cohesive segments can nucleate at arbitrary positions with arbitrary orientations, and the existing ones can grow in arbitrary paths when a critical condition is satisfied. There are a variety of the applications of cohesive crack modelling within the XFEM framework, such as modeling the quasi-brittle fracture in Functionally Graded Materials (FGM) by COMI and MARIANI (2007), modeling the cohesive crack propagation in concrete structures by UNGER *et al.* (2007), and so on. Consider a 2-D domain Ω with boundary Γ as shown in Figure 2.17. The domain includes m discontinuities $\Gamma_{d,j}$, where $j = 1, .., m$. It is assumed that the discontinuities do not cross. Each discontinuity divides the domain into two parts, which are stated accordingly as Ω_j^- and Ω_j^+ . For all discontinuities *j* in the domain, the following relation must hold

$$\Omega_j^- \cup \Omega_j^+ = \Omega \qquad \forall \qquad j = 1, ...j \tag{2.62}$$

The displacement field in the domain Ω contains a continuous regular displacement field $\hat{\mathbf{u}}$ plus *m* additional continuous displacement fields $[\![\mathbf{u}_j]\!]$ as follows (REMMERS *et al.*, 2003)

$$\mathbf{u}(\mathbf{x}, t) = \hat{\mathbf{u}}(\mathbf{x}, t) + \sum_{j=1}^{m} H_{\Gamma_{d,j}}(\mathbf{x}) [\![\mathbf{u}_j]\!](\mathbf{x}, t) \tag{2.63}$$

where $\mathbf{x}$ refers to the position of a material point, t is the time, and $H_{\Gamma_{d,j}}$ is the Heaviside step function, defined as

$$H_{\Gamma_{d,j}}(\mathbf{x}) = \begin{cases} 0, & \text{if } \mathbf{x} \in \Omega_j^- \\ 1, & \text{if } \mathbf{x} \in \Omega_j^+ \end{cases} \tag{2.64}$$

The strain field can be derived by taking the derivative of the displacement field in Eq. 2.63 as

$$\varepsilon(\mathbf{x}, t) = \nabla^s \hat{\mathbf{u}}(\mathbf{x}, t) + \sum_{j=1}^{m} H_{\Gamma_{d,j}}(\mathbf{x}) \nabla^s [\![\mathbf{u}_j]\!](\mathbf{x}, t) \tag{2.65}$$

where ∇^s denotes the symmetric differential operator

$$\nabla^s()_{ij} = \frac{1}{2}\left(\frac{\partial}{\partial x_i}()_j + \frac{\partial}{\partial x_j}()_i\right) \qquad i, j = 1, 2, 3 \tag{2.66}$$

It is noted that the strain field is not defined at the discontinuities $\Gamma_{d,j}$. The magnitude of the displacement jump at the discontinuities can be extracted by $[\![\mathbf{u}_j]\!]$ according to Eq. 2.67. Therefore, the discrete feature of the displacement field can be expressed using Eq. 2.63 as

$$\mathbf{u}(\mathbf{x}, t) = \mathbf{N}(\mathbf{x})\bar{\mathbf{u}}(t) + \sum_{j=1}^{m} H_{\Gamma_{d,j}}(\mathbf{x}) \mathbf{N}(\mathbf{x}) \bar{\mathbf{a}}_j(t) \tag{2.67}$$

in which the vector $\bar{\mathbf{u}}$ consists of the standard nodal DOF and $\bar{\mathbf{a}}_j$ contains the enriched nodal DOF related to the discontinuity $\Gamma_{d,j}$. The matrix $\mathbf{N}(\mathbf{x})$ contains the conventional shape functions. The discrete form of the strain field is denoted by differentiating Eq. 2.63 as

$$\varepsilon(\mathbf{x}, t) = \mathbf{B}^{std}(\mathbf{x})\bar{\mathbf{u}}(t) + \sum_{j=1}^{m} \mathbf{B}_j^{enr}(\mathbf{x}) \bar{\mathbf{a}}_j(t) \tag{2.68}$$

where $\mathbf{B}^{std}(\mathbf{x}) = \mathbf{L}\mathbf{N}(x)$ consists of the spatial derivatives of the standard shape functions and $\mathbf{B}_j^{enr}(\mathbf{u}) = \mathbf{L}\mathbf{N}_j^{enr}(\mathbf{x})$ includes the spatial derivatives of the enriched shape functions, where $\mathbf{N}_j^{enr}(\mathbf{u}) = H_{\Gamma_{d,j}}\mathbf{N}(\mathbf{x})$ is referred to as the matrix of the enriched shape functions for the discontinuity $\Gamma_{d,j}$, and $\mathbf{L}$ is a differential operator matrix expressed in the Cartesian coordinate system as

$$\mathbf{L} = \begin{bmatrix} \partial/\partial x & 0 \\ 0 & \partial/\partial y \\ \partial/\partial y & \partial/\partial x \end{bmatrix} \tag{2.69}$$

Lastly, the discretized displacement jump at the discontinuity $\Gamma_{d,j}$, can be stated according to Eq. 2.67 by $[\![\mathbf{u}_j]\!] = \mathbf{N}(\mathbf{x})\bar{\mathbf{a}}_j$. In the cohesive segments method (REMMERS *et al.*, 2003), the cohesive segments are not considered at the starting of the procedure. This means that an initially rigid cohesive constitutive relation must be employed, contrary to the methods in which the cohesive interface elements are inserted into inter-element boundaries in advance, and consequently, cohesive constitutive expressions with an initial elastic branch is utilized. Boundary condition along the crack, Γ_d , is $\sigma.\mathbf{n}_{\Gamma_d} = \mathbf{t}_d$, where $\mathbf{n}_{\Gamma_d}$ is the unit normal vector to the discontinuity Γ_d pointing to Ω^+, and $\mathbf{t}_d$ is the cohesive traction transferred along Γ_d, which is associated with the displacement jump at the discontinuity using the cohesive law. It should be noted that behavior of the fracturing material in the FPZ (explained in Section 2.6) is represented by a traction-separation law relating the cohesive traction to the relative displacement as

$$\mathbf{t}_d = \mathbf{t}_d([\![\mathbf{u}_j]\!]) \tag{2.70}$$

where $\mathbf{t}_d = t_n\mathbf{n}_{\Gamma_d} + t_s\mathbf{t}_{\Gamma_d}$ is the cohesive traction applied through the FPZ, with $\mathbf{n}_{\Gamma_d}$ and $\mathbf{t}_{\Gamma_d}$ representing the unit vector of normal and tangential directions, respectively, and t_n and t_s are normal and shear components of the 2-D traction vector, respectively. $[\![\mathbf{u}_j]\!]$ is expressed as the relative displacement vector across the discontinuity, the discrepancy between the displacement vectors at the two sides of the discontinuity. In quasi-brittle materials, when the failure limit is met, the cohesive zone extends in which the material launches to fail and presents a softening behavior. The softening caused by the material failure is modeled by means of a softening cohesive law. This means that the cohesive traction transmitted across the cohesive zone is a decaying function of the relative displacement.

One of the striking features of the cohesive segment method (REMMERS *et al.*, 2003) is that the segments are not needed to present in the material at the onset of the analysis, but are inserted and developed during the course of a simulation. When the stress condition in a particular integration point in the bulk material satisfies the yield criterion of the material, a new cohesive segment is added. The segment, which is presumed to be straight, passes over this integration point and is developed into the adjacent elements until it reaches the outer boundaries of these elements, as depicted in Figure 2.18. The patch of adjacent elements contains all elements that share one of the nodes of the central element that consists of the integration point in which the criterion was satisfied. The nodes that support these outer boundaries are not enriched to guarantee a zero crack opening at the tips of the new segments. The extension of a cohesive segment is modelled as follows (WELLS and SLUYS, 2001); when the maximum principal stress at the tip satisfies the fracture criterion for a specific angle, the segment is developed into the next element in the direction normal to the corresponding principal axis, until it touches the boundary of that element. The stress condition at the tip is not known exactly. Thus, the stresses are

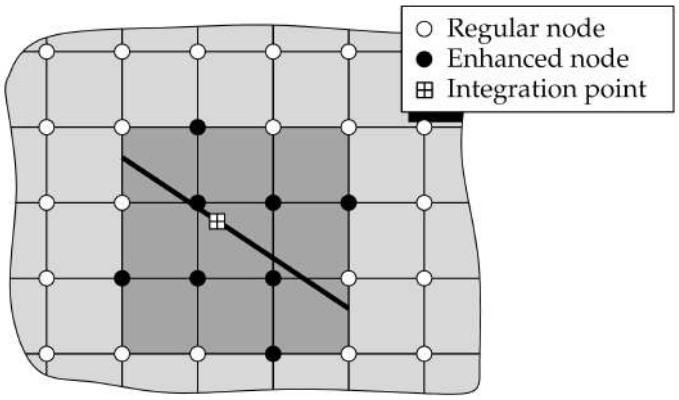

Figure 2.18: Creation of a new cohesive segment (bold line). (REMMERS, 2006)

estimated by calculating the average stress state in the proximity using a Gauss averaging criterion (WELLS and SLUYS, 2001).

2.8 Hydraulic fracture initiation

As demonstrated in Figure 1.2, when the borehole fluid pressure attains a critical value termed "breakdown pressure", the fracture starts to initiate. At breakdown, a droop in bottom hole pressure appear owing to the borehole fluid loss. The hydraulic fracture initiated from the wellbore is strongly associated with the magnitude and orientation of the in-situ stress field, which can be altered locally. In this section, we turn our attention to evaluation of the condition in which a fracture initiates from the borehole. To define the state of the near-wellbore stresses which is different form far-field ones, assume that rock formation is isotropic, homogenous, and linearly elastic. Herein, the orientation of the borehole with respect to the in-situ stress is defined by the wellbore azimuth, α, as the angle between the $\sigma_x(\sigma_{h,\min})$ direction and the projection of the borehole axis onto the $\sigma_x - \sigma_y$ plane, and the wellbore inclination, β, as the angle between the borehole axis and the σ_z direction as depicted in Figure 2.19. The rotation of the stresses from the in-situ coordinate system to the local wellbore coordinate system is expressed by

$$\begin{Bmatrix} \sigma_{xx} \\ \sigma_{yy} \\ \sigma_{zz} \\ \tau_{yz} \\ \tau_{xz} \\ \tau_{xy} \end{Bmatrix} = \begin{bmatrix} \sin^2\beta & \cos^2\beta\cos^2\alpha & \cos^2\beta\sin^2\alpha \\ 0 & \sin^2\alpha & \cos^2\alpha \\ \cos^2\beta & \sin^2\beta\cos^2\alpha & \sin^2\beta\sin^2\alpha \\ 0 & -\sin\alpha\cos\alpha\sin\beta & \sin\alpha\cos\alpha\sin\beta \\ -\sin\alpha\cos\beta & \sin\beta\cos\beta\cos^2\alpha & \sin\beta\cos\beta\sin^2\alpha \\ 0 & -\sin\alpha\cos\alpha\cos\beta & \sin\alpha\cos\alpha\cos\beta \end{bmatrix} \begin{Bmatrix} \sigma_z \\ \sigma_x \\ \sigma_y \end{Bmatrix} \tag{2.71}$$

where σ_x, σ_y, and σ_z are the far-field stresses. By employing the superposition of Kirsch's solution (JAEGER *et al.*, 2009), the anti-plane solution, and the solution for an internally

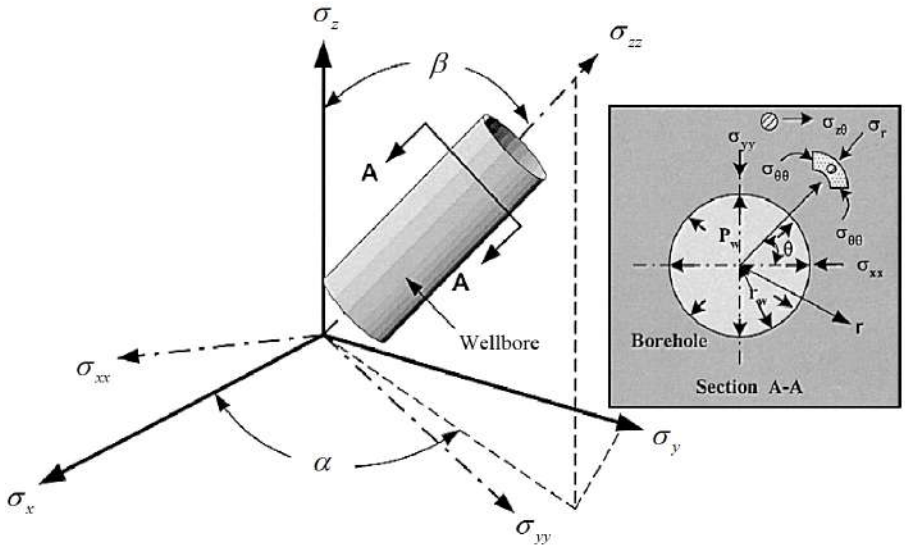

Figure 2.19: Pertinent parameters for an arbitrarily oriented wellbore configuration (HOSSAIN *et al.*, 2000).

pressure hole (BRADLEY, 1979; DEILY *et al.*, 1969; HUANG *et al.*, 2012), the filed stresses resulting from in-situ stresses and internal borehole pressure, p_w, are obtained as follow

$$\begin{aligned}\sigma_r = &\frac{1}{2}\left(\sigma_{xx}+\sigma_{yy}\right)\left(1-\frac{r_w^2}{r^2}\right)+\frac{1}{2}\left(\sigma_{xx}-\sigma_{yy}\right)\left(1-\frac{4r_w^2}{r^2}+\frac{3r_w^4}{r^4}\right)\cos 2\theta \\ &+\tau_{xy}\left(1-\frac{4r_w^2}{r^2}+\frac{3r_w^4}{r^4}\right)\sin 2\theta+\frac{r_w^2}{r^2}p_w\end{aligned} \tag{2.72}$$

$$\begin{aligned}\sigma_\theta = &\frac{1}{2}\left(\sigma_{xx}+\sigma_{yy}\right)\left(1+\frac{r_w^2}{r^2}\right)-\frac{1}{2}\left(\sigma_{xx}-\sigma_{yy}\right)\left(1+\frac{3r_w^4}{r^4}\right)\cos 2\theta \\ &-\tau_{xy}\left(1+\frac{3r_w^4}{r^4}\right)\sin 2\theta-\frac{r_w^2}{r^2}p_w\end{aligned} \tag{2.73}$$

$$\sigma_z = \sigma_{zz}-2v\left(\sigma_{xx}-\sigma_{yy}\right)\frac{r_w^2}{r^2}\cos 2\theta-4v\tau_{xy}\frac{r_w^2}{r^2}\sin 2\theta \tag{2.74}$$

$$\tau_{r\theta} = \left(-\frac{1}{2}\left(\sigma_{xx}+\sigma_{yy}\right)\sin 2\theta+\tau_{xy}\cos 2\theta\right)\left(1+\frac{4r_w^2}{r^2}-\frac{3r_w^4}{r^4}\right) \tag{2.75}$$

$$\tau_{rz} = \left(\tau_{xz}\cos\theta+\tau_{yz}\sin\theta\right)\left(1-\frac{2r_w^2}{r^2}\right) \tag{2.76}$$

$$\tau_{\theta z} = (-\tau_{xz}\sin\theta + \tau_{yz}\cos\theta)\left(1 + \frac{2r_w^2}{r^2}\right) \tag{2.77}$$

At the wall of the borehole ($r = r_w$), the above expression simplify to

$$\sigma_r = p_w \tag{2.78}$$

$$\sigma_\theta = (\sigma_{xx} + \sigma_{yy} - p_w) - 2(\sigma_{xx} - \sigma_{yy})\cos 2\theta - 4\tau_{xy}\sin 2\theta \tag{2.79}$$

$$\sigma_z = \sigma_{zz} - 2\upsilon(\sigma_{xx} - \sigma_{yy})\cos 2\theta - 4\upsilon\tau_{xy}\sin 2\theta \tag{2.80}$$

$$\tau_{r\theta} = \tau_{rz} = 0 \tag{2.81}$$

$$\tau_{\theta z} = 2(-\tau_{xz}\sin\theta + \tau_{yz}\cos\theta) \tag{2.82}$$

For a vertical well, one of the principal stress is parallel to the borehole axis. In this case, the breakdown pressure in the direction perpendicular to the minimum horizontal stress, ($\theta = \pi/2$) for an un-cased, smooth borehole is given by

$$p_{wf} = 3\sigma_x - \sigma_y - p + T \tag{2.83}$$

where p is the formation poe pressure and T is the formation tensile strength. The Eq. 2.83 is valid in the case of no fluid penetration (DETOURNAY and CHENG, 1988) and it gets an "upper bound" for the breakdown pressure. Nevertheless, if the leakage takes place before breakdown, a "lower bound" requires to be defined for the breakdown pressure as follows

$$p_{wf} = \frac{3\sigma_x - \sigma_y - 2\eta p + T}{2(1-\upsilon)} \tag{2.84}$$

where

$$\eta = \frac{\bar{\alpha}(1-2\upsilon)}{2(1-\upsilon)} \tag{2.85}$$

in which $\bar{\alpha}$ is the Biot's coefficient. Note that in HF jobs, when the low-viscosity fluids and/or low pumping rate are used, it is supposed that more fluid penetrates into the surrounding formation and, as a result, decreases the breakdown pressure (HOSSAIN *et al.*, 2000).

2.9 Numerical simulations of hydraulic fracturing

The simulation of HF, as a multi-physics problem which couples poro-mechanics, fluid mechanics, and fracture mechanics, has attracted considerable attention in not only unconventional resources, but also water well production enhancement, coal bed methane development, rock burst mitigation, and toxic or radioactive waste disposal. In this way, the most widely used distinguished computational methods for the simulation of HF will be explained in this section.

2.9.1 Boundary Element Method

First emerged in the work of CRUSE and RIZZO (1968) for elasticity problems, Boundary Element Method (BEM) was effectively introduced by BREBBIA and DOMINGUEZ (1977). Nowadays, BEM has been largely applied to solve many different kinds of engineering problems (BREBBIA *et al.*, 2012; MANSUR, 1983; TELLES, 2012; TREVELYAN, 1994) mainly because of the following advantages:

- BEM presents highly precise solutions for the problem.
- It is less computational expensive, in particular compared with FEM. It is because the problem is defined only at the boundaries of the body and, as a result, resulting systems of algebraic equations are significantly smaller.
- The results at any internal point of the domain can be obtained despite the boundary-only discretizing.
- The BEM presents its special advantages in specific classes of the problem including: ***(i)*** Infinite (or semi-infinite) domains, ***(ii)*** Discontinuous solution spaces. These problems are the main concern in wave propagation, fracture mechanics, re-entry corners and other stress intensity problems.

Nevertheless, BEM suffers from some drawbacks, which can be summarized as:

- A fundamental solution or Green's function, explaining the behaviour of a point load in an infinite medium of the material properties, is demanded as part of the kernel of the method. This restricts the application of the BEM to the specific problems where a Green's function is available.
- Calculation of the fundamental solution must be computationally efficient, thereby making explicit fundamental solution formulations desirable.
- The resulting system of equations is both non-symmetric and fully populated, leading to longer computing times, particularly in 3-D problems. In this case, special

techniques such as the fast multipole method (ROKHLIN, 1985) have been presented to speed up the solution.

- Non-linear material behavior causes problem in the application of the BEM.
- In some cases, BEM demands a re-meshing scheme to accommodate crack growth (RABCZUK *et al.*, 2010). The work of SIMPSON and TREVELYAN (2011) on enriched BEMs proposed the use of partition of unity method within the framework of BEM. However, this work has not been developed to multi-physics problems.
- The BEM formulation needs the evaluation of weakly singular, strongly singular and sometimes hypersingular integrals which must be carefully treated. This can be performed using a number of methods such as analytical regularisation (GARCIA *et al.*, 2004).

RUNGAMORNRAT *et al.* (2005) employed the BEM to treat elasticity problem associated with a fracture, and a Galerkin FEM to model the fluid flow within the fracture. In this work, th BEM was based on a weakly-singular, weak-form traction boundary integral equation which was applicable to non-planar fractures in Generally anisotropic media. The resulting coupled fracture/flow equations were solved using an iterative Newton-Raphson method. The results showed that during early stages of fracture growth, the fracture evolves from its initial elliptical shape toward a circular shape. As the fracture propagates into the stress showing area. the crack tends to propagate in the horizontal direction than in the vertical direction, as shown in Figure 2.20.

2.9.2 Displacement Discontinuity Method

In recent years, the Displacement Discontinuity Method (DDM) (SESETTY and GHASSEMI, 2015; VERDE and GHASSEMI, 2015) as one of the special sub-category of BEMs has been widely applied to simulate HF mechanism. Based on the DDM, when fractures propagate, new fracture elements are added without the re-meshing of the existing elements. Accordingly the element number is much less than that of the FEM. Because of that, DDM is an efficient technique in modelling of the complex fracture network during HF treatment.

MCCLURE (2012) developed a 2-D DDM model fully coupled with fluid flow and stresses induced by fracture opening and sliding, friction evolution, and fracture propagation in a pre-existing Discrete Fracture Network (DFN). One main drawback in McClure's approach is that the path of any new fracture, e.g., created from interaction with Natural Fractures (NF), must be predefined. In addition, one common restriction of 2-D models is not being able to model fracture height. This is not only an indispensable consideration in HF designs, but can also significantly have an impact on the fracture length growth.

REZAEI *et al.* (2015) studied fracture propagation from adjacent wells by using DDM. The developed numerical model was capable of simulating multiple fractures that may re-orient in space based on changing stress shadowing. Figure 2.22 (REZAEI *et al.*, 2015) shows the propagation of two hydraulic fractures that are spaced at 20 m in a half-length window of 300 m. It is shown here that for a case where fracture spacing is 20 m (Figure 2.22a), the fracture interference does not affect propagation path until after 100 m of propagation in the half-length window. In other words, the interference between fractures becomes effective when fracture tips are approximately 100 m away (Figure 2.22b). At that point, the fracture path is influenced by the presence of the other fracture and the two fractures propagate away from each other for about 25 m. As soon as the tips overlap (Figure 2.22c), the direction of maximum horizontal stress changes again and so the two fractures propagate toward each other from then on.

The results of a discrete element model numerical study of multi-well completions simulated in a fully hydro-mechanical coupled fashion were presented by NAGEL *et al.* (2014). Their 2-D numerical method was not capable of considering non-planar frac-

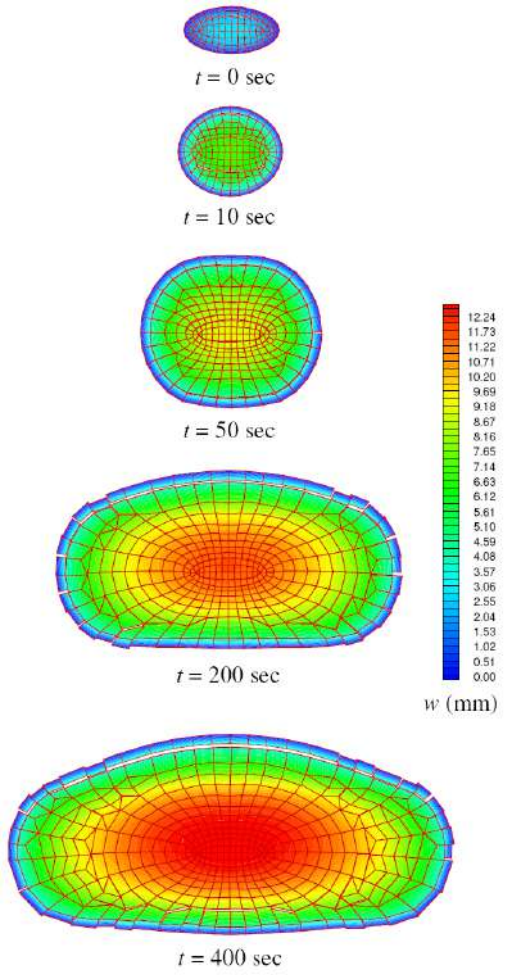

Figure 2.20: Evoluation of the fracture surface with time. contours are for crack opening. (RUNGAMORNRAT *et al.*, 2005).

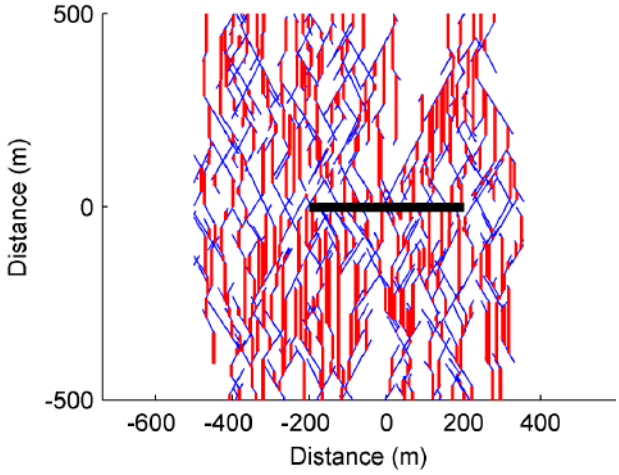

Figure 2.21: An example of a fracture network with hydraulic fractures by MCCLURE (2012). The black line is the wellbore; the blue lines are pre-existing fractures, and the red lines are the hydraulic fractures.

tures. As can be seen in Figure 2.23 (NAGEL *et al.*, 2014), the main interaction between hydraulic fractures in a Zipper-fracture configuration starts when the fracture tips are approaching each other (l1 = 120 m and l2 = 100 m) and increases as the fracture tips reach an overlap of 20 m.

2.9.3 Peridynamics

Recently, peridynamics based on the non-local theory of continuum mechanics has presented promising results for the HF problem. The essence of the peridynamics introduced by SILLING (2000) is that integration, instead of differentiation, is employed to determine the force at a material point. According to the peridynamic theory, internal forces are stated through non-local interactions between pairs of material points within a continuous body, and damage is a part of the constitutive model (HATTORI *et al.*, 2017).

Although, the advantages of the peridynamics theory for solid and fracture mechanics has been entirely demonstrated (GHAJARI *et al.*, 2014; SILLING *et al.*, 2010; SILLING, 2000; SILLING *et al.*, 2007), this theory has not been fully implemented in the numerical modelling of HF. The main works in this area can be referred to (OUCHI *et al.*, 2015a,b, 2017a,b), and the first doctorate dissertation in this topic by OUCHI (2016).

A 3-D peridynamic model was developed by OUCHI *et al.* (2015a,b) by modifying the existing peridynamic formulation of solid mechanics for porous and fractured media and coupling it with a developed peridynamic formulation of porous flow. Then, this work was extended to investigating the effect of different kinds of vertical reservoir heterogeneities on hydraulic fracture propagation (OUCHI *et al.*, 2017a,b). It has been demonstrated that the presence of bedding planes, layer interfaces and even smaller scale heterogeneities can result in fracture turning, kinking or branching. One of the key disadvantage of the

peridynamics is computational expenses of this technique, which can be solved in future with continuous advances in computation speed.

2.9.4 Discrete Element Method

Discrete (or discontinuous) modelling techniques, commonly referred to as the Discrete Element Method (DEM), deal with material directly as an assembly of divided blocks or particles. This technique was originally proposed by CUNDALL and HART (1992) and presented modelling of the interaction between elements via contact. According to this approach, the granular micro-structure of the material is modelled as an assembly of rigid circular particles of varying diameters. By applying cohesive bonds between particles to simulate the behaviour of rocks, the resultant model is commonly referred to as the

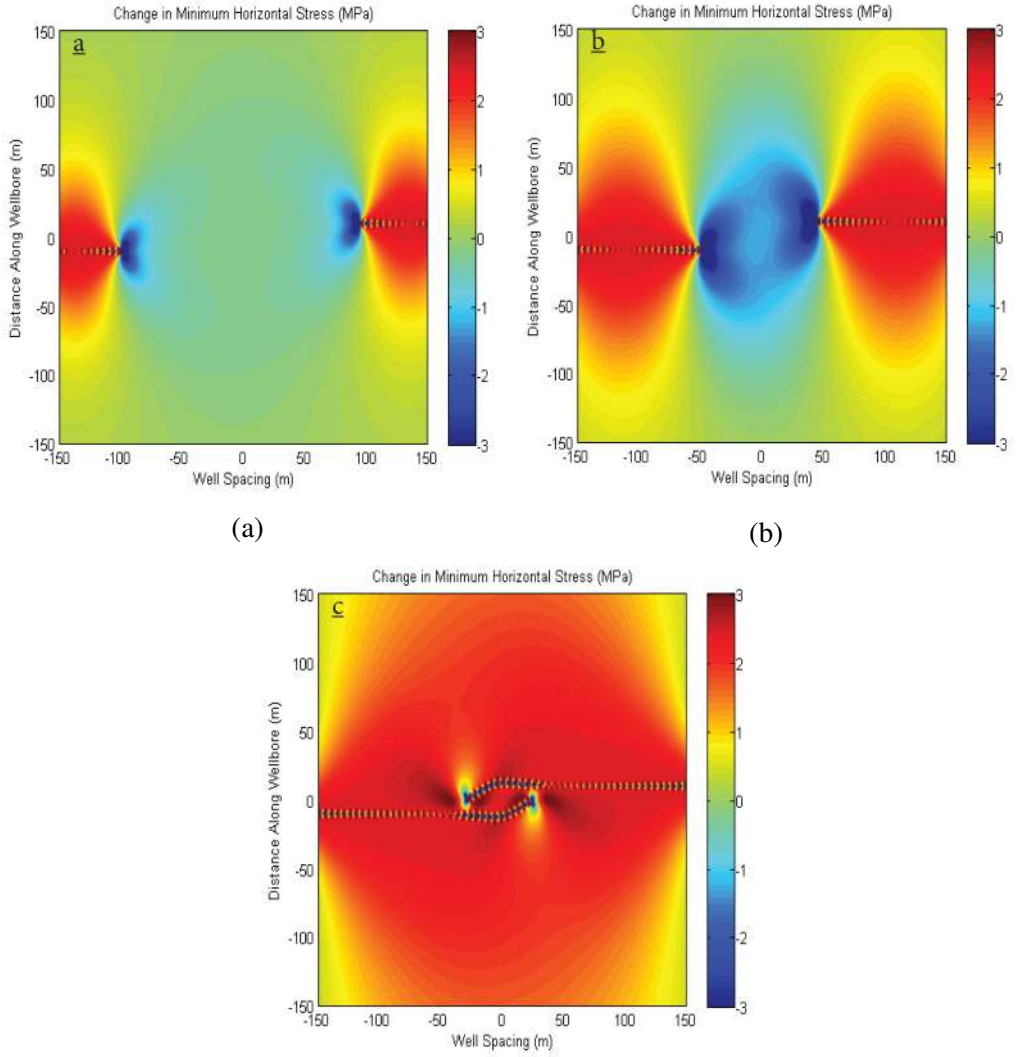

Figure 2.22: Change in minimum horizontal stress during the propagation of two hydraulic fractures spaced at 20 m (REZAEI *et al.*, 2015).

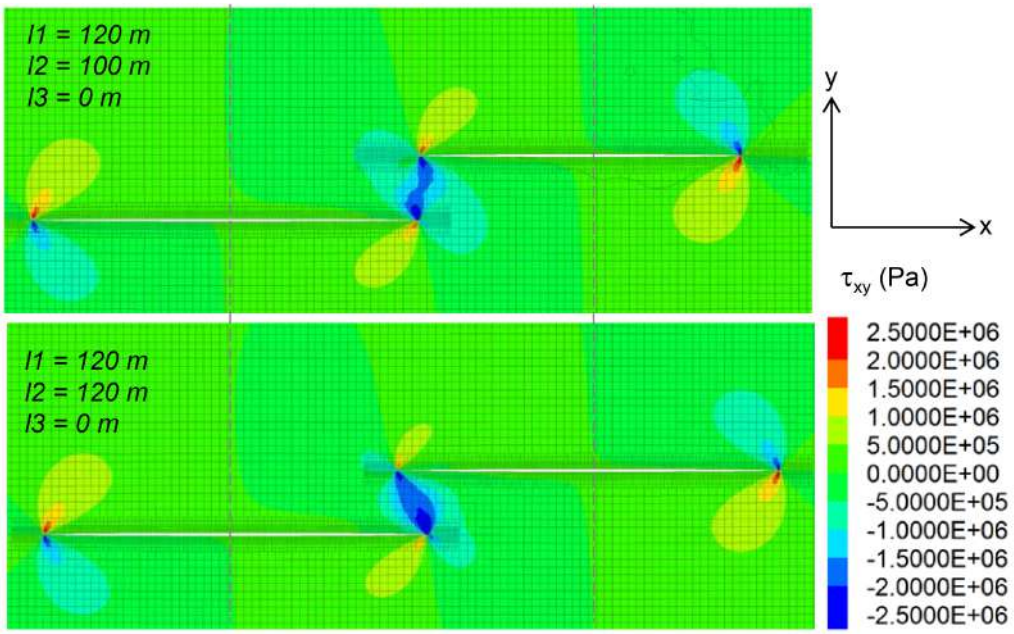

Figure 2.23: Variation of shear stresses around fractures (NAGEL *et al.*, 2014).

Bonded-Particle Model (BPM) for rock (POTYONDY and CUNDALL, 2004). In a BPM, the contact between particles are considered by elastic springs with constant normal and shear stiffnesses, k_n and k_s, acting at the contact points between particles, as shown in Figure 2.25. According to this method, crack nucleation is simulated through breaking of internal bonds whereas fracture propagation is modelled by coalescence of multiple bond breakages.

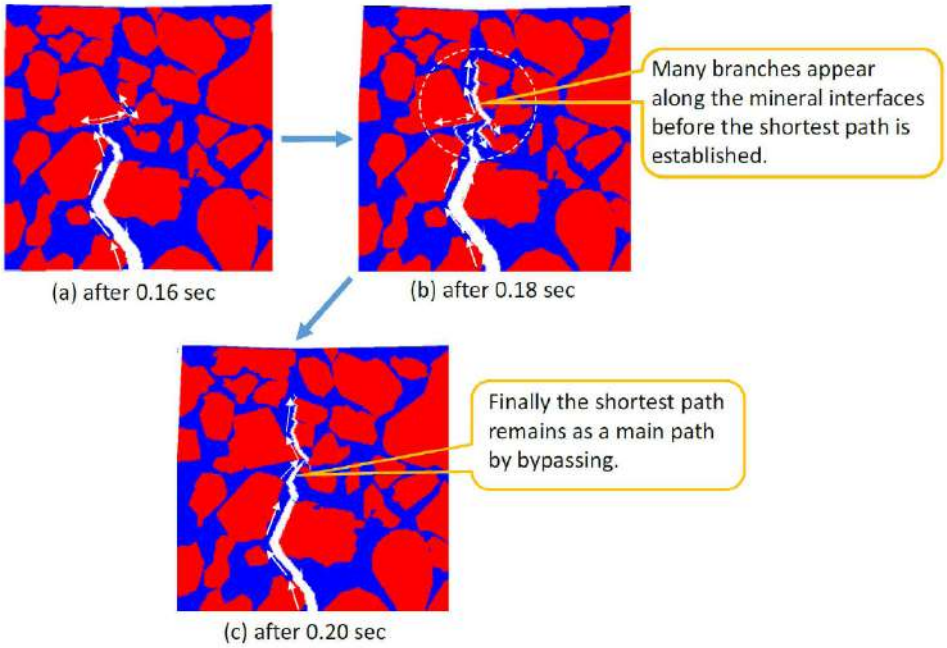

Figure 2.24: Fracture propagation with time based on a peridynamics model (OUCHI *et al.*, 2017b).

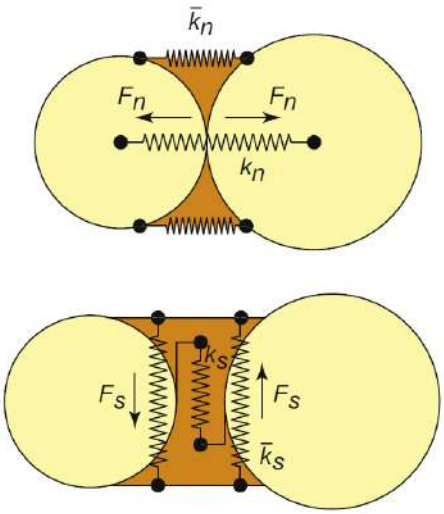

Figure 2.25: Normal and shear stiffnesses between particles in the Bonded-Particle Model (LISJAK and GRASSELLI, 2014).

DEM has been originally developed to treat solids characterized by pre-existing discontinuities having spacing comparable to the scale of interest of the problem. These problems encompasses: blocky rock masses, masonry structures, granular materials, and ice plates. In practice, DEM is employed in problems with a large number of elements, each element representing a body in contact.

The DEM can be divided into several subclasses, which differ in some aspects such as the contact treatment, material models, number of interacting bodies, fracturing, and integration schemes.

ZOU *et al.* (2016) used the DEM to investigate hydraulic fracture network propagation in naturally fractured shale formations. In this paper, the shale rock mass in this model was divided into several block elements (the blocks represent the continuous matrix of a shale formation), which were bonded by virtual springs, which play a role in transmitting the interaction forces among blocks. ZOU *et al.* (2016) concluded that although increasing the number of perforation clusters per fracturing stage is beneficial for improving fracture complexity, it does not mean that smaller perforation cluster spacing is better. As Figure 2.26 shows, the potential merging of fractures from neighboring perforation clusters increases as the perforation cluster spacing decreases, which may lead to the non-uniform development of hydraulic fractures in the far-wellbore regions, and ultimately reduce stimulation effectiveness.

In the work of WANG *et al.* (2017), a coupled BPM and Lattice Boltzmann Method (LBM) , named BPLBM, was proposed for the investigation of 2-D HF. In this work, the BPM was used to describe the inter-particle interactions, and the bonds between contacted particles were assumed to be broken when the tensional force and/or tangential force reach a certain critical value; whereas the LBM was employed to model the fluid phase, and the immersed moving boundary scheme was utilised to resolve the fluid-solid interac-

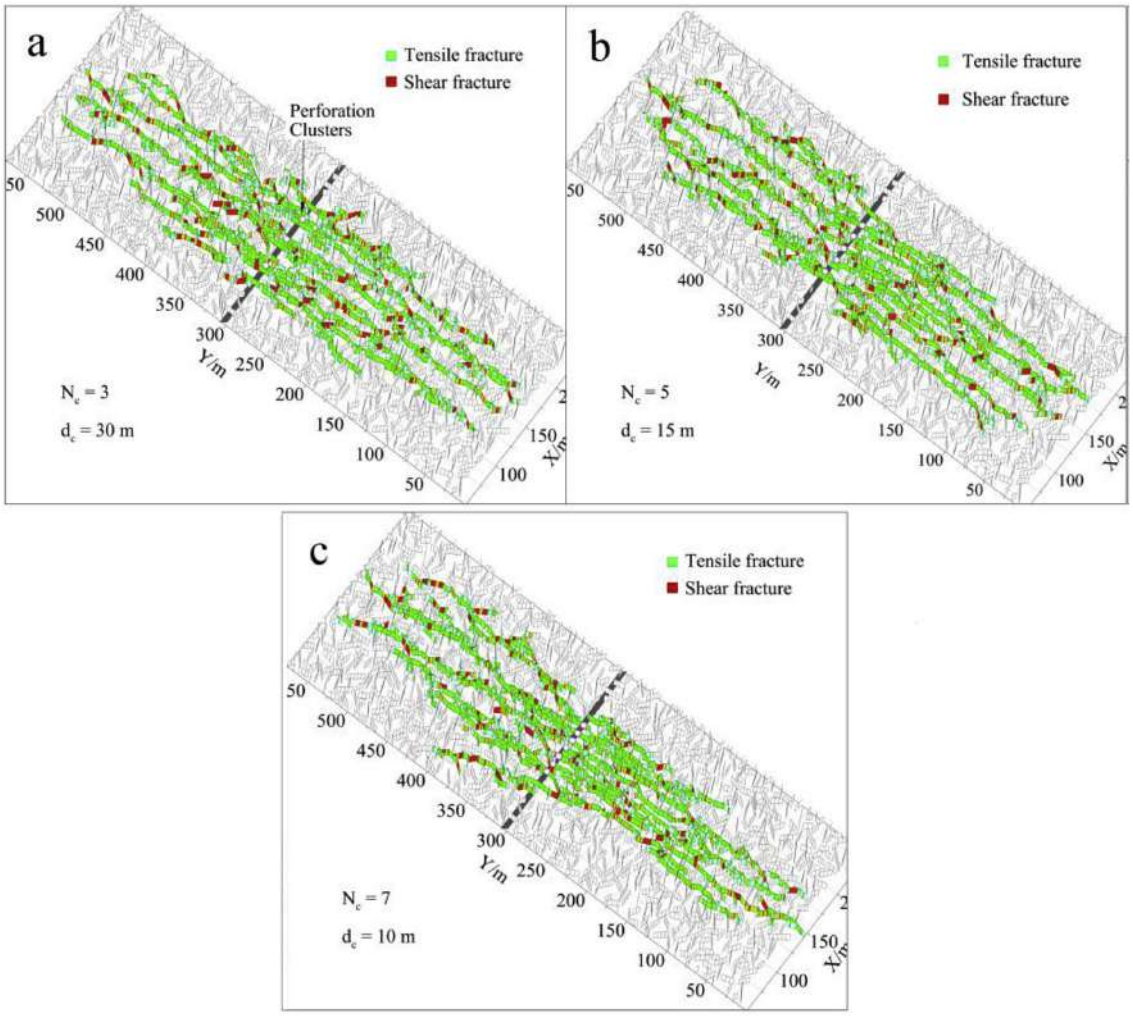

Figure 2.26: Fracture geometries for different perforation cluster numbers and spacing, N_c and d_c are number and spacing of perforation clusters (ZOU *et al.*, 2016).

tions. The BPLBM introduced by WANG *et al.* (2017) is a mesoscopic/microscopic-based method, which can process fluid-particle issues at the grain-level, which commonly ranges from hundreds of microns to several centimetres. The evolution of a fracture induced by hydraulic loading is depicted in Figure 2.27. At the beginning, a tiny crack is formed

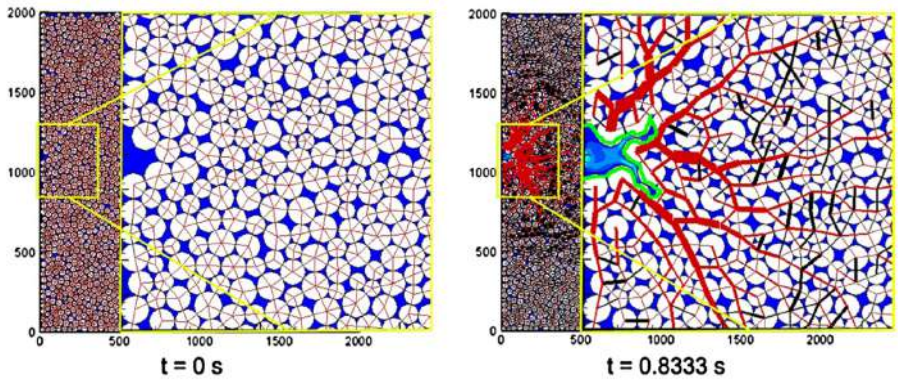

Figure 2.27: Evolution of a fracture induced by hydraulic loading (WANG *et al.*, 2017).

near the pressure pipe. With the increase of fluid pressure, the hydraulic fracture grows gradually. Later, a branch fracture captured at t=0.8333 s is formed.

2.9.5 Finite Element Method

SECCHI and SCHREFLER (2012) presented a model for 3-D HF based on a discrete fracture approach (Section 2.7.2), which uses re-meshing in an unstructured mesh together with automatic mesh refinement. As shown in Figure 2.28, a cohesive fracture model was adopted where the fracture followed the face of the elements around the fracture tip which was closest to the normal direction of the maximum principal stress at the fracture tip. The numerical results obtained showed a mesh-size dependence that can be only reduced with the adaptivity in space considered in the analysis.

HADDAD and SEPEHRNOORI (2015a) modelled simultaneously and sequentially HF in a quasi-brittle shale layer using the FEM incorporated with cohesive layers. According to this paper, Figure 2.29 demonstrates the fracture aperture due to the stress interactions in a simultaneous fracturing case with 33-ft fracture spacing. Despite the expected identical fracture growth at both perforations in this case, the stress interactions pushed the left and right fractures upward and downward, respectively, and resulted in an irregular right fracture pattern. This observation resembles the spontaneous upward and downward displacement of two identical plastic balls being pushed with increasing force against each other. In addition, HADDAD and SEPEHRNOORI (2015a) inferred that the best fracture geometries can be achieved in the simultaneously fracturing scenario.

HADDAD *et al.* (2016) employed the FEM incorporated with cohesive layers to simulate the growth of hydraulic fracture, and its interaction with natural fractures, fluid leak-off into natural fracture, and stress evolution over time through the whole computational domain. The methodology used in this paper was based on their previous work (HADDAD and SEPEHRNOORI, 2015a). The natural fracture location and orientation were

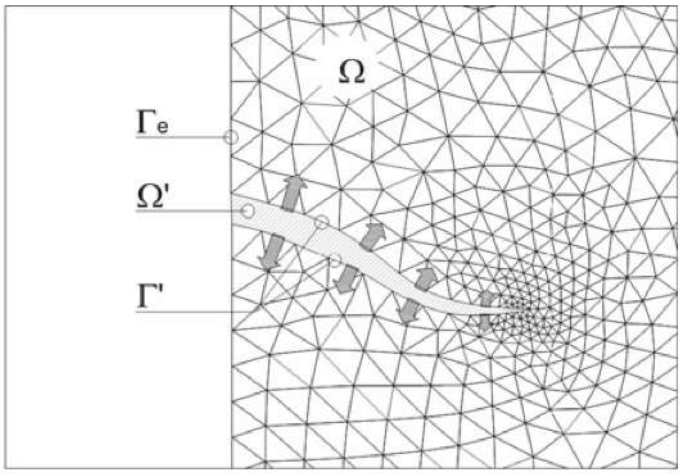

Figure 2.28: Hydraulic fracture domain (SECCHI and SCHREFLER, 2012).

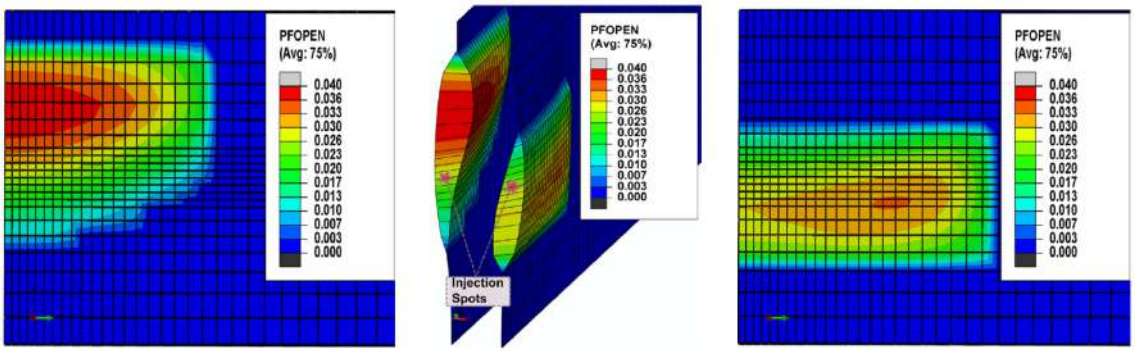

(a) Left fracture (b) Interaction (c) Right fracture

Figure 2.29: Fracture opening and interaction for the double-stage, simultaneous fracturing case with 33-ft spacing (HADDAD and SEPEHRNOORI, 2015a).

inferred from the microseismic events map and formation microImager log in a nearby vertical well, respectively. In this work, the interaction of intersecting hydraulic and natural fractures was modeled using two crossing layers of cohesive elements which were tied together at the intersection using the capabilities in ABAQUS® to define additional governing equations between the degrees of freedom of multiple nodes.

Since incorporation of cohesive layer in the FEM is much more appropriate and effective for the fracture problems with predefined crack path (ALFANO and CRISFIELD, 2001; REMMERS, 2006), taking the advantage of numerical methods, such as XFEM, with the benefits of initiation and propagation of the crack along an arbitrary, solution-dependent path may provide a more effective way for the simulation of multiple HF under the presence of stress shadowing effects.

2.9.6 XFEM

According to the author' literature survey, only few attempts have been made to employ the XFEM to hydraulically fluid-driven problems, which will be elaborated in the following.

DAHI-TALEGHANI *et al.* (2011) applied XFEM to model the hydraulic fracture pattern propagation. The coupling between fracture flow and mechanical model was obtained by a consecutive process where the results of fracture flow were used to update the solution from the mechanical model and vice versa.

A fully coupled numerical model was developed by MOHAMMADNEJAD and KHOEI (2013) for the modeling of the hydraulic fracture propagation in porous media using the XFEM. The numerical simulations demonstrated the ability of the method to resolve the details of the HF process. In this work, the size of the fluid lag region and the value of the pressure within it were obtained directly during the analysis as a result of the interaction between the fluid flow within the fracture and the fracture propagation.

GORDELIY and PEIRCE (2013) have explored the accuracy and convergence prop-

erties of a number of schemes and enrichment strategies useful for modeling hydraulic fracture propagation using the XFEM based on LEFM. They have derived a new set of enrichment functions that were required by the XFEM to model the multi-scale processes typically confronted for propagating hydraulic fracture propagation.

A new finite element has been implemented by CHEN *et al.* (2013) into Abaqus in order to incorporate the XFEM for the solution of hydraulic fracture problems. Verification of the user-defined element has been made by comparing the FEM predictions with the analytical solutions available in the literature. The preliminary result presented in that study was a first attempt to the promising application of the XFEM to the HF simulation.

LECAMPION (2009) employed the XFEM for the solution of hydraulic fracture problems. The presence of an internal pressure inside the crack is taken into account. Special tip functions encapsulating tip asymptotics typically encountered in hydraulic fractures were introduced. The results provided in that paper confirmed the difficulty in simulating the growth of hydraulic fractures in the case of large toughness/small viscosity where the fracture is driven by vanishingly small pressure gradient.

A numerical model based on XFEM was presented by WANG (2015) to capture non-planar hydraulic fracture propagation, a near wellbore region with fractures initiated from an unfavorable perforation angles. The program for numerical calculations was developed using FEA package ABAQUS®. As a fruitful result of that work, Figure 2.30 (WANG, 2015) demonstrates the fracture propagation path and the induced shear stress distribution,

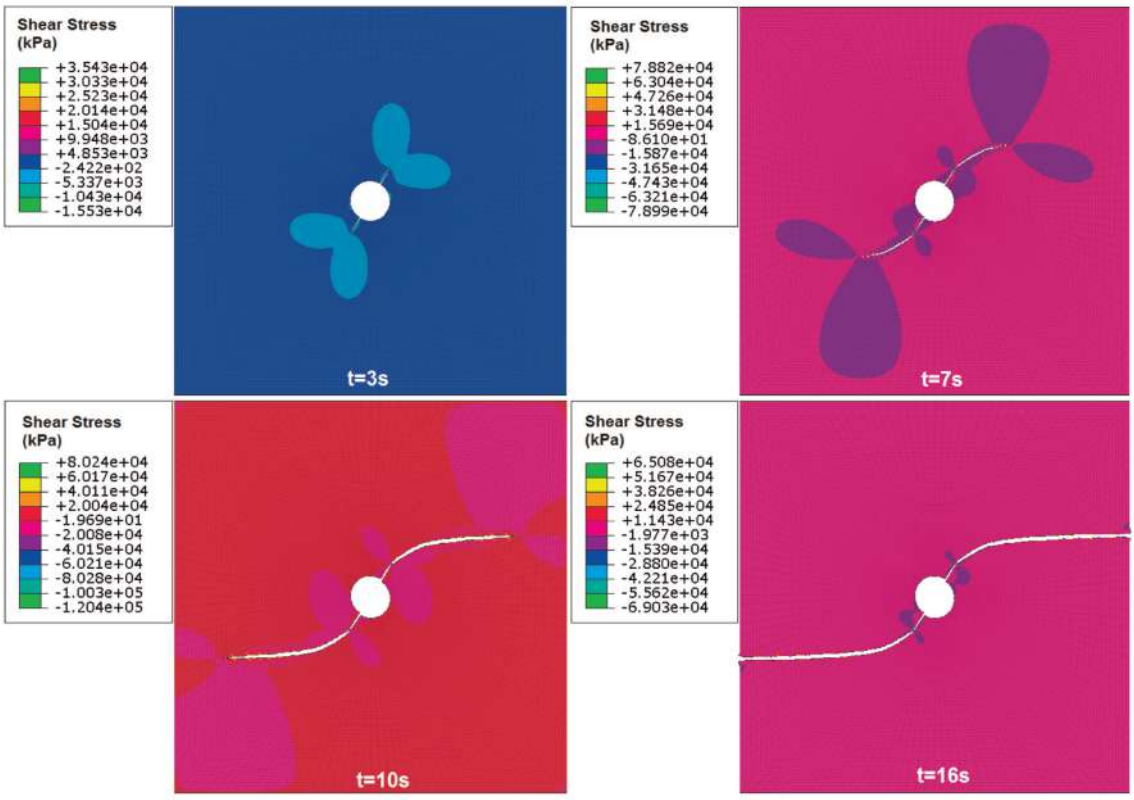

Figure 2.30: Shear stress induced by propagating hydraulic fracture (WANG, 2015).

it can be noted that the fracture first initiated along the direction of perforations, and then it gradually changes its propagation direction to align itself with the direction of Preferred Fracture Plane (PFP) until it hits the simulation boundary. It can be also observed that the in-situ shear stress is intensified in front of fracture tip, where a shear zone (appears as a two wing pattern) is developed due to local stress disturbance by propagating fracture.

KESHAVARZI *et al.* (2012) developed a 2-D XFEM model to investigate the propagation of the hydraulic fracture and interaction with a natural fracture in unconventional reservoir. In this paper, the fluid flow through fracture was ignored. RÉTHORÉ *et al.* (2008) presented a two-scale approach for fluid flow in fractured, deforming porous media using the XFEM technique to represent non-intersected cavity fractures.

An XFEM formulation was proposed by VAHAB and KHALILI (2017) in order to study the impacts of different flow regimes of the fracturing fluid on the HF process. To this end, the inflow and continuity equations of the fracturing fluid through the hydro-fracture were solved in conjunction with the momentum balance equation of the bulk in a sequential manner known as the staggered Newton method. The Reynolds number was applied in order to recognize the development of the laminar or turbulent flow regimes along the flow path line. As can be seen in Figure 2.31, for the imposed laminar solution the crack opening profile is intensified compared to the turbulent flow. This means that the efficiency of HF treatment is overestimated in an imposed laminar.

An endeavour has been made by IRZAL *et al.* (2010) to extend the two-scale model of propagating cracks in porous material into a finite strain framework with make the use of XFEM. The crack which was described as a propagating cohesive zone could be located

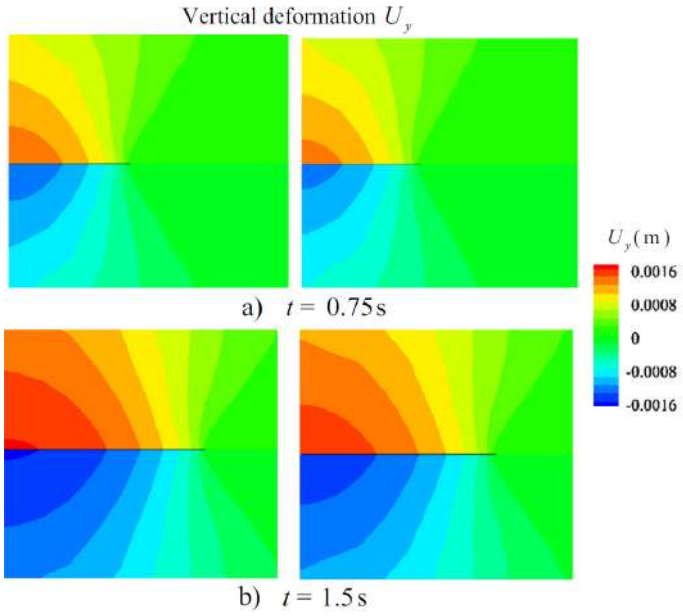

Figure 2.31: Contours for the vertical deformation at the final time step, the left and right hand side contours are the imposed laminar and real flow solutions, respectively. (VAHAB and KHALILI, 2017).

arbitrarily, independent from the underlying discretization of the material structure.

Chapter 3

Stress shadowing-based 3-D simulation of multi-stage hydraulic fracturing[1]

[1]This chapter forms the basis of the following publication:
– B. Sobhaniaragh, W.J. Mansur, F.C. Peters, Three-dimensional investigation of multiple stage hydraulic fracturing in unconventional reservoirs. Journal of Petroleum Science and Engineering 146 (2016): 1063-1078.
– B. Sobhaniaragh, W.J. Mansur, F.C. Peters, On the multiple hydraulic fracturing in unconventional reservoirs by using cohesive phantom node method, Society of Exploration Geophysicists (SEG) International Exposition and 86th Annual Meeting, Dallas-Texas (2016): 3422-3427.

3.1 Key goals

The main objective of the current chapter is to provide a fully coupled pore-pressure stress analysis of the 3-D non-planar hydraulically driven fracture problem by using CPNM. In fact, the numerical techniques used in the literature (BUNGER *et al.*, 2012; GU *et al.*, 2015; HADDAD and SEPEHRNOORI, 2015a; JENKINS *et al.*, 2016; MANCHANDA *et al.*, 2014; NAGEL *et al.*, 2014; PEIRCE, 2015b; ROUSSEL *et al.*, 2011), are not capable of modelling of non-planar fracture propagation. In reality, owing to stress shadowing effect, elaborated in Section 1.5, of the pre-existing and/or simultaneous fractures, a non-planar hydraulic fracture may occur, as observed in experimental observations (BUNGER *et al.*, 2011). However, the proposed CPNM is capable of the initiation and propagation of multiple cracks along an arbitrary, non-planar, solution-dependent path, providing a more realistic way for the study of multiple HF with the presence of stress shadowing effects. As discussed in Section 1.5, consideration of stress shadowing effects brings remarkable advantages with regard to effect and risk mitigation on the cost and profitability of HF operations.

In the present chapter, two different key scenarios including Sim-HF and Seq-HF are studied comprehensively. With respect to Seq-HF, after pumping stage in the first perforation, another transient analysis is conducted for this perforation to simulate the crack closure. The influences of the pre-existing or simultaneous growing fractures on the several parameters including pore pressure of the formation, crack propagation pattern, von Mises stresses, fracture opening, leak-off flow rate, and fracturing fluid pressure are studied in detail in this chapter.

3.2 Methodology

As depicted in Figure 3.1, a fracture is hydraulically driven as a viscous fluid is injected into a borehole and causes the fracture to advance into the porous medium. Modeling of the fluid-driven fracture propagation in a poro-elastic material comprises the coupling of diverse and extensive range of physical mechanisms including:

- Deformation of the solid skeleton induced by the fluid pressure on the fracture surfaces;
- Flow of the pore fluid through the poro-elastic medium surrounding the fracture;
- Flow of the fracturing fluid within the fracture;
- Fluid exchange between the fracture and poro-elastic medium;
- Propagation of hydraulically-driven fracture.

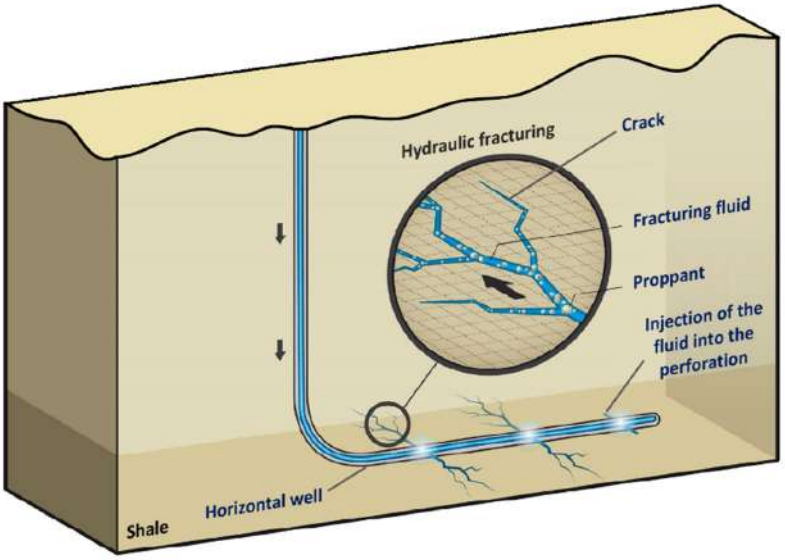

Figure 3.1: Representation of a fluid-driven fracture.

The partial differential equations governing the propagation of hydraulic fracture in the porous medium include the equilibrium equation for the porous medium, the continuity equation for fluid flow through the surrounding porous medium and within the fracture, and momentum equation for the pore fluid and fracturing fluid.

In this chapter, the porous rock is assumed to be an isotropic, poro-elastic material undergoing quasi-static deformation. The pores of the solid skeleton are assumed to be thoroughly filled up with a single phase fluid, presenting a fully saturated porous medium. It is presupposed that the two-phase porous medium encompassing the fracture remains under isothermal conditions.

3.2.1 Governing equations

The fundamental 3-D theory of poro-elasticity in which the fully coupled quasi-static poro-elastic equations were derived, was first introduced by BIOT (1941, 1962). Afterwards, the theory has been developed by a myriad of researchers, specifically, a physical significance to Biot's work was presented by RICE and CLEARY (1976). The stress at each point of the porous media can be decomposed into the effective stress, which operates among the solid grains and governs their deformation and loading capacity, and the pore pressure of fluid phases. By definition, the relation between the total stress and effective stress is given by (TERZAGHI *et al.*, 1996)

$$\boldsymbol{\sigma}' = \boldsymbol{\sigma} - \bar{\alpha} p \mathbf{I} \tag{3.1}$$

where $\boldsymbol{\sigma}'$ expressing the effective stress acting between solid grains, $\boldsymbol{\sigma}$ is the total stress tensor, and p is an average pressure of fluid phase, $\mathbf{I}$ is the second-order unit tensor. Pa-

rameter $\bar{\alpha}$ is Biot-Willis coefficient, in which for isotropic materials can be computed by $\bar{\alpha} = 1 - K_T/K_S$, where K_T and K_S indicate the bulk moduli of the porous rock and the solid grains, respectively. GHASSEMI and ROEGIERS (1996) has shown that variations in the parameter α has a negligible consequence on fracture geometry. This parameter is actually very close to unity for soil-like materials, although may be as low as 0.5 for rock-like materials with small porosity (ZIENKIEWICZ and SHIOMI, 1984). The equilibrium equation in the absence of body forces for the porous medium can be written as

$$\sigma_{ij,j} = 0 \tag{3.2}$$

The constitutive relation of the poroelastic medium can be expressed by (CHARLEZ, 1997; GUTIERREZ *et al.*, 2001)

$$\sigma_{ij}{}' - \sigma_{ij}{}'^{0} = 2G\varepsilon_{ij} + \left(K + \frac{2}{3}\bar{G}\right)\varepsilon_{ii} - \alpha\left(p - p^0\right)\delta_{ij} \tag{3.3}$$

where ε_{ij} and σ_{ij} are the strains and stresses in the solid matrix, p is the fluid pore pressure, $\sigma_{ij}{}^{0}$ is the initial principal in-situ stress, ε_{ii} is the volumetric strain which is simply the additional storage caused by the expansion of the solid skeleton, $\bar{G}$ is the shear modulus, and *K* is the bulk modulus, and p^0 is the initial fluid pore pressure. It should be noted that stresses and strains are replaced by their effective counterparts. The continuity equation for the flow of the fluid phase within the permeable porous medium can be written as (ZIENKIEWICZ and SHIOMI, 1984; ZIMMERMAN and BODVARSSON, 1996)

$$\frac{1}{Q}\dot{p} + \alpha\,\dot{\varepsilon}_{ii} + v_{i,i} = 0 \tag{3.4}$$

where v_i is the Darcy velocity of the pore fluid and Q is Biot's modulus which denotes the storage due to compressibility of the solid grains and fluid phase defined as

$$\frac{1}{Q} = \frac{\phi_0}{K_f} + \frac{\alpha - \phi_0}{K_S} \tag{3.5}$$

where K_f is the bulk modulus of the pore fluid and ϕ_0 is the initial porosity. The Darcy relation for the pore fluid flow through the porous rock shall be presented by

$$v_i = -\frac{k}{\mu}\,\nabla p \tag{3.6}$$

in which k denotes the permeability of the porous medium and μ designates the dynamic viscosity of the fluid. It is worth noting that the unit of permeability in ABAQUS® is LT^{-1}, which is generally used for hydraulic conductivity. The relation between permeability (k in $[\mathrm{L}^2]$) and hydraulic conductivity (k' in $[\mathrm{LT}^{-1}]$) is (KHOEI and MOHAMMADNEJAD,

2011)

$$k' = \frac{\gamma}{\mu} k \tag{3.7}$$

where γ is the specific weight of pore fluid. In some soil mechanics books (DAS, 2013), the permeability, k, is named as "intrinsic (or absolute) permeability".

Several fracturing fluids in HF mechanism exhibit temperature-related properties and rheological behavior. For the sake of avoiding complex fluid behavior, in this study incompressible and Newtonian fluid is presupposed. In addition, the fluid is under Stokes flow condition and fracture shape ratio, w/l , is very small, where $l\,(t)$ is the fracture length at any given time *t*, and *w* is the fracture opening or aperture. Further, the tangential velocity on the interface between the fluid and the crack walls is zero, i.e. no-slip condition. Considering aforementioned assumptions, fracturing fluid can be modeled by Lubrication theory. As a result, the momentum equation for flow of the fracturing fluid through narrow parallel plates leads to the so-called Poiseuille equation as follows (ECONOMIDES *et al.*, 2000)

$$\bar{q} = -\frac{w^3}{12\mu} \frac{\partial p_F}{\partial s} \tag{3.8}$$

where $\bar{q}$ is the local fracturing fluid flow rate per unit width, p_F is the pressure of the fracturing fluid along the crack surface parameterized with the curvilinear coordinate, s. The continuity equation for the fluid flow within the fracture, which imposes the conservation of mass in one dimensional flow, is written as (ZIMMERMAN and BODVARSSON, 1996)

$$\frac{\partial w}{\partial t} + \frac{\partial \bar{q}}{\partial s} + v_{top} + v_{bot} = 0 \tag{3.9}$$

where v_{top} and v_{bot} are sink terms denoting the normal flow velocities at which the fracturing fluid infiltrates through the top and bottom faces of the fracture into the porous medium. It is presumed that velocities v_{top} and v_{bot} are perpendicular to the axis of crack propagation. In other words, the fluid leak-off or infiltration is considered as a one-dimensional procedure.

Most studies on the modelling of HF have assumed a 1-D fluid loss pattern into the formation in a direction perpendicular to the fracture plane, based on an explicit Carter's fluid flow model (BUNGER *et al.*, 2005; CARTER, 1957). According to Carter's model, the fluid leak-off is expressed as an inverse square-root law of time of the form (CARTER, 1957)

$$v_L = \frac{c_L}{\sqrt{t}} \tag{3.10}$$

where v_L denotes the leak-off velocity, c_L (having units $[\mathrm{LT}^{-1/2}]$) is the Carter's leak-off coefficient, and t is the time elapsed since the beginning of the infiltration procedure. In addition, Carter (BUNGER *et al.*, 2005; CARTER, 1957) proposed that the volume of fluid leaked per unit area of the fracture, V_L, can be obtained from

$$V_L = 2c_L\sqrt{t} + S_p \tag{3.11}$$

where S_p is a spurt-loss coefficient, which is the volume of the fluid that percolates instantaneously before forming a filter cake. The deficiency of the Carter model, which is independent of fluid pressure of the filter cake, motivates this research to employ another approach. In this work, in order to treat the filter cake as a pressure-dependent layer, Settari's fluid leak-off model SETTARI *et al.* (1984, 1985) is employed by using a user-defined subroutine. By virtue of the proposed pressure-dependent model, the normal components of the fracturing fluid are defined as

$$v_{top} = c_t\left(p_F - p_{top}\right) \tag{3.12}$$

$$v_{bot} = c_t\left(p_F - p_{bot}\right) \tag{3.13}$$

where p_{top} and p_{bot} are the pore fluid pressures on the top and bottom faces of the crack, and c_t is total leak-off coefficient. According to Settari's model, the flow in the porous medium is divided into two zones: a invaded zone (or filtrate zone) and a reservoir zone. In this model, the fracturing fluid filtrates into the invaded zone perpendicular to the fracture face. In the invaded zone, it replaces the reservoir fluid pushing it further into the rock matrix. The reservoir zone is filled with an original reservoir fluid. The total leak-off coefficient, c_t, can be determined as a combination of invaded leak-off coefficient, c_i, and reservoir leak-off coefficient, c_r, ECONOMIDES *et al.* (2000); SETTARI *et al.* (1985)

$$c_t = \frac{2c_r c_i}{c_i + \sqrt{{c_i}^2 + 4{c_r}^2}} \tag{3.14}$$

where

$$c_i = \sqrt{\frac{k\varphi\Delta p_i}{2\mu_i}}, \quad c_r = \sqrt{\frac{kc_T\varphi}{\pi\mu_r}}\Delta p_r \tag{3.15}$$

where Δp_i is the pressure drop between the fracture and invaded zone interface, and Δp_r is pressure drop between reservoir interface and the far-field reservoir. k is the permeability of the rock formation, and c_T is compressibility of the reservoir fluid. μ_i and μ_r are the permeability of the invaded and reservoirs zones, respectively. The main drawback of Settari's model is the difficulty in designing a calibration test interpretation procedure that

is standardized ECONOMIDES *et al.* (2000).

It is worthwhile noting that the essence of the leak-off coefficient in Eqs. 3.12 and 3.13 shall be attributed to two patterns (ADACHI, 2001):

- One can be referred to the degree of the permeability matrix in such a way that high permeability formations, like poorly consolidated/unconsolidated sands, leads to the low fracturing fluid filtration on the fracture walls, which causes the formation of a thin filter cake, which is primarily a low permeability filter barrier that opposes fluid loss, with a comparatively high leak-off coefficient. For low permeability matrix, like tight sandstone or shales, the value of leak-off coefficient shall be very small, leading to thicker filter cake.

- The other pattern can be assigned to the characteristics of non-Newtonian fracturing fluids, although which is not the case herein. The most frequently used fracturing fluids include water-based high-molecular-weight polymer solutions whose characteristics are their layer-building property. Since those fracturing fluid seeps into the surrounding rock, some of the dense polymers begin to deposit on the crack inner walls, ultimately constituting a filter layer.

The essential boundary conditions prescribed on the external boundaries are described by

$$\begin{aligned} \mathbf{u} &= \bar{\mathbf{u}} \quad \text{on} \quad \Gamma_u \\ p &= \bar{p} \quad \text{on} \quad \Gamma_p \end{aligned} \tag{3.16}$$

and the natural boundary conditions imposed on the boundaries of the body are as follows

$$\dot{\mathbf{q}}_t . \mathbf{n}_\Gamma = \bar{q} \quad \text{on} \quad \Gamma_{in} \tag{3.17}$$

where $\bar{q}$ is the flow rate of the fracturing fluid imposed on the perforation Γ_{in}, and $\mathbf{n}_\Gamma$ denotes the unit outward normal vector to the external boundary. In addition, the following boundary conditions on the surfaces of the crack are prescribed

$$\begin{aligned} \boldsymbol{\sigma} . \mathbf{n}_{\Gamma_d} &= \mathbf{t}_d - p\mathbf{n}_{\Gamma_d} \\ [\![\mathbf{v}_f]\!] . \mathbf{n}_{\Gamma_d} &= q_{wd} \end{aligned} \tag{3.18}$$

where $\mathbf{t}_d$ denotes the cohesive traction acting in the FPZ, q_{wd} is the flux of the fluid leak-off along the fracture toward the surrounding formation, and $\mathbf{n}_{\Gamma_d}$ is the unit normal vector to the crack. The notation $[\![]\!]$ represents the discrepancy between the corresponding values at the two crack faces.

In order to derive the weak form of the governing equations, we integrate the equilibrium equation (Eq. 3.2) and continuity equation for the fluid flow (Eq. 3.3) with admissible

test functions over the analyzed domain. Employing the divergence theorem, imposing the natural boundary conditions, and satisfying the boundary conditions on the crack faces, the weak form of the equilibrium equation is found to be

$$\int_{\Omega} \nabla^s \boldsymbol{\eta} : \boldsymbol{\sigma} d\Omega + \int_{\Gamma_d} [\![\boldsymbol{\eta}]\!] . (\mathbf{t}_d - p\mathbf{n}_{\Gamma_d}) d\Gamma = 0 \tag{3.19}$$

where ∇^s is the symmetric part of the gradient operator. This expression must hold for any admissible test function for the displacement field, $\boldsymbol{\eta}$. It should be noted that the total stress $\boldsymbol{\sigma}$ in the integral Eq. 3.19 must be replaced by the effective stress in Eq. 3.1. The weak form of the continuity equation of fluid flow within the porous medium is given by

$$\int_{\Omega} \zeta \frac{1}{Q} \dot{p} d\Omega + \int_{\Omega} \zeta \alpha \nabla . \dot{\mathbf{u}} d\Omega + \int_{\Omega} \frac{k}{\mu} \nabla \zeta . \nabla p d\Omega - \int_{\Gamma_d} \zeta q_{wd} d\Gamma = - \int_{\Gamma_{in}} \zeta \bar{q}_w d\Gamma \tag{3.20}$$

which must hold for any admissible test function for the fluid pressure field ζ. The weak form of the Eq. 3.9 is determined in a similar manner. Afterwards, the weak forms of the equilibrium and continuity equations are rendered in a discrete form by employing the CPNM formulations presented in Eqs. 3.31 and 3.32, which will be explained in Section 3.2.3. Finally, the resultant equations representing coupled processes in the HF problem are required to be solved simultaneously. In the transient coupled pore pressure-effective stress analysis, the backward Euler formula (sometimes also referred to as the modified Crank-Nicolson operator), which provides unconditional stability, is used to integrate the continuity equation in time.

Generally, solutions for hydraulically fluid-driven fractures are rigorous to establish even for simple geometries. This difficulty comes from moving boundary conditions, and non-linearity of the governing equation for fluid flow in fractures. Non-linearity is attributed to the fact that fracture permeability is correlated to fracture width with a cubic function (DAHI-TALEGHANI *et al.*, 2011). The system of non-linear equations is solved numerically by an incremental-iterative solution, based on the Newton-Raphson technique. The integration procedure for consolidation analysis is reinforced by a minimum time step criterion proposed by VERMEER and VERRUIJT (1981) to avoid spurious oscillations which may occur in the solution. This criterion introduces a correlation between the minimum allowable time increment and the element size as follows

$$\Delta t \geq \frac{\gamma}{6\, E\, k} (\Delta h)^2 \tag{3.21}$$

where γ is the specific weight of fluid, k is the permeability of the porous medium, E is the elastic modulus of the soil skeleton, Δt is the time increment, and Δh is a typical element dimension.

3.2.2 Fracture initiation and propagation

In the last years, empirical methods and linear elastic fracture mechanics have formed the basis of the majority of the research on the HF in the oil and gas industry. Those approaches commonly make sensible predictions for the case of hydraulically driven fracture in hard rock. Nevertheless, when it comes to model HF in ductile shale and other soft rocks like weakly consolidated sandstone or clay, LEFM-based approach generally provide a conservative estimate. This stems from the role of the non-linear zone ahead of the crack tip owing to plasticity or micro-cracking, which is not trivial compared with other dimensions of the crack geometry. Those types of materials exhibit moderately strain hardening prior to reaching to the ultimate tensile capacity, similar to response of ductile materials such as high strength steels. Contrast to the latter, they are distinguished by an incline in deformation with declining tension carrying capacity, which is called strain-softening. The materials that manifest mild strain hardening prior to the ultimate tensile strength and subsequent strain-softening might be called quasi-brittle, such as geo-materials, concrete, and coarse-grained ceramics. The observed deviation of the attitude of quasi-brittle materials from the LEFM prediction is the developing of nonlinear fracture processes in front of the crack tip called the FPZ where the material progressively softens and the energy dissipation occurs due to the occurrence of micro-cracks.

In the present research, non-linear discrete fracture mechanics (HILLERBORG, 1985; NEEDLEMAN, 1987), based on CCM, which is formulated by specific traction-separation laws, independent of the constitutive behaviour of bulk material, is proposed. In the CCM, as presented in Section 2.6, it is presupposed that the near tip FPZ is aggregated into the crack line, in contrast to the LEFM in which the FPZ is regarded to take place at the crack tip. The leading assumption is the constitution of the FPZ, where the material, although damaged, is still able to transmit stresses normal to the fracture. From a meso-scale view point, in the quasi-brittle material, the micro-cracks are launched close to the interface between the matrix and aggregate, and a macro-crack is formed from the coalescence of micro-cracks, as shown in Figure 3.2a. The heterogeneous construction of such materials causes peculiar phenomena such as crack bridging, where parallel cracks are linked through an aggregate. This mechanism provides a possibility for the cohesive forces to be transmitted by virtue of an existing crack and, as a result, allows the model to explain materials that manifest strain-softening behavior.

According to CCM, two different kinds of crack tip are introduced including real crack tip and fictitious crack tip (CARPINTERI, 2012; HATTORI *et al.*, 2017), as demonstrated in Figure 3.2b. The former refers to the point separating the stress-free area from the FPZ, while the latter is regarded as the point separating the FPZ from the uncracked material. Furthermore, at the fictitious crack tip, the ultimate stress is equal to a finite stress. Consequently, stress singularity problem in the state of stress is overcome. In other words, the

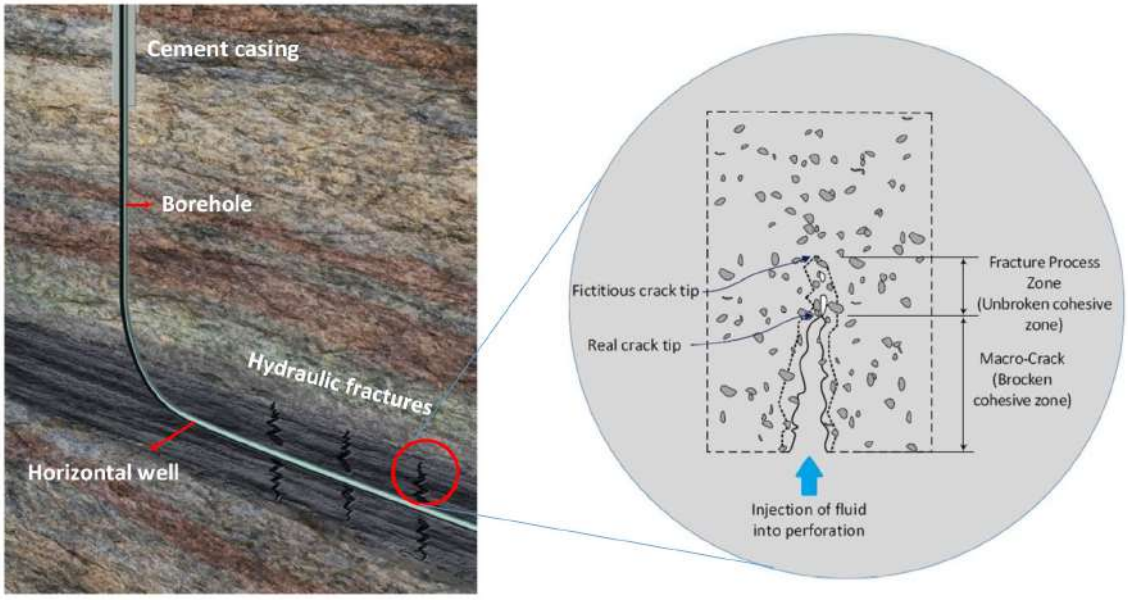

(a)

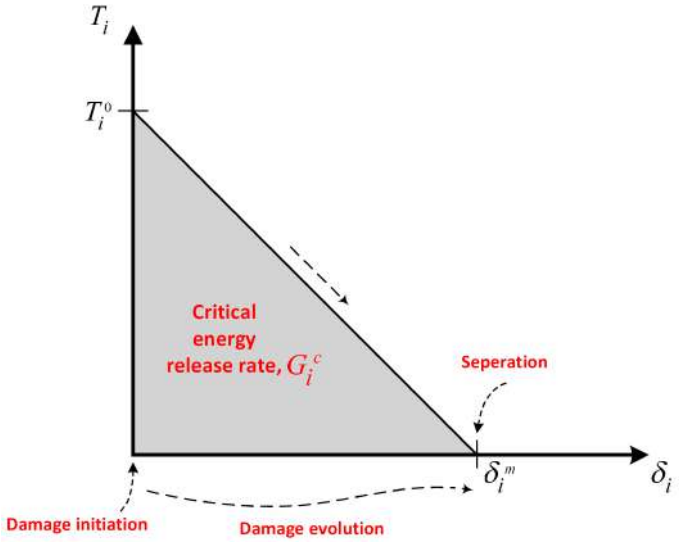

(b)

Figure 3.2: **a)** Embedded cohesive crack in a porous medium, **b)** Cohesive traction-separation law with linear damage evolution.

CCM mitigates the singularity of the crack tip stress field, an unrealistic assumption of LEFM. This advantage has enabled CCM to better solve the complex non-linear HF and convergence issues in comparison with LEFM.

Generally, cohesive models have been established as either intrinsic or extrinsic models (CAMACHO and ORTIZ, 1996; NEEDLEMAN, 1987; OLIVER, 1996; TVERGAARD and HUTCHINSON, 1992) into FE formulations. A literature survey of HF propagation problems reveals that in the majority of the studies intrinsic formulation has been used (CHEN, 2012; GONZALEZ-CHAVEZ *et al.*, 2015; HADDAD and SEPEHRNOORI, 2015a; SARRIS and PAPANASTASIOU, 2011; YAO, 2012; ZHANG

et al., 2010). The intrinsic formulation possesses initial (penalty) stiffness, characterized in the traction-separation law, up to the tensile strength of the material after which the strain-softening of the material initiates. In this model, the interface elements requires to be embedded in the model a priori. That is why this modelisation leads to some sorts of complications and obstacles. Not only does it alter the compliance of the structure and give rise to deformations in the interface prior to the onset of cracking, but it also demands pre-determination of the crack path, imposing an obstacle on modelling of non-planar unpredictable hydraulic fluid-driven crack. Therefore, in order to avoid aforementioned barriers, in the present study, the Extrinsic Cohesive Crack Model (ECCM) (CAMACHO and ORTIZ, 1996; TVERGAARD and HUTCHINSON, 1992) is implemented into the model. The prized features of the ECCM exploited are that it eliminates the initial stiffness requirements in the traction-separation law, and interface elements are just embedded in the model automatically whenever the bulk material satisfies a certain criterion for the onset of the crack. One of the underlying aspects of the CCM employed in this dissertation is that the cohesive model is implemented into the HF problem as an extrinsic model. In the ECCM formulation proposed here, constitutive relations are designated independently, in one hand, for the bulk material and, on the other hand, for one or more cohesive cracks. The cohesive constitutive relation incorporates the failure characteristics of the quasi-brittle material and identifies the decohesion process. The bulk material outside the crack treats elastically linear. Also, the crack is separated into two regions; the first is the crack surface, which is traction free, and the second is the cohesive surface, which comprises crack tips and is applied by cohesive stresses. ECCM used in the current study are characterized by a linear, rate dependent traction-separation law that correlates the displacement jump vector Δ and the cohesive traction vector $\mathbf{T}$ operating over the cohesive surface. Vectors Δ and $\mathbf{T}$ can be denoted with regard to their components as $\Delta = \{\delta_n, \delta_s, \delta_t\}^T$ and $\mathbf{T} = \{T_n, T_s, T_t\}^T$ in 3-D for mode-mix formulation. *n* denotes normal component, *s* and *t* refer to shear and tear components, respectively.

To better elaborate the concept of Figure 3.2b, consider pure mode I fracture (opening mode) and maximum principal stress criterion as the proposed damage initiation criterion. The FPZ initiates expanding if the normal traction, induced over the FPZ, approaches the maximum value ${T_n}^0$, whereas the real crack tip displacement, i.e., opening is still zero. Inasmuch as the crack tip opens up, the stress declines to zero, and ultimately the real crack tip displacement approaches a critical maximum value, ${\delta_n}^m$. The failure mechanism consists of two critical consecutive components including a damage initiation criterion and a damage evolution law, as described in the following:

- Considering maximum nominal stress criterion (INGRAFFEA *et al.*, 1977; SIH, 1973) as damage initiation criterion, the damage initiates when the maximum nominal stress ratio attains a particular value. The proposed criterion is described by

$$fc = \max\left\{\frac{\langle T_n\rangle}{{T_n}^0}, \frac{T_s}{{T_s}^0}, \frac{T_t}{{T_t}^0}\right\} \tag{3.22}$$

where fc is the value determining fracture criterion, the symbol $\langle\rangle$ represents the Macaulay bracket, and superscript *0* denotes the damage initiation. A crack is created or the crack length of an existing crack is expanded when the fracture criterion, fc, attains the value of 1.0 according to a given tolerance:

$$1.0 \leq fc \leq (1.0 + fc_{tol}) \tag{3.23}$$

If $fc > (1.0 + fc_{tol})$, the time increment is cut back such that the damage initiation criterion is met. Herein fc_{tol} is assumed to be 0.05.

- In order to deal with the damage evolution, two main components need to be introduced. As depicted in Fig. 3.2b, the first component includes specifying either the effective displacement at final failure, δ^m, or the fracture energy, G^c. The second one to characterize the damage evolution is setting out the nature of the evolution of the damage parameter, D, between damage initiation and complete failure. The damage evolution law relates the rate at which the stiffness of the material is degraded when the corresponding initiation criterion is met. In this work, a linear softening law is adopted. Hence, the normal and shear traction components are influenced by the damage in proportion to

$$T_n = \begin{cases} (1-D){T_n}^0, & {T_n}^0 \geq 0 \\ {T_n}^0, & {T_n}^0 < 0 \end{cases} \tag{3.24}$$

$$T_s = (1-D){T_s}^0 \tag{3.25}$$

$$T_t = (1-D){T_t}^0 \tag{3.26}$$

where *D* is the scalar damage parameter, which describes the overall damage in the material, and evolves from 0 to 1 upon more loading after the damage initiation.

Mainly, according to fracture mechanics, fracture energy is the critical energy release rate (material toughness) with the unit of energy per unit area, and is different from fracture toughness (critical SIF) given as stress times square root of crack length.

To characterize the evolution of damage and damage parameter *D* under a combination of normal and shear deformation over the interface, an effective displacement is defined

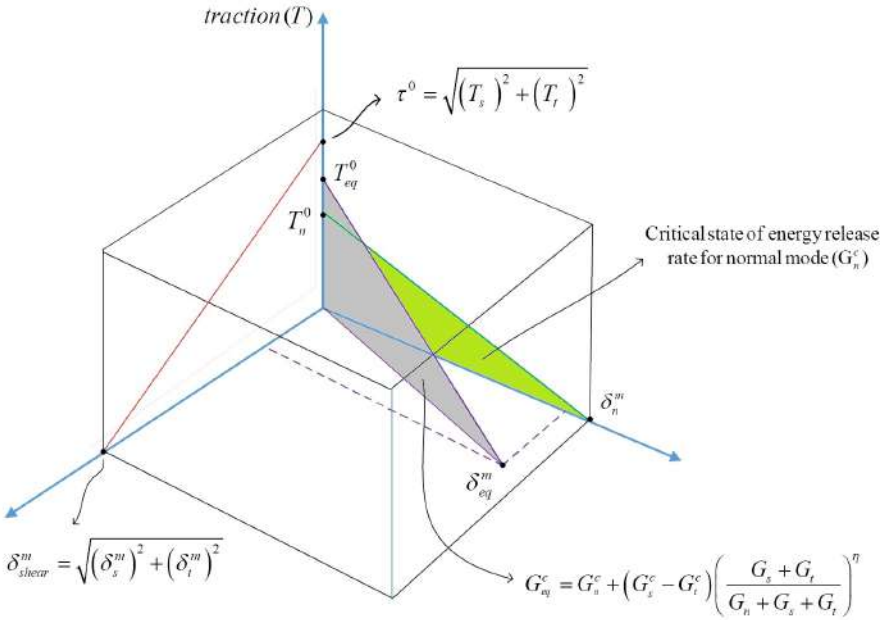

Figure 3.3: Damage initiation and evolution on the mixed-mode condition for the linear traction-separation law.

as

$$\delta_{eq} = \sqrt{\langle \delta_n \rangle^2 + {\delta_s}^2 + {\delta_t}^2} \tag{3.27}$$

It is worth noting that the area under the traction-separation law is equal to fracture energy, G^c, which is the energy dissipated per unit area of new developed crack surface.

Figure 3.3 demonstrates the dependence of damage initiation and evolution on the mixed-mode condition for a linear traction-separation law. As Figure 3.3 shows, the traction on the vertical axis and the shear separations along the horizontal axes are located. The response under pure normal and pure shear deformation are illustrated by unshaded triangles in the vertical coordinate planes. The intermediate vertical diagram shows the damage response under mixed-mode condition.

The Benzeggagh-Kenane (BK) model (BENZEGGAGH and KENANE, 1996) is considered here to relate the mixed-mode fracture propagation for computing the equivalent critical energy release rate, G_{eq}^c. This model establishes a power law relation assembling energy release rates in Mode I, Mode II, and Mode III into a single scalar fracture criterion. BK fracture criterion is defined as

$$G_{eq}^c = G_n^c + (G_s^c - G_t^c)\left(\frac{G_s + G_t}{G_n + G_s + G_t}\right)^\eta \tag{3.28}$$

where the superscript c denotes the critical state of energy release rate, G_n, G_s and G_t are normal, shear, and tear components of fracture energy release rates, respectively, and η is

a material property describing the contribution of the shearing and tearing modes to the equivalent critical energy release rate, and herein is equal to 2.3 for the case of quasi-brittle material.

3.2.3 Cohesive phantom node method

As explained in Section 2.7.3.1.6, the cohesive segments method proposed by REMMERS (2006); REMMERS *et al.* (2003, 2008) within the framework of XFEM was employed to model the nucleation, growth, coalescence, and branching of multiple cohesive cracks in quasi-brittle materials. On the other hand, HANSBO and HANSBO (2004) has introduced an alternative formalism to the XFEM. The primary contrast to the original XFEM is the way in which approximation space is enriched. In the original XFEM, additional degrees of freedom, which are added at the existing nodes, solely determine the crack kinematics, i.e. displacement jump. Hansbo and Hansbo proposed a method where the crack kinematics is achieved by overlapping elements rather than adding additional degrees of freedom. Although it was shown by SONG *et al.* (2006), who called their approach phantom node method, that the formulation of Hansbo and Hansbo is equivalent to the original XFEM, the method of Hansbo and Hansbo possesses remarkable merits with regard to the implementation of the other, which can be indicated that the implementation of Hansbo and Hansbo into commercial software packages, such as Abaqus, is much easier than that of original XFEM. It is because no additional degrees of freedom are added, which increase when the crack propagates (RABCZUK *et al.*, 2008).

In contrast to all aforementioned literature in Section 2.9, in the present research, inspired by Phantom node method proposed by HANSBO and HANSBO (2004) and cohesive segment method of REMMERS (2006); REMMERS *et al.* (2003, 2008), the cohesive segments method in combination with phantom nodes, named as CPNM, is employed to simulate 3-D non-planar hydraulically-driven fracture problem in a quasi-brittle shale medium. In the present work, this method implemented into a FEA package (ABAQUS®) is employed along with user-defined subroutines to simulate hydraulic fractures initiation and propagation. To this end, extra phantom nodes with pore pressure degrees of freedom are added on the edges of each enriched element to construct the model of fracturing fluid flow across the cracked element surfaces in combination with the phantom nodes which are overlain on the original real nodes in order to demonstrate the discontinuities of both displacement field and fluid pressure in a cracked element located in the porous medium. The activation of phantom node on each element edge is not performed unless it is intersected by a crack.

As shown in Figure 3.4, consider an element in a finite element mesh with nodes number of 1 to 4. This element is crossed by a crack at Γ_c, splitting the element domain into two subdomains, Ω_A and Ω_B. In the phantom node method, the discontinuity in the dis-

placement is constructed by adding phantom nodes marked by empty circles in Figure 3.4a superimposed to the original nodes. After damage initiation, each phantom node and its corresponding real node, including displacement and pore pressure degrees of freedom, are no longer tied together. The existing element is replaced by two new elements, referred to as element A and element B. The two sub-elements are constituted by the nodes number of 1 to 4 and $\tilde{1}$ to $\tilde{4}$. The elements do not share nodes, and consequently have independent displacement fields. Both elements are just partly active, the active part of element *A* is named as Ω_A and the active part of element *B* is regarded as Ω_B. This can be stated in the interpolation of displacement field as

$$\mathbf{u}^A(\mathbf{x},t) = \mathbf{N}_j(\mathbf{x})\mathbf{u}_j^A(t), \qquad \mathbf{x} \in \Omega_A \tag{3.29}$$

$$\mathbf{u}^B(\mathbf{x},t) = \mathbf{N}_j(\mathbf{x})\mathbf{u}_j^B(t), \qquad \mathbf{x} \in \Omega_B \tag{3.30}$$

Then, the approximation of the displacement field is represented by (RABCZUK *et al.*, 2008)

$$\mathbf{u}(\mathbf{x},t) = \sum_{j\in n_A} \underbrace{\mathbf{N}_j^u(\mathbf{x})u_j^A(t)}_{\mathbf{u}^A(\mathbf{x},t)} H(-\varphi(\mathbf{x})) + \sum_{j\in n_B} \underbrace{\mathbf{N}_j^u(\mathbf{x})u_j^B(t)}_{\mathbf{u}^B(\mathbf{x},t)} H(\varphi(\mathbf{x})) \tag{3.31}$$

where n_A and n_B are nodes sets of superposed elements *A* and *B*, respectively; $\varphi(\mathbf{x})$ is the signed distance measured from the crack, which is described in the subsequent discussion; $H(\mathbf{x})$ is the Heaviside step function; $\mathbf{N}_j^u$ is the standard finite element shape function of node *j*. This appearance corresponds to the form suggested by HANSBO and HANSBO

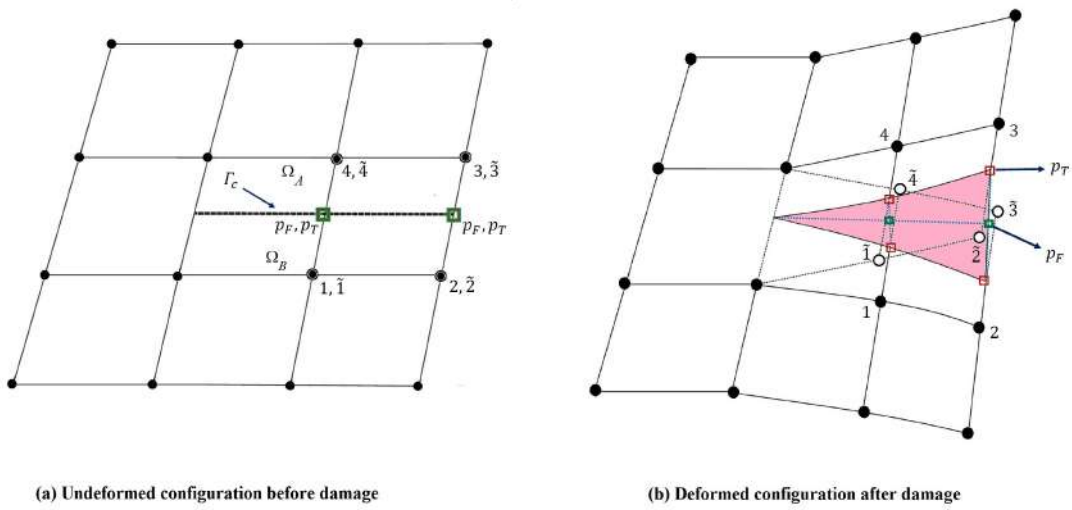

(a) Undeformed configuration before damage

(b) Deformed configuration after damage

Figure 3.4: Representation of crack opening with the phantom nodes method incorporated with fracturing fluid pressure.

(2004), although they did not present it in this pattern. It was formerly shown by AREIAS and BELYTSCHKO (2005) that the formulation of Hansbo and Hansbo is another form of the XFEM displacement field. Likewise, the pore fluid pressure $p(\mathbf{x}, t)$ is approximated in the similar manner as:

$$p(\mathbf{x},t) = \sum_{j \in n_A} \underbrace{\mathbf{N}_j^p(\mathbf{x}) p_j^A(t)}_{p^A(\mathbf{x},t)} H(-\varphi(\mathbf{x})) + \sum_{j \in n_B} \underbrace{\mathbf{N}_j^p(\mathbf{x}) p_j^B(t)}_{p^B(\mathbf{x},t)} H(\varphi(\mathbf{x})) \tag{3.32}$$

where p_j^A is the standard pressure degree of freedom for the node *j* which belongs to the element *A*; $\mathbf{N}_j^p$ is the standard finite element shape function of node *j*.

The fluid pressure within the discontinuity amounts to an independent variable p_F. As depicted in Figure 3.4, the pore fluid pressure p_T and p_B at the top and bottom faces of the discontinuity are computed by interpolation of the pore pressure degrees of freedom at the real nodes and phantom nodes. The discrepancy between the pressure of the fracturing fluid and the pore fluid pressure surrounding the crack is the driving force which dominates the leak-off from fracture into the porous formation in accordance with Eqs. (3.12) and (3.13).

The jump in the displacement over the crack is defined as the difference between the displacement fields of the two elements:

$$[\![\mathbf{u}(\mathbf{x})]\!] = \sum_{j \in n_A} \mathbf{N}_j(\mathbf{x})\, \mathbf{u}_j^A - \sum_{j \in n_B} \mathbf{N}_j(\mathbf{x})\, \mathbf{u}_j^B \tag{3.33}$$

The crack normal opening, δ_n', and the tangential sliding, δ_t', are given by (RABCZUK *et al.*, 2008)

$$\delta_n' = \mathbf{n}.[\![\mathbf{u}(\mathbf{x})]\!] \tag{3.34}$$

$$\delta_t' = \|[\![\mathbf{u}(\mathbf{x})]\!] - \mathbf{n}\delta'_n\| \tag{3.35}$$

In the proposed method herein, since the mesh generated is not necessitated to adjust with the crack geometry, taking the advantage of tracking moving interfaces methods can facilitate the treatment of the crack propagation. One of the powerful numerical techniques for the tracking of moving interfaces is the level set method, which is used for the description of interfaces in the domain (SETHIAN, 1999). In this method, the interface of interest is expressed as the zero level set of a function that is one dimension higher than the dimension of the interface. The evolution equation for the interface can then be represented as an equation for the evolution of level set function. Consider a domain Ω divided into two sub-domains Ω_1 and Ω_2, as depicted in Figure 3.5. The surface of discontinuity between these two sub-domains is designated by Γ_d. The most frequent level set function is the

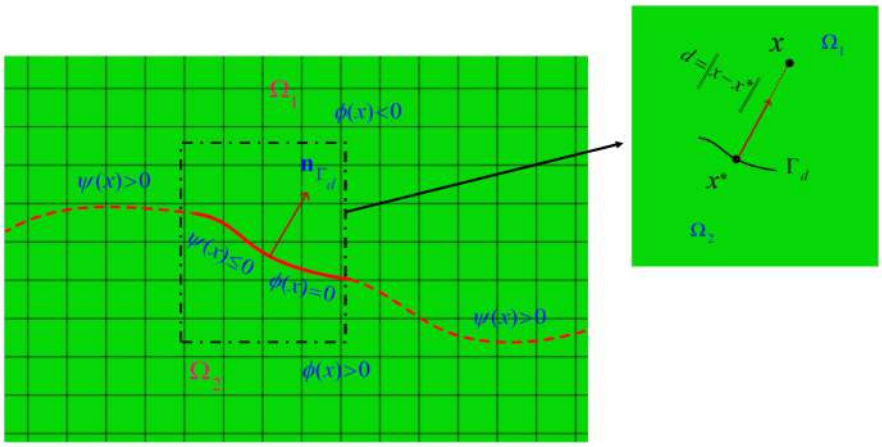

Figure 3.5: Illustration of a non-planar crack by two signed distance functions.

signed distance function, which is defined for the representation of the crack position as

$$\varphi(\mathbf{x}) = \|\mathbf{x} - \mathbf{x}^*\| \operatorname{sign}\left(\mathbf{n}_{\Gamma_d}.\left(\mathbf{x} - \mathbf{x}^*\right)\right) \tag{3.36}$$

where $\mathbf{x}^*$ is the nearest point projection of $\mathbf{x}$ on to the crack Γ_d, $\mathbf{n}_{\Gamma_d}$ is the normal vector to the crack surface at point $\mathbf{x}^*$. In this definition, $\|\|$ indicates the Euclidean norm, where $\|\mathbf{x} - \mathbf{x}^*\|$ denotes the distance of point $\mathbf{x}$ to the crack surface Γ_d. However, for tackling the crack propagation problem, just one level set φ is not generally sufficient to capture the crack geometry, and another level set ψ at the crack tip is needed. In this study, using the technique proposed by GRAVOUIL *et al.* (2002); MOËS *et al.* (2002); STOLARSKA *et al.* (2001) and implemented in ABAQUS, the crack geometry is defined by two, orthogonal, signed distance functions. The first, φ, is used for the crack surface, while the second, ψ, is used to establish an orthogonal surface so that the intersection of the two surfaces locates the crack tip. More details for crack-tracing procedure with level sets can be found in the works of GRAVOUIL *et al.* (2002); KHOEI (2014); MOËS *et al.* (2002); STOLARSKA *et al.* (2001).

3.3 Computational model

Figure 3.6 represents a $100\,\mathrm{m} \times 70\,\mathrm{m} \times 60\,\mathrm{m}$ computational domain for HF initiation and propagation simulation, which includes a horizontal wellbore, perforation holes, pay zone, and barriers. The model is discretized into a fully saturated porous domain with C3D8RP elements (8-node brick, displacement and pore pressure elements with reduced integration) together with enhanced hourglass control to remedy the problem of instabilities. Figure 3.6 shows the discretized model with 33048 number of nodes and 59850 number of elements. Three domains are contemplated for the problem, viz. barrier layers on the top and bottom of the model and pay zone in the middle, as depicted in Figure 3.6.

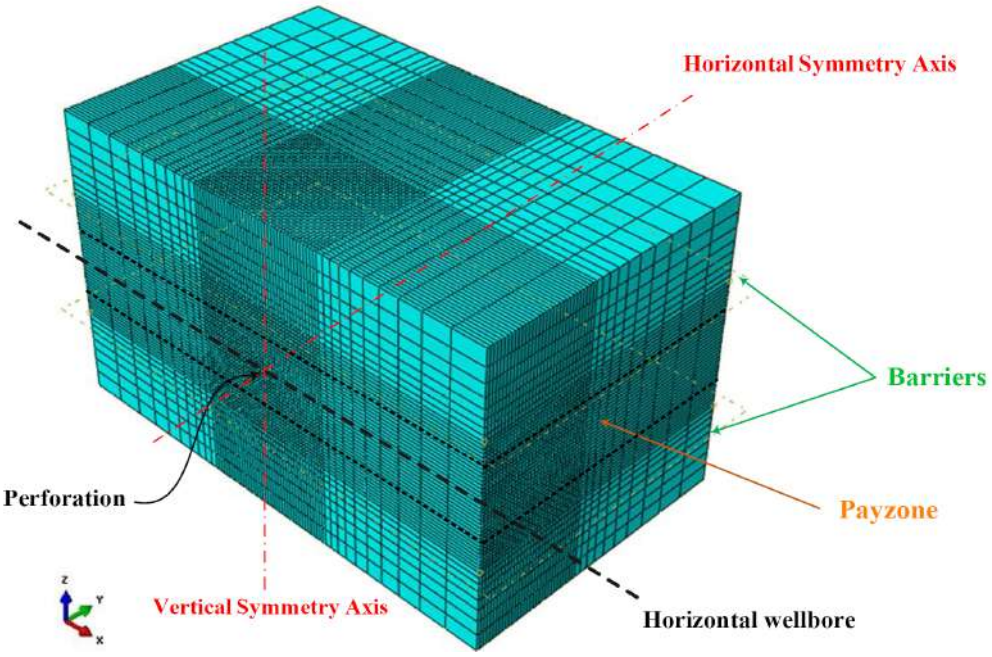

Figure 3.6: A schematic plot of the modeled reservoir.

The $x-y$ plane is situated in the middle of the pay layer and z-axis is toward up. Also, the three principal stresses are considered along the x-, y- and z axes in a Cartesian coordinate system. The horizontal wellbore is located in the plane of the horizontal stresses, $S_{h,\min}$ and $S_{H,\max}$, parallel to the minimum horizontal stress direction (x-axis). In the current study, the pay zone and the barrier layers are postulated to be fully bonded, so that interfacial slip does not appear in the model (ZHANG *et al.*, 2010). The fully coupled pore pressure-stress analysis consists of the following steps; the first step named as "*geostatic step*" is initially carried out where equilibrium is obtained after applying the initial pore

Table 3.1: Parameters for the hydraulic fracturing model.

Properties	Value
Elastic modulus of barrier layers	3.5 GPa
Elastic modulus of pay zone	1.294 GPa
Poisson's ratio	0.25
Fluid viscosity	1 cp
Critical fracture energy	28 kN/m
Damage Initiation Stress of barrier layers	0.36 MPa
Damage Initiation Stress of pay zone	0.32 MPa
Formation effective permeability	4.9346165e-19 m^2
Specific weight of fluid	9.8 $\mathrm{kN/m}^3$
Initial pore pressure	795 kPa
Pressure dependent leak-off coefficient	5.879e-10 $\mathrm{m}^3/\mathrm{kPa.s}$
Porosity	0.2
Injection rate per unit reservoir thickness	7.2e-4 m^3/s

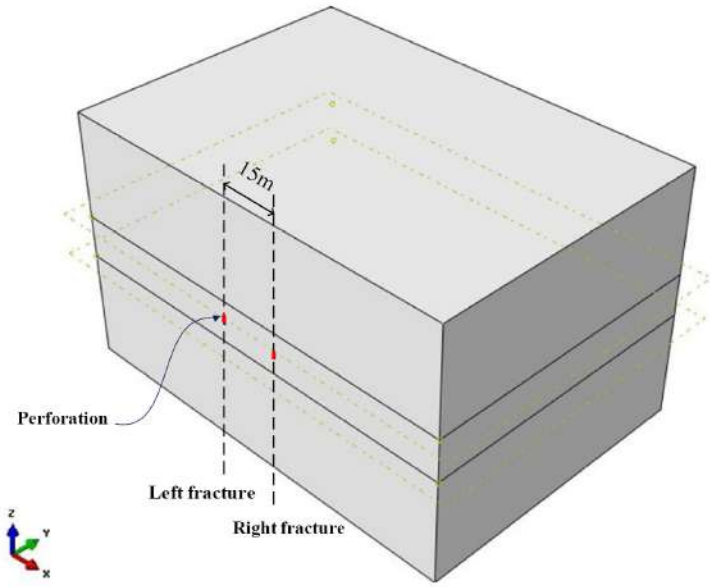

Figure 3.7: Double-stage hydraulic fracturing model with 15 m spacing. Perforations are situated on the vertical axis of the model and in the middle of the target formation.

pressure to the formation and the initial in-situ stresses. The next step "*fracturing step*" simulates the HF stage, where a specific volume of fluid is being injected along the perforations in the pay zone. In the proposed method, it is noted that the initial fractures or perforations are simulated by enrichment elements, and the fracturing fluid flow is applied directly to edge phantom nodes of the enriched elements. The simulation is conducted on a computer with 32 GB RAM, four CPUs (Intel® Core™ i7-4770) and 8 processors.

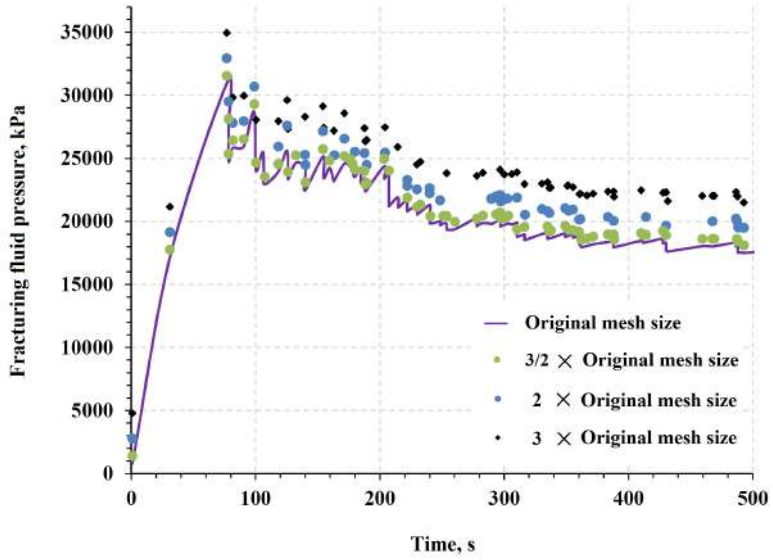

Figure 3.8: Variation of fracturing fluid pressure at the crack mouth with time for different mesh discretizations (Original mesh size= 0.6 m).

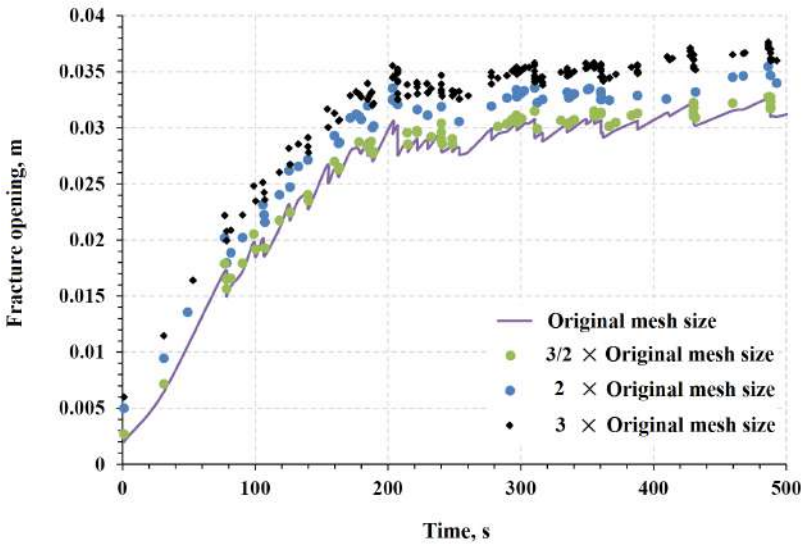

Figure 3.9: Fracture aperture at the crack mouth as a function of time for different mesh discretizations (Original mesh size= 0.6 m).

The formation geologic parameters and the material properties in pay zone and the two barriers are represented in Table 3.1 (HADDAD and SEPEHRNOORI, 2015b; SHOJAEI *et al.*, 2014). In-situ stresses of pay zone in the *x, y, z* directions, are -8.5 MPa, -12.5 MPa and -15 MPa, respectively. In-situ stresses of the two barriers in the *x, y, z* directions, are -10.5 MPa, -15.2 MPa and -17 MPa, respectively.

In order to achieve an acceptable mesh size for the area with fine mesh in Figure 3.6, leading to stable and accurate converged results, a convergence study is performed. According to Figures 3.8 and 3.9, the mesh size of 0.6 m in the area of interest for frac-

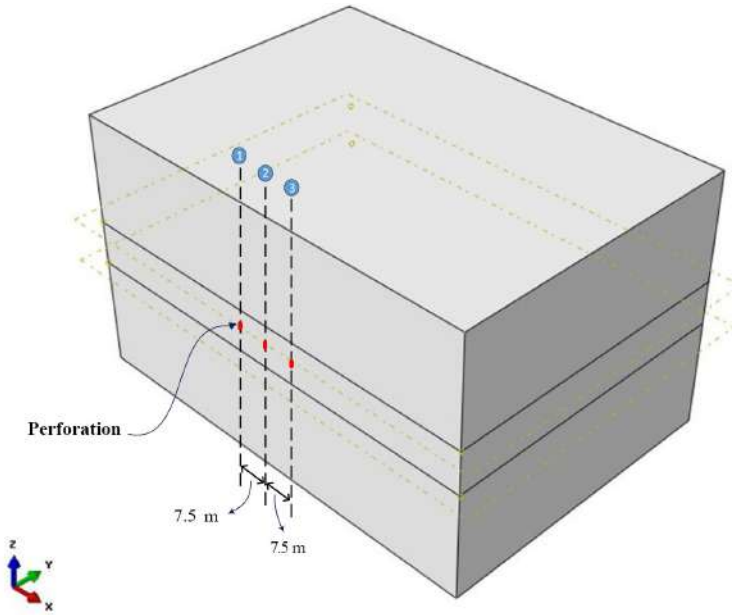

Figure 3.10: Triple-stage hydraulic fracturing model with 7.5 m spacing.

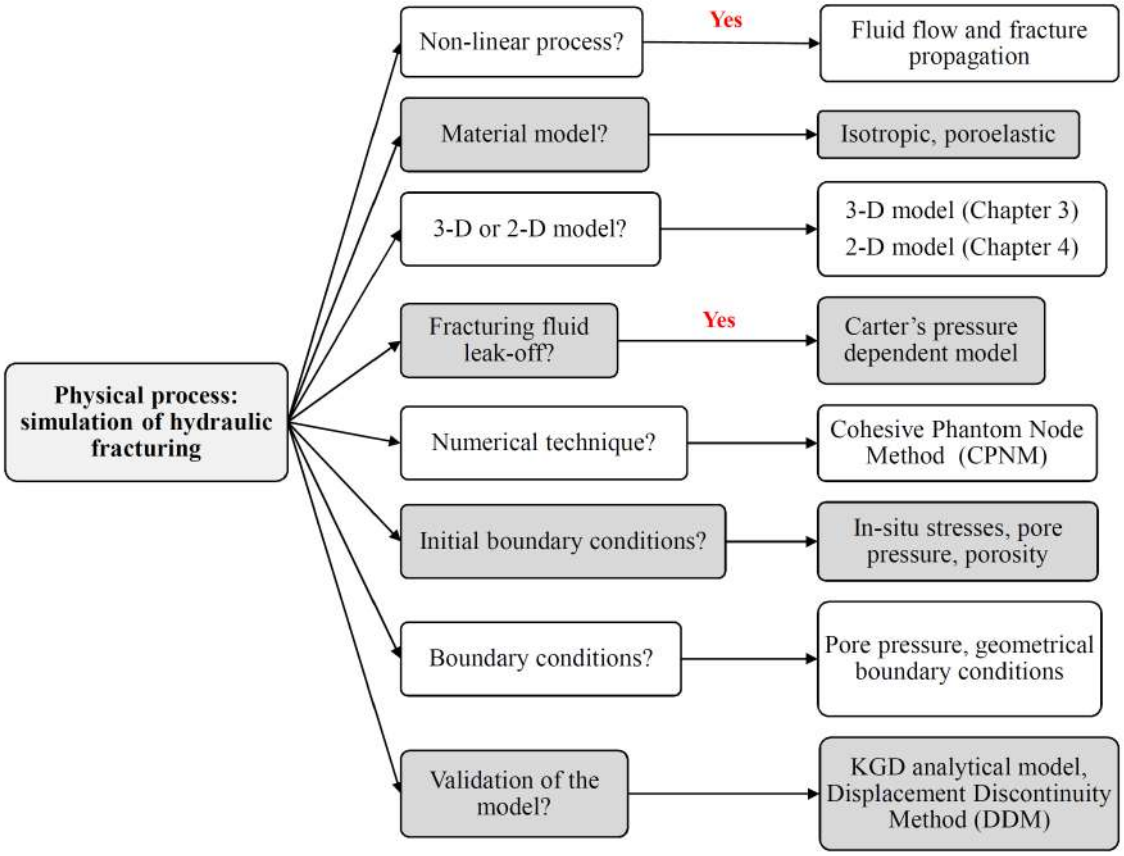

Figure 3.11: Schematic plot of physical process of HF model in this dissertation.

ture initiation and propagation is sufficient to obtain the converged results. Figures 3.8 and 3.9 evidently demonstrate that the fracturing fluid pressure and fracture opening at crack mouth converge with mesh refinement, respectively. Henceforth, the original mesh size of 0.6 m is used.

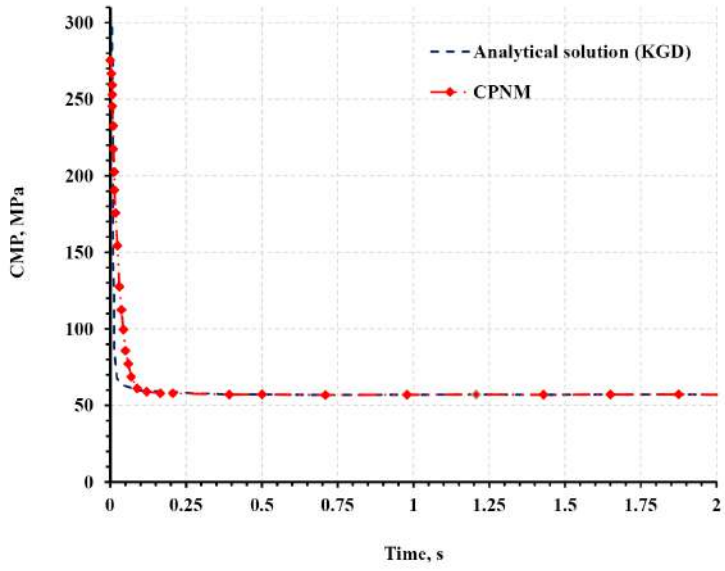

Figure 3.12: Comparison of CMP obtained by CPNM and analytical solution (KGD).

One of the main objectives of the present chapter is to investigate two different key scenarios of multiple HF operations including sequentially and simultaneously fracturing, which are depicted in Figures 3.7 and 3.10, respectively. In this regard, the crucial phenomenon encountered in such scenarios is stress shadowing effects. Considering the sequentially HF, the study is conducted for the double-stage with fracture spacing of 15 m, called "Seq-HF-1", and triple-stage with fracture spacing of 7.5 m, named as "Seq-HF-2". In this scenario, the injection of fracturing fluid flow is started from the left side perforations and then proceeds towards the right side, as depicted in Figure 3.7. In the second scenarios, i.e. simultaneously HF, two distinct patterns are introduced. One denotes double-stage HF with the fracture spacing of 15 m, called "Sim-HF-1", and the other elaborates triple-stage HF with the fracture spacing of 7.5 m, named as "Sim-HF-2".

3.4 Validation of numerical simulation

In order to validate the present numerical simulation, the results obtained for an individual hydraulically fluid-driven fracture are compared with the KGD model. This model is valid for a plane strain condition in the horizontal plane, purely viscous fluid in laminar flow regime, and a constant injection rate along the wellbore. In addition, the KGD model assumes the medium to be homogeneous, isotropic, and linearly elastic, and there is no leak-off into the formation. In order to mitigate unrealistic stress singularity ahead of the crack, zipper cracks introduced by VALK and ECONOMIDES (1995) provided a mild crack tip closure by virtue of a negative pressure dispersion in the vicinity of the crack tip within the un-wetted zone or cohesive zone. In a limiting approach, by assuming that the dry zone in front of crack tip is small, the shape of wet zone in the crack can be approximated by an ellipse with the width at location *x* identical to $\left(4E\hat{P}\Big/(1-v^2)\right)\sqrt{{x_c}^2-x^2}$ where $\hat{P}$ designates the constant fluid pressure within the crack, x_c denotes crack half-length, E is Young's modulus, v is Poisson's ratio. The Crack Mouth Pressure (CMP), Crack Mouth Opening Displacement (CMOD), and crack half-length (x_c) are expressed as (VALK and ECONOMIDES, 1995):

$$\mathrm{CMP} = S_{h,\min} + 1.09\left(\frac{E^2\mu}{(1-v^2)^2}\right)^{1/3} t^{-1/3} \tag{3.37}$$

$$\mathrm{CMOD} = 2.36\left(\frac{\mu\hat{Q}^3(1-v^2)}{Eh^3}\right)^{1/6} t^{1/3} \tag{3.38}$$

$$x_c = 0.539\left(\frac{E\hat{Q}^3}{(1-v^2)h^3}\right)^{1/6} t^{2/3} \tag{3.39}$$

where $\hat{Q}$ is the total injection rate, h denotes the crack height, μ is the viscosity of the fluid, and $S_{h,\min}$ minimum horizontal stress. The numerical results obtained by CPNM for CMP, fracture aperture profile, and CMOD depicted in Figures 3.12–3.14, respectively, are compared with analytical solution. From Figures 3.12–3.14, one can see that excellent agreement exist between the results of present method and those obtained by KGD model. As can be seen in Fig. 3.12, it is worthwhile noting that there is a significant difference between the proposed method and the analytical solution up to t= 0.5 s. This can be attributed to the fact that the KGD model does not consider any compressive boundary stress (TALEGHANI, 2009; WEBER, 2016). In the present modelling, however, the domain is initially compressed by in-situ stresses and, as a result, the fracture initiates only after enough fracture pressure is built for crack initiation. That is why the CMP based on the KGD model in Fig. 3.12 drops with time earlier than that based on CPNM.

In order to verify the present methodology, which considers the stress shadowing effect in the propagation of multiple fractures, it is compared against the DDM (SESETTY *et al.*, 2015) in simulating the propagation of double fluid-driven fractures. In the work of SESETTY *et al.* (2015), the model was based on 2-D plane strain and the DDM was used to predict fracture deformation and propagation. In addition, no fluid leak-off into the formation was considered and the fracture propagation direction was driven by the maximum principal tensile stress criterion. The FS between two fractures was set as 9m (30 ft.) and the fractures were stimulated sequentially. Figure 3.15 compares the fracture geometries of the first and second stages created along the horizontal wellbore by using

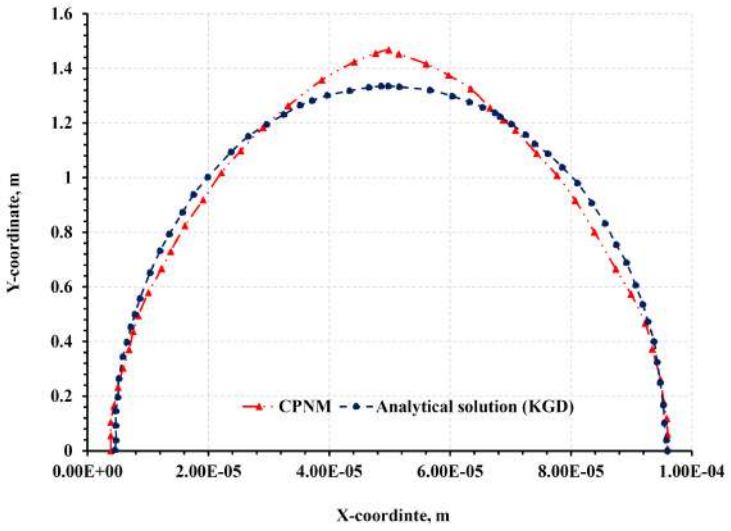

Figure 3.13: Comparison of fracture aperture profile obtained by CPNM and analytical solution (KGD).

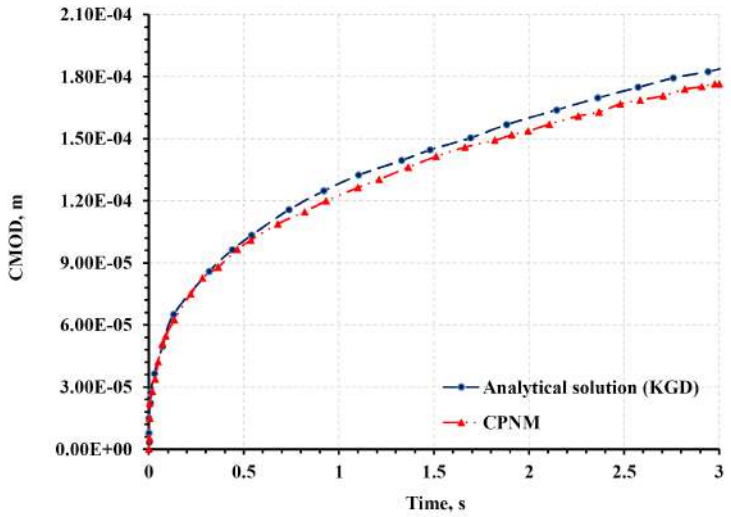

Figure 3.14: Comparison of CMOD obtained by CPNM and analytical solution (KGD).

the DDM and CPNM. In this figure, the discrepancy between the geometries of the first and second fractures is attributed to the stress shadowing effect. Figure 3.15 demonstrates a good agreement between fracture geometries obtained by the DDM and those by the CPNM.

3.5 Results and discussion

In this section, in order to present and classify results of the analysis including fracture opening, leak-off flow rate, and fracturing fluid pressure, two sub-sections namely, double-

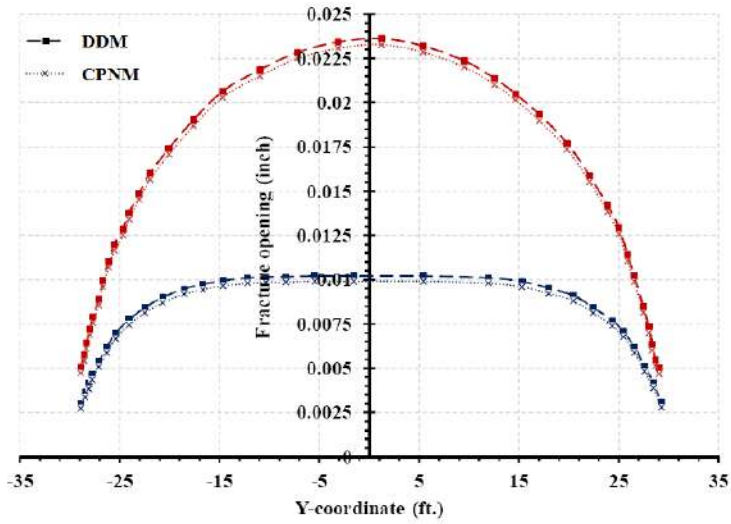

Figure 3.15: Comparison of fracture geometries of multiple fractures using DDM model (SESETTY *et al.*, 2015) and present CPNM (Injection rate=0.03 m^3/s, Fluid viscosity=1 cp), The red line denotes the first fracturing stage and the blue line represents the second fracturing stage.

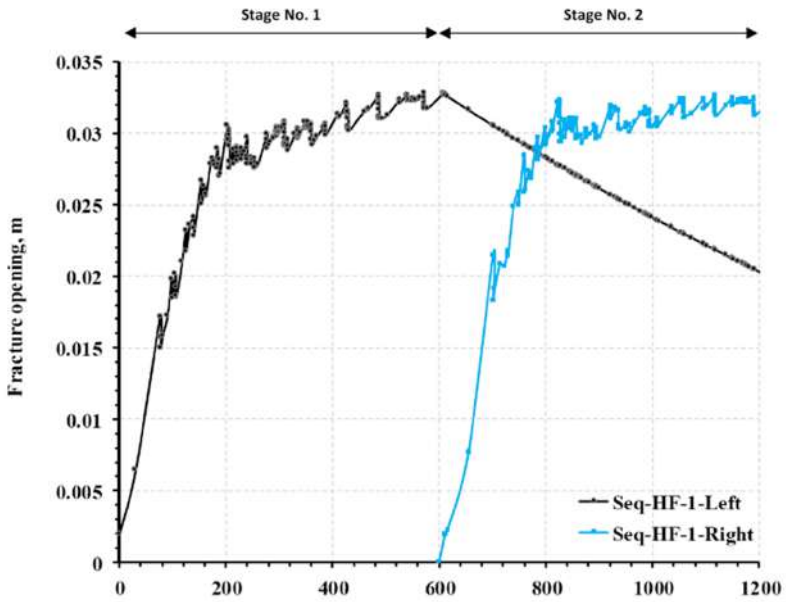

Figure 3.16: Fracture opening at the injection element for the case of Seq-HF-1.

stage HF and triple-stage HF are introduced. The fully coupled pore-pressure stress analysis for sequentially and simultaneously double- and triple-stage HF is conducted, and the pore pressure and von Mises stress contours are studied. In particular, influences of pre-existing fractures and stress shadowing effects in the case of sequentially and simultaneously fracturing scenarios are investigated.

3.5.1 Double-stage hydraulic fracturing

As far as sequentially HF is concerned, after pumping stage in the first perforation, another transient analysis is conducted for this perforation to simulate the crack closure. It is assumed that there is no fluid-flow in this fracture during closure and, as a result, the pressure imposing on the fracture surfaces is constant (PAPANASTASIOU, 1997). When the fluid injection into the first perforation is terminated, the built-up pore pressure in the crack is permitted to bleed off into the surrounding formation. Figure 3.16 shows the fracture opening at the injection element for the case of Seq-HF-1. As can be seen from this figure, after first stage of injection, the fracture aperture of left fracture gradually decreases while the fluid injection into the right perforation starts and the right fracture propagates. The depicted results show that considering the first 600-second injection for both left and right fractures, the fracture opening of the left fracture, which was injected by fracturing fluid earlier, picks lower figures than that of right fracture.

Figure 3.17 compares the fracture opening of sequentially double-stage and simultaneously double-stage HF. In this study, after several examination, a reasonable computational time was selected for the fluid-injection time to better elaboration of results. Considering

first 400-second injection, left and right fractures in the case of Sim-HF-1 present similar fracture opening trend. Interestingly, the values of fracturing opening of Sim-HF-1 are placed between values of sequentially fractures. Figure 3.18 represents the leak-off flow rate of sequentially double-stage and simultaneously double-stage HF for the first 400-second fluid injection.

The leak-off flow rate of the right fracture in the case of Seq-HF-1 demonstrates evidently greater values than those of other ones, whereas the left fracture attains the lowest values. It can be elaborated from this figure that the leak-off flow rate from the simultaneous fractures into the porous formation are located between the values of sequential fractures.

3.5.2 Triple-stage hydraulic fracturing

In order to scrutinize impacts of stress shadowing on triple-stage HF, variation of the fracturing opening at the injection spot with injection time for sequentially and simultaneously triple-stage fracturing scenarios are shown in Figures 3.19 and 3.20. To explain general trends of fractures in Figure 3.19, the entire time of injection is divided into two parts. At the first 200-second period, by injection of fracturing fluid into perforations, firstly all the perforations initiate to propagate upward and downward through the vertical plane and also in the x-y plane, increasing the value of the fracture opening at all injection points. Hence, all fractures demonstrate a similar trend at the first period.

At the second 200-second period, an obvious discrepancy between the fracture openings of fractures appears. At this period, with regard to side fractures, the greater amount of the fluid injected is allocated to enhance fractures through the z-direction compared

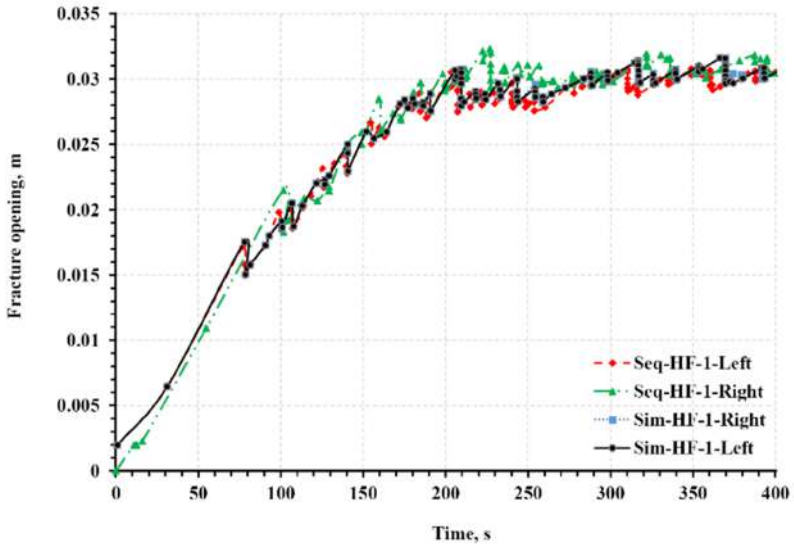

Figure 3.17: Comparison of fracture opening of sequentially double-stage and simultaneously double-stage hydraulic fracturing.

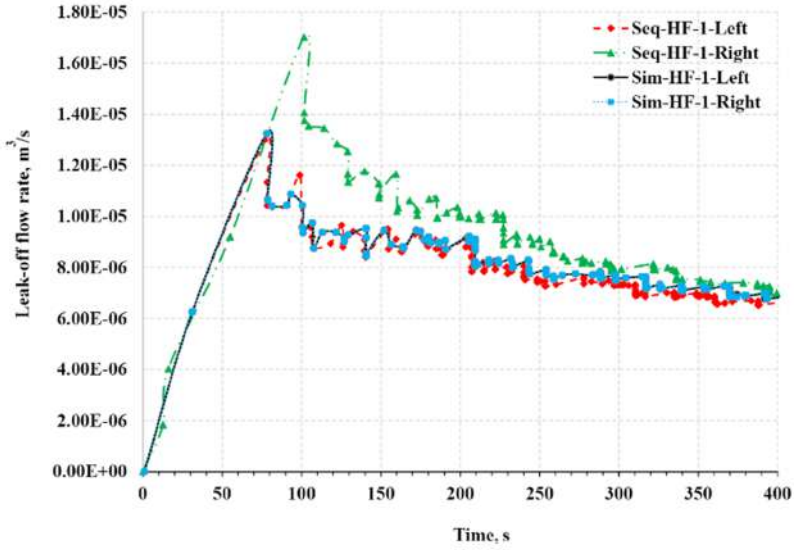

Figure 3.18: Comparison of the leak-off flow rate of sequentially double-stage and simultaneously double-stage hydraulic fracturing.

with that of the *y*–direction. However, the intermediate fracture appeals more to propagate along with the *y*-direction, exhibiting substantially more fracture length through the *x*-*y* plane. It is because at this period, due to consequence of stress interactions on the side fractures, the side ones have to exhibit non-planar fracture deviation toward the left and right boundaries instead of growing straightly. It should be noted that side fractures can overcome the obstacle of stress interactions thanks to higher in-situ stress through the *z*-direction and, as a result, tend to more propagate vertically. Consequently, much more amount of the fluid injected is allocated to the zone near the injection spots in side fractures, leading to greater fluid pressure and fracture opening at injection spots in side

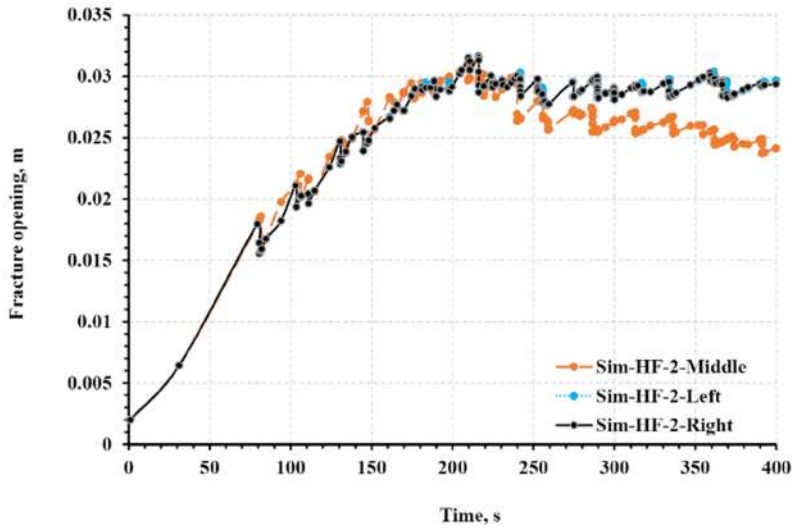

Figure 3.19: Variation of the fracturing opening at the injection element with injection time for simultaneously triple-stage fracturing.

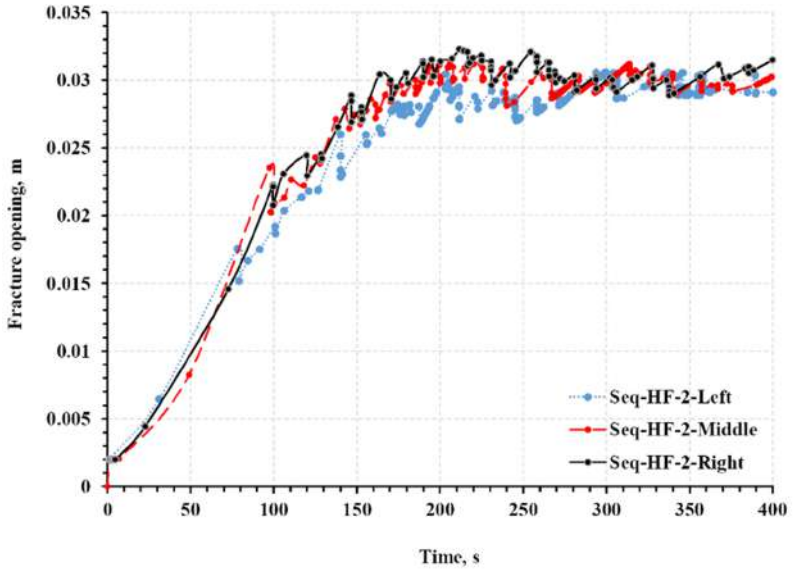

Figure 3.20: Comparison of the fracture opening of multiple fractures for sequentially triple-stage fracturing scenario.

fractures than that of middle fracture.

It is interesting to note that in the case of sequentially fracturing scenario shown in Figure 3.20, fracture aperture values incline at the next stages. Comparing Figures 3.19 and 3.20 reveals that later stages in sequentially HF mainly secure larger figures of fracture opening than that of simultaneously HF, which can be attributed to the effect of stress interactions of fractures on each other.

Figures 3.21 and 3.22 illustrate the leak-off flow rate of injection element to the formation for sequentially and simultaneously triple-stage HF, respectively. Certain important

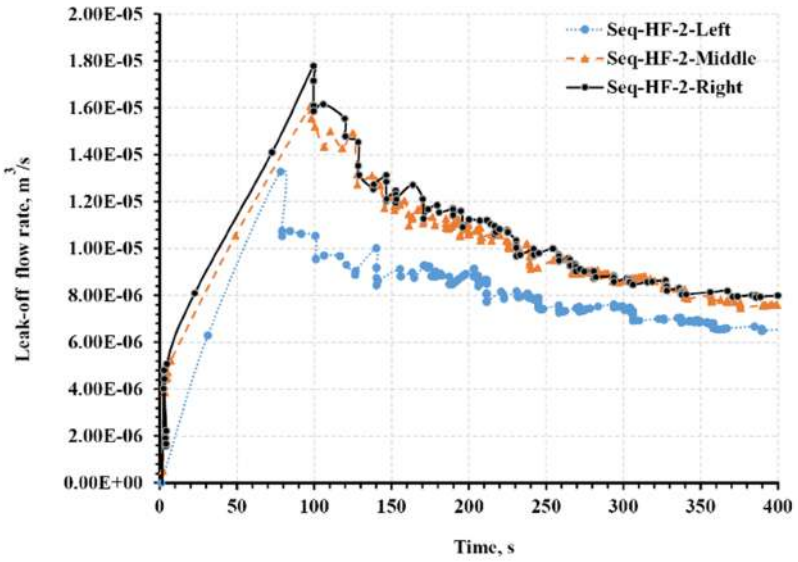

Figure 3.21: Variation of the leak-off flow rate with injection time for sequentially triple-stage hydraulic fracturing.

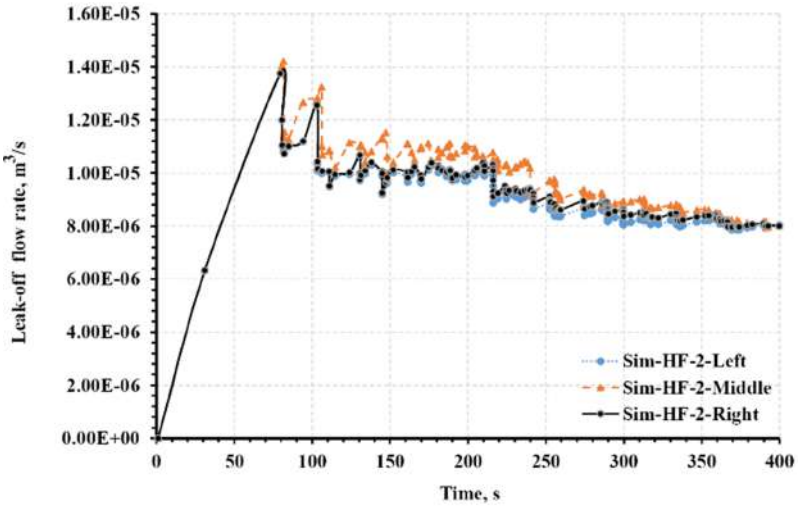

Figure 3.22: Variation of the leak-off flow rate with injection time for simultaneously triple-stage hydraulic fracturing.

observations apparent from Figures 3.21 and 3.22 are as follows: ***(i)*** The first fraturing stage for Seq-HF senario attains the lowest value of leak-off flow rate. ***(ii)*** The higher value of the leak-off flow rate occurs for later stages in sequentially fracturing senario. ***(iii)*** The middle fracture in the Sim-HF senario represents to some extent greater leak-off rate compared with those of side fractures.

Fracturing fluid pressure at the injection spot for the case of Seq-HF-2 within the whole injection time is illustrated in Figure 3.23. It should be noted that for the case of sequen-

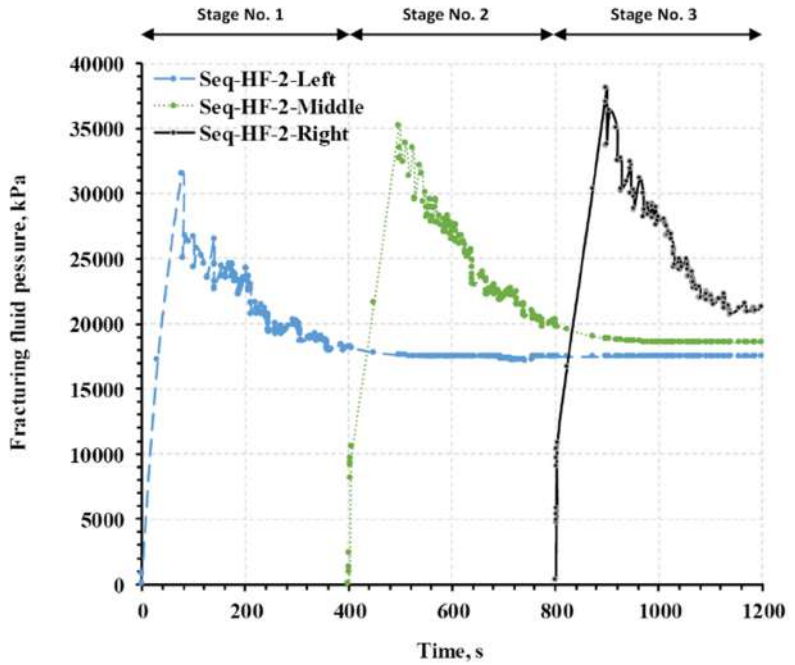

Figure 3.23: Fracturing fluid pressure at the injection spot for the case of Seq-HF-2 within the whole injection time.

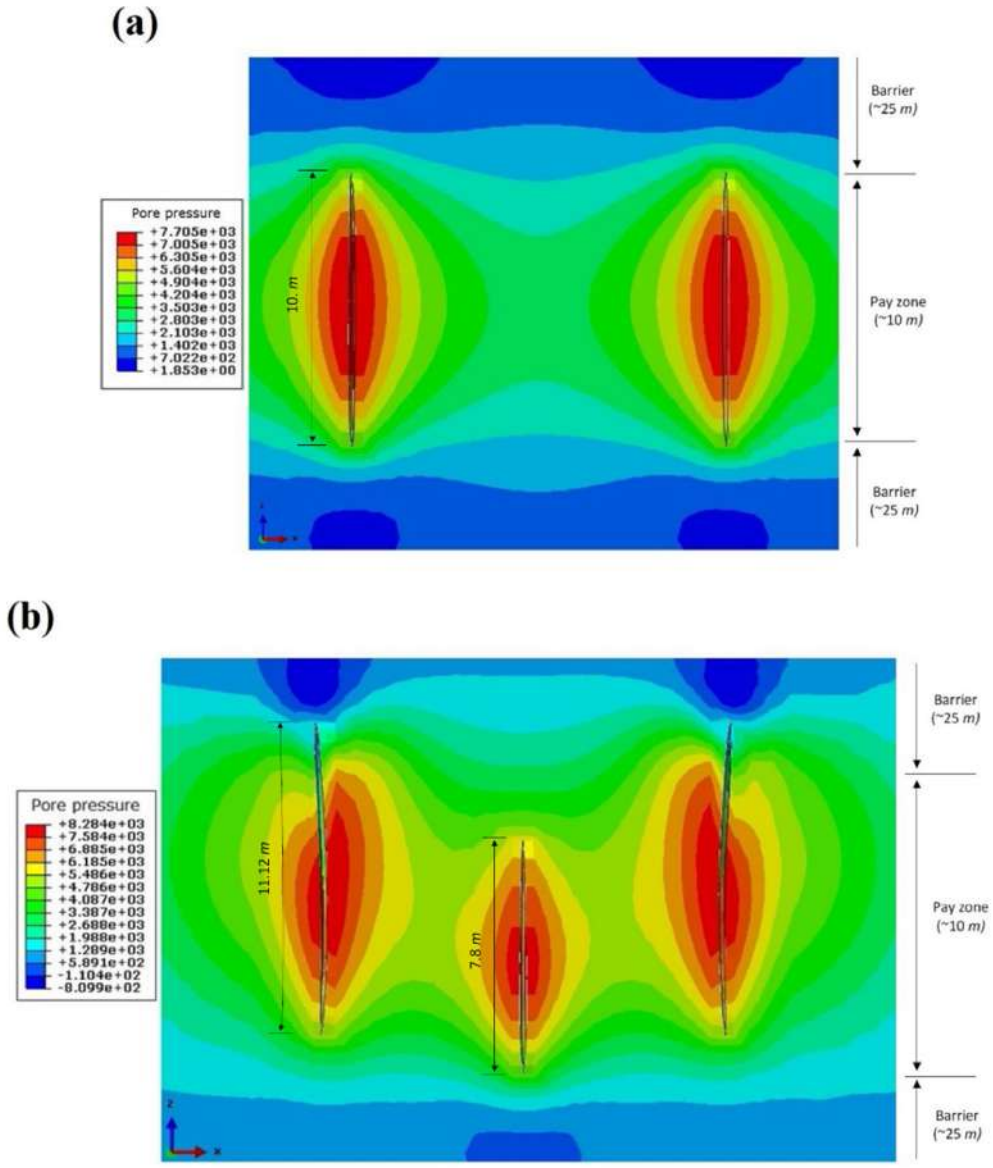

Figure 3.24: Pore pressure contours in kPa for the case of **a)** Sim-HF-1 and **b)** Sim-HF-2 in the porous medium.

tially triple-stage HF, similar double-stage one, after terminating the pumping stage in each fracture, additional step is performed to simulate the crack closure phenomenon. Because no fluid-flow exists in the fracture during closure, the pressure acting along the fracture surface is constant. As shown in Figure 3.23, after the first and second injection operations, the fluid pressure inside the fractures follows constant values for the next stages, proving correct simulation of sequentially HF. Another point that can be indicated from this figure is that later stages gain substantially higher fracturing fluid pressure than those of earlier ones.

Figures 3.24a and 3.24b demonstrate pore pressure contours for the case of Sim-HF-1 and Sim-HF-2 in the porous medium with low permeability, respectively. Comparing Figures 3.24a and 3.24b reveals that presence of middle fracture has a great impact on the

crack propagation pattern of sider hydraulic fractures. In the case of Sim-HF-1, the right and left fractures propagate symmetrically to some extent along the vertical direction, whereas in the case of Sim-HF-2 the feature of the crack propagation completely alters such that the right and left fractures track a similar trend upwards which is in the opposite direction of the middle one. It can be observed that a negative value of pore fluid pressure exists in front of the propagating crack. Such negative pore pressure does not take place in the highly permeable porous rock (MOHAMMADNEJAD and KHOEI, 2013).

From a physical point of view, the region near to the fracture tip where the pore fluid pressure attains a negative value can be interpreted as the fluid lag region. In spite of the slow rate of crack propagation, the fluid does not have sufficient time to invade the rock formation creating negative pore pressure at the fluid front position (MOHAMMADNEJAD and KHOEI, 2013; SARRIS and PAPANASTASIOU, 2011). What is more, such a negative value of the pore fluid pressure may imply that suction occurs in the near-tip region of the fracture.

Another point that can stand out from Figure 3.24b is that the right and left fractures track a similar trend upwards which is in the opposite direction of the middle one. It is because after fracturing of the initial elements along with increasing notably the effects of stress shadowing on the middle crack from the left and right ones, the rate of crack propagation in the middle fracture decreases compared with other ones. Consequently, the crack in the middle one proceeds to the next element just after growth of the cracks on the right and left sides. This trend turns to be more rigorous when right and left cracks capture an element upwards and impose substantially stress shadowing effects on the middle fracture and, as a result, the crack direction in this fracture inevitably alters downwards

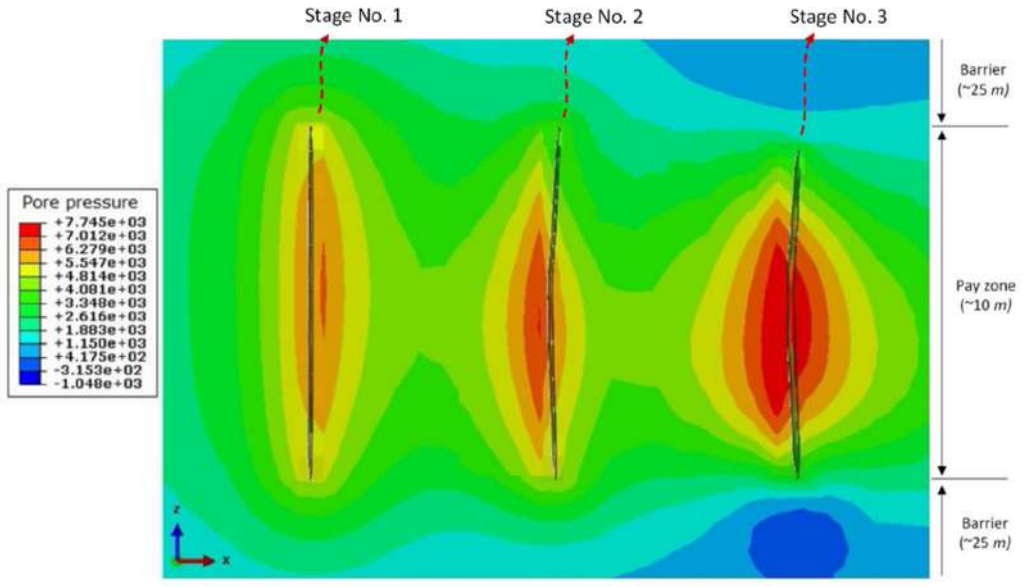

Figure 3.25: Pore pressure contours in kPa of the Seq-HF-2 scenario through the *x*-*z* plane with equal fluid injection timing for each stage.

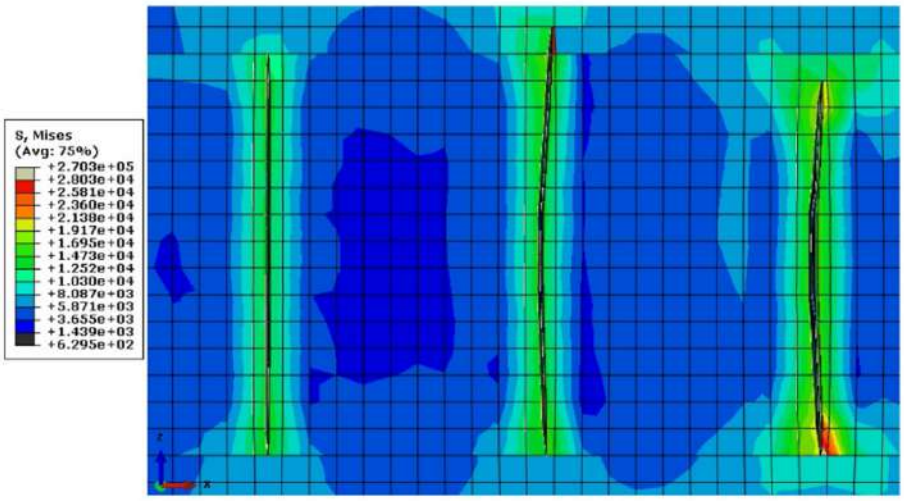

(a)

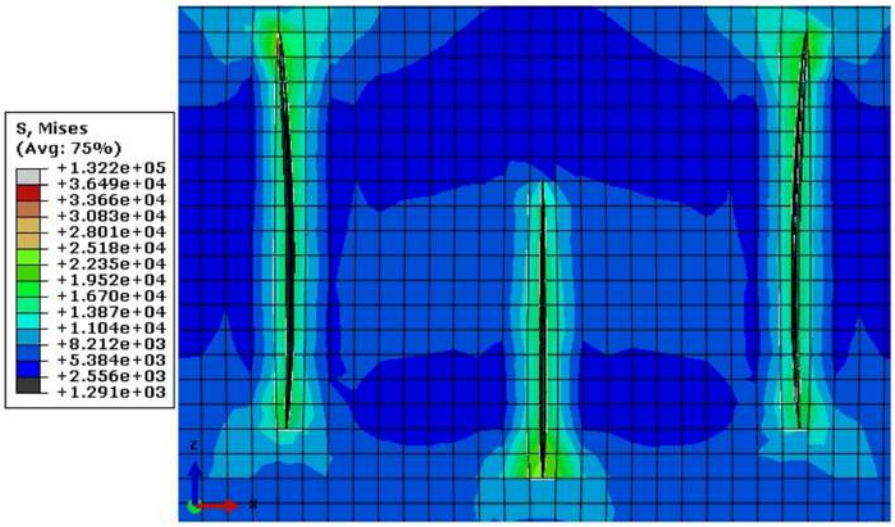

(b)

Figure 3.26: Von-Mises stress contours in kPa in the x-z plane for **a**) Seq-HF-2 and **b**) Sim-HF-2 scenarios.

under pressure the fracturing fluid inside the fracture. However, the growth of the crack in the middle one through the downward direction is faced with lower barrier layer, obtaining shorter crack length compared with other ones.

The pore pressure contours of the Seq-HF-2 scenario through the *x*-*z* plane is depicted in Figure 3.25. It can be inferred from this figure that the left fracture, which is propagated firstly, exhibits the straight crack path, while the later stages represents non-planar crack path owing to the stress shadowing effects of pre-existing fractures. It should be noted that with the same injection time for each stage, the first HF stage, the highest crack propagation length. Notwithstanding, subsequent fracturing stages demonstrate relatively less propagation length in the vertical direction because of non-planar crack preparation.

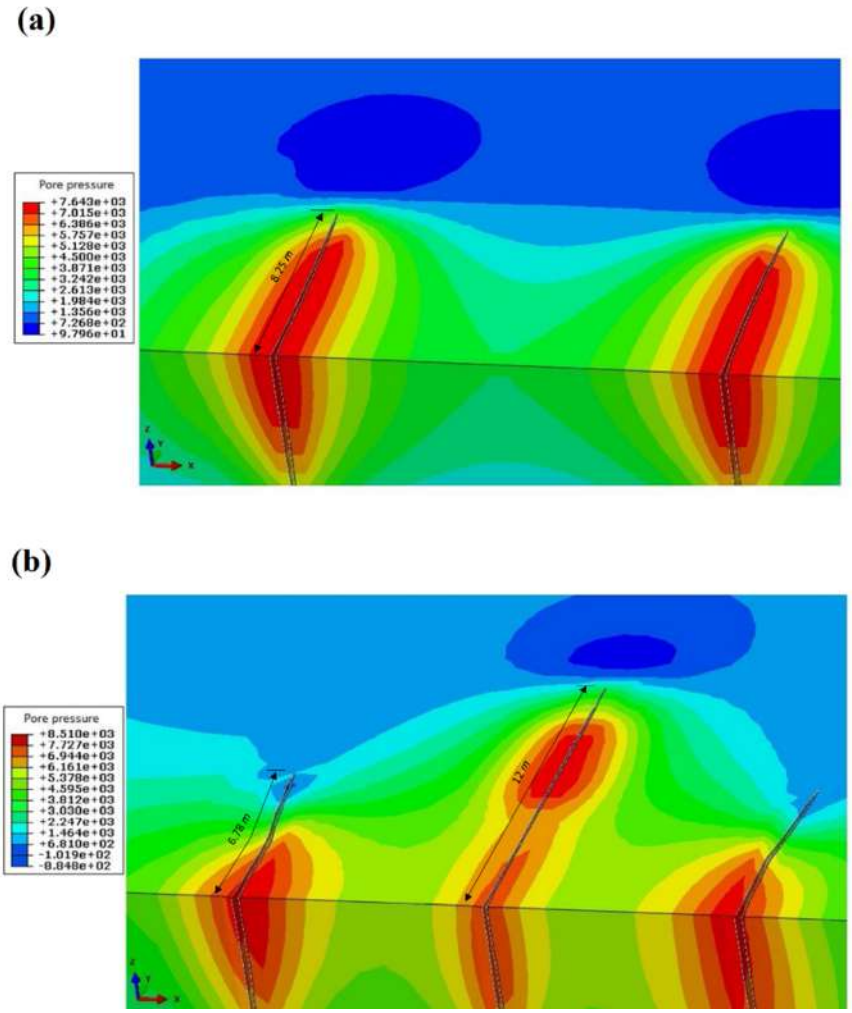

Figure 3.27: Pore pressure contours in kPa of **a)** Sim-HF-1 and **b)** Sim-HF-2 scenarios through the *x*-*y* plane.

Figures 3.26a and 3.26b represent von Mises stress contours of the sequentially and simultaneously triple-stage HF, respectively.

The high values of von Mises stress coincide with the stress concentration about the fracture tips, exhibiting the process of the mechanical failure. Figures 3.27a and 3.27b depict the pore pressure contours of the Sim-HF-1 and Sim-HF-2 scenarios through the *x*-*y* plane, respectively. From Figure 3.27a, it can be seen that the right and left fractures have a tendency to curve toward the boundaries, although the degree of the deviation is not considerable when it compares with that of side fractures in Figure 3.27b. Comparing Figures 3.24 and 3.27, one can find that left and right fractures tend more to propagate through the vertical direction while much attention of the fluid injection in the middle fracture is drawn to crack growth through the *x*-*y* plane (maximum horizontal direction). Also, it can be noted that due to stress interference caused by the middle fracture, crack paths of the left and right fractures are deviated toward the left and right boundaries. However, the middle fracture follows the straight crack path, leading to greater fracture length

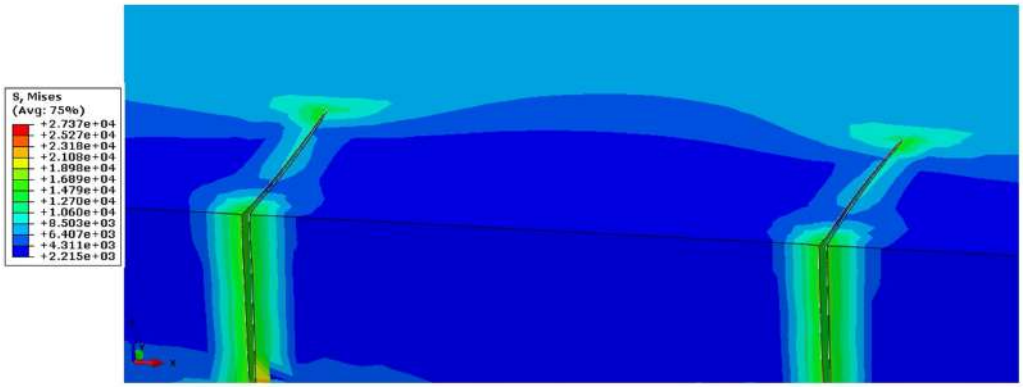

(a)

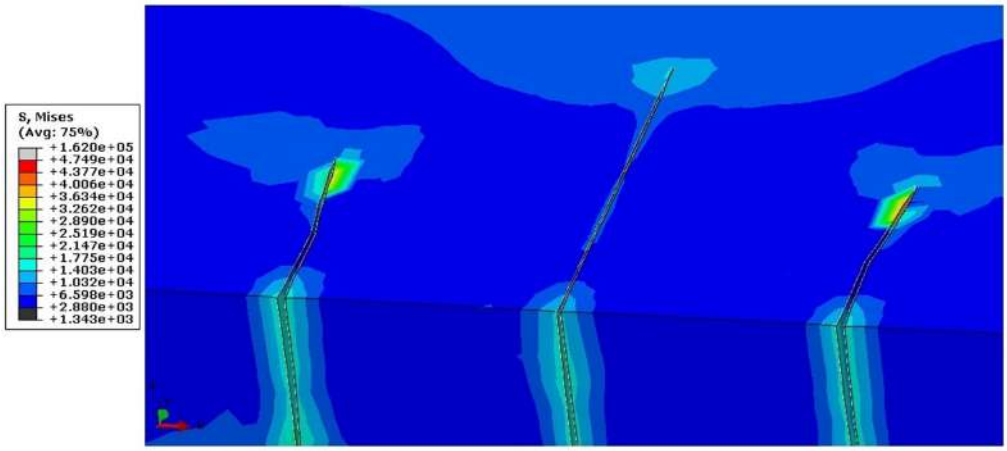

(b)

Figure 3.28: 3-D Von-Mises stress contours in kPa for **a)** Sim-HF-1 and **b)** Sim-HF-2 scenarios.

in comparison with that of sider ones.

Figures 3.28a and 3.28b represent 3-D Von-Mises stress contours for the scenarios of Sim-HF-1 and Sim-HF-2. Comparing Figures 3.28a and 3.28b demonstrates that strass filed between fractures considerably alter as a result of stress shadowing effects by decreasing the spacing between fractures.

3.6 Conclusion

In this chapter, a fully coupled pore-pressure stress analysis of the 3-D non-planar hydraulically fluid-driven fracture problem has been investigated by using CPNM. The non-linear discrete fracture mechanics, based on CCM, which was formulated by specific traction-separation laws, independent of the constitutive behaviour of bulk material, has been proposed to capture the softening effects at the fracture tip in a quasi-brittle shale. As

opposed to FEM incorporated with cohesive layers, the proposed CPNM has demonstrated its capability and efficiency to simulate the initiation and propagation of multiple crack along arbitrary, solution-dependent paths, providing a more realistic way for the study of multi-stage HF with the presence of stress shadowing impacts. With regard to Seq-HF, after pumping stage in the first perforation, another transient analysis was conducted for this peroration to simulate the crack closure. The following conclusions can be drawn from the present chapter:

- Numerical results showed that the later stages in Seq-HF mainly secure larger values of fracture opening than that of Sim-HF, which can be attributed to the effect of stress interactions of fractures on each other. This trend has been also observed for the fracturing fluid pressure and leak-off flow rate into the formation.

- It has been inferred from the results that left and right fractures tended more to propagate through the vertical direction while much attention of the fluid injection in the middle fracture was drawn to crack growth through the *x*-*y* plane.

- It can be noted that due to stress interference caused by the middle fracture, crack paths of the left and right fractures were deviated toward the left and right boundaries. However, the middle fracture followed the straight crack path, leading to greater fracture length in comparison with that of sider ones.

- In the simultaneously triple-stage fracturing scenario, the fracture opening demonstrated special attitude in such a way that at the first 200-second injection period all fractures presented a similar aperture, however, at the second 200-second period, an obvious discrepancy between the fracture openings appeared. It was because at the second period, much more amount of the fluid injected was allocated to the zone near the injection spots in side fractures, leading to greater fluid pressure and fracture opening at injection spots in side fractures than that of middle fracture.

Chapter 4

Closely spaced hydraulic Fracturing from two adjacent lateral wellbores[1]

[1]This chapter forms the basis of the following papers:
– B. Sobhaniaragh, J. Trevelyan, W.J. Mansur, F.C. Peters, Numerical Simulation of MZF Design with Non-planar Hydraulic Fracturing from Multi-lateral Horizontal Wells. Journal of Natural Gas Science & Engineering, 46 (2017) 93-107.
– B. Sobhaniaragh, V. P. Nguyen, W.J. Mansur, F.C. Peters, Pore Pressure and Stress Coupling in Closely-Spaced Hydraulic Fracturing Designs on Adjacent Horizontal Wellbores. European Journal of Mechanics - A/Solids, In Press, DOI: 10.1016/j.euromechsol.2017.08.010.
– B. Sobhaniaragh, W.J. Mansur, F.C. Peters, Fully Coupled Numerical Simulation of Altered-Stress Zones in Modified Zipper-Frac Completion Design. Technical Programme of 79th European Association of Geoscientists and Engineers (EAGE) Conference & Exhibition June 2017, Paris.
– B. Sobhaniaragh, W.J. Mansur, F.C. Peters, Numerical Simulation of Non-Uniform Modified Zipper-Fracture Design. 15th International Congress of the Brazilian Geophysical Society, August 2017, Rio de Janeiro.

4.1 Key goals

Recently, developments in oil and industry have evolved significantly in progressing and flourishing mechanical systems to perform HF jobs from multi-lateral wellbores, whereas the considerable achievement in the design of multiple hydraulic fractures with regard to FS, reservoir characterization, in-situ stress state, and overall production optimization demands a more deep understanding of their impacts. It is worth noting that for developing comprehensive and robust completion design for HF from multi-lateral wellbores with desirably closely spaced fractures, it is highly indispensable to contemplate stress shadowing effects.

On one hand, in the common approach in the MZF design used in the industry, the FS between all fractures is the same. However, by minimizing the FS to enhance the fracture complexity area between induced fractures, the FS requires to be revised so as to achieve longer and straight fracture path. On the other hand, the creation of initial fractures has the significant impact on the subsequent stages as result of induced stress interference area, in particular in the case of closely spaced hydraulic fractures. Nevertheless, few works in the available literature (MANCHANDA, 2015; ROUSSEL *et al.*, 2011) have concentrated on the propagation of next fractures after terminating the first fracturing stage.

In this chapter, conducting a 2-D numerical framework based on the CPNM introduced in chapter 3, a comprehensive study will be carried out using closely spaced fractures in several completion designs to enhance the complexity of the fracture network in the area between two adjacent horizontal wellbores. Inspired by the technique proposed by PEIRCE (2015a); WU *et al.* (2016), the stress shadowing effects are managed through non-uniform FS, introducing a modification to MZF design, termed M2ZF herein. By conducting a number of numerical simulations, this chapter is devoted to investigating the horizontal-stress contrast as well as in-plane shear stress of the formation to increase the probability of activating natural fractures and un-propped fractures, thereby enhancing the fracture complexity and higher drainage area.

4.2 Fracture complexity

In order to achieve an efficient HF job, establishing a complex interconnected network within the low permeable rock, which encompasses induced hydraulic fractures, primary and secondary natural fractures, is markedly crucial. According to well-testing analysis and field observations, it has been evident that hydraulic fracture-surface area is far larger than that of assessed in conventional fracturing design. Such circumstance can be resulted from two factors. One emanates from the fact that vast majority of tight sand and shale reservoirs are naturally fractured, such as Barnett shale (DAHI TALEGHANI *et al.*, 2013; GALE *et al.*, 2007). Besides the presence of natural fractures, the other factor may

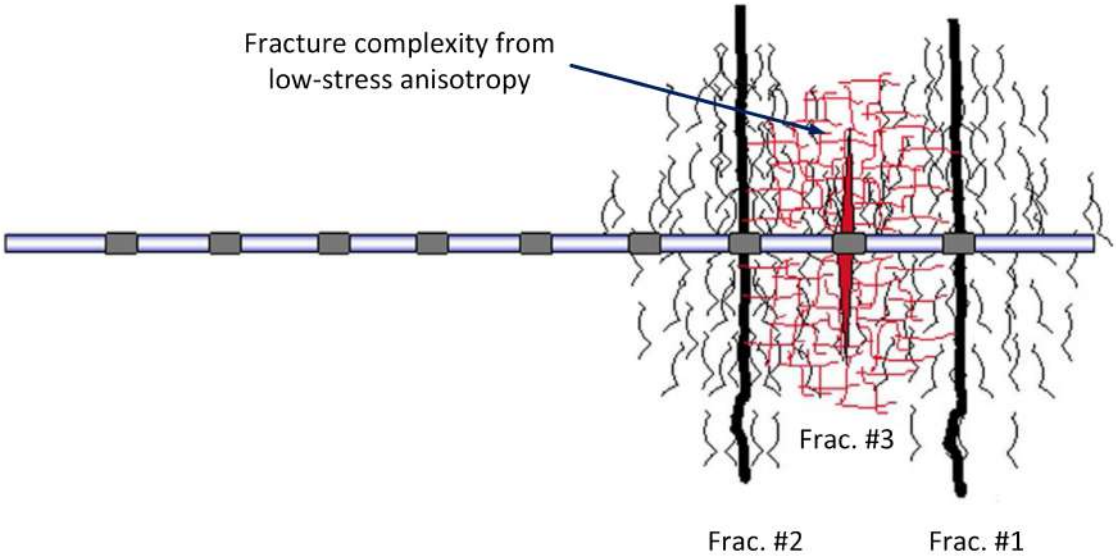

Figure 4.1: Placement of third fracture with stress interference between first and second fractures optimized to reduce stress anisotropy in Texas two-step design (SOLIMAN *et al.*, 2010).

be referred to the un-propped fractures, which can be induced as a result of stress shadowing effect during the inducing the main propped fracture. The un-propped fractures encompass micro-fractures stemming from the slippage along planes of weakness such as bedding planes, and the slippage of pre-existing natural faults or fissures (SHARMA *et al.*, 2015). Consequently, the complex network of un-propped fractures appear to be the primary reason explaining why some reservoirs demonstrate greater fracture complexity.

A number of attempts (MEYER *et al.*, 2011; NAGEL *et al.*, 2011) have been made to explain the fracture networks and their consequences on the induced fractures propagation. However, fundamental data on pre-existing networks are virtually out of the question to acquire. WU and POLLARD (2002) and OLSEN *et al.* (2009) demonstrated that the width at the intersection of the hydraulically induced fracture and the natural fractures is dependent on several parameters such as the stress anisotropy. The reduction in the stress anisotropy can activate the Mode I opening of planes of weaknesses, resulting in generating complex network which links hydraulically induced fractures to pre-existing natural fractures. Thus, presence of substantial fracture surface area causes higher drainage of the low permeability reservoir and maximizing the SRV. WENG *et al.* (2007) demonstrated that the hydraulic fracture geometry changes from a bi-wing fracture to a complex network of fractures as a result of a reduction in horizontal stresses contrast.

In recent years, thanks to significant advances in the engineering and technology, several sophisticated designs have been developed to generate the complex fracture network and achieve optimum. Among various completion designs, "Texas two-step" (as demonstrated in Figure 4.1) has been presented to reduce the FS and create greater fracture complexity (SOLIMAN *et al.*, 2010). According to this technique, after fluid injection into

first interval, by moving towards the heel, a second interval is stimulated and, as a result, there is a degree of stress interference between the two fractures. Afterwards, rather than continuing towards the heel of the well, the third interval is stimulated between the two previously fractured intervals with the aim of altering the stress in the rock so as to contribute to the generation of secondary fractures. Using a finite difference and explicit numerical scheme, ROUSSEL *et al.* (2011) and MANCHANDA *et al.* (2014) showed that the lower FS can be achieved in the scenario of Texas two-step compared with conventional simultaneously fracturing. In addition, they purported that a stress reversal region with stress re-orientation of 90^0 takes place in the adjacent to the main induced fracture. This zone imposes a confining condition on the FS which should be large enough to avoid the initiation of longitudinal fractures. Nevertheless, this hypothesis seems to be questionable because propagating of new fracture into the altered-stress region caused by the previous fracture can considerably change the local stresses, which will be discussed further in this chapter.

4.3 Completion designs on multi-lateral wellbores

Taking multi-lateral wellbores into account, the remarkable advances in completion design have offered several techniques to stimulate far field fracture complexity and maximize the total SRV. “Zipper-Frac”, as shown in Figure 4.2A, is one of a class of techniques in which two or more horizontal wellbores are fractured simultaneously in order to enhance stress perturbation close to the tips of each fracture. In this method, when opposing fractures move towards each other, to some extent the interference takes place ahead of fracture and encourages the fractures to propagate through the direction perpendicular to the horizontal wellbore.

Based on continuum geomechanics, RIOS *et al.* (2013) performed stress shadowing analysis and presented that Zipper-Frac creates an extensive region of ascended normal stresses and descended shear stresses, which has the impact of stabilizing natural fractures and weakness planes instead of enhancing their shear. QIU *et al.* (2015) used a complex fracture network model, termed unconventional fracture model, to study Zipper-Frac. The model had the capability to simulate complex fracture propagation under stress shadowing effect. This study concluded that Zipper-Frac provides operational efficiency by reducing the standby time compared with Seq-HF, which is mainly attributed to stress shadowing effects.

However, the application of Zipper-Frac is restricted because of two main deficiencies. Firstly, the creation of complex field is limited to the area close to the fractures tips. Secondly, it is associated with the risk of connection of adjacent wellbores if opposing fractures become very close.

In another method, known as MZF introduced by SOLIMAN *et al.* (2013), motivated

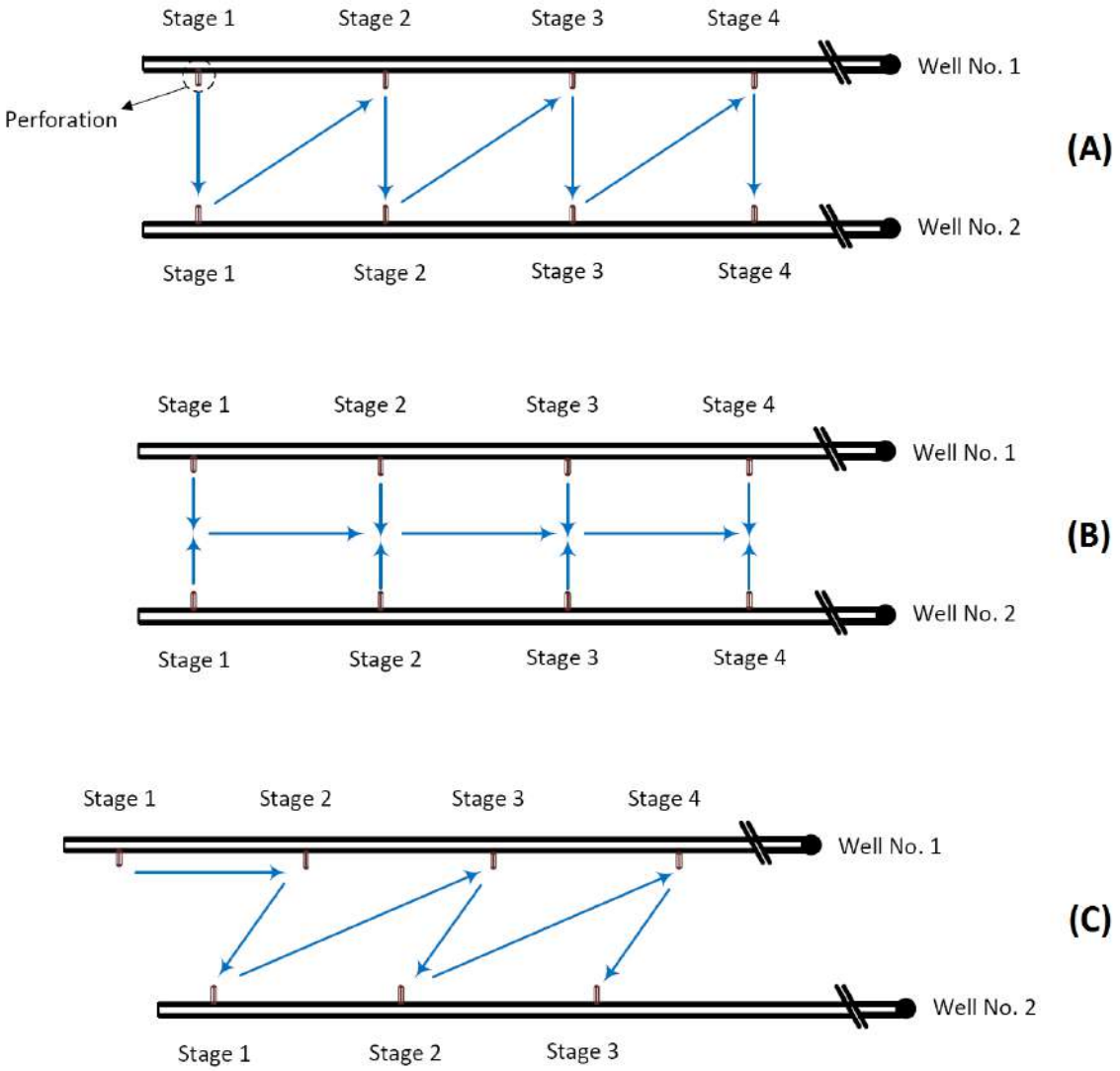

Figure 4.2: Various types of hydraulic fracturing scenarios on two horizontal lateral wellbores; **(A)**: Zipper-Frac scenario, **(B)**: Sim-HF scenario, **(C)**: MZF scenario (modified after (VERMYLEN *et al.*, 2011)).

by the advantages of the presence of middle fracture between two consecutive fractures used in Texas two-step, fractures on two lateral wells are situated in a staggered pattern, as depicted in Figure 4.2C. MZF design can potentially increase the stress interference between the fractures and create an effective SRV to enhance hydrocarbon production (RAFIEE *et al.*, 2012). Although the MZF has presented promising results in increasing desired far-field complexity associated with alternating fracturing with no operational issues, it still requires more investigation for far more mechanistic understanding of the parameters involved in this design.

RAFIEE *et al.* (2012) studied the advantages of Zipper-Frac and the MZF by using analytical stress interference calculations around various fracture geometries. They showed that the MZF completion potentially increases the stress interference between the fractures and provides more fracture complexity compared with Zipper-Frac. However, this study

did not consider the curving propagation of hydraulic fracture which plays important role in closely spaced fractures.

By taking the advantage of the DEM, NAGEL *et al.* (2014, 2013) found out that the improvement in well stimulation using Zipper-Frac and MZF is greatly dependent upon the in-situ pore pressure, natural fracture mechanical properties, and natural fracture characteristics. For example, for the cases presented with orthogonal/parallel natural fractures, a Zipper-Frac configuration did not increase the amount of sheared natural fractures around the hydraulic fracture.

Using a fully coupled hydraulic fracture simulation code in GEOS [1], IZADI *et al.* (2015) studied some of the fundamental effects which influence planar fracture growth during stimulation of three wellbores by using three different completion designs including conventional (Seq-HF), Zipper-Frac, and MZF. The results obtained from this work showed that MZF provides more larger fracture surface area compared with Seq-HF and Zipper-Frac. Furthermore, IZADI *et al.* (2015) concluded that wider well spacing provides smaller induced compressive stress by neighbouring wellbores and it leads to a greater fracture surface area at the expense of fracture aperture/width. This behaviour was more pronounced when MZF was emplyed insetad of either Seq-HF or Zipper-Frac.

Recently, KUMAR and GHASSEMI (2016a) implemented boundary element model with capabilities to simulate any number of fractures for simultaneous or sequential hydraulic fracture propagation. Their results demonstrated that in Zipper-Frac, the fractures propagate in nearly planar manner with probability of coalescence of their tips. In the case of the MZF, the likelihood of fracture tips coalescence decreases because of the offset between fractures.

4.4 Fundamental Framework

First and foremost, it should be mentioned that mathematical framework of the present chapter has been mainly established based on previous chapter, restricting the computational model to 2-D owing to computational expenses of the 3-D model. Consequently, the CPNM used in this chapter is the 2-D form of the one proposed in the previous chapter. Thus, the fracture initiation and propagation criteria and also description of the method are not repeated herein.

4.4.1 Fracturing Fluid Model

The primary task of fracturing fluids is to crack the porous rock and enforce initiated fractures to propagate. Continual pumping of fracturing fluid extends a conductive path

[1] Developed by Lawrence Livermore National Laboratory, GEOS is an open source multi-physics platform for massively parallel simulations originally introduced for addressing the hydraulic fracture problem.

deep into a formation to transmit large amount of propping agent inside the induced fractures. The flow model of the fracturing fluid within the fracture between the cohesive faces is depicted in Figure 4.3. In this figure, element number 1 and 2 are fractured and element number 3 is intact. In the proposed model, the fluid flow through the fracture is decomposed into two components; one refers to the tangential flow along the cracked element faces, and other is the normal flow across the cracked element surface rendering the infiltration mechanism into the surrounding formation. Based on Lubrication theory, the momentum equation for the tangential fluid flow within the fracture is formulated by Poiseuille's law (Eq. 3.8).

In addition, the continuity equation of mass conservation for the fracturing fluid flow is described by Eq. 3.4. Similar to chapter3, in order to treat the filter cake as a pressure-dependent layer, Settari's fluid leak-off model is employed by using a user-defined subroutine. By virtue of the proposed pressure-dependent model, the normal components of the fracturing fluid are defined according to Eqs. 3.12 and 3.13.

4.5 Model construction

Figure 4.4 represents 3-D configuration of the two horizontal wellbores. The trajectories of the horizontal wellbores are aligned with minimum horizontal stress, resulting in transverse fractures. The computational finite element domain, demonstrated in Figure. 4.5, is a 2-D horizontal plane where the out-of-plane stress is vertical, which includes two horizontal wellbores, and perforation holes. The area "ABCD" is discretized into a fully saturated porous domain with CPE4RP elements (4-node bilinear displacement and pore pressure, reduced integration with hourglass control) together with enhanced hourglass control (BELYTSCHKO *et al.*, 1984) to remedy the problem of instabilities for the case of reduced-integration modelling, as shown in Fig 4.5. Figure 4.5 shows the discretized model with 82142 number of elements. Note that the "ABCD" domain with the size of $510\,m \times 50\,m$ is considered large enough to eliminate consequences of geomet-

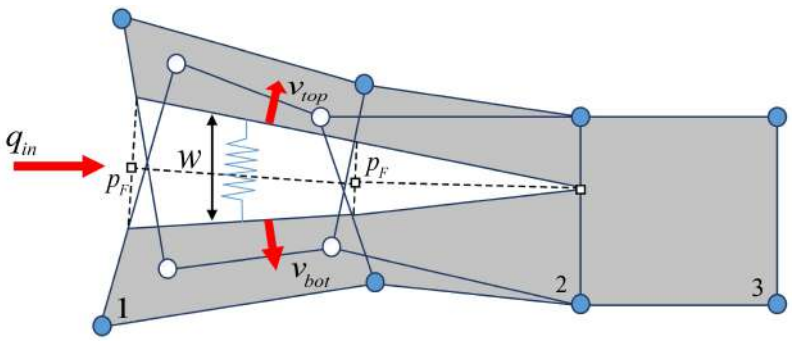

Figure 4.3: Schematic plot of the fluid flow pattern model within the framework of CPNM, $\mathbf{v}_{top}$ and $\mathbf{v}_{bot}$ point out the normal flow velocities at which the fracturing fluid leaks off from the top and bottom surfaces of the crack into the formation.

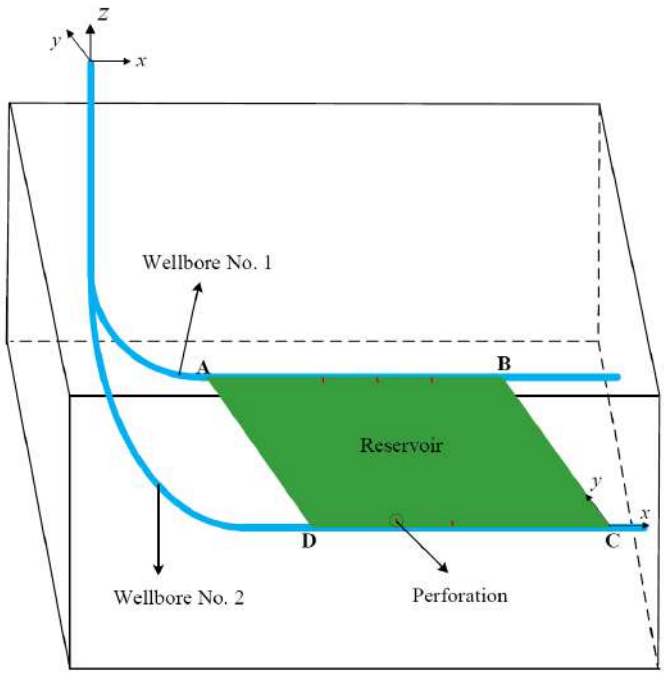

Figure 4.4: 3-D configuration of the two lateral horizontal wellbores.

rical and pore pressure boundary conditions. The horizontal wellbores No. 1 and No. 2 are located in the plane of the horizontal stresses, $S_{h,\min}$ and $S_{H,\max}$, at the top and lower sides of the whole computational domain. Similar to Section 3.3, the first step is "*geo-static step*", followed by fluid injection steps. The formation geologic parameters and the material properties have been represented in Table 3.1. In-situ stresses in the *x*, *y*, and *z* directions, are supposed to be -19.0 MPa, -20.5 MPa and -19.0 MPa, respectively, unless otherwise stated. As depicted in Figure 4.5, the area $\bar{\mathrm{A}}\bar{\mathrm{B}}\bar{\mathrm{C}}\bar{\mathrm{D}}$ is the domain of interest for fracture initiation and propagation, and the mesh size in this area should be small and the

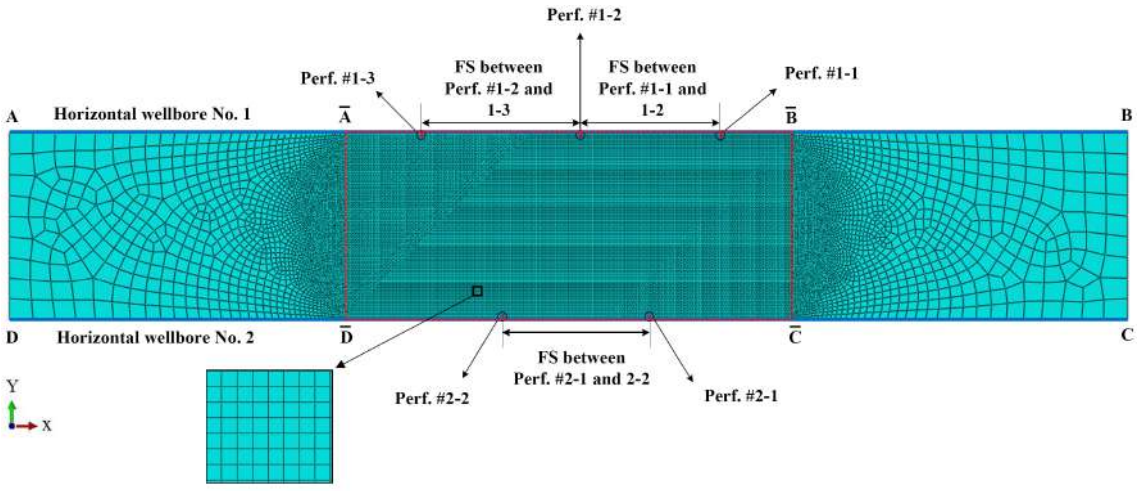

Figure 4.5: Finite element domain of modelled reservoir for the simulation of hydraulic fracturing from two lateral wellbores.

value of which is determined by a mesh convergence study shown in Figures 4.6 and 4.7. In these figures, the original mesh size refers to 0.4 m. Figures 4.6 and 4.7 obviously show that the results obtained using the CPNM converge with mesh refinement. From now on, the original mesh size is used.

4.6 Results and discussion

In the succeeding work, employed the CPNM with fully coupled pore-pressure stress analysis, various scenarios for HF from two horizontal lateral wellbores are developed and scrutinized. In order to better elaborate this section, the results obtained are categorized into two sections namely first cycle in MZF design and second cycle in MZF design. Indeed, one cycle in MZF design is completed after terminating the first three HF stages. Afterwards, in the second cycle, the attention is drawn to the first five HF stages.

4.6.1 First cycle in MZF design

In this section, taking the MZF completion design into consideration, the effects of stress shadowing effects affected by FS on the stress anisotropy, pore pressure, leak-off flow rate of the formation are studied in detail by conducting a myriad of simulation runs. One of the main contributions of the present work is shedding light on the altered-stress

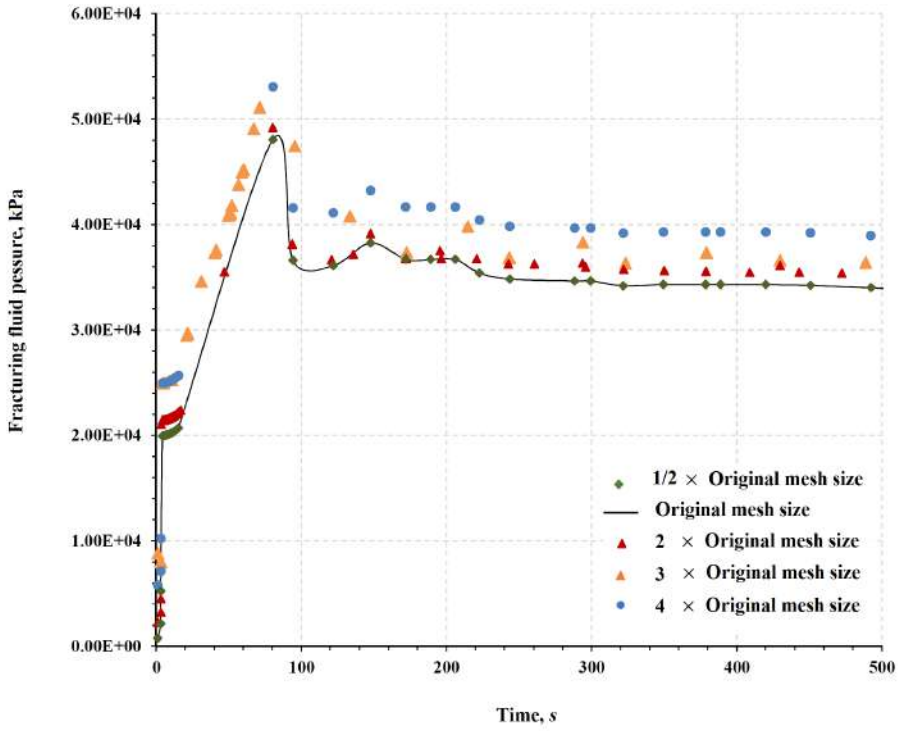

Figure 4.6: Variation of the fracturing fluid pressure at the crack mouth with time for different mesh discretizations (Original mesh size= 0.4 m).

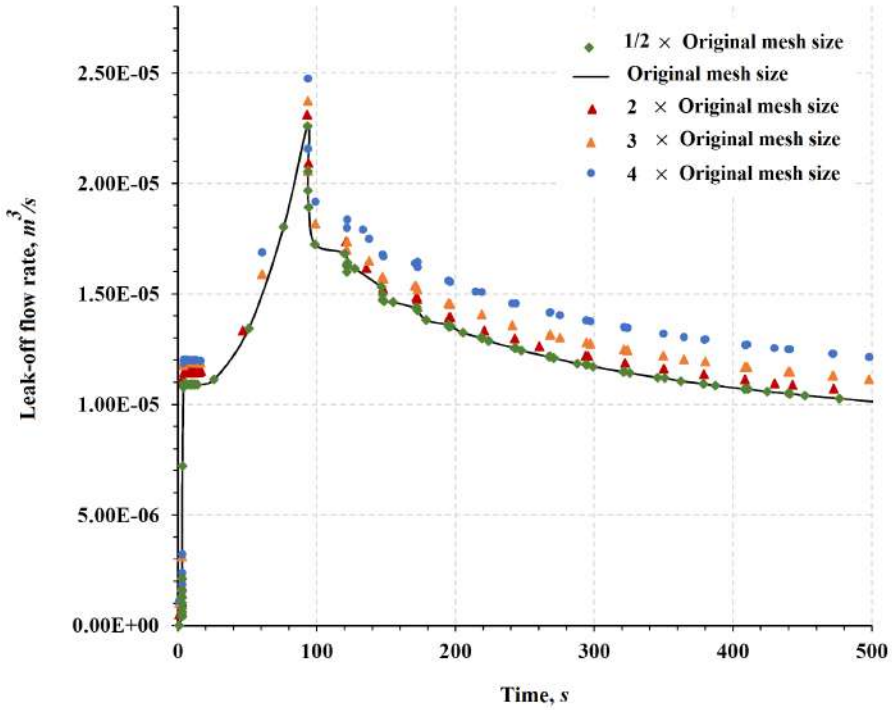

Figure 4.7: Leak-off flow rate at the crack mouth as a function of time for different mesh discretizations (Original mesh size= 0.4 m).

zone around the induced fractures, dividing into different zones, which is mainly affected by FS. In particular, in this section we take the advantage of evaluating horizontal stress contrast in the area near the fracture tip, opposed to the works of MANCHANDA *et al.* (2014); ROUSSEL *et al.* (2011) which considered only the point of the fracture initiation along the wellbore. Considering Figure 4.5, it should be noted that in the MZF design, the first stage (Fr. #1-1) of Well No. 1 is followed by the second stage (Fr. #1-2) on the same wellbore. Afterwards, the fracturing proceeds with the first stage (Fr. #2-1) on the Well No. 2. This scenario continues from the toe to the heel of the lateral wellbores. The placement of the Fr. #2-1 on the opposite well is located in the middle of the Frs. #1-1 and #1-2.

4.6.1.1 Pore pressure of the porous formation

Pore pressure contours in the formation for the case of an MZF design with FS=18 m and FS=31 m are shown in Figures 4.8a and 4.8b. In this example, the fracturing fluid is injected into the first perforation on Well No. 1 for a period of 60 minutes, and at the end of this stage fracture number 1 (Fr. #1) is created. Then, the second perforation on Well No. 1 is fractured, and this is followed by the first stage on Well No. 2. It should be noted that FS used in this section denotes the spacing between the first and second perforation on Well No. 1. Also, according to MZF, the perforation created on Well No. 2 is situated midway between the first and second perforations on Well No. 1. It is evident from Figure 4.8a that

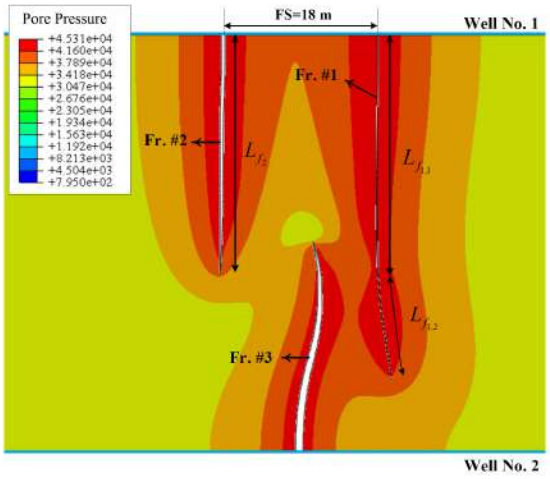

(a)

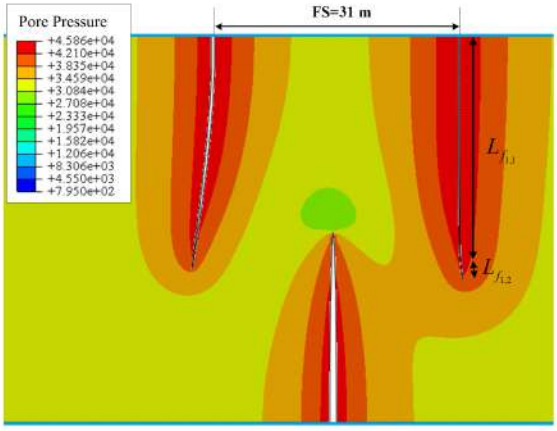

(b)

Figure 4.8: Pore pressure contours of the formation for the case of MZF design with: **a)** FS=18 m and **b)** FS=31 m.

the length of Fr. #1 is divided into $L_{f_{1,1}}$ and $L_{f_{1,2}}$. This is because after terminating the first stage on Well No. 1 and creating $L_{f_{1,1}}$, the second stage starts and Fr. #2 propagates, altering the local stresses between Fr. #1 and Fr. #2 and imposing forces on the surface of Fr. #1. Accordingly, the fracturing fluid in Fr. #1 plays a role as a driving force so that $L_{f_{1,2}}$ is created as the Fr. #2 propagates. It is worth noting that the length of $L_{f_{1,2}}$ is considerably smaller than that of Figure 4.8b owing to the larger FS and, as a result, there are reduced stress shadowing effects. Under closer inspection, it can be seen that Fr. #3 first propagates in the direction of maximum in-situ horizontal stress, and afterwards it reorients itself in the direction of the local maximum horizontal stress induced by the stress shadowing effects of other fractures. Also observed from Figures 4.8a and 4.8b is that by choosing FS=18 m, the Fr. #1 on Well No. 1 grows in a straight path whereas by selecting FS=31 m, the Fr. #3 on Well No. 2 propagates straight towards the area in the middle of two other fractures. This point will be further discussed in the following.

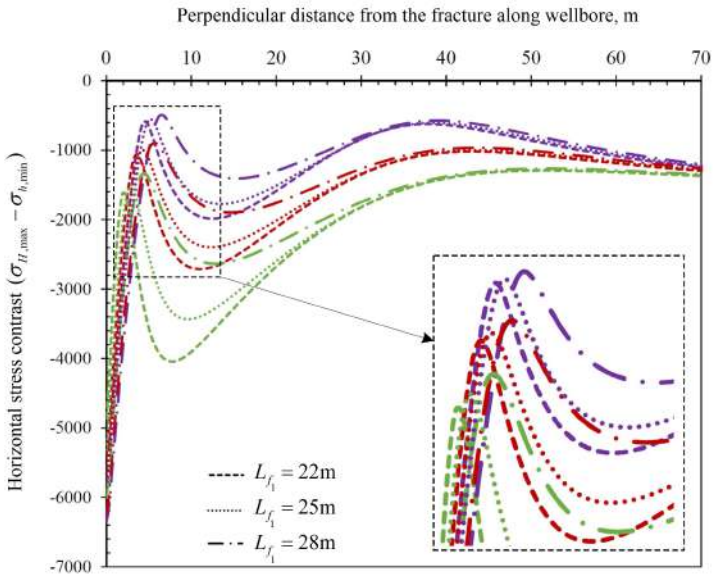

Figure 4.9: Variation in horizontal-stress contrast along the wellbore with perpendicular distance from Fr. #1 before starting the second stage. Green lines: $L_1^1 = 6$ m, Red lines: $L_2^1 = 12$ m, Violet lines: $L_3^1 = 18$ m.

4.6.1.2 Stress anisotropy

Figure 4.9 demonstrates the variation in the horizontal stress contrast $(\sigma_{H,\max} - \sigma_{h,\min})$ along the wellbore with perpendicular distance from the fracture in the first stage for various fracture lengths, L_{f_1}, and several distances (L_i^1) from the horizontal wellbore No. 1. It should be noted that the horizontal stress contrast presented in this figure has been obtained after terminating the first stage and before staring the second stage, i.e. using the

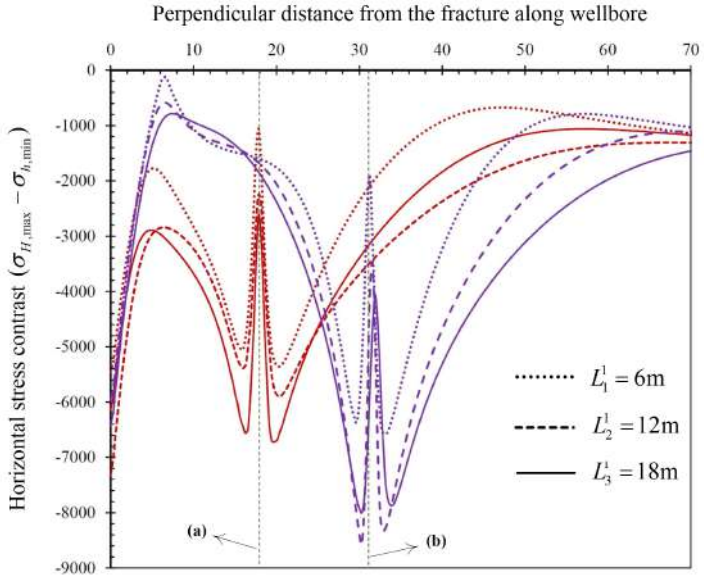

Figure 4.10: Illustration of variation in horizontal-stress contrast in the direction perpendicular to Fr. #1 for **a)** FS=18 m and **b)** FS=31 m.

same strategy used by MANCHANDA *et al.* (2014); ROUSSEL *et al.* (2011). It can be inferred from Figure 4.9 that by increasing the fracture length, the region of low stress contrast due to stress shadowing effects moves away from the fracture. In addition, it can be seen that for the case with the same fracture length, the horizontal stress contrast decreases with increasing distance form the horizontal wellbore, which implies that the region of low horizontal stress contrast is deviated from the first fracture owing to the stress shadowing effect.

Figure 4.10 shows the variation in the horizontal stress contrast in the direction perpendicular to the first fracture for FS=18 m and FS=31 m. In these results, the horizontal stress contrast is shown for three specific distances ($L_1^1 = 6$ m, $L_2^1 = 12$ m, and $L_3^1 = 12$ m) from Well No. 1 when the fracture tip approaches those distances. Figure 4.9 shows a different behaviour in the results obtained after terminating the first stage. Several simulation runs have been conducted in this research, and eventually it has been concluded that with FS of 18 m in the MZF scenario, the second fracture is not deviated from the first fracture, and follows a straight propagation path owing to a low horizontal stress gradient, as depicted in Figure 4.10. Further, the horizontal stress contrast significantly decreases in the area near the fracture tip by decreasing the FS, while the overall horizontal stress contrast between fractures is considerably lower for the cases with larger FS. It is worth noting that the reduction in horizontal stress contrast as a result of stress shadowing plays an important role in opening the natural fractures and eventually increasing the fracture complexity (DAHI TALEGHANI *et al.*, 2013; SOLIMAN *et al.*, 2010). MANCHANDA *et al.* (2014); ROUSSEL *et al.* (2011) concluded that in a region of low stress contrast, in particular in the middle of two fractures, there is a high probability that an induced fracture will propagate along a straight path transversely and tap into a pre-existing fracture network. In contrast, a comparison of Figures 4.9 and 4.10 reveals that a new fracture growing into the altered-stress region has the capability to alter the local stresses.

The direction of maximum horizontal stress in the area between two horizontal wellbores is depicted in Figure 4.11a. It is interesting to note that after completing the first stage, the direction of the second induced fracture cannot be estimated only by considering the direction of the maximum horizontal stress. This is because the propagation of the second fracture alters the existing local stress and imposes new stress shadowing conditions in the area, changing its propagation path. Based on several simulation results conducted in this study, the stress-altered zones, which have an effect on the second stage on Well. No. 1, are divided into attraction and repulsion zones. If the second stage started in the attraction zone, the Fr. $\#2$ would follow a curving crack path due to the stress shadowing effect caused by Fr. $\#1$, as shown in Figure 4.11b. By increasing the FS to the critical value of 18 m, the Fr. $\#2$ is not deviated and follows a straight propagation path while the Fr. $\#3$ on Well No. 2, which is situated in the curving zone, follows a curving path.

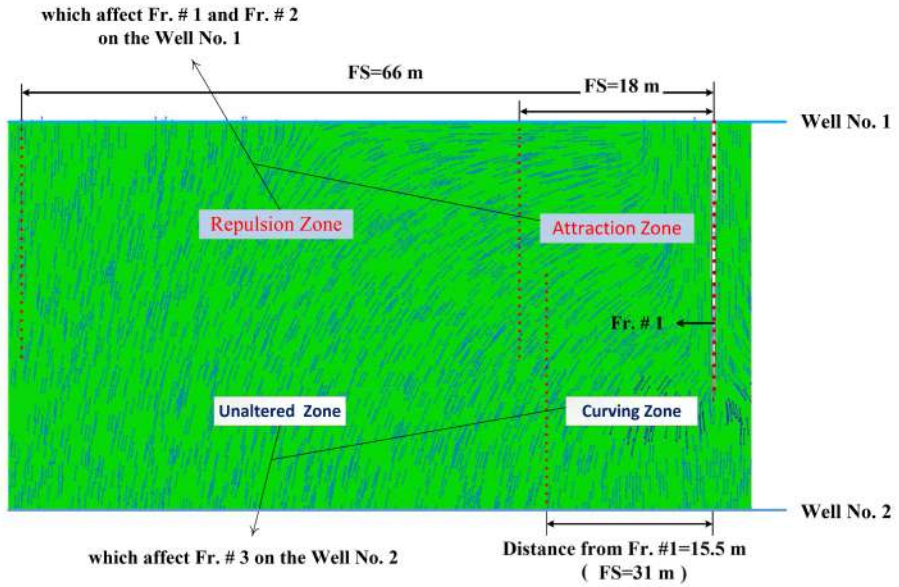

(a)

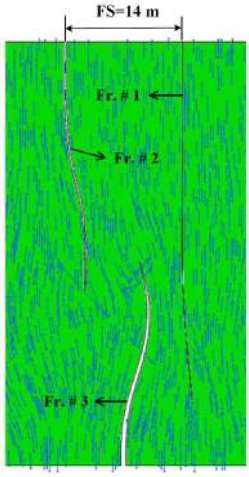

(b)

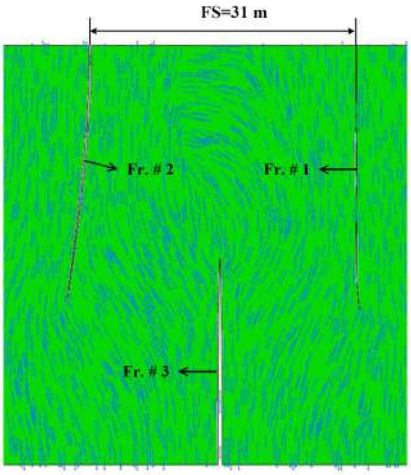

(c)

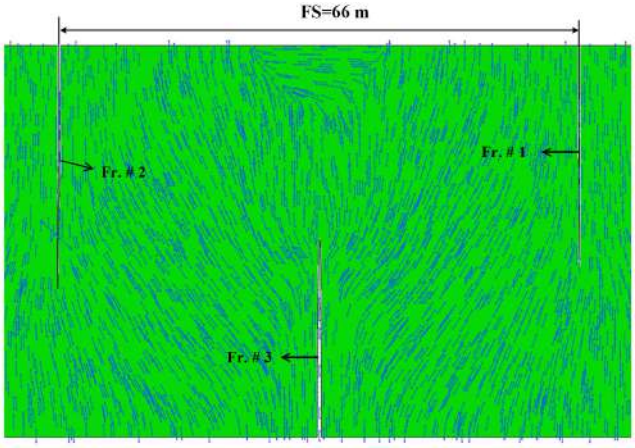

(d)

Figure 4.11: Direction of maximum horizontal stress: **a)** Illustration of various zones after creating Fr. #1. **b)** MZF design with FS= 14 m in which Fr. #23 is located in the attraction zone whereas Fr. #2 is in the curving zone. **c)** MZF design with FS= 31 m in which Fr. #2 is located in the repulsion zone while Fr. #3 propagates in a straight path. **d)** MZF design with FS= 66 m in which Fr. #2 and Fr. #3 grow straight.

On the other hand, when the FS in the MZF design reaches a value of 31 m, in other words, the distance of Fr. #3 on Well No. 2 attains a value of 15.5 m from the Fr. #1, Fr. #3 exhibits an unchanged crack path as shown in Figure 4.11c. In addition, by increasing the FS from the critical value of 18 m, the Fr. #2 is located in the repulsion zone, which implies that it is deviated from the first fracture, although the degree of deviation decreases by moving away from the Fr. #1. Furthermore, the Fr. #3 on Well No 2 retains its straight propagation path moving away from the Fr. #1. We conclude that the stress-altered area near Well No. 2 comprises two specific zones, including curving and unaltered zones.

4.6.1.3 In-plane shear stress

Figures 4.12a–4.12d show the effect of the propagation of the Fr. #3 into the area between two pre-existing fractures (Fr. #1 and Fr. #2) on the shear stress for the MZF design with various FS. The results obtained show that after creating the Fr. #2, the shear stress in the region between two fractures is suppressed owing to stress shadowing effects. As the Fr. #3 invades this area, it not only considerably alters the magnitude of shear stress, but doest it also cause far more of the reservoir to be exposed to alteration in shear stress. Consequently, this promotes activation of the planes of weakness and natural fractures which exist in unconventional reservoirs such as shale plays (RAFIEE *et al.*, 2012; REZAEI *et al.*, 2015).

As depicted in Figures 4.12a–4.12d, the propagation of the Fr. #3 into the repulsion zone between Fr. #1 and Fr. #2 has a greater effect on the shear stress than those located in the attraction zone. Importantly, growth of the third fracture from the offset wellbore can change the direction of the shear stress, increasing the probability of activating pre-existing natural fractures and, as a result, promoting greater fracture complexity.

4.6.1.4 Leak-off flow rate

The variation in the leak-off flow rate in the cracked element adjacent to the wellbore, during the HF time of operation, is shown in Figure 4.13. In this example, HF time for each stage is taken to be 4000 second. Specific observations apparent from Figure 4.13 are as follows: (**i**) The leak-off flow rate becomes considerably larger as the HF job in MZF design proceeds to the subsequent stages; (**ii**) by increasing the FS in the repulsion zone, the leak-off flow rate in the second stage is reduced, although this observation is reversed in the third stage which is performed on the offset wellbore.

4.6.2 Second cycle in MZF design

In this section, the 2-D numerical modelling of the curving hydraulic fractures from two adjacent lateral horizontal wellbores in the low-permeable reservoir is performed by considering the first five HF stages. The present section concentrates on the numerical

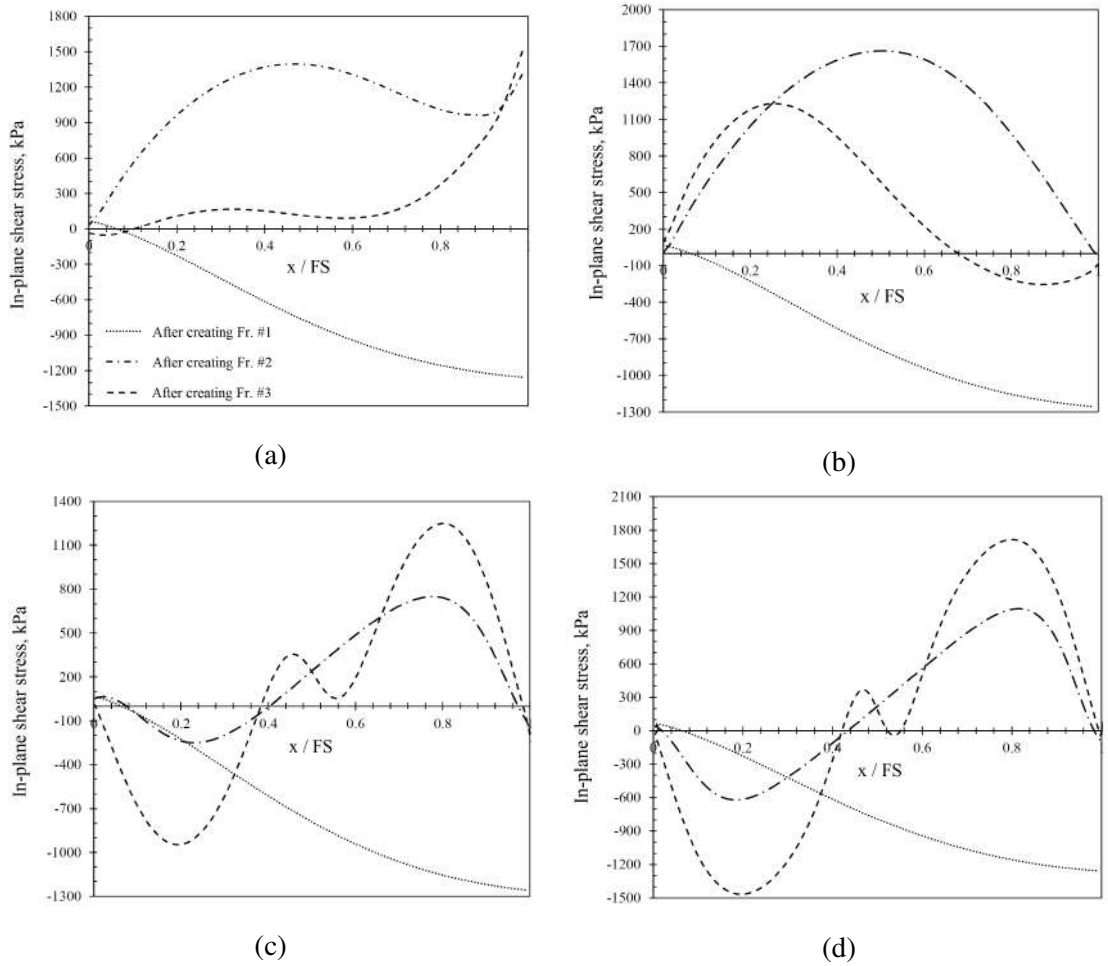

Figure 4.12: Distribution of in-plane shear stress along the horizontal wellbore with perpendicular distance from Fr. $\#1$ ($L^1 = 18\,\mathrm{m}$) for MZF design with: **a)** FS=14 m. **b)** FS=18 m. **c)** FS=50 m. **d)** FS=66 m.

simulation of the various fracturing designs in adjacent lateral wellbores including Sim-HF, Seq-HF, MZF, and M2ZF. Noted that for the case of Sim-HF and Seq-HF designs, the pattern of the perforations follows that of MZF design in order to mitigate the possible risk of wellbores connection.

4.6.2.1 Pore pressure of the formation

The minimum FS between the Frs. $\#1$-1 and $\#1$-2 is obtained in such a way that the Fr. $\#1$-2 as well as the Fr. $\#2$-1 propagates along the straight path (without deviation) to achieve the desired maximum fracture lengths. As depicted in Figure 4.14a, the minimum FS between the Frs. $\#1$-1 and $\#1$-2 is 66 m. At the fourth stage, the minimum FS of 46 m is required so that Fr. $\#1$-3 grows within the straight propagation pathway under the stress shadowing effects. However, the opposite fracture, i.e. Fr. $\#2$-2, is deviated towards the Fr. $\#1$-3 owing to alteration in local maximum horizontal stress, leading to asymmetric distribution of the pore pressure and increasing the risk of well communication. In Fig-

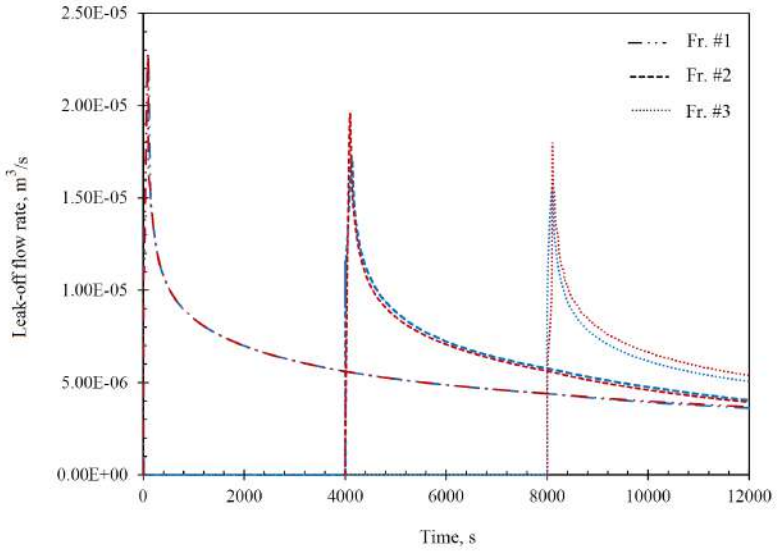

Figure 4.13: Variation of the leak-off flow rate in injection time for three fracturing stages; Blue line corresponds to FS=31 m, and red line denotes FS= 66 m.

ure 4.14b, one can see that by assuming uniform FS in accordance with SOLIMAN *et al.* (2010), the Fr. #2-2 tends to deviate toward the opposite fracture. In order to mitigate the stress shadowing effects on the Fr. #2-2, by conducting a number of simulation runs, the desired minimum FS of 141 m between the Frs. #1-2 and #1-3 is achieved such that both the Frs. #1-3 and #2-2 propagates in a straight path with maximum fracture length, as shown in Fig. 4.14c. Herein, note that the modification to MZF with non-uniform FS is called "M2ZF".

With the aim of enhancing the fracture complexity, achieving maximum fracture length and the straight propagation path, and mitigating fracturing operation time, besides MZF and M2ZF designs, two other completion designs are studied in this section. The first one denotes to Sim-HF in which, all perforations are fractured simultaneously. In the other scenario, named Seq-HF, all the perforations on the Well No. 1 are fractures simultaneously, followed by fracturing of the perforations on the Well No. 2. Noted that placement of the perforations on two wellbores in these designs is according to MZF design to reduce the rick of wellbore connection. Figures 4.15a and 4.15b exhibit the pore pressure contours of the formation for the case of Seq-HF design with FS=66 m after first and second stages, respectively. The results obtained demonstrate that all created fractures after the first stage show virtually straight propagation pathways. The outer fractures attain the same fracture length which is higher than that of the middle fracture (Fr. #1-2) due to the stress shadowing effect. In addition, the other fractures propagated from the opposite wellbore follow straight paths with considerably smaller length than those of opposite fractures. The pore pressure contour of the rock formation for the case of Sim-HF design with FS=66 m is shown in Figure 4.16. As depicted in this figure, the middle fracture on the Well No. 1 attains the smaller length than those of others. Comparing Figures 4.14b, 4.15b, and 4.16

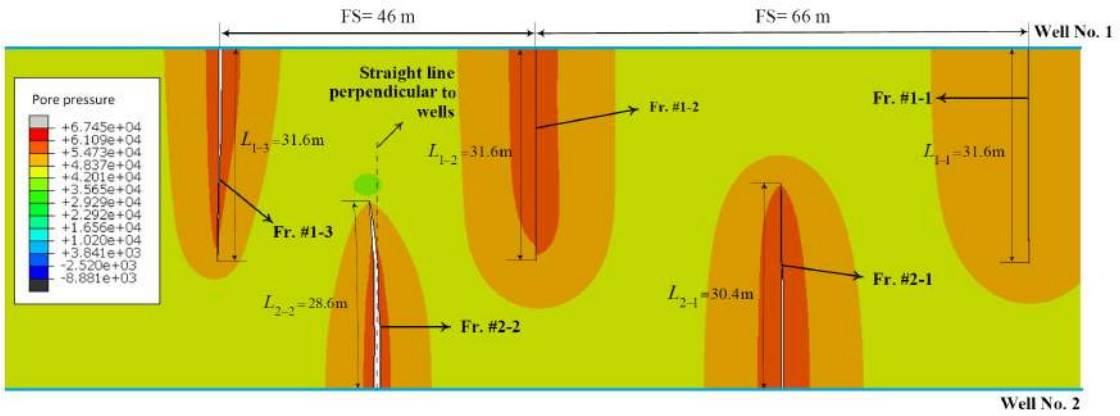

(a)

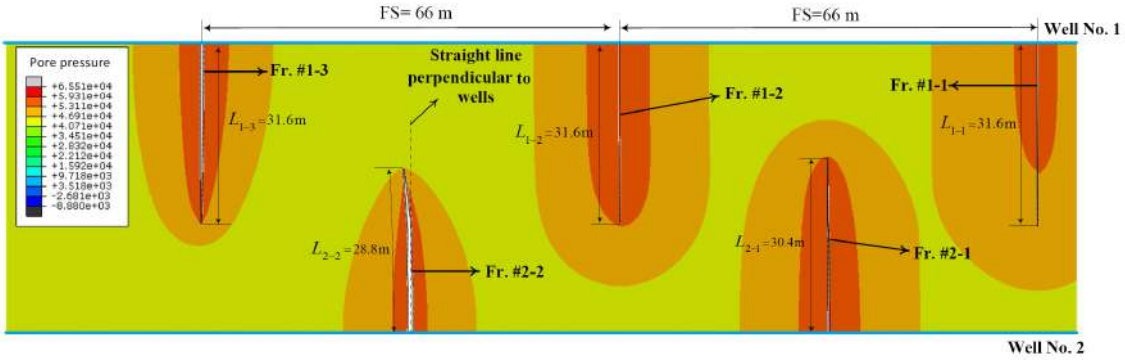

(b)

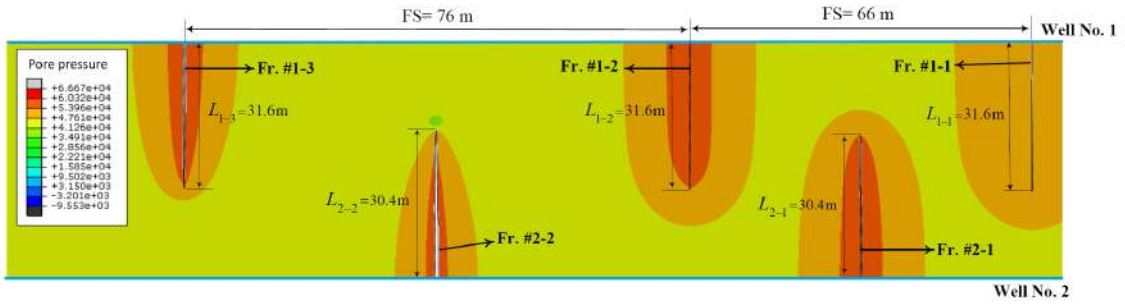

(c)

Figure 4.14: Pore pressure contours of the formation for the case of: **a)** M2ZF with FS of 46 m between Fr.#1-2 and Fr.#1-3, **b)** MZF with uniform FS, **c)** M2ZF with FS of 141 m between Fr.#1-2 and Fr.#1-3.

or in other words the MZF, Seq-HF, and Sim-HF designs reveals that the pore pressure of the rock formation substantially increases as a result of Sim-HF design. However, the MZF design yields notably higher fracture lengths than those of others, although the later fracture in this design deviates towards the opposite fracture. Furthermore, it is resulted that Sim-HF design is completed far more sooner than others, thereby mitigating fracturing operation time.

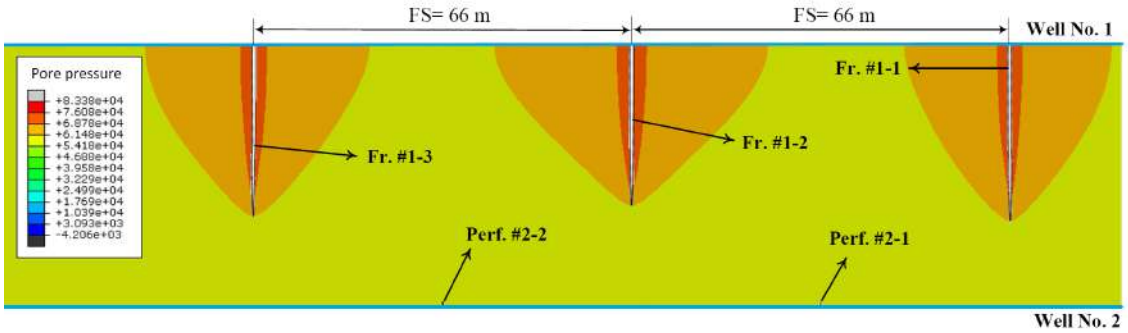

(a)

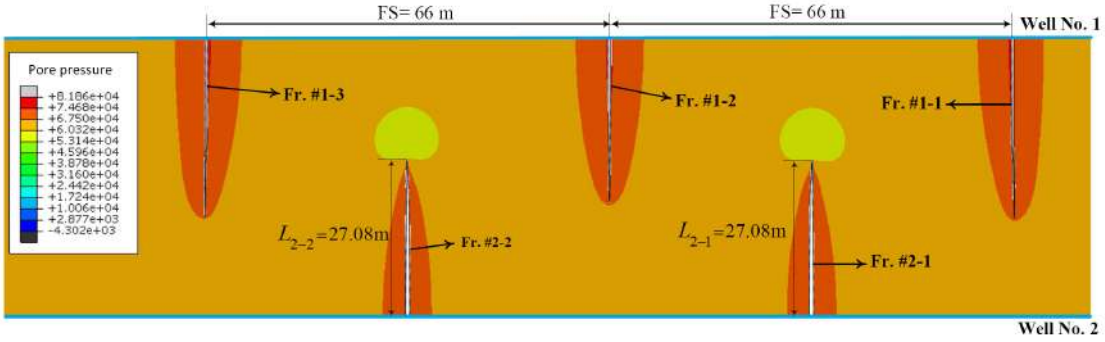

(b)

Figure 4.15: Pore pressure contours for the case of Seq-HF design: **a)** After first stage, **b)** After second stage.

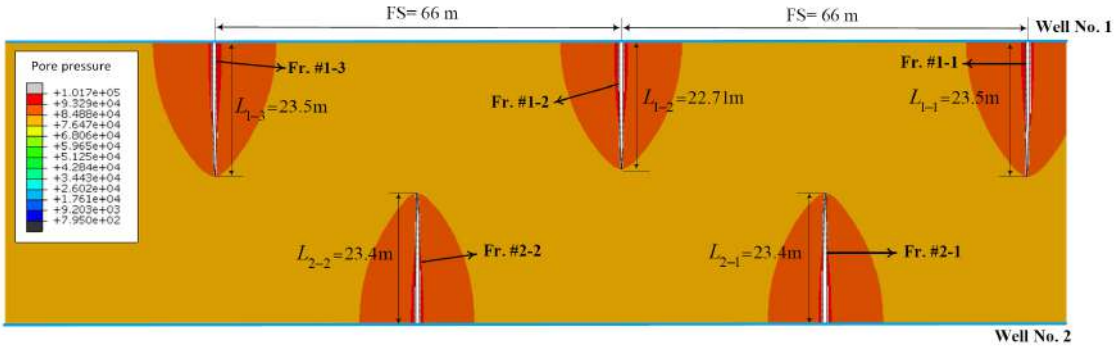

Figure 4.16: Pore pressure contours for the case of Sim-HF design.

4.6.2.2 Stress anisotropy

Figure 4.17 shows that the variation in the horizontal-stress contrast in the direction perpendicular to the first fracture for various completion designs including Sim-HF, Seq-HF, MZF, and M2ZF. Note that in all designs, except M2ZF, the FS between all fractures is set 66 m. In the case of M2ZF, the FS between Fr. #1-2 and Fr. #1-3 is 141 m, as shown in Figure 4.14c. It is concluded from Figure 4.17 that simultaneous fractures notably reduce the horizontal-stress contrast as a result of higher induced stress shadowing. Consequently, the fracture complexity is enhanced by opening the natural fractures and creating a network

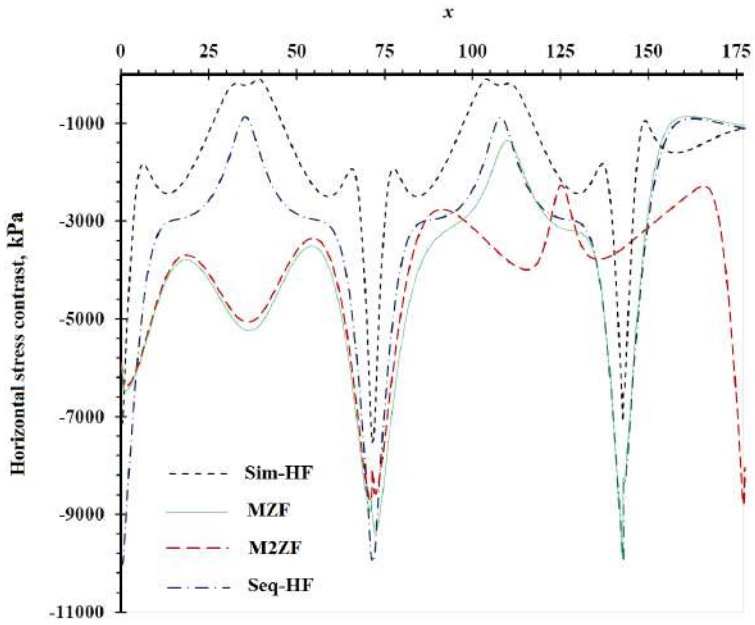

Figure 4.17: Compariosn of horizontal-stress contrast in the direction perpendicular to Fr. #1 for different completion designs.

of un-propped fractures (DAHI TALEGHANI *et al.*, 2013; SHARMA *et al.*, 2015).

The direction of maximum horizontal stress in the area between two horizontal wellbores in Sim-HF design is shown in Figure 4.18. In this figure, the FS between all fractures is set 30 m in order to investigate the effect of the reduction of the FS on the fracture propagation direction. Before starting the fracturing job, the direction of the in-situ maximum

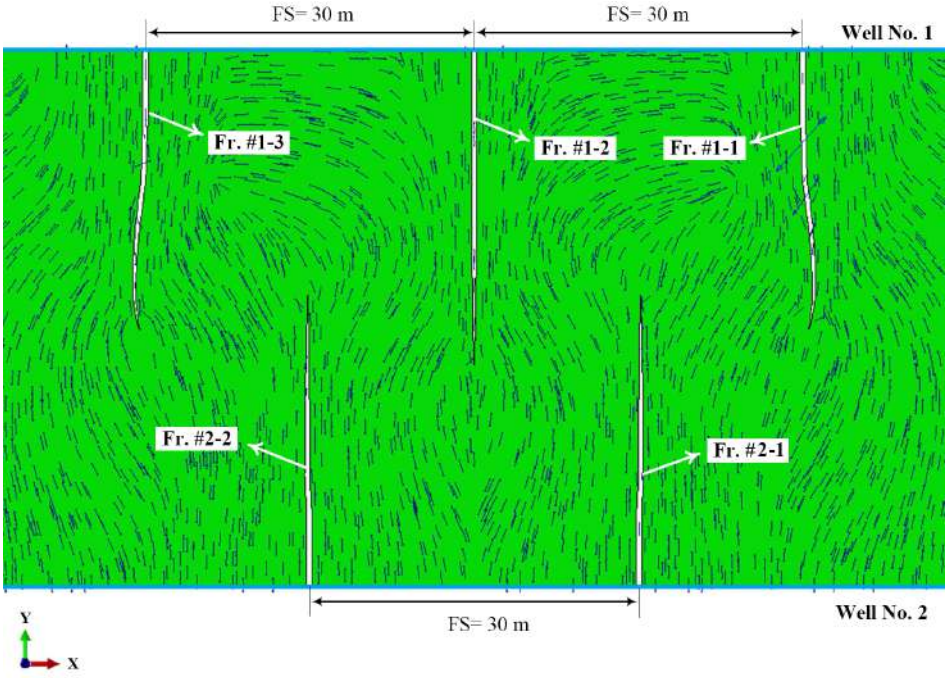

Figure 4.18: Direction of maximum horizontal stress in the area between two horizontal wellbores in Sim-HF design.

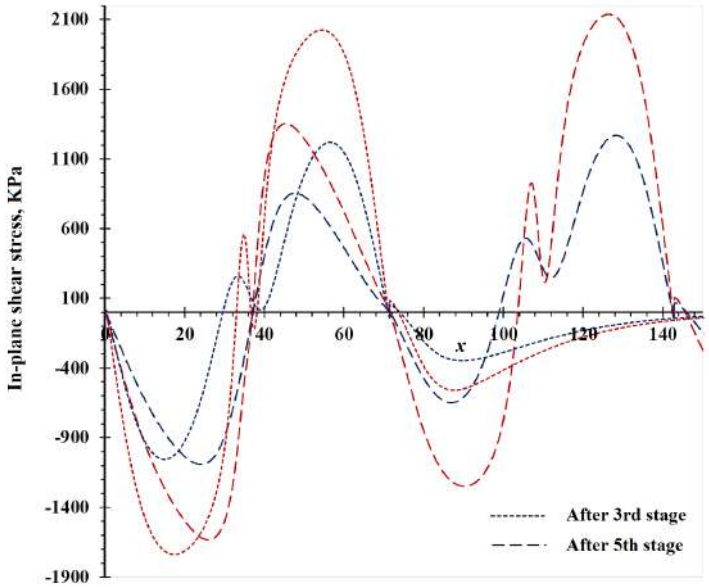

Figure 4.19: Illustration of variation in in-plane shear stress in the direction perpendicular to Fr. #1-1 for MZF with uniform FS, Blue line: $L^1 = 12\,\mathrm{m}$, Red line: $L^1 = 18\,\mathrm{m}$.

horizontal stress is along the *y*-direction. Nonetheless, as fractures propagate towards each other, the local horizontal stress around the fractures considerably changes. The Frs. #1-1 and #1-3 firstly deviate toward the left and right vertical boundaries, however, the middle fracture (Fr. #1-2) follows the straight crack path, resulting in the higher fracture length in comparison with those of sider ones. It is worthwhile noting that when the tips of Frs. #1-1 and #1-3 approach to the opposite ones growing from the Well No. 2, the fracture

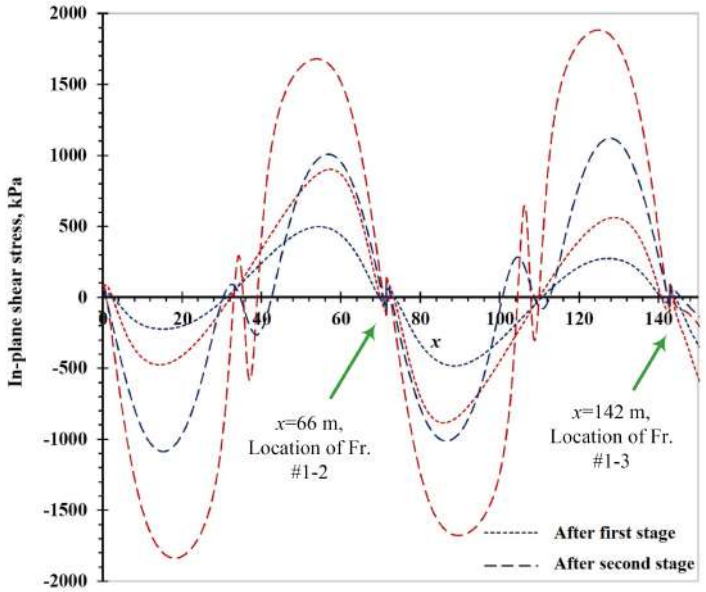

Figure 4.20: Variation in shear stress within the formation in the direction perpendicular to Fr. #1-1 for Seq-HF, Blue line: $L^1 = 12\,\mathrm{m}$, Red line: $L^1 = 18\,\mathrm{m}$.

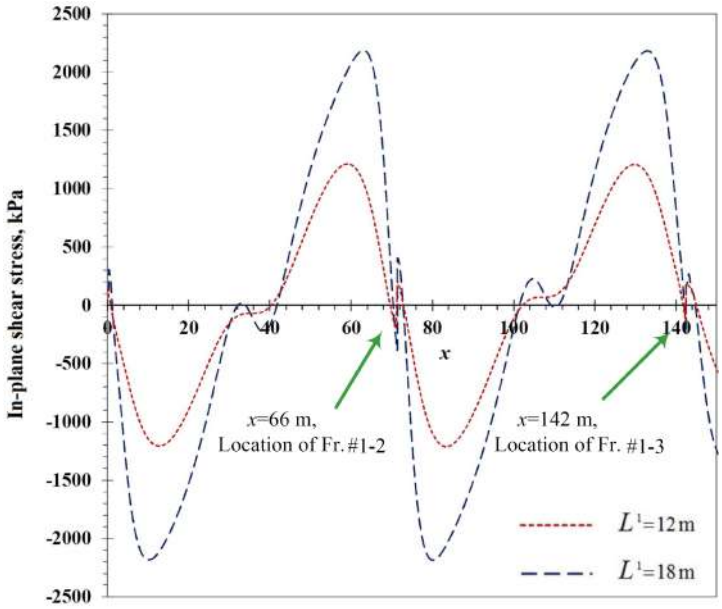

Figure 4.21: Variation in in-plane shear stress within the formation in the direction perpendicular to Fr. #1-1 for Sim-HF.

tips are re-oriented towards the tips of the Frs. #2-1 and #2-2.

4.6.2.3 In-plane shear stress

Now we turn our attention to investigating the variation of the in-plane shear stresses in the rock material by considering various completion designs. Figure 4.19 demonstrates the variation of the in-plane shear stress in the direction perpendicular to first fracture (Fr. #1-1) after the third and fifth stages. In this figure, L^1 refers to the distance from the Well No. 1. In Figure 4.19, the impact of the propagation of the Fr. #2-2 into the area between two pre-existing fractures (Fr. #1-2 and Fr. #1-3) on the shear stress for the MZF design with the FS of 66 m can be studied. As the Fr. #2-2 invades this area, not only it substantially alters the magnitude of shear stress, but does it also cause that far more of the reservoir is exposed to the alteration in the shear stress. Hence, this results in activating the planes of weaknesses and natural fractures.

Another point to notice is that the area near the fracture tip of the Fr. #2-2 experiences more alteration in the in-plane shear stress. As can be seen in Figure 4.19, the magnitude of shear stress between Fr. #1-1 and Fr. #1-2 reduced remarkably as the fracturing job proceeds to the next stage. Furthermore, as the fracturing job proceeds to the next stage, the magnitude of the shear stress between the Fr. #1-1 and the Fr. #1-2 reduces remarkably, leading to the closure of the un-propped fractures created in the reservoir owing to the stress shadowing. Hence, it can be inferred that the operation time between consecutive stages plays a crucial role in the production performance of the wellbores. The variation in the shear stress in the direction perpendicular to first fracture (Fr. #1-1) for Seq-HF and Sim-HF design are studied in Figures 4.20 and 4.21, respectively. Comparing

Figures 4.19, 4.20 and 4.21 results that the Sim-HF design has the higher capability to increase the value of the shear stress of the formation as a result of enhancing the stress interference between simultaneous fractures.

4.7 Conclusion

This chapter has devoted particular attention to the 2-D numerical modelling of HF from two lateral wellbores using several completion designs. Taking the stress shadowing effects into account, the CPNM, has been established to simulate the propagation of curving hydraulic fractures. In order to treat the filter cake as a pressure-dependent layer, Settari's fluid leak-off model was employed by means of a user-defined subroutine. A large number of numerical simulations using CPNM have been carried out to investigate several factors, such as the stress isotropy, the in-plane shear stresses, and the leak-off flow rate. Taking both effect and side effect of stress shadowing into account, it can be concluded from this chapter that MZF design should be revised in order not only to achieve much more fracture length and straight fracture paths but also to enhance more fracture complexity. For the sake of better elaboration of the findings, the results obtained have been categorized into two sections namely first cycle in MZF design and second cycle in MZF design.

In the case of first cycle in MZF design, the following conclusions can be made:

- The results has shown that the stress-altered zones, which have a crucial effect on the second stage on Well No. 1, are divided into attraction and repulsion zones. On the other hand, the area near Well No. 1, where the third fracture propagates, is partitioned into curving and unaltered zones.

- The simulation results show that as a third fracture from the offset wellbore propagates into the area between pre-existing fractures, not only does it considerably alter the magnitude of shear stresses, but it also causes far more of the reservoir to become exposed to some alteration in shear stress. Accordingly, this leads to activation of pre-existing planes of weakness and natural fractures in non-conventional reservoirs such as shale plays. This point also highlights the benefits of the MZF design in decreasing the magnitude of shear stresses through stress shadowing effects.

- The simulation results suggest that a new fracture growing into the altered-stress region has the capability to alter the local stresses and change the low-stress contrast region. In addition, the numerical results have revealed that the horizontal stress contrast significantly decreases in the area near the fracture tip when the fracture spacing is reduced, while overall horizontal stress contrast between fractures is considerably lower for the cases with larger fracture spacing. It has been also shown

that the leak-off flow rate increases substantially as the hydraulic fracturing process in the MZF design proceeds to its later stages.

As far as the second cycle in MZF design is concerned, subsequent conclusions can be drawn:

- Based on the achieved results in MZF design, the altered stress area demonstrates peculiar alteration after creating the third fracture. The FS between the third and fourth fractures considerably reduces in such a way that the fourth fracture can propagate through the straight path, however, the fifth fracture on the opposite wellbore deviates towards the previous fracture owing to stress shadow effects, leading to increase the risk of opposite wellbores communications. As a result, the FS between the first and fourth fractures increases nearly to a value more than that of the FS between the first and second fractures so as to maintain the straight path of the fifth fracture, resulting in introducing M2ZF design.
- The simulation results showed that both MZF and M2ZF designs attain greater value of the fracture length compared with Seq-HF and Sim-HF designs.
- It has been concluded that the operation time between consecutive stages in MZF design plays a crucial role in the production performance of the wellbores.
- The numerical results have revealed that the Sim-HF design has the higher capability to increase the value of shear stress of the formation as a result of enhancing the stress interference between the fractures. In addition, simultaneous fractures notably reduce the horizontal-stress contrast due to the higher induced stress shadowing. However, greater stress shodawing effect in Sim-HF design, less fracture length and more deviated fractures.

Chapter 5

Conclusions and recommendations for future research

5.1 Overview

The present dissertation has elaborated on the development of generic numerical modelling technique in order to simulate non-planar multi-stage hydraulic fractures in low-permeable shale reservoirs. Particular attention has been given to contemplate the stress shadowing effect in various completion designs. The individual objectives of the study are summarised as follows:

- Developing a 3-D FE model, which takes into account the propagation of the multiple fractures in an individual horizontal well based on CPNM. Two different well-known scenarios in the industry, i.e. sequentially and simultaneously multiple HF, in a quasi-brittle multi-layer shale have been studied.

- Developing a 2-D FE model for simulating multi-stage HF from two adjacent lateral horizontal wellbores, which was aimed not only to comprehensively investigate the available completion designs on horizontal multi-lateral wellbores, but also to enhanced the current MZF by considering stress shadowing effect. Alteration in shear stress near the fracture tips, which is imperative phenomenon in the micro-seismic monitoring (BENNETT *et al.*, 2005; SOLIMAN *et al.*, 2010), has been investigated in detail in various HF designs.

5.2 Methodology used in this work

In this research, in order to capture the propagation of multiple the hydraulic fractures in a porous medium, the CPNM was employed, which was implemented into a FEA package (ABAQUS®) along with user-defined subroutines. To this end, extra phantom nodes with pore pressure degrees of freedom were added on the edges of each enriched element to construct the model of fracturing fluid flow across the cracked element surfaces in combination with the phantom nodes which were overlain on the original real nodes. The activation of phantom node on each element edge was not performed unless it was intersected by a crack. After damage initiation, each phantom node and its corresponding real node, including displacement and pore pressure degrees of freedom, were no longer tied together. In order to capture the crack geometry, two signed distance functions per node were needed. The first represents the crack surface, whereas the second is employed to establish an orthogonal crack surface so that the intersection of the two surfaces gives the crack tip.

On the other hand, the ECCM has been used to model the damage initiation and propagation, formulated by specific traction-separation laws. Based on the ECCM, it was presupposed that the near tip FPZ was aggregated into the crack line, in contrast to the LEFM in which the FPZ was regarded to take place at the crack tip. The leading assumption

was the constitution of the FPZ, where the material, although damaged, was still able to transmit stresses normal to the fracture. Considering ECCM in HF problem has brought the following merits. Firstly, the ECCM effectively prevented the stress singularity at the crack tip region, which remarkably imposed challenges on numerical modelling based on LEFM. In addition, the location of the crack tip in ECCM was not an input parameter but a natural, direct consequence of the solution, which rose the computation efficiency. What is more, the ECCM has taken the advantage of the promising capability of modelling micro-structural damage mechanisms inherent in quasi-brittle materials such as initiation of micro cracking, coalescence, and propagation.

In addition, the infiltration of the normal flow of the fracturing fluid into the surrounding medium was modeled with making use of pressure-dependent leak-off model given by SETTARI *et al.* (1984) by using a user-defined subroutine. It is imperative to note that the leak-off fluid is considered as Newtonian. This implies that no polymer leaks off into the surrounding formation. It is worth noting that this study was a fully coupled pore-pressure/stress analysis, which has considered the pore pressure of the formation, as opposed to most available literature (DAHI-TALEGHANI *et al.*, 2011; SETTARI *et al.*, 1984; WU *et al.*, 2012), which has not considered the rock formation as a porous medium.

In order to verify the numerical simulation, the results obtained for an individual hydraulic fracture are compared with the KGD analytical model. The numerical results obtained by CPNM for CMP, fracture aperture profile, and CMOD have been compared with analytical solution, representing excellent agreement between the results of present method and those obtained by KGD model. Additionally, considering the stress shadowing effect in multiple fracture propagation, the verification of present numerical technique against the DDM (SESETTY *et al.*, 2015) has been performed. In the work of SESETTY *et al.* (2015), the model was based on 2-D plane strain and used the DDM to calculate fracture deformation and propagation. what is more, no fluid leak-off into the formation was considered and the fracture propagation direction relied on the maximum principal tensile stress criterion. The fracture geometries of the first stage and the second stage created along the horizontal wellbore by using the DDM and CPNM have been compared. The comparison demonstrated a good agreement between fracture geometries obtained by the DDM and those by CPNM.

On one hand, in the common approach in the MZF design used in the industry, the FS between all fractures is the same. However, by minimizing the FS to enhance the fracture complexity area between induced fractures, the FS demands to be revised in order to achieve longer and straight fracture path. On the other hand, the creation of initial fractures has the significant impact on the subsequent stages as result of induced stress interference area, particularly in the case of closely spaced hydraulic fractures. Nevertheless, few works in the available literature (MANCHANDA, 2015; ROUSSEL *et al.*, 2011) have concentrated on the propagation of next fractures after terminating the first fractur-

ing stage. Accordingly, motivated by the technique proposed by PEIRCE (2015a); WU *et al.* (2016), in this dissertation the stress shadowing effects have been managed through non-uniform FS, introducing a modification to MZF design, named M2ZF.

5.3 Main conclusions

The significant findings of the work presented in this dissertation can be summarized into subsequent rudimentary categories as follows:

5.3.1 3-D modelling of multi-stage hydraulic fracture propagation

In the 3-D model, three domains have been contemplated for the problem, viz. barrier layers on the top and bottom of the model and a pay zone in the middle. As opposed to FEM incorporated with cohesive layers, the proposed CPNM has demonstrated its capability and efficiency to simulate the initiation and propagation of multiple crack along arbitrary, solution-dependent paths, providing a more realistic way for the study of multi-stage HF with the presence of stress shadowing impacts. With regard to simulating the Seq-HF, after pumping stage in the first perforation, another transient analysis was conducted for this peroration to simulate the crack closure. Detailed parametric studies shed new light on the impacts of pre-existing or simultaneous fluid-driven fractures on the pore pressure of the formation, crack propagation pattern, von Mises stresses, fracture opening, leak-off flow rate, and fracturing fluid pressure. From this work, the following conclusions can be drawn:

- Numerical results show the later stages in Seq-HF mainly secure larger values of fracture opening than that of Sim-HF, which can be attributed to the effect of stress interactions of fractures on each other. This trend has been also observed for the fracturing fluid pressure and leak-off flow rate into the formation.

- It has been concluded from the results that left and right fractures tended more to propagate through the vertical direction while much attention of the fluid injection in the middle fracture was drawn to crack growth through the *x*-*y* plane.

- It can be noted that due to stress interference caused by the middle fracture, crack paths of the left and right fractures were deviated toward the left and right boundaries. However, the middle fracture followed the straight crack path, leading to greater fracture length in comparison with that of sider ones.

- In the simultaneously triple-stage fracturing scenario, the fracture opening demonstrated special attitude in such a way that at the first 200-second injection period all fractures presented a similar aperture, however, at the second 200-second period,

an obvious discrepancy between the fracture openings appeared. It was because at the second period, much more amount of the fluid injected was allocated to the zone near the injection spots in side fractures, leading to greater fluid pressure and fracture opening at injection spots in side fractures than that of middle fracture.

5.3.2 Closely spaced hydraulic Fracturing from two horizontal wellbores

In order to investigate various completion designs with several fracturing stages from two adjacent horizontal wellbores, a 2-D computational FE domain has been developed. A comprehensive study has been presented for closely spaced fractures to enhance the complexity of the fracture network in the area between two adjacent horizontal wellbores. A large number of numerical simulations using CPNM have been carried out to investigate several factors, including the stress isotropy, the in-plane shear stresses, and the leak-off flow rate. Taking both effect and side effect of stress shadowing into consideration, it can be concluded from the results obtained that MZF design should be revised in order not only to achieve much more fracture length and straight fracture paths but also to enhance more fracture complexity. For the sake of better elaboration of the findings, the results obtained have been categorized into two sections namely first cycle in MZF design and second cycle in MZF design.

5.3.2.1 First cycle in MZF design

Concentrated on MZF design, the main contributions of this part was investigating in detail the effects of the stress shadowing as a function of the FS on the horizontal stress contrast, direction of maximum local stress, leak-off flow rate, in-plane shear stress, and pore pressure of the formation.

On one hand, the results suggest that the stress-altered zones, which have an crucial effect on the second stage on the Well. No. 1, are divided into attraction and repulsion zones. On the other hand, the area near the Well. No. 1, where the third fracture propagates, is partitioned into curving and unaltered zones.

The simulation results show that as the third fracture from the offset wellbore propagates into the area between pre-existing fractures, not only does it considerably alter the magnitude of shear stresses, but it also causes far more of the reservoir to become exposed to some alteration in shear stress. Accordingly, this leads to activation of pre-existing planes of weakness and natural fractures in non-conventional reservoirs such as shale plays. This point also highlights the advantage of the MZF design in decreasing the magnitude of shear stresses through stress shadowing effects.

It has been concluded from the results obtained that a new fracture growing into the altered-stress region has the capability to alter the local stresses and change the low-stress

contrast region. In addition, the numerical results have revealed that the horizontal stress contrast significantly decreases in the area near the fracture tip when the fracture spacing is reduced, while overall horizontal stress contrast between fractures is considerably lower for the cases with larger fracture spacing. It has been also shown that the leak-off flow rate increases substantially as the hydraulic fracturing process in the MZF design proceeds to its later stages.

5.3.2.2 Second cycle in MZF design

This study has been conducted to contribute to the existing body of knowledge, in particular with regard to the simulation of stress shadowing effects in the various fracturing designs in adjacent lateral wells including Sim-HF, Seq-HF, MZF, and M2ZF. By conducting a number of simulation runs, the essential endeavour was made to determine the minimum FS in MZF to enhance the fracture complexity. From this work, the following conclusions can be made:

- Based on the achieved results in MZF design, the altered stress area demonstrates peculiar alteration after creating the third fracture. The FS between the third and fourth fractures considerably reduces in such a way that the fourth fracture can propagate through the straight path, however, the fifth fracture on the opposite wellbore deviates towards the previous fracture owing to stress shadowing effects, leading to increase the risk of opposite wellbores communications. As a result, the FS between the first and fourth fractures increases nearly to a value more than that of the FS between the first and second fractures so as to maintain the straight path of the fifth fracture, resulting in introducing M2ZF design.
- The simulation results showed that both MZF and M2ZF designs attain greater value of the fracture length compared with Seq-HF and Sim-HF designs.
- Tt has been concluded that the operation time between consecutive stages in MZF design plays a crucial role in the production performance of the wellbores.
- The numerical results have revealed that the Sim-HF design has the higher capability to increase the value of shear stress of the formation as a result of enhancing the stress interference between the fractures. In addition, simultaneous fractures notably reduce the horizontal-stress contrast due to the higher induced stress shadowing.

5.4 Recommendations for future research

The work presented in the present dissertation opens new opportunities for further research. As a direct result of this study the following suggestions can be made:

- As indicated in Section 4.2, the large volumes of tight sand and shale reservoirs are naturally fractured, such as Barnett shale (DAHI TALEGHANI *et al.*, 2013; GALE *et al.*, 2007). In those reservoirs, the interaction of hydraulic fractures with NFs can result in branching and offset at the natural fractures and, as a result, lead to the complex fracture network. The creation of the hydraulic fracture network and interaction between induced fractures and pre-existing NFs are involved with many technical challenges. In recent years, considerable progress has been made in the development of complex fracture models to deal with the demands for more effective design tools for the unconventional reservoirs compared with the conventional planar fracture models. Nevertheless, some aspects of complex fracture network are still not entirely understood with respect to their effect on the fracture geometry, or the complexity of simulating them is still beyond the current simulation capabilities. Hence, these models will carry on to evolve in the next years.

  In this perspective, the interaction between HFs and NFs plays a critical role in creating fracture complexity during HF job in the naturally fractured reservoirs. Apart from recent numerical techniques including DDM (ZENG and YAO, 2016; ZHANG and JEFFREY, 2014), DEM (DAMJANAC *et al.*, 2010; ZOU *et al.*, 2016), FEM (GONZALEZ-CHAVEZ *et al.*, 2015; HADDAD *et al.*, 2016), the XFEM (DAHI-TALEGHANI *et al.*, 2011; KHOEI *et al.*, 2015) has been employed to study the interactions of the HFs and NFs. Nonetheless, in the Ref. (KHOEI *et al.*, 2015), the cross/arrest behavior between the HF and frictional NF was not taken into account; the fracture propagation behaviour after the two fractures merge has not been studied. In the work of DAHI-TALEGHANI *et al.* (2011), just the L-shaped fracture formed by the intersection between a HF and a cemented NF was investigated; no frictional slip along NF and no T-shaped fracture were taken into account. Indeed, both the frictional and cemented NFs exist in shale simultaneously. Owing to the different mechanical properties of the NF, the processes of the interactions between the HFs and the two types of NFs are significantly different. Possible scenarios of HF interaction with NF, which can result in fracture branching and complexity, have been discussed by WENG (2015). Accordingly, the future extension of this dissertation can be a development of the CPNM in order to establish a HF model considering the frictional and cemented NFs. Furthermore, various effects of the two types of NFs on the propagation of HFs and complex fracture network generated can be studied. In addition, much more sophisticated approach such as peridynamics, introduced in Section 2.9.3, can be employed to simulate fracture turning, kinking or branching.

- Conventional HF simulators, which are commonly based on poro-elasticity, underestimate the down-hole pressures observed in field operations. VAN DAM *et al.*

(1997) presented that net-pressures (discrepancy between fracturing pressure and far-field in-situ stress) are 50 percent to 100 percent higher than the net-pressures proposed by HF simulators. To remedy the observed high net pressures, PAPANASTASIOU (1999) carried out an elasto-plastic analysis to evaluate the consequence of inelastic rock characteristic, specially the effect of dilation on the fracture tip behavior. They concluded that higher net pressure is required to propagate an elasto-plastic fracture than that of an elastic fracture of the same length or the same pumping time. A poro-elastic model with effective toughness using Abaqus in order to predict fracture propagation in brittle and ductile rocks was developed by YAO (2012). The fundamental concept of employing effective toughness was to adapt the poro-elastic model by aggregating all plastic-deformation effects into the fracture toughness increased ahead of the fracture tip. Nevertheless, the idea of effective fracture toughness is only able to moderately deal with increased fracture toughness in the area very close to fracture tip (WANG, 2016b). Thus, it collapses when it comes to include plastic deformation influences, in particular when is not constrained to the adjacent area of the fracture tip.

On the other hand, most available studies (GONZALEZ-CHAVEZ *et al.*, 2015; KUMAR and GHASSEMI, 2016b; TAHERI-SHAKIB *et al.*, 2016) ignore the fact that the poorly consolidated/unconsolidated sands and also many shales, such as the Haynesville shales and the Eagle Ford, can undergo plastic deformations. Consequently, just use of the cohesive zone method, which only takes inelastic behavior ahead of the fracture tip into account, is not satisfactory to capture overall impacts of plastic damage within the whole area affected.

By considering aforementioned points, the future works can be regarding the impact of the plastic behavior of formation on the fracturing fluid pressure and other involving parameters. To this end, the results obtained can be compared with existing elastic models and effective fracture toughness method (YAO, 2012). In addition, Mohr-Coulomb and extended Drucker-Prager plasticity models (ANANDARAJAH, 2011; LEWIS and SCHREFLER, 1998) shall be exploited into the model. In this way, it is desired to seek for the circumstances, such as a specific range of in-situ stress contrast, which control the effect of formation plasticity.

- The other extension of the present work is developing a 3-D FE model, which takes into account the propagation of the multiple fractures from multi-lateral horizontal wellbores based on the CPNM. To approach more realistic geological conditions, a multiple-layer model including a target formation and upper and lower formations are developed and three in-situ stresses are varied as a function of the depth, which are implemented into the model by virtue of user-defined subroutines. This situation may have an appreciable effect on the fracture profiles, fracture aperture, void ratio

distribution, and fracturing fluid pressure, thereby motivating further investigation.

- The CPNM developed in this work for the numerical modelling of hydraulic fracture propagation by using the FEA package ABAQUS® has the substantial potential to be employed in other fracture mechanics problems, particularly in modelling of the fracture propagation in steel pipelines transporting CO_2.

  The CCS is one of the technologies that has been proposed to reduce emissions of CO_2 to the atmosphere from fossil fuel power stations. To achieve this scenario, CO_2 must be transported from the points of capture to the storage sites. A large fraction of the captured CO_2 is likely to be transported in pipeline networks. The CO_2 pipelines shall be more susceptible to long running-ductile fractures than e.g. natural-gas pipelines (MAHGEREFTEH *et al.*, 2012). Accordingly, fracture propagation control plays a crucial role that demands careful consideration in the design and operation of CO_2 pipelines. A coupled fluid-structure model for the prediction of running-ductile fracture in CO_2-transport pipelines has been presented by AURSAND *et al.* (2013, 2016). The coupled fluid-structure problem was modelled using the structure models of implemented in the LS-DYNA code (HALLQUIST *et al.*, 2007), and the thermo and fluid dynamics models implemented in an in-house code.

  As a further extension of the present numerical technique employed in this dissertation, a fracture-fluid-pipe model can be developed in the ABAQUS® software to simulate scenarios of pipeline failure involving fracture propagation. To this end, the CPNM is employed to model dynamic fracture propagation in the pipeline steel, in which the dynamic SIF and crack velocity are determined ahead of the crack tip at each step of the crack growth. The suggested model couples the fluid dynamics of the escaping fluid from the pipe and the fracture mechanics of the deforming pipe subjected to internal and back-fill pressures.

Bibliography

ADACHI, J., SIEBRITS, E., PEIRCE, A., et al., 2007, "Computer simulation of hydraulic fractures", *International Journal of Rock Mechanics and Mining Sciences*, v. 44, n. 5, pp. 739–757.

ADACHI, J. I., 2001, "Fluid-driven fracture in permeable rock", *University of Minnesota, Minneapolis*.

AHMED, U., MEEHAN, D., 2016, *Unconventional oil and gas resources: exploitation and development*. CRC Press.

ALFANO, G., CRISFIELD, M., 2001, "Finite element interface models for the delamination analysis of laminated composites: mechanical and computational issues", *International journal for numerical methods in engineering*, v. 50, n. 7, pp. 1701–1736.

ALLIX, O., LADEVÈZE, P., 1992, "Interlaminar interface modelling for the prediction of delamination", *Composite structures*, v. 22, n. 4, pp. 235–242.

ANANDARAJAH, A., 2011, *Computational methods in elasticity and plasticity: solids and porous media*. Springer Science & Business Media.

ANDERSON, T., ANDERSON, T., 2005, *Fracture mechanics: fundamentals and applications*. CRC press.

AREIAS, P., BELYTSCHKO, T., 2005, "Analysis of three-dimensional crack initiation and propagation using the extended finite element method", *International Journal for Numerical Methods in Engineering*, v. 63, n. 5, pp. 760–788.

ATKINSON, B. K., 2015, *Fracture mechanics of rock*. Elsevier.

ATKINSON, B., 1987, "Introduction to fracture mechanics and its geophysical applications", *Fracture mechanics of rock*, pp. 1–26.

AURSAND, E., AURSAND, P., BERSTAD, T., et al., 2013, "CO 2 pipeline integrity: A coupled fluid-structure model using a reference equation of state for CO 2", *Energy Procedia*, v. 37, pp. 3113–3122.

AURSAND, E., DUMOULIN, S., HAMMER, M., et al., 2016, "Fracture propagation control in CO 2 pipelines: Validation of a coupled fluid–structure model", *Engineering Structures*, v. 123, pp. 192–212.

AZADI, H., KHOEI, A., 2011, "Numerical simulation of multiple crack growth in brittle materials with adaptive remeshing", *International journal for numerical methods in engineering*, v. 85, n. 8, pp. 1017–1048.

BABUŠKA, I., MELENK, J., 1997, "The partition of unity method", *International journal for numerical methods in engineering*, v. 40, n. 4, pp. 727–758.

BARENBLATT, G., 1962, "The mathematical theory of equilibrium cracks in brittle fracture", *Advances in applied mechanics*, v. 7, pp. 55–129.

BARRY, N., RAGHU, N., GEXIN, S., 1992, *Rock fracture mechanics principles design and applications*. ELSEVIER, Amsterdam-London-New York-Tokyo.

BATHE, K.-J., 2006, *Finite element procedures*. Klaus-Jurgen Bathe.

BAZANT, Z., PLANAS, J., 1997, *Fracture and size effect in concrete and other quasibrittle materials*, v. 16. CRC press.

BELYTSCHKO, T., BLACK, T., 1999, "Elastic crack growth in finite elements with minimal remeshing", *International journal for numerical methods in engineering*, v. 45, n. 5, pp. 601–620.

BELYTSCHKO, T., ONG, J., L, W., et al., 1984, "Hourglass control in linear and nonlinear problems", *Computer Methods in Applied Mechanics and Engineering*, v. 43, n. 3, pp. 251–276.

BELYTSCHKO, T., FISH, J., ENGELMANN, B., 1988, "A finite element with embedded localization zones", *Computer methods in applied mechanics and engineering*, v. 70, n. 1, pp. 59–89.

BELYTSCHKO, T., GRACIE, R., VENTURA, G., 2009, "A review of extended/generalized finite element methods for material modeling", *Modelling and Simulation in Materials Science and Engineering*, v. 17, n. 4, pp. 043001.

BENNETT, L., CALVEZ, J., SARVER, D. R., et al., 2005, "The source for hydraulic fracture characterization", *Oilfield Review*, v. 17, n. 4, pp. 42–57.

BENZEGGAGH, M., KENANE, M., 1996, "Measurement of mixed-mode delamination fracture toughness of unidirectional glass/epoxy composites with mixed-mode bending apparatus", *Composites science and technology*, v. 56, n. 4, pp. 439–449.

BERUMEN, S., TIAB, D., RODRIGUEZ, F., 2000, "Constant rate solutions for a fractured well with an asymmetric fracture", *Journal of Petroleum Science and Engineering*, v. 25, n. 1, pp. 49–58.

BIOT, M., 1941, "General theory of three-dimensional consolidation", *Journal of applied physics*, v. 12, n. 2, pp. 155–164.

BIOT, M., 1962, "Mechanics of deformation and acoustic propagation in porous media", *Journal of applied physics*, v. 33, n. 4, pp. 1482–1498.

BOBET, A., EINSTEIN, H., 1998, "Fracture coalescence in rock-type materials under uniaxial and biaxial compression", *International Journal of Rock Mechanics and Mining Sciences*, v. 35, n. 7, pp. 863–888.

BOYER, C., CLARK, B., JOCHEN, V., et al., 2011, "Shale gas: a global resource", *Oilfield review*, v. 23, n. 3, pp. 28–39.

BRADLEY, W., 1979, "Failure of inclined boreholes", *Journal of Energy Resources Technology*, v. 101, n. 4, pp. 232–239.

BREBBIA, C., DOMINGUEZ, J., 1977, "Boundary element methods for potential problems", *Applied Mathematical Modelling*, v. 1, n. 7, pp. 372–378.

BREBBIA, C. A., TELLES, J. C. F., WROBEL, L. C., 2012, *Boundary element techniques: theory and applications in engineering*. Springer Science & Business Media.

BROBERG, K., 1999, *Cracks and fracture*. Academic Press.

BUNGER, A. P., DETOURNAY, E., GARAGASH, D. I., 2005, "Toughness-dominated hydraulic fracture with leak-off", *International journal of fracture*, v. 134, n. 2, pp. 175–190.

BUNGER, A., JEFFREY, R., KEAR, J., et al., 2011, "Experimental investigation of the interaction among closely spaced hydraulic fractures". In: *45th US Rock Mechanics/Geomechanics Symposium*. American Rock Mechanics Association.

BUNGER, A., ZHANG, X., JEFFREY, R., et al., 2012, "Parameters affecting the interaction among closely spaced hydraulic fractures", *SPE Journal*, v. 17, n. 01, pp. 292–306.

CAMACHO, G. T., ORTIZ, M., 1996, "Computational modelling of impact damage in brittle materials", *International Journal of solids and structures*, v. 33, n. 20, pp. 2899–2938.

CARPINTERI, A., 2012, *Nonlinear crack models for nonmetallic materials*, v. 71. Springer Science & Business Media.

CARTER, R., 1957, "Derivation of the general equation for estimating the extent of the fractured area", *Appendix I of ŞOptimum Fluid Characteristics for Fracture Extension,Ť Drilling and Production Practice, GC Howard and CR Fast, New York, New York, USA, American Petroleum Institute*, pp. 261–269.

CHARLEZ, P., 1997, *Rock mechanics: petroleum applications*, v. 2. Editions Technip.

CHEN, Z., 2012, "Finite element modelling of viscosity-dominated hydraulic fractures", *Journal of Petroleum Science and Engineering*, v. 88, pp. 136–144.

CHEN, Z., OTHERS, 2013, "An ABAQUS implementation of the XFEM for hydraulic fracture problems". In: *ISRM International Conference for Effective and Sustainable Hydraulic Fracturing*. International Society for Rock Mechanics.

CIPOLLA, C. L., WARPINSKI, N., MAYERHOFER, M., et al., 2008, "The relationship between fracture complexity, reservoir properties, and fracture treatment design". In: *SPE Annual Technical Conference and Exhibition*. Society of Petroleum Engineers.

CIPOLLA, C., LOLON, E., MAYERHOFER, M., et al., 2009, "Fracture design considerations in horizontal wells drilled in unconventional gas reservoirs". In: *SPE Hydraulic Fracturing Technology Conference*. Society of Petroleum Engineers.

COMI, C., MARIANI, S., 2007, "Extended finite element simulation of quasi-brittle fracture in functionally graded materials", *Computer Methods in Applied Mechanics and Engineering*, v. 196, n. 41, pp. 4013–4026.

COPE, R., RAO, P., CLARK, L., et al., 1980, "Modelling of reinforced concrete behaviour for finite element analysis of bridge slabs", *Numerical Methods for Nonlinear Problems, Pineridge Press, Swansea*, v. 1980, pp. 457–470.

COX, B., MARSHALL, D., 1991, "The determination of crack bridging forces", *International Journal of Fracture*, v. 49, n. 3, pp. 159–176.

CRUSE, T. A., RIZZO, F. J., 1968, "A direct formulation and numerical solution of the general transient elastodynamic problem. I", *Journal of Mathematical Analysis and Applications*, v. 22, n. 1, pp. 244–259.

CUNDALL, P. A., HART, R. D., 1992, "Numerical modelling of discontinua", *Engineering computations*, v. 9, n. 2, pp. 101–113.

DAHI-TALEGHANI, A., OLSON, J. E., OTHERS, 2011, "Numerical modeling of multistranded-hydraulic-fracture propagation: Accounting for the interaction between induced and natural fractures", *SPE journal*, v. 16, n. 03, pp. 575–581.

DAHI TALEGHANI, A., AHMADI, M., OLSON, J., et al., 2013, "Secondary Fractures and Their Potential Impacts on Hydraulic Fractures Efficiency". In: *ISRM International Conference for Effective and Sustainable Hydraulic Fracturing*. International Society for Rock Mechanics.

DAMJANAC, B., GIL, I., PIERCE, M., et al., 2010, "A new approach to hydraulic fracturing modeling in naturally fractured reservoirs". In: *44th US Rock Mechanics Symposium and 5th US-Canada Rock Mechanics Symposium*. American Rock Mechanics Association.

DANESHY, A., OTHERS, 2011, "Hydraulic fracturing of horizontal wells: Issues and insights". In: *SPE Hydraulic Fracturing Technology Conference*. Society of Petroleum Engineers.

DAS, B. M., 2013, *Advanced soil mechanics*. CRC Press.

DAUX, C., MOËS, N., DOLBOW, J., et al., 2000, "Arbitrary branched and intersecting cracks with the extended finite element method", *International Journal for Numerical Methods in Engineering*, v. 48, n. 12, pp. 1741–1760. ISSN: 1097-0207.

DÁVILA, C., CAMANHO, P., DE MOURA, M., 2001, "Mixed-mode decohesion elements for analyses of progressive delamination". In: *Proceedings of the 42nd AIAA/ASME/ASCE/AHS/ASC structures. Structural dynamics and materials conference, Seattle, Washington*, pp. 16–19.

DEILY, F., OWENS, T., OTHERS, 1969, "Stress around a wellbore". In: *Fall Meeting of the Society of Petroleum Engineers of AIME*. Society of Petroleum Engineers.

DETOURNAY, E., CHENG, A.-D., 1988, "Poroelastic response of a borehole in a non-hydrostatic stress field". In: *International Journal of Rock Mechanics and Mining Sciences & Geomechanics Abstracts*, v. 25, pp. 171–182. Elsevier.

DOLBOW, J., MOËS, N., BELYTSCHKO, T., 2001, "An extended finite element method for modeling crack growth with frictional contact", *Computer methods in applied Mechanics and engineering*, v. 190, n. 51, pp. 6825–6846.

DUGDALE, D., 1960, "Yielding of steel sheets containing slits", *Journal of the Mechanics and Physics of Solids*, v. 8, n. 2, pp. 100–104.

ECONOMIDES, M. J., NOLTE, K. G., OTHERS, 2000, *Reservoir stimulation*, v. 18. Wiley New York.

ELGUEDJ, T., GRAVOUIL, A., COMBESCURE, A., 2006, "Appropriate extended functions for X-FEM simulation of plastic fracture mechanics", *Computer Methods in Applied Mechanics and Engineering*, v. 195, n. 7, pp. 501–515.

ENGELDER, T., 1987, "Joints and shear fractures in rock", *Fracture mechanics of rock*, pp. 27–69.

ESHELBY, J., 1974, "The Calculation of energy release rates. In: Sih GC, Van Elst HC, Broek D. (eds)", *Prospects of Fracture Mechanics, Noordhoff International*, pp. 69–84.

GALE, J. F., REED, R. M., HOLDER, J., 2007, "Natural fractures in the Barnett Shale and their importance for hydraulic fracture treatments", *AAPG bulletin*, v. 91, n. 4, pp. 603–622.

GANDOSSI, L., 2013, "An overview of hydraulic fracturing and other formation stimulation technologies for shale gas production", *Eur. Commisison Jt. Res. Cent. Tech. Reports*.

GARCIA, F., SÁEZ, A., DOMINGUEZ, J., 2004, "Traction boundary elements for cracks in anisotropic solids", *Engineering analysis with boundary elements*, v. 28, n. 6, pp. 667–676.

GEERTSMA, J., DE KLERK, F., OTHERS, 1969, "A rapid method of predicting width and extent of hydraulically induced fractures", *Journal of Petroleum Technology*, v. 21, n. 12, pp. 1–571.

GHAJARI, M., IANNUCCI, L., CURTIS, P., 2014, "A peridynamic material model for the analysis of dynamic crack propagation in orthotropic media", *Computer Methods in Applied Mechanics and Engineering*, v. 276, pp. 431–452.

GHASSEMI, A., ROEGIERS, J., 1996, *Three-dimensional poroelastic hydraulic fracture simulation using the displacement discontinuity method*. PhD Thesis, University of Oklahoma.

GONZALEZ-CHAVEZ, M., DAHI TALEGHANI, A., OLSON, J., et al., 2015, "A Cohesive Model for Modeling Hydraulic Fractures in Naturally Fractured Formations". In: *SPE Hydraulic Fracturing Technology Conference*. Society of Petroleum Engineers.

GORDELIY, E., PEIRCE, A., 2013, "Coupling schemes for modeling hydraulic fracture propagation using the XFEM", *Computer Methods in Applied Mechanics and Engineering*, v. 253, pp. 305–322.

GRAVOUIL, A., MOËS, N., BELYTSCHKO, T., 2002, "Non-planar 3D crack growth by the extended finite element and level setsŮPart II: Level set update", *International Journal for Numerical Methods in Engineering*, v. 53, n. 11, pp. 2569–2586.

GREBE, J., STOESSER, M., 1935, "Increasing crude production 20,000,000 bbl. from established fields", *World Petroleum J*, pp. 473–82.

GREGORY, K. B., VIDIC, R. D., DZOMBAK, D. A., 2011, "Water management challenges associated with the production of shale gas by hydraulic fracturing", *Elements*, v. 7, n. 3, pp. 181–186.

GRIFFITH, A., 1921, "The phenomena of rupture and flow in solids", *Philosophical transactions of the royal society of london. Series A, containing papers of a mathematical or physical character*, v. 221, pp. 163–198.

GU, M., DAO, E., MOHANTY, K., 2015, "Investigation of ultra-light weight proppant application in shale fracturing", *Fuel*, v. 150, pp. 191–201.

GUTIERREZ, M., LEWIS, R., MASTERS, I., et al., 2001, "Petroleum reservoir simulation coupling fluid flow and geomechanics", *SPE Reservoir Evaluation & Engineering*, v. 4, n. 03, pp. 164–172.

HADDAD, M., SEPEHRNOORI, K., 2015a, "Simulation of hydraulic fracturing in quasi-brittle shale formations using characterized cohesive layer: Stimulation controlling factors", *Journal of Unconventional Oil and Gas Resources*, v. 9, pp. 65–83.

HADDAD, M., SEPEHRNOORI, K., 2015b, "Integration of XFEM and CZM to Model 3D Multiple-Stage Hydraulic Fracturing in Quasi-brittle Shale Formations: Solution-Dependent Propagation Direction". In: *Proceedings of the AADE National Technical Conference and Exhibition, AADE2015, San Antonio, Texas, 8-9 April 2015*, b.

HADDAD, M., DU, J., VIDAL-GILBERT, S., et al., 2016, "Integration of dynamic microseismic data with a true 3D modeling of hydraulic fracture propagation in Vaca Muerta Shale". In: *SPE Hydraulic Fracturing Technology Conference*. Society of Petroleum Engineers.

HALLQUIST, J. O., OTHERS, 2007, "LS-DYNA keyword user's manual", *Livermore Software Technology Corporation*, v. 970.

HANSBO, A., HANSBO, P., 2004, "A finite element method for the simulation of strong and weak discontinuities in solid mechanics", *Computer methods in applied mechanics and engineering*, v. 193, n. 33, pp. 3523–3540.

HARELAND, G., RAMPERSAD, P., DHARAPHOP, J., et al., 1993, "Hydraulic fracturing design optimization". In: *SPE Eastern Regional Meeting*. Society of Petroleum Engineers.

HATTORI, G., TREVELYAN, J., AUGARDE, C. E., et al., 2017, "Numerical simulation of fracking in shale rocks: current state and future approaches", *Archives of Computational Methods in Engineering*, v. 24, n. 2, pp. 281–317.

HILLERBORG, A., 1978, "A model for fracture analysis", *Report TVBM*.

HILLERBORG, A., 1983, "Analysis of one single crack", *Fracture Mechanics of Concrete (Developments in civil engineering)*, pp. 223–249.

HILLERBORG, A., 1985, "The theoretical basis of a method to determine the fracture energyG F of concrete", *Materials and structures*, v. 18, n. 4, pp. 291–296.

HILLERBORG, A., MODER, M., PETERSSON, P.-E., 1976, "Analysis of crack formation and crack growth in concrete by means of fracture mechanics and finite elements", *Cement and concrete research*, v. 6, n. 6, pp. 773–781.

HOSSAIN, M., RAHMAN, M., RAHMAN, S., 2000, "Hydraulic fracture initiation and propagation: roles of wellbore trajectory, perforation and stress regimes", *Journal of Petroleum Science and Engineering*, v. 27, n. 3, pp. 129–149.

HOWARTH, R. W., INGRAFFEA, A., ENGELDER, T., 2011, "Natural gas: Should fracking stop?" *Nature*, v. 477, n. 7364, pp. 271–275.

HUANG, J., GRIFFITHS, D., WONG, S.-W., 2012, "Initiation pressure, location and orientation of hydraulic fracture", *International Journal of Rock Mechanics and Mining Sciences*, v. 49, pp. 59–67.

INGLIS, C., 1997, "Stresses in a plate due to the presence of cracks and sharp corners", *Spie Milestone series MS*, v. 137, pp. 3–17.

INGRAFFEA, A. R., HEUZ, F. E., KO, H.-Y., et al., 1977, "An analysis of discrete fracture propagation in rock loaded in compression". In: *The 18th US Symposium on Rock Mechanics (USRMS)*. American Rock Mechanics Association.

INGRAFFEA, A., SAOUMA, V., 1985, "Numerical modeling of discrete crack propagation in reinforced and plain concrete". In: *Fracture mechanics of concrete: structural application and numerical calculation*, Springer, pp. 171–225.

IRWIN, G., 1948, "Fracture Dynamics, Fracture of Metals", *American Society for Metals*, pp. 147–166.

IRWIN, G., 1957, "Analysis of Stress and Strain near the End of a Crack Traversing a Plate", *Journal of Applied Mechanics*, v. 24, pp. 361–364.

IRWIN, G., 1997a, "Analysis of stresses and strains near the end of a crack traversing a plate", *Spie Milestone series MS*, v. 137, n. 167-170, pp. 16.

IRWIN, G., 1997b, "Plastic zone near a crack and fracture toughness", *Proceedings of the 7th Sagamore Research Conference, New York*.

IRZAL, F., REMMERS, J., HUYGHE, J., et al., 2010, "A two-scale approach for propagating cracks in a fluid-saturated porous material". In: *IOP Conference Series: Materials Science and Engineering*, v. 10, p. 012044. IOP Publishing.

IZADI, G., GAITHER, M., CRUZ, L., et al., 2015, "Fully 3D Hydraulic Fracturing Model: Optimizing Sequence Fracture Stimulation in Horizontal Wells". In: *49th US Rock Mechanics/Geomechanics Symposium*. American Rock Mechanics Association.

JAEGER, J. C., COOK, N. G., ZIMMERMAN, R., 2009, *Fundamentals of rock mechanics*. John Wiley & Sons.

JENKINS, A., FATHI, E., BELYADI, F., 2016, "Stress field behavior induced by hydraulic fracture in shale reservoirs: A practical view on cluster spacing", *Journal of Natural Gas Science and Engineering*.

JOUSSET, P., RACHIK, M., 2014, "Comparison and evaluation of two types of cohesive zone models for the finite element analysis of fracture propagation in industrial bonded structures", *Engineering Fracture Mechanics*, v. 132, pp. 48–69.

KAZERANI, T., 2011, *Micromechanical study of rock fracture and fragmentation under dynamic loads using discrete element method*. PhD Thesis, École Polytechnique Fédérale de Lausanne.

KEMENY, J., COOK, N., 1986, *Crack models for the failure of rocks in compression*. Relatório técnico, Lawrence Berkeley Lab., CA (USA).

KESHAVARZI, R., MOHAMMADI, S., BAYESTEH, H., et al., 2012, "Hydraulic fracture propagation in unconventional reservoirs: the role of natural fractures". In: *46th US Rock Mechanics/Geomechanics Symposium*. American Rock Mechanics Association.

KHOEI, A., 2014, *Extended finite element method: theory and applications*. John Wiley & Sons.

KHOEI, A., MOHAMMADNEJAD, T., 2011, "Numerical modeling of multiphase fluid flow in deforming porous media: A comparison between two-and three-phase models for seismic analysis of earth and rockfill dams", *Computers and Geotechnics*, v. 38, n. 2, pp. 142–166.

KHOEI, A., HIRMAND, M., VAHAB, M., et al., 2015, "An enriched FEM technique for modeling hydraulically driven cohesive fracture propagation in impermeable media with frictional natural faults: Numerical and experimental investigations", *International Journal for Numerical Methods in Engineering*, v. 104, n. 6, pp. 439–468.

KHOSROKHAVAR, R., GRIFFITHS, S., WOLF, K.-H., 2014, "Shale gas formations and their potential for carbon storage: opportunities and outlook", *Environmental Processes*, v. 1, n. 4, pp. 595–611.

KHRISTIANOVIC, S., ZHELTOV, A., 1955, "3. Formation of Vertical Fractures by Means of Highly Viscous Liquid". In: *4th World Petroleum Congress*. World Petroleum Congress.

KIM, T. H., CHO, J., LEE, K. S., 2017, "Evaluation of CO 2 injection in shale gas reservoirs with multi-component transport and geomechanical effects", *Applied Energy*, v. 190, pp. 1195–1206.

KNOPS, H., 1994, *Numerical simulation of crack growth in pressurized fuselages*. TU Delft, Delft University of Technology.

KUMAR, D., GHASSEMI, A., 2016a, "A three-dimensional analysis of simultaneous and sequential fracturing of horizontal wells", *Journal of Petroleum Science and Engineering*.

KUMAR, D., GHASSEMI, A., 2016b, "A three-dimensional analysis of simultaneous and sequential fracturing of horizontal wells", *Journal of Petroleum Science and Engineering*, v. 146, pp. 1006–1025.

LACAZETTE, A., ENGELDER, T., 1992, "Fluid-driven cyclic propagation of a joint in the Ithaca siltstone, Appalachian Basin, New York", *International Geophysics*, v. 51, pp. 297–323.

LECAMPION, B., 2009, "An extended finite element method for hydraulic fracture problems", *Communications in Numerical Methods in Engineering*, v. 25, n. 2, pp. 121–133.

LEMAITRE, J., CHABOCHE, J.-L., 1994, *Mechanics of solid materials*. Cambridge university press.

LEWIS, R. W., SCHREFLER, B. A., 1998, *The finite element method in the static and dynamic deformation and consolidation of porous media*. John Wiley.

LI, F., SHIH, C., NEEDLEMAN, A., 1985, "A comparison of methods for calculating energy release rates", *Engineering Fracture Mechanics*, v. 21, n. 2, pp. 405–421.

LISJAK, A., GRASSELLI, G., 2014, "A review of discrete modeling techniques for fracturing processes in discontinuous rock masses", *Journal of Rock Mechanics and Geotechnical Engineering*, v. 6, n. 4, pp. 301–314.

MAHGEREFTEH, H., BROWN, S., DENTON, G., 2012, "Modelling the impact of stream impurities on ductile fractures in CO 2 pipelines", *Chemical engineering science*, v. 74, pp. 200–210.

MALVERN, L. E., 1969, *Introduction to the Mechanics of a Continuous Medium*. N. Monograph.

MANCHANDA, R., 2015, *A general poro-elastic model for pad-scale fracturing of horizontal wells*. PhD Thesis.

MANCHANDA, R., SHARMA, M. M., OTHERS, 2014, "Impact of Completion Design on Fracture Complexity in Horizontal Shale Wells", *SPE Drilling & Completion*, v. 29, n. 01, pp. 78–87.

MANSUR, W. J., 1983, *A time-stepping technique to solve wave propagation problems using the boundary element method*. PhD Thesis, University of Southampton.

MARIANI, S., PEREGO, U., 2003, "Extended finite element method for quasi-brittle fracture", *International Journal for Numerical Methods in Engineering*, v. 58, n. 1, pp. 103–126.

MAZARS, J., PIJAUDIER-CABOT, G., 1989, "Continuum damage theory-application to concrete", *Journal of Engineering Mechanics*, v. 115, n. 2, pp. 345–365.

MCCLURE, M. W., 2012, *Modeling and characterization of hydraulic stimulation and induced seismicity in geothermal and shale gas reservoirs*. PhD Thesis, Stanford University Stanford, California.

MEYER, B. R., BAZAN, L. W., OTHERS, 2011, "A discrete fracture network model for hydraulically induced fractures-theory, parametric and case studies". In: *SPE Hydraulic Fracturing Technology Conference*. Society of Petroleum Engineers.

MOËS, N, D. J., BELYTSCHKO, T., 1999, "A finite element method for crack growth without remeshing", *International journal for numerical methods in engineering*, v. 46, n. 1, pp. 131–150.

MOËS, N., BELYTSCHKO, T., 2002, "Extended finite element method for cohesive crack growth", *Engineering fracture mechanics*, v. 69, n. 7, pp. 813–833.

MOËS, N., GRAVOUIL, A., BELYTSCHKO, T., 2002, "Non-planar 3D crack growth by the extended finite element and level setsŮPart I: Mechanical model", *International Journal for Numerical Methods in Engineering*, v. 53, n. 11, pp. 2549–2568.

MOHAMMADI, S., 2008, *Extended finite element method: for fracture analysis of structures*. John Wiley & Sons.

MOHAMMADNEJAD, T., KHOEI, A., 2013, "An extended finite element method for hydraulic fracture propagation in deformable porous media with the cohesive crack model", *Finite Elements in Analysis and Design*, v. 73, pp. 77–95.

MOOS, D., 2006, "Geomechanics applied to drilling engineering", *Petroleum engineering handbook*, v. 2.

NAGEL, N., SHEIBANI, F., LEE, B., et al., 2014, "Fully-Coupled Numerical Evaluations of Multiwell Completion Schemes: The Critical Role of In-Situ Pressure Changes and Well Configuration". In: *SPE Hydraulic Fracturing Technology Conference*. Society of Petroleum Engineers.

NAGEL, N., SANCHEZ-NAGEL, M., ZHANG, F., et al., 2013, "Coupled numerical evaluations of the geomechanical interactions between a hydraulic fracture stimulation and a natural fracture system in shale formations", *Rock mechanics and rock engineering*, v. 46, n. 3, pp. 581–609.

NAGEL, N. B., GIL, I., SANCHEZ-NAGEL, M., et al., 2011, "Simulating Hydraulic Fracturing in Real Fractured Rocks-Overcjavascript: overcoming the Limits

of Pseudo3D Models". In: *SPE Hydraulic Fracturing Technology Conference*. Society of Petroleum Engineers.

NEEDLEMAN, A., 1987, "A continuum model for void nucleation by inclusion debonding", *Journal of applied mechanics*, v. 54, n. 3, pp. 525–531.

NORDGREN, R., OTHERS, 1972, "Propagation of a vertical hydraulic fracture", *Society of Petroleum Engineers Journal*, v. 12, n. 04, pp. 306–314.

OLIVER, J., 1996, "Modelling strong discontinuities in solid mechanics via strain softening constitutive equations. Part 1: Fundamentals", *International journal for numerical methods in engineering*, v. 39, n. 21, pp. 3575–3600.

OLSEN, T. N., BRATTON, T. R., THIERCELIN, M. J., et al., 2009, "Quantifying proppant transport for complex fractures in unconventional formations". In: *SPE Hydraulic Fracturing Technology Conference*. Society of Petroleum Engineers.

OROWAN, E., 1949, "Fracture and strength of solids", *Reports on progress in physics*, v. 12, n. 1, pp. 185.

ORTIZ, M., LEROY, Y., NEEDLEMAN, A., 1987, "A finite element method for localized failure analysis", *Computer methods in applied mechanics and engineering*, v. 61, n. 2, pp. 189–214.

OUCHI, H., 2016, *Development of peridynamics-based hydraulic fracturing model for fracture growth in heterogeneous reservoirs*. PhD Thesis.

OUCHI, H., KATIYAR, A., FOSTER, J., et al., 2015a, "A peridynamics model for the propagation of hydraulic fractures in heterogeneous, naturally fractured reservoirs". In: *SPE Hydraulic Fracturing Technology Conference*. Society of Petroleum Engineers, a.

OUCHI, H., KATIYAR, A., YORK, J., et al., 2015b, "A fully coupled porous flow and geomechanics model for fluid driven cracks: a peridynamics approach." *Computational Mechanics*, v. 55, n. 3.

OUCHI, H., AGRAWAL, S., FOSTER, J. T., et al., 2017a, "Effect of Small Scale Heterogeneity on the Growth of Hydraulic Fractures". In: *SPE Hydraulic Fracturing Technology Conference and Exhibition*. Society of Petroleum Engineers, a.

OUCHI, H., FOSTER, J. T., SHARMA, M. M., 2017b, "Effect of reservoir heterogeneity on the vertical migration of hydraulic fractures", *Journal of Petroleum Science and Engineering*, v. 151, pp. 384–408.

PADULA, V., 1969, "Oil shale of Permian Irati Formation, Brazil", *AAPG Bulletin*, v. 53, n. 3, pp. 591–602.

PAPANASTASIOU, P., 1997, "The influence of plasticity in hydraulic fracturing", *International Journal of Fracture*, v. 84, n. 1, pp. 61–79.

PAPANASTASIOU, P., 1999, "An efficient algorithm for propagating fluid-driven fractures", *Computational Mechanics*, v. 24, n. 4, pp. 258–267.

PARK, K., 2009, *Potential-based fracture mechanics using cohesive zone and virtual internal bond modeling*. University of Illinois at Urbana-Champaign.

PARMIGIANI, J., THOULESS, M., 2007, "The effects of cohesive strength and toughness on mixed-mode delamination of beam-like geometries", *Engineering Fracture Mechanics*, v. 74, n. 17, pp. 2675–2699.

PEIRCE, A., . B. A., 2015a, "Interference Fracturing: Nonuniform Distributions of Perforation Clusters That Promote Simultaneous Growth of Multiple Hydraulic Fractures", *SPE Journal*, v. 20, n. 02, pp. 384–395.

PEIRCE, A, B. A., 2015b, "Interference fracturing: Non-uniform distributions of perforation clusters that promote simultaneous growth of multiple hydraulic fractures", *SPE Journal*, v. 20, n. 02, pp. 1028–1040.

PERKINS, T., KERN, L., OTHERS, 1961, "Widths of hydraulic fractures", *Journal of Petroleum Technology*, v. 13, n. 09, pp. 937–949.

PETIT, J.-P., BARQUINS, M., 1988, "Can natural faults propagate under mode II conditions?" *Tectonics*, v. 7, n. 6, pp. 1243–1256.

POLLARD, D., AYDIN, A., 1988, "Progress in understanding jointing over the past century", *GSA Bulletin*, v. 100, n. 8, pp. 1181–1204.

POTYONDY, D., CUNDALL, P., 2004, "A bonded-particle model for rock", *International journal of rock mechanics and mining sciences*, v. 41, n. 8, pp. 1329–1364.

QIU, F., PORCU, M. M., XU, J., et al., 2015, "Simulation study of zipper fracturing using an unconventional fracture model". In: *SPE/CSUR Unconventional Resources Conference*. Society of Petroleum Engineers.

RABCZUK, T., ZI, G., GERSTENBERGER, A., et al., 2008, "A new crack tip element for the phantom-node method with arbitrary cohesive cracks", *International Journal for Numerical Methods in Engineering*, v. 75, n. 5, pp. 577–599. ISSN: 1097-0207.

RABCZUK, T., BORDAS, S., ZI, G., 2010, "On three-dimensional modelling of crack growth using partition of unity methods", *Computers & structures*, v. 88, n. 23, pp. 1391–1411.

RAFIEE, M., SOLIMAN, M., PIRAYESH, E., et al., 2012, "Hydraulic fracturing design and optimization: a modification to zipper frac". In: *SPE Annual Technical Conference and Exhibition*. Society of Petroleum Engineers.

REMMERS, J., 2006, *Discontinuities in materials and structures: a unifying computational approach*. TU Delft, Delft University of Technology.

REMMERS, J., DE BORST, R., NEEDLEMAN, A., 2003, "A cohesive segments method for the simulation of crack growth", *Computational mechanics*, v. 31, n. 1-2, pp. 69–77.

REMMERS, J., DE BORST, R., NEEDLEMAN, A., 2008, "The simulation of dynamic crack propagation using the cohesive segments method", *Journal of the Mechanics and Physics of Solids*, v. 56, n. 1, pp. 70–92.

RÉTHORÉ, J., DE BORST, R., ABELLAN, M.-A., 2008, "A two-scale model for fluid flow in an unsaturated porous medium with cohesive cracks", *Computational Mechanics*, v. 42, n. 2, pp. 227–238.

REZAEI, A., RAFIEE, M., SOLIMAN, M., et al., 2015, "Investigation of Sequential and Simultaneous Well Completion in Horizontal Wells using a Non-planar, Fully Coupled Hydraulic Fracture Simulator". In: *49th US Rock Mechanics/Geomechanics Symposium*. American Rock Mechanics Association.

RICE, J. R., 1968, "A path independent integral and the approximate analysis of strain concentration by notches and cracks", *Journal of applied mechanics*, v. 35, n. 2, pp. 379–386.

RICE, J. R., CLEARY, M. P., 1976, "Some basic stress diffusion solutions for fluid-saturated elastic porous media with compressible constituents", *Reviews of Geophysics*, v. 14, n. 2, pp. 227–241.

RIOS, A., GUTIERREZ, G., NAGEL, N., et al., 2013, "Stress Shadow Evaluations For Chicontepec–Evaluating New Completion Options". In: *47th US Rock Mechanics/Geomechanics Symposium*. American Rock Mechanics Association.

ROKHLIN, V., 1985, "Rapid solution of integral equations of classical potential theory", *Journal of computational physics*, v. 60, n. 2, pp. 187–207.

ROUSSEL, N. P., SHARMA, M. M., OTHERS, 2011, "Strategies to minimize frac spacing and stimulate natural fractures in horizontal completions". In: *SPE Annual Technical Conference and Exhibition*. Society of Petroleum Engineers.

RUBIN, A., 1995, "Propagation of magma-filled cracks", *Annual Review of Earth and Planetary Sciences*, v. 23, pp. 287–336.

RUNGAMORNRAT, J., WHEELER, M. F., MEAR, M. E., et al., 2005, "Coupling of fracture/non-newtonian flow for simulating nonplanar evolution of hydraulic fractures". In: *SPE Annual Technical Conference and Exhibition*. Society of Petroleum Engineers.

SAGONG, M., BOBET, A., 2002, "Coalescence of multiple flaws in a rock-model material in uniaxial compression", *International Journal of Rock Mechanics and Mining Sciences*, v. 39, n. 2, pp. 229–241.

SARRIS, E., PAPANASTASIOU, P., 2011, "Modeling of hydraulic fracturing in a poroelastic cohesive formation", *International Journal of Geomechanics*, v. 12, n. 2, pp. 160–167.

SCHEIDER, I., 2001, "Cohesive model for crack propagation analyses of structures with elastic–plastic material behavior Foundations and implementation", *GKSS research center, Geesthacht*.

SCHELLEKENS, J., DE BORST, R., 1993, "On the numerical integration of interface elements", *International Journal for Numerical Methods in Engineering*, v. 36, n. 1, pp. 43–66.

SCHWALBE, K.-H., SCHEIDER, I., CORNEC, A., 2012, *Guidelines for applying cohesive models to the damage behaviour of engineering materials and structures*. Springer Science & Business Media.

SECCHI, S., SCHREFLER, B., 2012, "A method for 3-D hydraulic fracturing simulation", *International journal of fracture*, v. 178, n. 1-2, pp. 245–258.

SESETTY, V., GHASSEMI, A., 2015, "A numerical study of sequential and simultaneous hydraulic fracturing in single and multi-lateral horizontal wells", *Journal of Petroleum Science and Engineering*, v. 132, pp. 65–76.

SESETTY, V., GHASSEMI, A., OTHERS, 2015, "Simulation of Simultaneous and Zipper Fractures in Shale Formations". In: *49th US Rock Mechanics/Geomechanics Symposium*. American Rock Mechanics Association.

SETHIAN, J., 1999, *Level set methods and fast marching methods: evolving interfaces in computational geometry, fluid mechanics, computer vision, and materials science*, v. 3. Cambridge university press.

SETTARI, A., PRICE, H., OTHERS, 1984, "Simulation of hydraulic fracturing in low-permeability reservoirs", *Society of Petroleum Engineers Journal*, v. 24, n. 02, pp. 141–152.

SETTARI, A., OTHERS, 1985, "A new general model of fluid loss in hydraulic fracturing", *Society of Petroleum Engineers Journal*, v. 25, n. 04, pp. 491–501.

SHARMA, M., MANCHANDA, R., OTHERS, 2015, "The Role of Induced Un-propped (IU) Fractures in Unconventional Oil and Gas Wells". In: *SPE Annual Technical Conference and Exhibition*. Society of Petroleum Engineers.

SHIH, C., HUTCHINSON, J., 1976, "Fully plastic solutions and large scale yielding estimates for plane stress crack problems", *Journal of Engineering Materials and Technology*, v. 98, n. 4, pp. 289–295.

SHOJAEI, A., DAHI-TALEGHANI, A., LI, G., 2014, "A continuum damage failure model for hydraulic fracturing of porous rocks", *International Journal of Plasticity*, v. 59, pp. 199–212.

SIERRA, J., KAURA, J., GUALTIERI, D., et al., 2008. "DTS Monitoring Data of Hydraulic Fracturing: Experiences and Lessons Learned. Paper SPE 116182 presented at the SPE Annual Technical Conference and Exhibition, Denver, 21–24 September". .

SIH, G., 1973, "Some basic problems in fracture mechanics and new concepts", *Engineering fracture mechanics*, v. 5, n. 2, pp. 365–377.

SILLING, S., WECKNER, O., ASKARI, E., et al., 2010, "Crack nucleation in a peridynamic solid", *International Journal of Fracture*, v. 162, n. 1, pp. 219–227.

SILLING, S. A., 2000, "Reformulation of elasticity theory for discontinuities and long-range forces", *Journal of the Mechanics and Physics of Solids*, v. 48, n. 1, pp. 175–209.

SILLING, S. A., EPTON, M., WECKNER, O., et al., 2007, "Peridynamic states and constitutive modeling", *Journal of Elasticity*, v. 88, n. 2, pp. 151–184.

SIMMONS, G., RICHTER, D., 1976, "Microcracks in rocks", *The physics and chemistry of minerals and rocks*, pp. 105–137.

SIMO, J., OLIVER, J., ARMERO, F., 1993, "An analysis of strong discontinuities induced by strain-softening in rate-independent inelastic solids", *Computational mechanics*, v. 12, n. 5, pp. 277–296.

SIMPSON, R., TREVELYAN, J., 2011, "A partition of unity enriched dual boundary element method for accurate computations in fracture mechanics", *Computer Methods in Applied Mechanics and Engineering*, v. 200, n. 1, pp. 1–10.

SNEDDON, I., 1946, "The distribution of stress in the neighbourhood of a crack in an elastic solid". In: *Proceedings of the Royal Society of London A: Mathematical, Physical and Engineering Sciences*, v. 187, pp. 229–260. The Royal Society.

SOLIMAN, M., RAFIEE, M., PIRAYESH, E., 2013. "Methods and Devices for Hydraulic Fracturing Design and Optimization: A Modification to Zipper Frac". ago. 20. US Patent App. 13/970,880.

SOLIMAN, M., EAST, L., AUGUSTINE, J., et al., 2010, "Fracturing design aimed at enhancing fracture complexity". In: *SPE EUROPEC/EAGE Annual Conference and Exhibition*. Society of Petroleum Engineers.

SONG, J.-H., AREIAS, P., BELYTSCHKO, T., 2006, "A method for dynamic crack and shear band propagation with phantom nodes", *International Journal for Numerical Methods in Engineering*, v. 67, n. 6, pp. 868–893.

SOOKPRASONG, P., GILL, C. C., HURT, R. S., et al., 2014, "Lessons Learned from DAS and DTS in Multicluster, Multistage Horizontal Well Fracturing: Interpretation of Hydraulic Fracture Initiation and Propagation through Diagnostics". In: *IADC/SPE Asia Pacific Drilling Technology Conference*. Society of Petroleum Engineers.

SØRENSEN, B., JACOBSEN, T., 2003, "Determination of cohesive laws by the J integral approach", *Engineering fracture mechanics*, v. 70, n. 14, pp. 1841–1858.

SPAIN, D. R., GIL, I. R., SEBASTIAN, H. M., et al., 2015, "Geo-Engineered completion optimization: An integrated, multi-disciplinary approach to improve stimulation efficiency in unconventional shale reservoirs". In: *SPE Middle East Unconventional Resources Conference and Exhibition*. Society of Petroleum Engineers.

SRIVASTAVA, D., ENGELDER, T., 1991, "Fluid evolution history of brittle-ductile shear zones on the hanging wall of Yellow Spring Thrust, Valley and Ridge Province, Pennsylvania, USA", *Tectonophysics*, v. 198, n. 1, pp. 23–34.

STEVENS, P., 2012, "The shale gas revolution: Developments and changes", *Chatham House*, pp. 2–3.

STOLARSKA, M., CHOPP, D., MOËS, N., et al., 2001, "Modelling crack growth by level sets in the extended finite element method", *International journal for numerical methods in Engineering*, v. 51, n. 8, pp. 943–960.

SUKUMAR, N., MOËS, N., MORAN, B., et al., 2000, "Extended finite element method for three-dimensional crack modelling", *International Journal for Numerical Methods in Engineering*, v. 48, n. 11, pp. 1549–1570.

SUKUMAR, N., HUANG, Z., PRÉVOST, J.-H., et al., 2004, "Partition of unity enrichment for bimaterial interface cracks", *International journal for numerical methods in engineering*, v. 59, n. 8, pp. 1075–1102.

TAHERI-SHAKIB, J., GHADERI, A., HOSSEINI, S., et al., 2016, "Debonding and coalescence in the interaction between hydraulic and natural fracture: Accounting for the effect of leak-off", *Journal of Natural Gas Science and Engineering*, v. 36, pp. 454–462.

TALEGHANI, A. D., 2009, *Analysis of hydraulic fracture propagation in fractured reservoirs: an improved model for the interaction between induced and natural fractures*. PhD Thesis, The University of Texas at Austin.

TELLES, J. C. F., 2012, *The boundary element method applied to inelastic problems*, v. 1. Springer Science & Business Media.

TERZAGHI, K., PECK, R., MESRI, G., 1996, *Soil mechanics in engineering practice*. John Wiley & Sons.

TREVELYAN, J., 1994, *Boundary elements for engineers: theory and applications*, v. 1. Computational Mechanics.

TVERGAARD, V., HUTCHINSON, J., 1992, "The relation between crack growth resistance and fracture process parameters in elastic-plastic solids", *Journal of the Mechanics and Physics of Solids*, v. 40, n. 6, pp. 1377–1397.

UNGER, J., ECKARDT, S., KÖNKE, C., 2007, "Modelling of cohesive crack growth in concrete structures with the extended finite element method", *Computer Methods in Applied Mechanics and Engineering*, v. 196, n. 41, pp. 4087–4100.

UNITED STATES, ENERGY INFORMATION ADMINISTRATION, 2011, *World shale gas resources: an initial assessment of 14 regions outside the United States*. US Department of Energy.

VAHAB, M., KHALILI, N., 2017, "Numerical investigation of the flow regimes through hydraulic fractures using the X-FEM technique", *Engineering Fracture Mechanics*, v. 169, pp. 146–162.

VALK, P., ECONOMIDES, M., 1995, *Hydraulic fracture mechanics*. Wiley, New York.

VAN DAM, D., DE PATER, C., ROMIJN, R., 1997, "Experimental study of the impact of plastic rock deformation on hydraulic fracture geometry". In: *International Journal of Rock Mechanics and Mining Sciences and Geomechanics Abstracts*, v. 3, p. 439.

VEATCH JR, R., MOSCHOVIDIS, Z., 1986, "An overview of recent advances in hydraulic fracturing technology". In: *International Meeting on Petroleum Engineering*. Society of Petroleum Engineers.

VENGOSH, A., JACKSON, R. B., WARNER, N., et al., 2014, "A critical review of the risks to water resources from unconventional shale gas development and hydraulic fracturing in the United States", *Environmental science & technology*, v. 48, n. 15, pp. 8334–8348.

VERDE, A., GHASSEMI, A., 2015, "Modeling injection/extraction in a fracture network with mechanically interacting fractures using an efficient displacement discontinuity method", *International Journal of Rock Mechanics and Mining Sciences*, v. 77, pp. 278–286.

VERMEER, P., VERRUIJT, A., 1981, "An accuracy condition for consolidation by finite elements", *International Journal for numerical and analytical methods in geomechanics*, v. 5, n. 1, pp. 1–14.

VERMYLEN, J., ZOBACK, M., OTHERS, 2011, "Hydraulic fracturing, microseismic magnitudes, and stress evolution in the Barnett Shale, Texas, USA". In: *SPE Hydraulic Fracturing Technology Conference*. Society of Petroleum Engineers.

WANG, H., 2016a, "Numerical investigation of fracture spacing and sequencing effects on multiple hydraulic fracture interference and coalescence in brittle and ductile reservoir rocks", *Engineering Fracture Mechanics*, v. 157, pp. 107–124.

WANG, H., 2015, "Numerical modeling of non-planar hydraulic fracture propagation in brittle and ductile rocks using XFEM with cohesive zone method", *Journal of Petroleum Science and Engineering*, v. 135, pp. 127–140.

WANG, H., 2016b, "Numerical investigation of fracture spacing and sequencing effects on multiple hydraulic fracture interference and coalescence in brittle and ductile reservoir rocks", *Engineering Fracture Mechanics*, v. 157, pp. 107–124.

WANG, M., FENG, Y., WANG, C., 2017, "Numerical investigation of initiation and propagation of hydraulic fracture using the coupled Bonded Particle–Lattice Boltzmann Method", *Computers & Structures*, v. 181, pp. 32–40.

WARPINSKI, N., BRANAGAN, P., OTHERS, 1989, "Altered-stress fracturing", *Journal of Petroleum Technology*, v. 41, n. 09, pp. 990–997.

WARPINSKI, N., MAYERHOFER, M., VINCENT, M., et al., 2009, "Stimulating unconventional reservoirs: Maximizing network growth while optimizing fracture conductivity", *Journal of Canadian Petroleum Technology*, v. 48, n. 10, pp. 39–51.

WEBER, N., 2016, *The XFEM for hydraulic fracture mechanics*. PhD Thesis, Dissertation, Rheinisch-Westfälische Technische Hochschule Aachen, 2016.

WEIJERS, L., 1995, *The near-wellbore geometry of hydraulic fractures initiated from horizontal and deviated wells*. PhD Thesis, TU Delft, Delft University of Technology.

WELLS, G., SLUYS, L., 2001, "A new method for modelling cohesive cracks using finite elements", *International Journal for Numerical Methods in Engineering*, v. 50, n. 12, pp. 2667–2682.

WENG, X., 2015, "Modeling of complex hydraulic fractures in naturally fractured formation", *Journal of Unconventional Oil and Gas Resources*, v. 9, pp. 114–135.

WENG, X., SIEBRITS, E., OTHERS, 2007, "Effect of production-induced stress field on refracture propagation and pressure response". In: *SPE Hydraulic Fracturing Technology Conference*. Society of Petroleum Engineers.

WESTERGAARD, H., 1997, "Bearing pressures and cracks", *Spite milestone series MS*, v. 137, pp. 18–22.

WILLIAMS, M., 1961, "The bending stress distribution at the base of a stationary crack", *Journal of applied mechanics*, v. 28, n. 1, pp. 78–82.

WINEGARDEN, W., 2016, *Regulating the upstream energy industry*.

WRIGHT, C., DAVIS, E., WEIJERS, L., et al., 1998, "Downhole tiltmeter fracture mapping: a new tool for directly measuring hydraulic fracture dimensions". In: *SPE Annual Technical Conference and Exhibition*. Society of Petroleum Engineers.

WU, H., POLLARD, D. D., 2002, "Imaging 3-D fracture networks around boreholes", *AAPG bulletin*, v. 86, n. 4, pp. 593–604.

WU, K., OLSON, J., BALHOFF, M. T., et al., 2016, "Numerical Analysis for Promoting Uniform Development of Simultaneous Multiple-Fracture Propagation in Horizontal Wells", *SPE Production & Operations*.

WU, R., KRESSE, O., WENG, X., et al., 2012, "Modeling of interaction of hydraulic fractures in complex fracture networks". In: *SPE Hydraulic Fracturing Technology Conference*. Society of Petroleum Engineers.

XIAO, Q., KARIHALOO, B., 2006, "Improving the accuracy of XFEM crack tip fields using higher order quadrature and statically admissible stress recovery", *International Journal for Numerical Methods in Engineering*, v. 66, n. 9, pp. 1378–1410.

XU, X.-P., NEEDLEMAN, A., 1993, "Void nucleation by inclusion debonding in a crystal matrix", *Modelling and Simulation in Materials Science and Engineering*, v. 1, n. 2, pp. 111.

XU, X.-P., NEEDLEMAN, A., 1994, "Numerical simulations of fast crack growth in brittle solids", *Journal of the Mechanics and Physics of Solids*, v. 42, n. 9, pp. 1397–1434.

YAO, Y., 2012, "Linear elastic and cohesive fracture analysis to model hydraulic fracture in brittle and ductile rocks", *Rock mechanics and rock engineering*, v. 45, n. 3, pp. 375–387.

ZANG, A., WAGNER, F. C., STANCHITS, S., et al., 2000, "Fracture process zone in granite", *Journal of Geophysical Research: Solid Earth*, v. 105, n. B10, pp. 23651–23661.

ZENG, Q., YAO, J., 2016, "Numerical simulation of fracture network generation in naturally fractured reservoirs", *Journal of Natural Gas Science and Engineering*, v. 30, pp. 430–443.

ZHANG, G., LIU, H., ZHANG, J., et al., 2010, "Three-dimensional finite element simulation and parametric study for horizontal well hydraulic fracture", *Journal of Petroleum Science and Engineering*, v. 72, n. 3, pp. 310–317.

ZHANG, X., JEFFREY, R. G., 2014, "Role of overpressurized fluid and fluid-driven fractures in forming fracture networks", *Journal of Geochemical Exploration*, v. 144, pp. 194–207.

ZHOU, F., MOLINARI, J.-F., SHIOYA, T., 2005, "A rate-dependent cohesive model for simulating dynamic crack propagation in brittle materials", *Engineering Fracture Mechanics*, v. 72, n. 9, pp. 1383–1410.

ZIENKIEWICZ, O., SHIOMI, T., 1984, "Dynamic behaviour of saturated porous media; the generalized Biot formulation and its numerical solution", *International journal for numerical and analytical methods in geomechanics*, v. 8, n. 1, pp. 71–96.

ZIMMERMAN, R. W., BODVARSSON, G. S., 1996, "Hydraulic conductivity of rock fractures", *Transport in porous media*, v. 23, n. 1, pp. 1–30.

ZOU, Y., ZHANG, S., MA, X., et al., 2016, "Numerical investigation of hydraulic fracture network propagation in naturally fractured shale formations", *Journal of Structural Geology*, v. 84, pp. 1–13.